TOPICS IN GENERAL RELATIVITY: THE HOOP CONJECTURE, AND THEORETICAL ASPECTS OF GRAVITATIONAL WAVE DETECTION.

Thesis by
Éanna E. Flanagan

In Partial Fulfillment of the Requirements
for the Degree of
Doctor of Philosophy

California Institute of Technology
Pasadena, California
1994
(Defended Sept 23, 1993)

Thesis Advisor:
Kip S. Thorne,
The Richard P. Feynman Professor
of Theoretical Physics

To my parents, Finola and Michael Flanagan.

Acknowledgments

Legend has it that many years ago in the place that we now call Caltech there lived a tribe called the Cohenim...

According to the oral tradition passed down to us, young warriors would come into their late adolescence to dwell with the Cohenim, and to pass through a lengthy and painful rite, in order to attain the honour of being called Chieftain, so that they could go off into the world to gain honour, some even to become Chiefs and to collect tribute called 'grants' from the Council of the Tribes...

During the ritual the young warrior would be guided by an older and, in some ways, wiser Chief of the Tribe who would protect him from all worldly concerns while the warrior honed his skills...

To become a chieftain the warrior would study the ways of the chief and help him with his hunts. The warrior would in this manner prepare himself. To complete the ritual he would need to make a kill on his own. Often the kill would require a few crucial arrows from the warrior's guiding chief, but it was traditional for the elders to turn their eyes from this.

Taken from the legend of Osci Basci, first set down by Richard Price.

To have been a student of Kip Thorne's has been, for me, a great privilege and also a great experience. I would like to thank him for the many hours he has spent trying to pass on some of his accumulated wisdom, for always being there to give much-needed advice, and for his warmth, support and encouragement. He has taught me much about how to think about, communicate, and "do" physics; but also by example he has taught me the importance of integrity, humility, and of treating with respect and dignity students and colleagues alike. These things I will not forget; I only hope that when I leave here I will carry with me some small fraction of his quality as a scientist and as an individual.

At Caltech and elsewhere many other people have unselfishly given of their time to help me learn. For patiently answering barrages of silly questions from me in classes or in their offices, and/or for many stimulating conversations about physics, I thank Roger Blandford, Steven Frautschi, Ted Jacobson, Jeff Kimble, Daniel Kennefick, Gunnar Klinkhammar, Draza Markovic, Amos Ori, Eric Poisson, John Preskill, Alice Quillen, Bharat Rhatra, Tom Roman, Jennie Traschen, Matt

Visser, and Bob Wald. I particularly want to thank Curt Cutler for his patience with a slow collaborator, for his friendship, and for the time he spent working with me and showing me the ropes. I thank Lars Bildsten for always having a ready ear, and for taking the time to explain a great many issues in astrophysics to an ignorant relativist. I also thank Fay Dowker for her hospitality when I was visiting Chicago.

I must mention Shirley Hampton and Donna Driscoll, who provided such a friendly and cheerful defense against the local bureaucracy.

I have been lucky enough to have had as friends here over the last few years Finbar Sheehy, Michael Lough, the never-conventional Barry Ryan, Chris Walter, Kate Schoelberg, Eric Poisson, Stuart Mc Muldroch, Srihari Murthy, Fatima Ebrahim and others. Thanks to you all for the times we have shared — especially lunches at Chandler, skiing, hangliding, cacophony, dinners, sessions in the Ath and Lucky Baldwins, running, and hiking; for helping me to laugh at aspects of graduate student life, and in general for preserving my sanity.

Life in Pasadena would to me be unthinkable without a place on the Chemistry GSC soccer team. To Amit Kumar, Tim Herzog and everyone else - thanks for all the exercise, and all the fun!

Back home in Dublin there are many people who come to mind. I dedicate this thesis to my parents, Finola and Michael Flanagan, as a small gesture of appreciation for their steady support, love, and encouragement over the years. I also undertake to give them an intelligible translation! I thank all my friends in Dublin - particularly Richard, Rory and Karen, and Larry and Dympna - for helping to make my regular trips home something to be looked forward to. My sister Niamh, my brother Cormac and Mum and Dad, and Richard and David at various times made the long trek to Pasadena and dragged me away from my work - táim buíoch díobh go léir.

Finally, my apologies to those I have omitted - you have not been forgotten.

This thesis consists of four main chapters concerned with two topics in general relativity: the formation of horizons in nonspherical gravitational collapse (chapters 2 and 3), and aspects of the effort to detect gravitational waves from cosmic sources (chapters 4 and 5). More specifically:

Chapters 2 and 3 deal with a conjecture, put forward in the early 1970's by Kip Thorne, concerning the formation of black-hole horizons. This so-called hoop conjecture states, in effect, that an event horizon will form around a collapsing body of mass M when and only when the body becomes smaller than $\sim GM/c^2$ (i.e., smaller than its "gravitational radius") in all three spatial dimensions. As an example, the conjecture implies that a long thin spindle can contract radially to arbitrarily high densities without forming a horizon. We show in chapter 2 that some static, axisymmetric solutions to Einstein's equations are consistent with this conjecture. We also discuss which particular mathematically precise statements of the conjecture look plausible and which do not. Chapter 3 considers solutions of Einstein's initial value equations — in particular solutions which are momentarily static, conformally flat and axisymmetric. We show for solutions of the initial-value equations that, whenever the minimum value of the circumferences (or of the square roots of the areas) of all surfaces surrounding the source region is greater than a constant times the "ADM mass," then none of the level surfaces of the conformal factor can be "outer trapped." This result is along the lines of the hoop conjecture.

In chapter 4 we identify the optimal data analysis method for searching for a stochastic background of gravitational waves with a network of laser-interferometer gravitational-wave detectors, and we analyze the network's sensitivity to the background radiation, paying particular attention to how this sensitivity depends on the the orientations of the detectors. We show, for example, that a pair of detectors which subtends an angle at the center of the Earth of $\lesssim 70°$ should for optimum sensitivity have their arms make angles of 45° (modulo 90°) with the arc of the great circle that joins them. Detectors which are separated farther should instead have one arm each aligned with this arc. We also show that the minimum detectable stochastic energy-density for the LIGO pair of detectors, with their planned orientations, is $\sim 3\%$ greater than what it would be if the orientations were optimal, and is ~ 4 times what it would be if their separation were $\lesssim$ a few kilometers instead of the actual distance of $\sim 3000\,\mathrm{km}$. In the frequency range $20\,\mathrm{Hz} \lesssim f \lesssim 70\,\mathrm{Hz}$, the sensitivity level of the LIGO detector pair at an advanced stage of development will be roughly $\Omega_{\mathrm{gw}} \sim 5 \times 10^{-10}$, which is about 4 orders of

magnitude worse than the likely level of relic waves produced during inflation.

Chapter 5 explores the information that can be extracted, by LIGO and its European companion VIRGO, from the gravitational waves emitted by inspiralling neutron-star/neutron-star binaries, neutron-star/black-hole binaries, and black-hole/black-hole binaries. We show, for example, that from the inspiral waveforms: (i) a particular combination of the binaries' two masses will be measurable to within $\sim 0.1\% - 1\%$, (ii) the individual masses will be measurable to within $\sim 10\%$, and (iii) the distance to the source will typically be measurable to within $\sim 30\%$.

Contents

Chapter 1

Introduction

The body of this thesis consists of four chapters (2 through 5), each of which is a paper that has been published in or submitted for publication to *Physical Review D*. I am the sole author of chapters 2, 3, and 4; Curt Cutler coauthored chapter 5 with me.

These four chapters deal with two topics in general relativity: the formation of horizons in nonspherical gravitational collapse (chapters 2 and 3), and some theoretical aspects of the effort to detect gravitational waves from cosmic sources (chapters 4 and 5). These four chapters were written largely for experts in the topics they cover. As an aid to general readers, I shall give in this introductory chapter some background information about chapters 2 through 5 and a nontechnical overview of their contents.

1 The hoop conjecture and cosmic censorship

Chapters 2 and 3 were in part motivated by the question of cosmic censorship [1]. I start this introduction with a brief discussion of the meaning and relevance of the cosmic censorship idea, and then describe the background for and the contents of chapters 2 and 3.

Consider as an example a binary system of two $10M_\odot$ black holes in a distant galaxy. Due to the singularity theorems of Hawking and Penrose [2], we can be reasonably confident that the black holes contain regions — the so-called singularities — where classical general relativity fails and whose behavior is governed by the as-yet-unknown laws that unify quantum mechanics and gravity. The black holes will spiral together and merge, emitting a strong burst of gravitational radiation. Their horizons will coalesce to form a single horizon, and presumably the singularities inside the holes will also merge; such black-hole mergers may in a decade's time be regularly detected by gravitational wave detectors [3]. Naively, one might expect that a successful description of this process would require an understanding of the black-hole singularities.

The by-now-conventional wisdom is of course the opposite: it is generally believed that in strong-gravitational-field situations, there is a *decoupling* between the high-curvature physics and the more familiar low-curvature physics, something akin to the renormalization paradigm of quantum field theory. The mechanism of this decoupling is that first suggested by Penrose [4]: the causal structure of the classical regions of spacetime generically prevents the high-curvature region from influencing distant, low curvature regions. Colloquially, the singularity is "hidden

behind the horizon," although it is equally valid in the example of the merging black holes to simply say that the singularities have not yet formed either before, during, or after the merger, which prevents their influencing the merger's outcome. Precise mathematical formulations of this cosmic-censorship conjecture [1] invoke the structure of the spacetime in the infinitely distant future, because the event horizon, behind which the singularity is conjectured to lie, is defined as the boundary of the region which can send signals to future null infinity. More loosely, however, one can ascribe an approximate physical meaning to cosmic censorship in a given, finite region of spacetime by asking whether or not high curvature (e.g., Planck-scale curvature) regions can causally influence low curvature regions in which physicists can live and perform experiments. It is only this approximate notion, obtained by specifying some high curvature scale, that can be probed by numerically integrating Einstein's equations.

Rather surprisingly, it is now known that in classical general relativity, low curvature initial data can evolve to form regions of *arbitrarily high* curvature that subsequently disperse leaving once more low curvature everywhere. This is an implication of the recent work of Choptuik and others [5] showing that suitably fine-tuned scalar-field initial data can form (or almost form) arbitrarily small black holes. Moreover, we know that Planck-scale curvatures will develop outside the horizon of a black hole at a sufficiently late stage in its evaporation [6]. However, both of these "counterexamples to cosmic censorship" essentially involve at most roughly one Planck volume of Planck-scale curvature. The physical question of whether or not a macroscopic gravitational field with source mass much greater than the Planck mass can ever terminate in a naked singularity remains unanswered. This is the real issue of cosmic censorship.

Although anathema to some, the failure of cosmic censorship would not imply any inconsistencies, nor do violence to any of our cherished notions of physics. Rather it would simply mean that our ignorance is more far-reaching than we would have thought (and perhaps that classical general relativity is not as beautiful a theory as we would like). Moreover, such a failure of cosmic censorship would improve our prospects of one day obtaining experimental data relevant to Planck-scale physics—in particular gravitational radiation from naked singularities could propagate out freely to us through intervening matter once it reached regions of sub-Planckian curvature.

Cosmic censorship remains a conjecture today, 24 years after its formulation [4]. Although in principle the issue can be resolved by integrating Einstein's equa-

tions, in practice these equations are non-linear partial differential equations which are very difficult to solve analytically except in special situations. Moreover, very little is known or can be proved about general, global solutions of non-linear partial differential equations (although Ref. [7] is an important exception in this regard). A variety of circumstantial evidence, however, has given rise to a widespread belief in the validity of the conjecture. This evidence includes: (i) detailed analytical understanding of spherically symmetric gravitational collapse [8, 9], (ii) analyses of small perturbations away from spherical symmetry, (iii) examples of numerically generated aspherical spacetimes in which horizons are seen to form, and (iv) general consistency arguments against the formation of the classic Reissner-Nordstrom and Kerr type naked singularities. See the review articles by Thorne [10] and by Wald [11] for more details and references. We note, however, that the strongest of this evidence applies only to either nearly spherically symmetric or nearly stationary situations. In particular, it seems particularly unlikely that static naked singularities of the Reissner-Nordstrom type can form, but this does not rule out "dynamic" naked singularities (i.e., singularities in a neighbourhood of which there are no time translation symmetries). Moreover, one might imagine that very anisotropic gravitational fields would be more likely to violate cosmic censorship than spherically symmetric ones, because information might be able to propagate away in those directions in which the field is weakest.

Results that hinted against cosmic censorship were provided by Thorne [10] in one of the first investigations of horizon formation in very aspherical situations. Thorne showed that horizons do not form in idealized planar and cylindrical collapse, in contrast with the spherical case. While these examples of exact symmetry are unphysical, it is possible to use them to draw inferences about more realistic matter configurations. Consider in particular a slightly prolate spheroid of self-gravitating, noninteracting particles ("dust") that is initially at rest [12]. It had been shown by Lin, Mestel and Shu that such a configuration would evolve into a spindle singularity in Newtonian gravity [13]. Thorne showed that for some initial conditions, the Newtonian approximation is valid until the late stages of collapse, after a thin spindle has formed, and that subsequently cylindrical symmetry is a good approximation near to the spindle, allowing the use of the general relativistic analysis of cylindrical collapse. Hence, the collapse can be quantitatively understood everywhere (except near the ends of the spindle at the late stages of the collapse), suggesting that a naked singularity may be formed. This analysis is valid when the initial circumference $\mathcal{C}$ of the spheroid is much greater than $4\pi M$,

where M is the spheroid's mass and we use, here and throughout, units with the speed of light and Newton's gravitational constant equal to one (so M is also half the spheroid's "gravitational radius"). Motivated by this result, and by a similar analysis of oblate spheroids, Thorne made the following conjecture [10, 14], which later became known as the "hoop conjecture": *Black holes with horizons form when and only when a mass M gets compacted into a region whose circumference in every direction is $\mathcal{C} \lesssim 4\pi M$.* Roughly speaking, the required condition is that a hoop of circumference $\mathcal{C}$ can be slipped over the region and rotated through 360°.

The evidence for a naked singularity in the collapse of a dust spheroid, although suggestive, was not conclusive, for the following reason. The details of the gravitational field at a point a distance d from one of the spindle ends and away from the spindle can be well understood until a time $\sim d$ after the formation of the singularity. Consider the point at the center of the spindle at the moment the spindle singularity forms. At this moment, light is locally propagating away freely from the spindle in the radial direction (since there is no event horizon in the cylindrical approximation). A particular photon will travel a distance $\sim \mathcal{L}/\sqrt{2}$ before it enters a region in which the Newtonian approximation to the spacetime structure becomes invalid, where $\mathcal{L}$ is the length of the spindle. Since one would expect that the spindle would contract axially to form a spherical black hole on a timescale of order $\sim \mathcal{L}$, it is not entirely clear that the photon would escape.

In recent years a new tool has become available for investigating cosmic censorship, which can probe highly aspherical, dynamical, and nonlinear gravitational collapse. This tool is the use of 2.5 and 3 (spatial) dimensional numerical relativity codes on supercomputers [15]. It seems likely that in the next 10 to 20 years, numerical relativity will have decided the question one way or the other: either a convincing naked singularity will be generated numerically, or several different groups will independently find that a wide variety of different conditions give rise to "clothed singularities." One of the first calculations of this type by Stuart Shapiro and Saul Teukolsky at Cornell University [16] followed up on the above-described calculations of Thorne, and hinted at the failure of cosmic censorship. Their results have generated considerable interest and controversy in the relativity community in the last year or two, and as we now describe, provided the motivation for the hoop-conjecture investigations in this thesis.

Before we describe the calculations of Shapiro and Teukolsky, we first clarify an important issue: the common use of two different notions of horizon. As indicated above, the validity of cosmic censorship depends on the existence and/or location

of the so-called *absolute event horizon*, which is defined as the boundary of the region which can causally communicate with future null infinity. However, this absolute-horizon concept has no meaning in finite regions of a spacetime, such as are generated by numerical relativity codes. A useful alternative concept is that of *apparent horizon* or "outermost trapped surface," whose definition we now review.

Consider a closed, 2-dimensional surface. From a given tiny region on the surface, send off in the inward and outward directions normal to the surface two thin pencils of light rays. The rates of change of the cross-sectional areas of these pencils are called the inward and outward expansions $\theta_{\rm in}$ and $\theta_{\rm out}$. In flat spacetime and for convex surfaces, $\theta_{\rm in} < 0$ (converging pencil) and $\theta_{\rm out} > 0$ (diverging pencil); these quantities simply measure the intrinsic curvature of the surface. In curved spacetimes, the gravitational field can focus the bundles of light rays, and so roughly speaking the expansions give a measure of a combination of the strength of the gravitational field and the curvature of the surface. A *trapped surface* is one for which $\theta_{\rm out} < 0$ everywhere on the surface, so that a wavefront emitted by the surface would initially get smaller even though propagating away and outwards.

The relevance of trapped surfaces for gravitational collapse is two-fold. First, as is well-known, the Hawking-Penrose singularity theorems [2] guarantee that once a trapped surface has formed, gravitational collapse to more and more singular states will continue until classical general relativity breaks down (assuming only that matter energy densities are positive) [17]. Second, a somewhat less well-known recent result of Werner Israel's shows that trapped surfaces exhibit the same "confinement" property as event horizons [8]. Israel shows that if a trapped surface forms, then subject to some technical assumptions there exists a spacelike cylinder formed of trapped surfaces which acts as a one way causal membrane — so that the interior cannot influence the exterior. Thus, the existence of a trapped surface is probably sufficient to guarantee existence of an event horizon. Moreover, being trapped is a locally defined concept; in any finite region of spacetime it is straightforward to determine whether or not there are any trapped surfaces present.

We now turn to a description of the numerical relativity calculations of Shapiro and Teukolsky. They considered spheroids of collisionless dust particles which were initially slightly prolate or oblate and at rest, of various sizes and eccentricities. They evolved the spheroids forward in time, solving self consistently for the gravitational field of the particles and for their motions, and testing for the formation of trapped surfaces. As expected, the prolate spheroids collapsed to form spindle singularities. In the case that Thorne argued cannot produce a horizon (a spin-

dle with length $\mathcal{L} \gg$ mass M), they indeed found that no trapped surfaces were formed. More nearly spherical initial data did give rise to trapped surfaces surrounding the singularities. In general, they found that trapped surfaces appeared and enclosed the singularity when and only when a certain quantity $\mathcal{C}_{\rm min}$, roughly the circumference of the spheroid, became less than 4π times the total mass, to within 10%. Thus, they found approximate necessary and sufficient conditions for the formation of trapped surfaces, which were along the lines of Thorne's hoop conjecture. We give in chapter 2 the precise definition of the quantity $\mathcal{C}_{\rm min}$ [Eqs. (??) and (??) below].

Of course, as Shapiro and Teukolsky acknowledged, the absence of trapped surfaces does not imply that the singularity necessarily is naked: an event horizon *could* be present. As we mentioned above, the existence of a trapped surface is a sufficient condition for causal confinement of the singularity, but it is not a necessary one. However, it is generally believed that trapped surfaces generically form inside event horizons, in part because newly formed black holes are believed to quickly settle down to a stationary state, and stationary black holes always contain trapped surfaces [18]. Invoking this line of reasoning, Shapiro and Teukolsky interpreted their results as indicating a possible failure of cosmic censorship [19].

My interest was aroused by the simplicity of the necessary and sufficient conditions for the presence of trapped surfaces that Shapiro and Teukolsky's numerical spacetimes seemed to exhibit. I therefore embarked on an effort to prove general theorems that put such conditions on a firm footing; such theorems, it seemed to me, could be powerful tools for probing cosmic censorship (although proving the existence of a counterexample to cosmic censorship would require in addition making precise the handwaving argument of the previous paragraph, and also taking into account a point made by Wald [19]). Chapters 2 and 3 of this thesis constitute a first effort towards proving such theorems.

An additional, separate motivation for studying the hoop conjecture is provided by the singularity theorems discussed above. The formation of a trapped surface during gravitational collapse signifies that a point of no return has been passed; a singularity must form. Sufficient conditions that guarantee this to be the case are of interest in their own right. Of course, in situations where there is only one relevant lengthscale $\mathcal{L}$, the condition is essentially that the collapsing body reach a size $\mathcal{L} \lesssim M$, where M is its mass. The issue is to find a precise mathematical formulation of this condition in the general relativistic context. One might imagine that the (square root of) the area of a collapsing body's surface, or the maximum

proper distance from its center to its surface, would constitute suitable measures of its size, and that when they fall below $\sim M$ a trapped surface must be formed [21]. Rather surprisingly, this is *not* so (not even approximately): we find that the quantity that is most relevant to trapped surface formation is the quantity $\mathcal{C}_{\min}$ (the minimum circumference) which is precisely defined in chapter 2 [22].

We now turn to a description of the contents of chapters 2 and 3. In chapter 2, we first consider the nontrivial issue of mathematically formulating the hoop conjecture in the context of generic solutions of Einstein's equations. In particular we suggest different precise definitions of "circumference" and of "mass" for which the hoop conjecture is meaningful and plausible. [The quantity $\mathcal{C}_{\mathrm{mim}}$ referred to above applies only to axisymmetric spacetimes.] Next, because it is difficult to prove anything about generic solutions to Einstein's equations, we specialize to the simplest non-trivial special class of solutions: static, vacuum, axisymmetric spacetimes. Now, clearly horizons are not formed in static spacetimes, so of what relevance is the hoop conjecture in this context? The answer is that a *necessary* condition for the formation of horizons would imply as a special case the following result: a static body of given mass must be larger than a certain size (where size is defined in terms of "circumference"); otherwise its strong gravitational field would overcome all resistance to collapse.

The next subtlety to be discussed is how anything can be learned by looking at purely vacuum spacetimes. Consider the external gravitational field of a static gravitating body such as a pen. The external field can be analytically continued into the interior of the pen (where it ceases to be the physical gravitational field) and will typically diverge there. One can discard the pen and consider the resulting field in its own right; it is the field generated by an infinitely thin, infinitely dense source (but of finite mass). This is the type of spacetime we consider. Conversely, given this divergent field, one can choose any closed 2-surface surrounding the region of divergence, and hope to find a suitable choice of source (energy-density) that fills the volume inside the surface and which also generates the given external field outside the surface. The hoop conjecture would apply to all such sources, and hence would imply [cf. previous paragraph] that the circumferences of *all* surfaces surrounding the singular source region be $\gtrsim 4\pi M$. This is a nontrivial property that must be satisfied by all static vacuum solutions of Einstein's equations if the hoop conjecture is correct. Thus, although far removed from the dynamic collapse situations which served as our original motivation, static vacuum spacetimes form a useful testbed in which to test the hoop conjecture idea.

In the second half of chapter 2 we describe some evidence which indicates that all Weyl spacetimes (i.e., static vacuum axisymmetric spacetimes) probably satisfy the constraint that all surfaces surrounding the singular region have circumferences $\gtrsim 4\pi M$. We show that several particular spacetimes and one-parameter families of spacetimes obey it. We also consider arbitrary vacuum static axisymmetric spacetimes, and prove some results which we show (in an addendum to chapter 2) can be given the following loose interpretation: generic, sufficiently elongated (prolate) Weyl spacetimes satisfy the hoop conjecture. More specifically, each Weyl spacetime can be labeled by its asymptotic mass m_∞, and by a dimensionless parameter Γ which is roughly the square root of m_∞^3/(mass quadrupole moment of source). By making a suitable choice of units, we can without loss of generality take $m_\infty = 1$. Then the space of Weyl spacetimes has a natural fiber bundle structure, for which the surfaces $\Gamma = \text{const}$ are cross-sections. We show that for a large class of fibers, the the spacetimes at sufficiently large values of Γ satisfy the hoop conjecture.

In chapter 3, we turn to a completely different technique for investigating properties of solutions of Einstein's equations: use of the so-called initial value equations. These are simply the non-dynamical components of the equations of motion (analogous to $\nabla \cdot \mathbf{E} = 0$ in source-free electrodynamics). Initial data sets for Einstein's equations consist of a Riemannian 3-metric h_{ab}, an extrinsic curvature tensor K_{ab} (related to the time derivative of the 3-metric), an energy density ρ_M, and a momentum density j_a. The initial value equations or constraints (which constitute 4 of the 10 Einstein field equations) are a set of nonlinear elliptic partial differential equations that must be satisfied by these variables. We again specialize to the simplest non-trivial case: that of axisymmetric, momentarily static ($K_{ab} = 0$), conformally flat initial data sets. We also as before focus on vacuum regions exterior to a source, using the constraint equations only in such vacuum exterior regions, so that our results are independent of the nature of the source.

For this simple class of initial data sets we show that: (i) Sources whose size, as measured by $\mathcal{C}_{\text{min}}$, is sufficiently small cannot be momentarily static; i.e., they must be collapsing. (ii) No outer trapped level surfaces can be present whenever $\mathcal{C}_{\text{min}}$ is greater than a constant times the mass. The second result confirms for this special class of initial data sets the necessary condition for the appearance of trapped surfaces noted by Shapiro and Teukolsky, *except* that our analysis applies only to level surfaces of the conformal factor and not arbitrary surfaces. This is not too much of a restriction because a sufficiently large region of outer trapped

surfaces will contain outer trapped level surfaces [23].

In summary, Chapters 2 and 3 show that the quantity $\mathcal{C}_{\rm min}$, identified by Shapiro and Teukolsky [24] as being useful to indicate the presense/absence of trapped surfaces, does indeed do so in a variety of special situations.

2 Gravitational radiation - the stochastic background

We now turn to a description of the contents of chapters 4 and 5 of the thesis. They are concerned with gravitational radiation — ripples in the curvature of spacetime that propagate with the speed of light. The production of gravitational waves is an incredibly puny process in all terrestrial environments — for example train crashes produce only on the order of a single graviton, or about 10^{-27} ergs of radiated energy. However, in astrophysical situations the emission of gravitational radiation can become a dominant physical process, and very large energy fluxes can be generated. The two $10M_\odot$ black holes referred to near the start of this Introduction would radiate during their inspiral and merger on the order of $M_\odot c^2$ energy in gravitational waves. The energy flux incident on the Earth from such a source at 200 Mpc, during its last 10 ms, would be comparable to the flux of sunlight reflected by the moon. As is well known, efforts are underway to detect and analyze such waves, and the prospects look good. By the turn of the century it is hoped that there will be in operation a network of laser-interferometer detectors, including the American LIGO (Laser Interferometer Gravitational Wave Observatory) [25], the French/Italian VIRGO [26] and possibly others. These detectors will eventually be sensitive to strain amplitudes of the order of $h \sim 10^{-21}$ or smaller, in a broad range of frequencies, $10\,{\rm Hz} \lesssim f \lesssim 500\,{\rm Hz}$.

The imminent successful operation of this network has invigorated an already existing program by theorists to try to pin down likely gravitational-wave-source strengths, characteristics, and event rates [3, 27, 28]. One of the motivations for considering these issues today, before the detectors come on line, is that information on the likely ultimate capabilities and uses of the network provides important theoretical guidance for details of its final design and construction. For example, the choice of 4 km for the arm lengths of the LIGO L-shaped interferometers was guided by estimates of event rates and strengths of gravitational waves from coalescing compact binaries.

Chapter 4 of this thesis presents a detailed analysis of an issue that is relevant to the choice of orientations of L-shaped, kilometer-size interferometers. Their orientations clearly cannot be altered once they are constructed, and so information on the implications of this or that choice of orientation is useful. The issue is the sensitivity of the network to the gravitational wave stochastic background. This is an isotropic, homogeneous, random background "noise" of gravitational waves for which various possible sources have been suggested, and which is quite analogous to the electromagnetic (microwave) background except that its energy spectrum is not expected to be thermal. The possible sources include (i) the random superposition of many weak signals from binary-star systems, (ii) decaying cosmic strings and first-order phase transitions in the early Universe, and (iii) parametric amplification of quantum mechanical zero-point fluctuations in the metric tensor during inflation. References for these sources are given in chapter 4; for extensive reviews see Refs. [3, 27, 29]. Because the physics underlying many of the proposed sources is speculative, the detection of the stochastic background or the placement of upper limits on its strength would yield valuable information. For example, some theories of structure formation involving cosmic strings will be falsifiable by LIGO.

The mechanism by which the stochastic background can be detected is the following. The background gives rise to small contributions to the Gaussian noise in each detector that are indistinguishable from that detector's intrinsic noise. However, these contributions are correlated between detectors, so that measurements of the correlation made by integrating the output of one detector against that of another will yield information about the stochastic background spectrum. By using this method, the LIGO pair of detectors will have a sensitivity to the background radiation of the order of $\Omega_{\rm gw} = 5 \times 10^{-10}$ at frequencies near $\sim 50\,{\rm Hz}$. A pair of detectors which are separated by a distance $\gtrsim$ (the wavelength of gravitational waves in the detectable frequency band) and/or which are not aligned parallel to one another will suffer a reduction in sensitivity compared with coincident, aligned detectors. The reasons are that (i) detectors which are not parallel couple to different gravitational-wave polarization components, and orthogonal polarization components of the stochastic background are expected to be statistically independent; and (ii) for each gravitational-wave mode, the travel time between the detectors gives rise to a phase lag in the cross-correlation whose magnitude depends on the mode's direction of propagation. Hence, the contributions to the cross-correlation from different modes can interfere destructively, decreasing the

cross-correlation.

A formal expression for the reduction in sensitivity as a function of frequency was worked out by Christensen [29]. In chapter 4 we derive an explicit expression for this function, and straightforwardly apply it to determine the optimum choice of orientations for a pair of detectors. More importantly, since sensitivity to the stochastic background is not the only issue to be taken into account when choosing orientations, we determine how the sensitivity varies with the orientations of both detectors. This work was in part motivated by a concern that the choices that had been made for the LIGO pair of detectors could be unnecessarily and severely detrimental to the sensitivity to the stochastic background. Our results showed this not to be the case: the chosen LIGO orientations are very in fact nearly optimal.

Chapter 4 also contains a detailed derivation and analysis of the optimal data processing scheme that will need to be used by the LIGO/VIRGO network when searching for stochastic background radiation. We take into consideration the effects of any sources of noise that are correlated between detectors (which could mimic the effect of the stochastic background). Using a sequence of approximations, we derive an expression for the Bayesian probability distribution for the background energy spectrum, given the detector outputs. This automatically identifies the appropriate statistic or filtering method to be used in the data analysis.

3 Gravitational waves from coalescing compact binaries

It is the task of the gravitational wave theorist to identify likely astrophysical sources of gravitational radiation, and, for each type of source, to anticipate the likely signal strengths and event rates. Such information can be used in conjunction with estimates of detector noise levels to assess the potential capabilities and viability of proposed detection systems, and to guide their design. Because gravitational wave sources are typically inconspicuous electromagnetically, there is considerable uncertainty in the event rates and/or signal strengths for most types of source [27].

An important exception in this regard are gravitational waves from coalescing compact binaries, i.e., neutron star/neutron star (NS/NS), neutron star/black hole (NS/BH), and black hole/black hole (BH/BH) binaries. These are systems like the

famous binary pulsar PSR 1913+16, that spiral together driven by gravitational radiation reaction, and emit a characteristic "chirp" waveform whose amplitude and frequency both sweep upwards as time passes. The waves' frequency enters the LIGO/VIRGO waveband at $\sim 10\,\mathrm{Hz}$ several minutes before the final merger of the compact objects, and typically several thousand cycles of signal follow. The importance of this type of source was first recognised by Thorne in 1984 [3]. A key point here is the fact that the quantity relevant to the detectability of a burst of waves is not the total energy carried by the waves, but rather the signal-to-noise ratio for the detection process when optimal filtering of the detectors' outputs is used. This signal-to-noise ratio is considerably enhanced for sources (such as coalescing binaries) for which the waveform is predictable and dependent only on a small number of parameters.

Today, the anticipation of large numbers of detections of waves of this type forms an integral part of the LIGO design strategy—these waves will constitute LIGO's "bread and butter" source [25]. The high degree of confidence with which the waves are expected is due in part to relatively firm event-rate estimates in the case of NS/NS binaries, which are based on the statistics of successful and unsuccessful searches for NS/NS binaries in our galaxy [30, 31]. (Three NS/NS binaries that will merge within a Hubble time have been found to date). When combined with the LIGO team's estimate of the detector sensitivity levels that might be attained a few years after initial operation [25] (and that imply detectability of NS/NS coalescences out to ~ 1000 Mpc, far beyond our Galaxy), these event-rate estimates imply an event-detection rate of $\sim 10^2$ per year, uncertain to a factor ~ 8 [32].

In the last two years our understanding of waves from coalescing compact binaries has changed considerably. It is now realized that the waves are strongly influenced by complex post-Newtonian effects, and that the amount of accessible information they carry is far more than had been expected [28]. This understanding has come about largely through the work of the Caltech relativity group (ruefully dubbed "the Juggernaut" by other relativity groups working on this topic).

Chapter 5 of this thesis consists of a paper that I have written in collaboration with Curt Cutler as part of this large group effort [33]. We address the following issue: how accurately can the binary's masses, spins, orbital elements, distance, etc. be extracted from the waveforms measured by the LIGO/VIRGO network? Several previous preliminary investigations of this rather complicated problem have been carried out [32, 34, 35]. We by no means give a definitive analysis: we estimate

that, because of a number of complicating effects which we neglect, our results for parameter extraction accuracies are uncertain to within a factor of ~ 2. However, we extend the previous analyses in several key respects, obtaining much more accurate results, which differ significantly from those obtained previously. Our analyses suggest that, for example, (i) a particular combination of the binaries' two masses will be measured to within $\sim 0.1\% - 1\%$, (ii) the individual masses will be measurable to within $\sim 10\%$, and (iii) the distance to the source will typically be measurable to within $\sim 30\%$. Our detailed results were used by Marković in an analysis of the feasibility of determining the cosmological parameters of the Universe using a statistical analysis of the measured parameters of a large number of binary systems [36]. Marković finds that the Hubble constant will be measurable to within a few percent using this method.

Bibliography

[1] This issue is part of the standard lore of general relativity, see, e.g., R.M. Wald, *General Relativity* (University of Chicago press, Chicago, 1984), p. 299; also C.W. Misner, K.S. Thorne, and J.A. Wheeler, *Gravitation* (W. H. Freeman, San Francisco, 1973) (which henceforth will be referred to as MTW), p. 603.

[2] R. Penrose, Phys. Rev. Lett. 14, 57 (1965); S.W. Hawking and R. Penrose, Proc. Roy. Soc. Lon. A314, 529-548 (1970).

[3] K.S. Thorne, in *300 Years of Gravitation*, edited by S.W. Hawking and W. Israel (Cambridge University Press, Cambridge, England, 1987), pp. 330–458.

[4] R. Penrose, Riv. Nuovo. Ciment. 1, 252 (1969).

[5] M.W. Choptuik, Phys. Rev. Lett. 47, 1471 (1993); A.M. Abrahams, C.R. Evans, Phys. Rev. Lett. 70, 2980 (1993).

[6] These points were particularly emphasised by G.T. Horowitz in a talk at the conference *Quantum Aspects of Black Holes*, ITP, Santa Barbara, June 1993.

[7] D. Christodoulou and S. Klainerman, *Non-linear stability of Minkowski space*, Lect. N. Math. 1402 (1989).

[8] W. Israel, Can. J. Phys. 64, 120 (1986).

[9] D. Christodoulou, Com. P. A. Math., 44, 339 (1991).

[10] K.S. Thorne, in *Magic Without Magic : John Archibald Wheeler*, edited by J. Klauder (Freeman, San Francisco, 1972), p. 231.

[11] R.M. Wald, *Weak cosmic censorship*, unpublished.

[12] A realistic system of self-gravitating particles such as a globular cluster of course obeys the virial theorem. In the approximation that the individual interparticle interactions can be neglected, there is no gravitational collapse —

there is a global existence theorem for solutions of the Poisson-Vlasov equation. The actual evolution of such systems depends strongly on the interactions of pairs of particles. Nevertheless, we can in principle consider the unrealistic initial condition of placing all the particles at rest. (The subsequent occurrence of a singularity in Newtonian evolution does not contradict the global existence theorem for solutions of the Poisson-Vlasov equation because the initial particle distribution function on momentum space, being a delta function, is not smooth, which is one of the requirements of the theorem). The fact that the initial conditions are unlikely has no bearing on the issue of principle being probed—possible natures of the final stages of the collapse. Moreover, in full relativity it seems likely that is not necessary that the particles start exactly at rest—they merely need to have sufficiently small initial velocities that the system of particles evolves to a state where non-linear gravitational effects become important.

[13] C.C. Lin, L. Mestel, and F.H. Shu, App. J. **142**, 1431 (1965).

[14] MTW, p. 867.

[15] "2 and a half- dimensional" is conventionally used to describe 2-dimensional codes that simulate 3-dimensional axisymmetric phenomenon.

[16] S.L. Shapiro and S.A. Teukolsky, Phys. Rev. Lett. **66**, 994 (1991), Am. Scientist **79** 330 (1991).

[17] This is a somewhat loose statement of the theorems. We ignore the possibility that the spacetimes could be future geodesically incomplete without containing curvature singularities, as it is generally believed that this will not occur in realistic gravitational collapse. We also ignore some technical details, such as the precise nature of the non-negative-energy condition that is required by the theorems (the "null energy condition").

[18] More precisely, in stationary spacetimes, event horizons and apparent horizons coincide. Hence, stationary black holes always contain trapped surfaces except in the extremal limit when they contain only a marginally trapped surface (i.e., one satisfying $\theta_{\rm out} = 0$ everywhere).

[19] A potential flaw in this argument was subsequently pointed out by Wald [20]. The spacetime regions numerically generated by Shapiro and Teukolsky were

sandwiched between two spacelike surfaces, one being the initial data set, and the second being the final time slice which touched the high curvature region. At each time step in their calculation a particular algorithm was used to determine the so-called lapse function, which essentially gives the spatial variation of the time increment. (A "constant" time increment has no intrinsic meaning in relativity.) Their choice of lapse function and consequent choice of spacetime slicing affected the region of spacetime they were able to generate: a different slicing could push further into the future past their final hypersurface in regions away from the singularity. Thus, essentially they generated only some region of spacetime that extended into the future far enough to touch the singularity at one point. Conceivably, they had not pushed far enough into the future to detect the trapped surfaces. Wald showed that such regions which touch the singularity and yet contain no trapped surfaces exist in well-understood spherically symmetric spacetimes that obey cosmic censorship. He concluded that it would be necessary to integrate farther into the future in their examples.

[20] R. M. Wald, Phys. Rev. D 44, 3719 (1992).

[21] Note that Euclidean geometric relationships, e.g., (Volume enclosed) = $\sqrt{4\pi}(\text{Area}/3)^{3/2}$ for a spherically symmetric surface, can be violated by large factors in curved spacetimes, so that different measures of size need not even be commensurate.

[22] As we discuss in chapter three, measures of size other than $\mathcal{C}_{\text{min}}$ are relevant when combined with measures of mass other than the asymptotic mass measured by distant observers using Kepler's laws.

[23] Momentarily static initial data sets which contain outer trapped surfaces are unphysical, as I have been reminded by Eric Poisson, because they evolve to a singularity in finite time when evolved to the past as well as to the future. Thus, they cannot arise starting with a low-curvature initial data set. However, in the space of solutions to the initial value equations, the location of the boundary between data sets that contain trapped surfaces and those that don't is still of physical interest. Our results can be described as an approximate specification of the position of this boundary.

[24] They do not express their results in the manner that we have described, but the quantity that they calculate is essentially $\mathcal{C}_{\text{min}}$.

[25] A. Abramovici *et al.*, Science 256, 325 (1992).

[26] C. Bradaschia *et al.*, Nucl. Instrum. & Methods A289, 518 (1990).

[27] K.S. Thorne, in *Recent Advances in General Relativity*, edited by A. Janis and J. Porter (Birkhauser, Boston, 1991).

[28] C. Cutler, T. A. Apostolatos, L. Bildsten, L. S. Finn, É. E. Flanagan, D. Kennefick, D. M. Marković, A. Ori, E. Poisson, G. J. Sussman, and K. S. Thorne, Phys. Rev. Lett. 70, 2984 (1993).

[29] N.L. Christensen, Ph. D. thesis, Massachusetts Institute of Technology, 1990 (unpublished); also Phys. Rev. D 46, 5250, (1992).

[30] E. S. Phinney, Astrophys. J. 380, L17 (1991).

[31] R. Narayan, T. Piran, and A. Shemi, Astrophys. J. 379, L17 (1991).

[32] L. S. Finn and D. F. Chernoff, Phys. Rev. D 47, 2198 (1993).

[33] My contribution to the paper consists essentially of Sec. IV together with the three appendices, together with some input on the introduction (Sec. I) and mass measurement accuracy sections (Secs. II and III).

[34] S.V. Dhurandhar, A. Krolak, B.F. Schutz and W.J. Watkins, *Gravitational Wave Astronomy with Broadband Detectors. I. Extraction of Coalescing Binary Signals*, in preparation.

[35] P. Jaranowski and Andrzej Krolak, *Optimal solution to the inverse problem for the gravitational wave signal of a coalescing compact binary*, in preparation.

[36] Marković's distance-measurement accuracy analysis was carried out independently; our analysis in Sec. IV of chapter 5 constitutes an extension of his results, made after his paper was completed.

Chapter 2

The hoop conjecture for black-hole horizon formation

(Originally appeared in Phys. Rev. D 44, 2409 (1991).)

Abstract

The hoop conjecture was proposed by Thorne in 1972 as a loosely formulated necessary and sufficient condition for the formation of a horizon in nonspherical gravitational collapse. In this paper we discuss some issues that arise in formulating various precise interpretations of the conjecture, and review some of the small amount of literature that has appeared on this subject. We farther specialise the conjecture to static, vacuum, axisymmetric spacetimes and show that it is satisfied in three particular cases of such spacetimes. We also prove a theorem for oblate geometries giving a sufficient condition for the conjecture to be satisfied.

1 INTRODUCTION AND SUMMARY

It is well known that spherical gravitational collapse produces (i) an event horizon, which seals off the collapsing matter and prevents it from causally influencing the external universe, and (ii) a singularity, at which classical general relativity breaks down. It is the simultaneous occurrence of (i) and (ii) which ensures that external observers can never witness any such breakdown. In his 1972 review of nonspherical gravitational collapse, Thorne showed that horizons do not form in idealized planar and cylindrical collapse, in contrast to the spherical case [1]. This suggests the following question: Do horizons always form in the collapse to a singularity of realistic configurations of matter? This 'Cosmic Censorship' [2] question has been called by Hawking "the most important unsolved problem in classical general relativity" [3].

Thus it is of interest to have sufficient and/or necessary conditions for the formation of horizons. On the basis of his observations above, Thorne made the following conjecture [1, 4], which later became known as the hoop conjecture (HC): *Black holes with horizons form when and only when a mass M gets compacted into a region whose circumference in every direction is $\mathcal{C} \lesssim 4\pi M$.* Roughly speaking, the required condition is that a hoop of circumference $\mathcal{C}$ can be slipped over the region and rotated through 360 degrees. This criterion is sufficiently loosely formulated to allow many different precise interpretations; in particular different definitions of mass, horizon, and of circumference are all possible. It is thus essentially a suggestion as to the form a rigorous result might take, while encapsulating the crucial physical idea that the collapsing matter must be strongly compacted in all three spatial dimensions in order for a horizon to be formed. The relation $\mathcal{C} \lesssim 4\pi M$ is intended as an order of magnitude guideline, so that different numeric constants (not necessarily 4π) may be required for the separate 'if' and 'only if' parts of the conjecture.

What evidence is there in favor of such a conjecture? Some reasons for believing it are that (i) no compelling counterexamples are known, (ii) it is in accord with the behaviour of spherical, cylindrical, and planar collapse [1], (iii) it is in accord with the results of several numerical relativity calculations of nonrotating, axially symmetric collapse [5, 6, 15, 16], and (iv) several examples of static solutions of Einsteins equations are known to be consistent with it [9, 10, 11, 12, 13, 14, 15]. We proceed to present some of this evidence and briefly summarize past research in this area.

The HC in momentarily static, nonsingular, axisymmetric spacetimes was investigated by Redmount [9]. By imposing the weak energy condition in the matter-containing region he succeeded in deriving geometric constraints that the matter-vacuum boundary must satisfy in any such spacetime. Although these constraints were unfortunately not directly related to HC criterion, he found no counter evidence to the HC in the particular geometries that he examined (the Γ metric [10] and the Bach-Weyl ring metric [11]), and his work inspired future research [6, 12]. In [12] and [13], Bonnor considered static spheres of charged perfect fluid with charge q greater than their mass m. He showed that if a suitable energy condition is satisfied then $\mathcal{C} > 2\pi m$, where $\mathcal{C}$ is the circumference of the matter surface, thus supporting the spirit if not the letter of the conjecture. Chamorro et al. [14] showed that solutions of Einsteins' equations representing static finite thin discs satisfy the HC, without the imposition of an energy condition being necessary, and subsequently Lamberti et al. [15] gave a similar demonstration for thin discs of counterrotating particles.

Investigations of horizon formation in evolving dynamic spacetimes have been mostly numeric. Early numerical calculations by Nakamura and Sato of the collapse of nonrotating, axisymmetric fluid bodies indicated that apparant horizons could be formed in highly non-spherical situations, but that for certain initial conditions apparant horizons are *not* formed during the collapse [5]. Subsequently, Nakamura, Shapiro and Teukolsky analytically solved the initial value problem for momentarily static dust spheroids, both prolate and oblate [15]. They numerically analysed the resulting 3-dimensional manifolds for various values of the eccentricity to determine the minimum circumference of surfaces surrounding the spheroids, and to check whether or not apparent horizons occur. More recently, Shapiro and Teukolsky [16] numerically modeled the full dynamical collapse of such spheroids, again calculating minimum circumferences and testing for horizon formation. In these calculations, both momentarily static and collapsing, apparent horizons were found to be present whenever the minimum circumference $\mathcal{C}$ was less than 4π times the mass, and not otherwise, to within 10 percent. This is strong evidence for both the necessary and the sufficient condition aspects of the HC.

In a more general setting, several investigations have been made concerning the question 'What is a sufficient degree of compactification of matter to ensure horizon formation?' [7, 17, 5]. In 1983 a striking development took place with the proof by Schoen and Yau [6] of the following very powerful and general theorem, motivated by previous work on the HC.

Theorem 1 [Schoen & Yau] *Suppose Σ is any spacelike hypersurface in spacetime, and Ω is a bounded region in Σ on which $\rho - \sqrt{J_\mu J^\mu} \geq \Lambda > 0$, for some $\Lambda > 0$. Here $\rho \equiv T_{\mu\nu} n^\mu n^\nu$ and $J_\mu \equiv T_{\mu\nu} n^\nu + \rho n_\mu$ are the energy density and flux, and n^μ is the unit normal to Σ. If $\mathcal{R}(\Omega) > \pi\sqrt{3/2\Lambda}$, where $\mathcal{R}(\Omega)$ is a suitably defined measure [25] of the radius of Ω, then Σ contains an apparent horizon.*

Thus by assuming a lower bound for the mass density, they derive an upper bound for the matter radius for spacetimes without black holes.

Given such a definitive result, one may well ask what motivation is there for continuing to study the HC as originally formulated. The following are some reasons.

Firstly, the HC purports to give a sufficient condition for horizons *not* to form, unlike Schoen and Yau's theorem above, which would be relevant to cosmic censorship. Recent work by Bzion, Malec and O'Murchadadh [Eq. (67) of Ref. [12]], in which they derive such a condition for spherically symmetric systems, indicate that there is hope to prove this portion of the HC generally.

Secondly, from a physical point of view, one would like to have a criterion applicable to measurements made by an observer external to the collapsing body. External observers can measure circumferences but not radii, and mass but not density. Such criteria, if provable, might be a consequence of the vacuum field equations holding outside the body, and thus may be independent of the equations of state, singularities, etc. of the interior.

The most important reason, however, for continued interest in the HC is the recent strong numerical evidence in its favor described above [15, 16]. In the light of this new evidence, it now seems likely that some version of the HC is true. However, to date very little attention has been paid to the issue of finding precise formulations of the HC in a general setting; most investigations have been restricted to static spacetimes. Accordingly, one of the two principal purposes of this paper is to identify issues that one must confront in trying to find and prove such a precise and general formulation, and to propose some routes that one might follow. This we undertake in section 2, where we consider various ways of defining mass, horizon and circumference. We identify two likely candidate formulations, one *global* in spirit based on the asymptotic ADM definition of mass [8], and one *local* in spirit incorporating some suitable 'quasi-local' definition of mass. We also distinguish between two approaches towards finding a proof: an *interior* approach which tries to make deductions from energy conditions, etc. holding inside the matter region, and an *exterior* approach which instead works from the vacuum

field equations which hold outside.

The second principal purpose of this paper is to present some new evidence in favor of the HC in static, vacuum, axisymmetric spacetimes, evidence which indicates that the exterior approach has a good chance of succeeding. In particular, in section 3 we show that several particular such spacetimes are consistent with the HC, and we derive sufficient conditions for oblate geometries to satisfy the conjecture. A similar result is also obtained for prolate geometries. Although these results leave much room for improvement and do not by any means constitute a proof of the HC in these spacetimes, they do at least demonstrate that there is hope to make progress along the directions we outline.

2 MAKING THE HOOP CONJECTURE PRECISE: ISSUES AND TOOLS

2.1 Apparent horizon versus event horizon

Although ideally one would like to obtain a result involving absolute event horizons, in practice it is usually difficult to determine whether or not one exists. This is the case if one is working with data specified on an initial spacelike hypersurface, as the existence of an absolute event horizon depends on the structure of the spacetime in the far future. It is easier to prove the existence of an apparent horizon, or what is a slightly stronger condition, that a closed trapped surface exists (see [22] for definitions of these types of surface). They are closely related as the boundary of a region containing closed trapped surfaces is always an apparent horizon [22], and it is expected that generically trapped surfaces lie inside apparent horizons, with exceptions forming a set of 'measure zero'[1].

We now consider the question of to what extent the two types of horizon are equivalent. It is not known whether trapped surfaces are always accompanied by absolute event horizons. Israel[23] presents evidence in this direction, and suggests an approach towards a direct proof. If one assumes cosmic censorship[2], then Penrose's singularity theorem[24] implies that the result is true under quite general circumstances. The following is essentially the same result in a different guise: In spacetimes which are future asymptotically predictable, absolute event horizons must be present when one has a marginally trapped surface, or an outer trapped surface which is the boundary of a three-dimensional region([30], p. 310). (Asymptotic predictability is a technical condition related to the absence of naked

singularities[22].) However the recent work of Nakamura et al.[15] referred to above casts doubts on the unqualified validity of this cosmic censorship hypothesis. In the converse direction, it is not true that the formation of an absolute event horizon implies that there is an apparent horizon nearby. However, if an absolute event horizon forms, it is believed at least that an apparent horizon will at some stage be formed, as it is generally accepted that black holes eventually settle down into a stationary state, and for stationary black-hole spacetimes both types of horizon exist and coincide[22].

In conclusion, it seems that outer trapped surfaces or apparent horizons are probably an acceptable substitute for absolute event horizons when dealing with sufficient conditions for horizon formation, but they might not be so when dealing with necessary conditions.

2.2 The hoop concept

In this section we consider how to define an appropriate measure of the size of a collapsing body that could be used to diagnose horizon formation in the spirit of the HC. Suppose that we have an asymptotically flat spacelike slice of spacetime Σ, and a connected region Ω in Σ such that the stress-energy tensor vanishes outside Ω. As discussed in the introduction, there exists a definition of radius $\mathcal{R}(\Omega)$ due to Schoen and Yau[6] which is useful in this context. This $\mathcal{R}(\Omega)$ is essentially the size of the largest torus that fits inside Ω[25]. However, in this paper we are interested in measures that depend only on the surface $S = \partial\Omega$ of Ω, and not on its interior. Some quantities that could be considered are the area of the surface $\mathcal{A}(S)$, and its circumference $\mathcal{C}(S)$. We discuss these in turn.

One might expect that the dimensionless quantity $\mathcal{A}(S)/m^2$ (where m is the ADM mass of Σ[8]) would be useful as a measure of degree of compactification. However there exists a class of static spacetimes [Eq. (5.12) of Ref. [9]] in which $\mathcal{A}(S)/m^2$ can be arbitrarily small. Hence this quantity cannot provide a sufficient condition for the formation of horizons, and we are led to consider alternative measures (see below). On the other hand area does appear in the following necessary condition for the formation of trapped surfaces, namely that closed trapped surfaces of area $\mathcal{A}$ must satisfy

$$\mathcal{A} \leq 16\pi m^2. \tag{2.1}$$

This result is true for surfaces S of spherical topology in spacetimes which are asymptotically flat at past null infinity, and for which there exists a non-singular

null hypersurface connecting S to past null infinity[26]. It is also a simple consequence of some suitable form of the cosmic censorship assumption such as asymptotic predictability[22], together with the black-hole uniqueness and no-hair theorems; see Eq. (3.20) of Ref. [15]. Criteria involving area may also be useful in conjunction with the Hawking definition of mass, see section 2.3.

The most appropriate external measure, however, seems to be circumference, in accordance with the HC as it is usually interpreted[15]. How does one define the circumference of a surface in general? For axisymmetric surfaces S, one can simply take the maximum of the lengths of those closed curves which are the analogs of lines of longitude and latitude. [Call this quantity $\mathcal{C}_1(S)$.] This is the definition for which we have the most evidence that the HC is true[15, 16, 9], and it is this definition which we shall adopt in our discussion of vacuum axisymmetric spacetimes in section 3. In this section, however, we consider how to define circumference more generally.

The most straightforward definiton one might try is

$$\mathcal{C}_2(S) = 2\max\{\, d_S(x,y) \mid x,y \in S \,\}, \tag{2.2}$$

where $d_S(x,y)$ is the length of the shortest smooth curve in S joining x to y. However this definition is not suitable: although it gives the correct answer for spherical surfaces, we show in appendix A that for axisymmetric sufaces it does not reduce to the definition discussed above. Moreover we show that there exist horizon-free spacetimes containing surfaces S for which $\mathcal{C}_2(S)/m$ can be arbitrarily small.

A more promising notion of circumference is the following. Given a surface S of spherical topology, fix a point $\mathcal{P}$ in S and consider families of closed curves $D(\mathcal{P},\lambda)$, for $0 \leq \lambda \leq 1$, which contain $\mathcal{P}$ and such that all points other than $\mathcal{P}$ on S lie on exactly one of the curves $D(\mathcal{P},\lambda)$. Such families of curves start at $\mathcal{P}$, sweep around the surface and then return to $\mathcal{P}$. Now take the length of the longest curve in the family, minimise over all such families, and then maximise over all points $\mathcal{P}$. This yields the definition

$$\mathcal{C}_3(S) = \max_{\mathcal{P}} \min_{\{D(\mathcal{P},\lambda)\}} \max_{\lambda} \; L[D(\mathcal{P},\lambda)]. \tag{2.3}$$

While this does not always equal $\mathcal{C}_1(S)$ for axisymmetric surfaces, as shown in Fig. 2.1, it may be appropriate and useful in formulating the HC. Another definition of circumference which may be a generalisation of $\mathcal{C}_1$ is the following. Let K be a 2-dimensional plane whose extrinsic curvature tensor in the spacelike slice Σ is

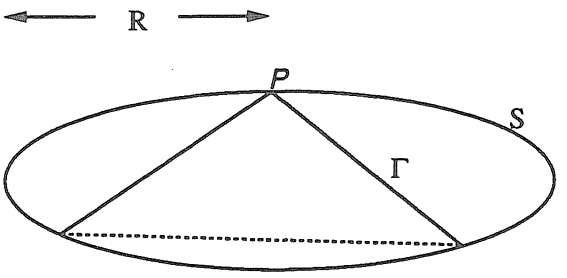

Figure 2.1: For a pancake shaped surface S, the circumference function $C_3(S)$ is given by the length of the curve Γ. The dashed portion of the curve is on the underside of the surface. Notice that this length is less than $C_1(S)$ which is $2\pi R$.

traceless. Define $C_K(S)$ to be the maximum of the lengths of the closed curves which make up $S \cap K$, and put $C_4(S) = \max_K C_K(S)$. This definition depends on the extrinsic and intrinsic geometries of S.

Suppose now that we have chosen a suitable definition of circumference $C(S)$. If we consider various closed surfaces S surrounding a matter-containing region Ω, sometimes the minimum circumference $\inf_S C(S)$ is not achieved by the matter surface $\partial\Omega$, but by some surface outside this[15]. Hence we should actually use the measure

$$C_e(\Omega) \equiv \inf_S C(S), \tag{2.4}$$

where the minimum is taken over all closed surfaces S on some spacelike hypersurface Σ that contain Ω in their interior.

Now in a general spacetime with no special symmetries, there is no preferred family of spacelike slices Σ to which to apply the HC criterion. One might hope to establish some criterion which would be applicable to *all* spacelike hypersurfaces. However this is not possible, since the 3-geometry as perceived on piecewise almost-null hypersurfaces will be distorted due to Lorentz contraction. For example, let f be a suitably smoothed periodic sawtooth function of compact support, whose amplitude A and period λ satisfy $0 < 1 - 2A/\lambda \ll 1$ and $\lambda \ll 1$. Then in a local Lorentz frame with nearly Lorentzian coordinates $\{t, x, y, z\}$, such a hypersurface Σ will be given by $t = f(x)$. Upon averaging over length scales large compared to λ, the effective 3-metric of Σ will be given by ${}^{(3)}ds^2 = \varepsilon^2 dx^2 + dy^2 + dz^2$, for some constant $\varepsilon \ll 1$. If T is a world tube of the form $x^2/a^2 + y^2/b^2 + z^2/b^2 \leq 1$ with $b \ll a$, then on such a hypersurface Σ the circumference of T will be $C_e(T \cap \Sigma) \approx 2b$ instead of the expected value of $\approx 2a$. This clearly violates the spirit of the type

of measure we are trying to construct.

Thus it is necessary to restrict the class of hypersurfaces in some way, for example by placing constraints on their extrinsic curvature. In particular one could demand that only maximal slices of spacetime be considered (i.e., that the extrinsic curvature be traceless); this would not be not too restrictive as given any closed smooth spacelike 2 surface of spherical topology one can always find a spacelike hypersurface that contains the 2 surface and is maximal inside it[27]. These considerations lead to an expression of the HC of the following form: If T is the timelike worldtube of a collapsing body, a horizon is formed if and only if $\mathcal{C}_e(T \cap \Sigma) \leq 4\pi m$ for some spacelike hypersurface Σ satisfying a suitable extrinsic flatness condition.

An alternative approach is the following. Define for each point p inside a world tube T

$$\mathcal{C}(T,p) \equiv \sup_{\Sigma} \mathcal{C}_e(\Sigma \cap T) \tag{2.5}$$

where the maximum is taken over all asymptotically flat spacelike hypersurfaces Σ containing p. Then a possible criterion could be $\mathcal{C}(T,p) \leq 4\pi m$ for some $p \in T$. In appendix B we show that in the case of static spacetimes $\mathcal{C}(T,p) = \mathcal{C}_e(\Sigma_o \cap T)$ for all points p, where Σ_o is any hypersurface which is everywhere orthogonal to the timelike killing vector field. Thus $\mathcal{C}(T,p)$ reduces to the usual definition of circumference in this case.

2.3 Definitions of mass and the effects of gravitational radiation

It has been customary to interpret the mass that appears in the HC inequality as the ADM mass[8] of a slice of spacetime. While this seems reasonable in static spacetimes where the HC has usually been considered, there are problems associated with this interpretation in more general spacetimes, and also sometimes even in static ones. For example, if the region external to the collapsing matter is not vacuum, there will be contributions to the asymptotic mass from stress-energy outside the matter. This applies in particular to electrovacuum spacetimes. A more serious problem is the fact that in any realistic gravitational collapse spacetime there will be gravitational waves extending outside the matter source, which in principle could have a mass as large as that of the matter. In these situations the asymptotic mass is not a good measure of the actual mass undergoing collapse.

One approach to the problem of gravitational radiation is suggested by the

calculations of Shapiro and Teukolsky discussed above[16]. Gravitational radiation is emitted by the collapsing spheroids in these calculations, but only at a level of less than one percent of the total mass, so that they are still in accord with the HC. It might be possible to prove a result that deals with realistic initial configurations of matter and establishes as a byproduct that such configurations never emit so much gravitational radiation as to become a serious problem for the HC.

However, we suggest that the best way to avoid the problems associated with the use of asymptotic mass is to use instead some 'quasi-local' definition of mass: Although gravitational energy is traditionally considered to be nonlocalisable, recently several such quasi-local definitions (i.e., definitions based on surface integrals rather than volume integrals) have been suggested[28, 29]. Also in the special case of stationary spacetimes there is a useful formulation of local mass due to Komar[30, 30]. Using some such appropriate interpretation of 'mass inside Ω' $m(\Omega)$, a suitable quasi-local reformulation of the HC could be: If Ω is any region in a suitably chosen hypersurface Σ (cf. previous section), then a trapped surface will be formed whenever $\mathcal{C}(\partial\Omega)$ is less than $4\pi m(\Omega)$. A stronger result would be to assert that $\partial\Omega$ itself would be a trapped surface, but this is less likely to be true. In any such formulation, the definition of mass cannot depend solely on the stress energy tensor, as it is known that imploding nearly spherical shells of gravitational radiation can form black holes[32].

In favor of the above interpretation of the HC as a local statement is the following fact: some examples of spacetimes which were found to violate the HC bound of $4\pi m$ by a factor of two[12, 33] are in accord with a version of the HC which uses the local Komar mass. We sketch a proof of this result: The spacetimes consist of static spheres of charged perfect fluid joined onto an exterior Reissner-Nordstrom region, where the join occurs at a value of the Schwarzschild radial coordinate $r = r_o > r_+ \equiv m + \sqrt{m^2 - q^2}$. Here m and q have their usual meanings, and $m > q$. If S_a is the surface given by $r = a$ for $a > r_o$, then the Komar mass of the volume interior to this surface is $m(S_a) = m - q^2/a$. We find that

$$\inf_a \frac{\mathcal{C}(S_a)}{4\pi m(S_a)} = g(\frac{q}{m}) \tag{2.6}$$

where

$$g(x) \;=\; \begin{cases} 2x^2 \;\text{ for } \frac{\sqrt{3}}{2} \le x \le 1\,, \\ \frac{(1+\sqrt{1-x^2})^2}{2(1-x^2+\sqrt{1-x^2})} \;\text{ for } 0 \le x \le \frac{\sqrt{3}}{2}\,; \end{cases} \tag{2.7}$$

see Fig. 2.2. In particular it can be seen that

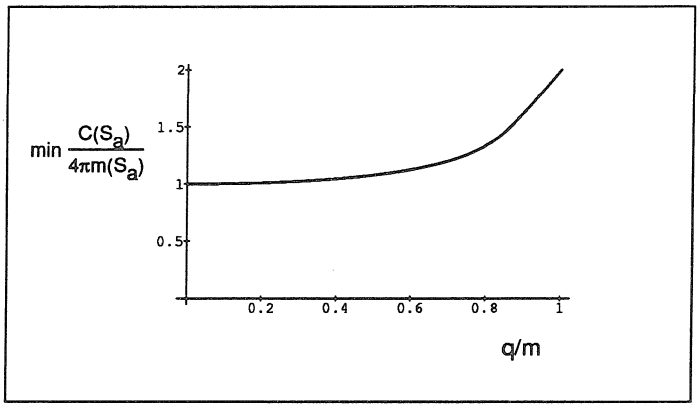

Figure 2.2: The minimum circumference to mass ratio [Eq. (4)] for spherical surfaces enclosing static spheres of charged perfect fluid, as a function of the fluid's charge to mass ratio. The circumference to mass ratio is always greater than 4π in accordance with the hoop conjecture. The use of mass enclosed instead of mass at infinity is important in this regard; see text.

$$\mathcal{C}(S_a) \geq 4\pi m(S_a) \quad \forall \; a > r_+ \text{ and } q < m \tag{2.8}$$

as claimed.

There are also some indications in favor of a quasi-local version of the HC incorporating the Hawking[28] definition of mass. In spherically symmetric spacetimes, the Hawking mass $m(S)$ of a spherical surface S coincides with the "mass $m(r)$ inside Schwarzschild radius r"[34], which plays a central role in the standard theory of spherical systems[35]. Moreover, for this $m(r)$ a local version of the HC is known to be valid: spheres of Schwarzschild radius r where $r < 2m(r)$ must be trapped. In addition, if S is any closed 2-surface in a static, possibly non-spherical spacetime, which is everywhere orthogonal to the timelike killing field, then the Hawking mass $m(S)$ satisfies[36]

$$m(S)^2 \leq \mathcal{A}(S)/16\pi. \tag{2.9}$$

Hence if as seems plausible $\mathcal{A}(S)$ is bounded above by some multiple of $\mathcal{C}(S)^2$, we then obtain a result of the form

$$m(S) \leq k\, \mathcal{C}(S) \tag{2.10}$$

for some constant k.

We now address the following question: under what conditions will the use of asymptotic mass be appropriate? If we grant that some local form of the HC is valid, and Ω_o is a region such that

$$m(\Omega) \simeq m_\infty \quad \forall\ \Omega \supset \Omega_o \tag{2.11}$$

where m_∞ is the asymptotic mass, it then follows that a horizon will be formed whenever

$$m_\infty \gtrsim \inf\{\mathcal{C}(\partial\Omega) \mid \Omega \supset \Omega_o\} \tag{2.12}$$

so that we recover a formulation of the conjecture which incorporates the definition (2.4) of circumference used above. If we constrain the initial value hypersurface in such a way as to ensure that gravitational radiation is unimportant on that hypersurface, then for reasonable definitions of mass Eq. (2.11) will be satisfied when Ω_o is taken to be the region where the stress energy tensor is nonzero. Thus we obtain the normal global version of the HC (but with a gravitational radiation caveat) as a consequence of the local version.

In investigating the HC there are two different approaches which can be adopted. One is an interior approach, which focuses on the interior of the matter-containing region, and by imposing energy conditions, etc. there tries to derive constraints on the spacetime geometry. This was the procdure followed by Redmount, and by Schoen and Yau. The other is an exterior approach, which instead works with the vacuum field equations that hold outside the matter region. It may be that the HC property is a consequence of these exterior field equations, and independent of the detials of interior solutions. Some indication that this might be the case comes from the fact that surfaces of minimal circumference are sometimes located in the vacuum *outside* the matter region [c.f. the discussion preceeding Eq. (2.4) above]. The exterior approach is also easier to analyse. To do so it is not necessary to consider any matching of interior matter solutions to exterior vacuum solutions; as Redmount has suggested[9] one can consider purely vacuum spacetimes.

Accordingly, we next consider how the conjecture applies to static vacuum spacetimes with singular sources. As trapped surfaces cannot occur in static regions of spacetime and gravitational radiation is absent, the HC reduces in this case to the following statement: there are no surfaces S enclosing the source region which satisfy $\mathcal{C}(S) < 4\pi m_\infty$, where m_∞ is the asymptotic mass. The same conclusion can be reached if one considers event horizons instead of trapped surfaces, since if an event horizon can be found then by Israel's black hole uniqueness theorem[37]

the spacetime must be a portion of the static region of the Schwarzschild spacetime for which no surfaces satisfying the above inequality exist.

3 EVIDENCE IN SUPPORT OF THE EXTERIOR APPROACH: STATIC, AXISYMMETRIC SPACETIMES

In this section we present evidence in support of our view that the exterior approach to proving the HC has a good chance of succeeding, at least in static, vacuum spacetimes. For such spacetimes the appropriate version of the conjecture is as follows (c.f. the end of section 2.3).

The HC for vacuum static spacetimes: *The circumferences of all surfaces surrounding the singular source region should be greater than or of the order of* $4\pi m$*, where* m *is the asymptotic mass.*

We shall investigate the validity of this conjecture in axisymmetric, static spacetimes.

We start in section 3.1 by briefly describing the Weyl formalism[38] for solving the static, axisymmetric, vacuum Einstein field equations, and we then show that in the case of three particular Weyl spacetimes or families of spacetimes, the conjecture holds true. In section 3.2 we specialize to oblate geometries and show that under certain circumstances, for a spacetime to satisfy the conjecture it is sufficient to have $\mathcal{C}(S) \geq 4\pi m$ for those surfaces S which are level surfaces of the lapse function. This result considerably simplifies any analyses of the HC in these spacetimes, and we use it to derive a simple sufficient condition for it to hold true. Finally in section 3.3 we turn to prolate geometries and show that if S is a convex level surface of the lapse function, then $\mathcal{C}(S) \geq 4\pi m$ whenever the value of the lapse on the surface is sufficiently large.

3.1 General Weyl spacetimes

We start by recalling the Weyl description of static, vacuum, axisymmetric spacetimes[38]. In these spacetimes there exist coordinates $\{t, \rho, z, \phi\}$ such that the line element takes the form

$$ds^2 = -e^{2\psi}dt^2 + e^{2(\gamma-\psi)}(d\rho^2 + dz^2) + \rho^2 e^{-2\psi}d\varphi^2, \qquad (2.13)$$

where $\psi = \psi(\rho, z)$, and $\gamma = \gamma(\rho, z)$. The vacuum Einstein field equations reduce to

$$ {}^{(F)}\nabla^2\psi \equiv \rho^{-1}(\rho\psi_{,\rho})_{,\rho} + \psi_{,zz} = 0, \tag{2.14} $$

$$ \gamma_{,\rho} = \rho(\psi_{,\rho}^2 - \psi_{,z}^2), \quad \text{and} \quad \gamma_{,z} = 2\rho\psi_{,\rho}\psi_{,z} \, . \tag{2.15} $$

Here the Laplacian ${}^{(F)}\nabla^2$ is calculated with respect to a flat, non-physical 3-metric, which is given by ${}^{(F)}ds^2 = d\rho^2 + dz^2 + \rho^2 d\varphi^2$. The appropriate boundary conditions for these equations are that $\gamma = 0$ at $z = 0$ (except at singularities), and that $\psi \to 0$ at least as fast as $1/r$ as $r \to \infty$, where $r = \sqrt{\rho^2 + z^2}$ [39]. Eqs. (2.15) may be solved by quadrature, so that solutions of Eq. (2.14) determine the geometry. The asymptotic mass of the 3-geometry is[30]

$$ m = \frac{1}{4\pi} \int_S {}^{(3)}\frac{\partial e^{\psi}}{\partial n} \; {}^{(3)}d^2S, \tag{2.16} $$

where S is any surface enclosing the matter region, the prefix ${}^{(3)}$ means that the calculation is to be carried out in the physical curved 3-geometry, and $\partial/\partial n$ denotes the derivative in the direction of the outward pointing normal to S. From the metric (2.13) with $dt = 0$ one obtains that

$$ m = \frac{1}{4\pi} \int_S {}^{(F)}\frac{\partial \psi}{\partial n} \; {}^{(F)}d^2S \, , \tag{2.17} $$

i.e., the asymptotic mass is that of the corresponding Newtonian problem.

Consider now surfaces enclosing the singular source region in these spacetimes. We shall restrict attention to axisymmetric surfaces S as it seems plausible that those surfaces for which the circumference function $\mathcal{C}(S)$ is a minimum do not break the symmetry of the surrounding spacetime. Any such surface S of spherical topology is determined by a curve D in the ρz half plane by rotation about the z axis; see Fig. 2.3. We will from here on always use D and S to denote a curve and a surface related in this way.

In terms of D the asymptotic mass of the 3-geometry is

$$ m = \frac{1}{2} \int_D \rho \frac{\partial \psi}{\partial n} \; d\ell. \tag{2.18} $$

The maximum lengths of azimuthal and polar curves on S, i.e., those curves which are the analogs of lines of latitude and longitude, are

$$ L_e = \sup_D \; 2\pi\rho e^{-\psi}, \tag{2.19} $$

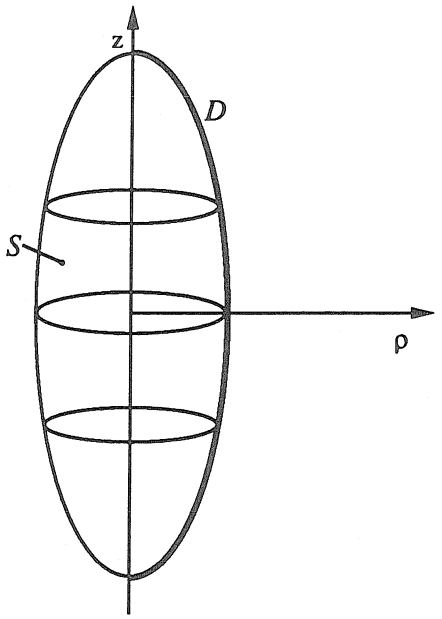

Figure 2.3: An axially symmetric surface S in Euclidean 3-space with a cylindrical coordinate system determines and is determined by a unique curve D in the ρz half plane.

and

$$L_p = 2\int_D e^{\gamma-\psi}\ d\ell. \tag{2.20}$$

The definition of circumference that we use is (c.f. section 2.2)

$$\mathcal{C}(S) = \max(L_e, L_p). \tag{2.21}$$

In the above equations $d\ell$ denotes the element of proper length with respect to the flat non-physical geometry on the ρz half plane determined by the metric ${}^{(2)}ds^2 = d\rho^2 + dz^2$, and $\sup_D f$ means $\sup\{f(x) \mid x \in D\}$. We will call a surface oblate if $L_e(S) > L_p(S)$ and prolate otherwise, and similarly we will call a Weyl spacetime oblate (prolate) if the surfaces on which ψ is constant are oblate (prolate). Thus in these spacetimes consideration of the HC naturally divides into two cases. While it is not always true that $L_p \geq 4\pi m$, or that $L_e \geq 4\pi m$, it may well be that $\mathcal{C}(S) = \max(L_e, L_p) \geq 4\pi m$ always.

For several solutions of the vacuum field equations (2.14) and (2.15) it is straightforward to show that indeed $\mathcal{C}(S)$ is greater than $4\pi m$ for all axisymmetric surfaces S. The simplest example is the Curzon solution given by

$$\psi = -\frac{m}{r}, \quad \gamma = -\frac{m^2\sin^2\theta}{2r^2}, \tag{2.22}$$

where the coordinates (r, θ) are defined by $z = r\cos\theta$, $\rho = r\sin\theta$. From Eq. (2.19) we obtain, for any axisymmetric surface S,

$$\begin{aligned} \mathcal{C}(S) &\geq L_e = \sup_D\ 2\pi r\sin\theta\, e^{m/r} \\ &\geq \inf_r\ 2\pi r e^{m/r} = 2\pi m e, \end{aligned} \tag{2.23}$$

so that $\mathcal{C}(S) > 4\pi m$ always.

As a second example we take a fictitious source for Laplace's equation consisting of a line of uniform linear mass density $\Gamma/2$ on the symmetry axis from $z = -a$ to $z = a$. Define coordinates $\{u, v\}$ by $z + i\rho = a\mathrm{Cosh}(u + iv)$, for $0 \leq u < \infty$ and $0 \leq v \leq \pi$. Then the metric is given by[10]

$$\psi = \Gamma\ln\tanh\frac{u}{2},\ \gamma = -\frac{\Gamma^2}{2}\ln\left(1 + \frac{\sin^2 v}{\sinh^2 u}\right), \tag{2.24}$$

and the mass is $m = \Gamma a$. A calculation of the Riemann invariant $R_{\mu\nu\lambda\rho}R^{\mu\nu\lambda\rho}$ reveals that the coordinate singularity at $u = 0$ is a physical singularity except when $\Gamma = 1$, in which case it is the Schwarzschild horizon. Numerical studies by Redmount ([9], p. 711) have indicated that $\mathcal{C}(S_u) \geq 4\pi m$ for all the ellipsodial

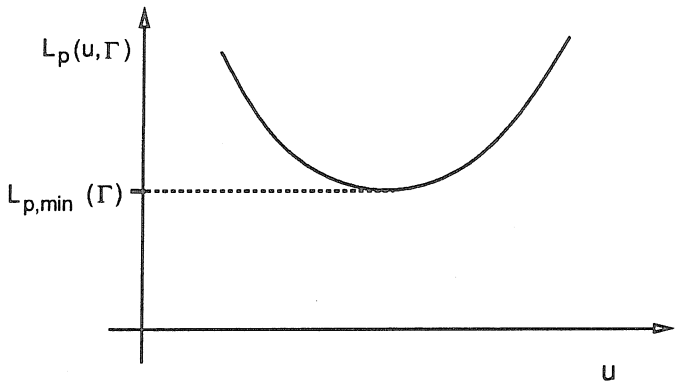

Figure 2.4: A graph of the lengths of polar curves on the ellipsoidal surfaces of constant u in the Γ-metric spacetimes. Notice that this length (and consequently also the circumference $\mathcal{C}_1$ of the surfaces) diverges as u tends towards zero, even though the corresponding surfaces are nested inside each other and apparantly getting smaller and smaller.

u = constant surfaces in these spacetimes. In the case where $0 < 1 - \Gamma \ll 1$ corresponding to a prolate but almost spherical geometry, this can be confirmed by explicit calculation: we find that

$$L_{\mathrm{p,min}}(\Gamma) = 4\pi m\left[1 - \varepsilon\,\ln\varepsilon + O(\varepsilon)\right], \tag{2.25}$$

where $\varepsilon = 1 - \Gamma$ and $L_{\mathrm{p,min}}$ is the smallest of the polar circumferences $L_p(S_u)$. This is illustrated in Figs. 2.4 and 2.5.

In the case $\Gamma > 1$, corresponding to an oblate geometry, it is possible to show that the conjecture is satisfied for all closed surfaces by using the same technique as in the above Curzon case. If S is an arbitrary axisymmetric surface, then from Eq. (2.19),

$$\begin{aligned}
\mathcal{C}(S) &\geq L_e = \sup_D\ 2\pi\rho e^{-\psi} \\
&= \sup_D\ 2\pi a\,\sinh u\,\sin v\,\tanh^{-\Gamma}(u/2) \\
&\geq \inf_{u>0}\ 2\pi a\,\sinh u\,\tanh^{-\Gamma}(u/2) \\
&= 2\pi a\,(\Gamma+1)\left(\frac{\Gamma-1}{\Gamma+1}\right)^{(1-\Gamma)/2},
\end{aligned} \tag{2.26}$$

so that using $m = \Gamma a$,

$$\frac{\mathcal{C}(S)}{4\pi m} \geq h(\Gamma) \equiv \frac{\Gamma+1}{2\Gamma}\left(\frac{\Gamma-1}{\Gamma+1}\right)^{(1-\Gamma)/2}. \tag{2.27}$$

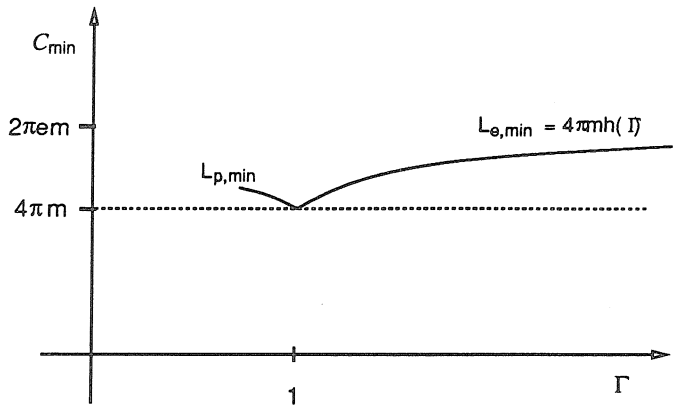

Figure 2.5: A graph of the minimum obtainable circumference to mass ratio $\mathcal{C}_1(S)/m$ in the Γ-metric spacetimes as a function of the 'oblateness' parameter Γ. For $\Gamma < 1$ the longest curves on the surfaces of constant u are polar, while for $\Gamma > 1$ they are equatorial. Again the hoop conjecture is validated.

The function h satisfies $h(\Gamma) \geq 1$ for all $\Gamma > 1$ as shown in Fig. 2.5.

Finally consider the class of spacetimes given by

$$\psi(r,\theta) = -\frac{m}{r} + \frac{\alpha}{r^{n+1}} P_n(\cos\theta)\,, \tag{2.28}$$

where α is any real number and P_n is the nth Legendre polynomial. Define θ_n to be such that $\cos\theta_n$ is the smallest positive root of the equation $P_n(x) = 0$. Then we obtain

$$\begin{aligned} \frac{\mathcal{C}(S)}{4\pi m} &\geq \sup_D \frac{r}{2m} \sin\theta \exp\left[\frac{m}{r} - \frac{\alpha}{r^{n+1}} P_n(\cos\theta)\right] \\ &\geq \inf_r \frac{re^{m/r}}{2m} \sin\theta_n \geq \frac{1}{2}\alpha_n e, \end{aligned} \tag{2.29}$$

where $\alpha_n = \sin\theta_n$. The sequence (α_n) starts out $(1, \sqrt{2/3}, \sqrt{2/5}, 0.88, 0.71, \ldots)$ and is bounded below, so that $\mathcal{C}(S) \gtrsim 4\pi m$ for all axisymmetric surfaces S.

3.2 Oblate Weyl spacetimes

In investigating the validity of the HC in general Weyl spacetimes, the most natural course of action is to consider the spacetime geometry as fixed and to calculate the circumferences of various surfaces in this spacetime. However we have found the following approach to be more useful. We choose a closed surface S in the unphysical flat background geometry, and specify the value of the potential ψ on

S. Then ψ on the region exterior to S will be determined as the solution of the following boundary value problem: ${}^{(F)}\nabla^2\psi = 0$ outside S, $\psi_{|S}$ = as specified, and $\psi \to 0$ as $r \to \infty$. Thus the pair $(S, \psi_{|S})$ determines a solution of the vacuum field equations, and all exterior solutions may be obtained in this way. If we specify S and the corresponding curve D by a smooth function $\rho = R(z)$, for $z_0 \leq z \leq z_1$, then the normal derivative $\partial\psi/\partial n_{|D}$ is determined from R and $\psi_{|D}$ by solving the boundary value problem. The value of the function $\gamma_{|D}$ at a point p on D is determined by integrating $\nabla\gamma$ along that portion of D joining the z-axis to p, where $\nabla\gamma$ is given in terms of $\psi_{|D}$ and $\partial\psi/\partial n_{|D}$ by Eqs. (2.15). The mass of the spacetime and the circumference of S are then given by Eqs. (2.18) to (2.20), i.e., are functionals of R and $\psi_{|D}$, and the hoop conjecture will be true in these Weyl spacetimes if

$$\mathcal{C}(R, \psi_{|D}) \geq 4\pi m(R, \psi_{|D}) \tag{2.30}$$

always.

We now show that for oblate surfaces it is sometimes sufficient to consider the special case $\psi_{|D}$ = constant. If, in any Weyl spacetime, we define S_λ for $\lambda > 0$ to be the surface $\{\, p \mid \psi(p) = -\lambda \,\}$, then specifically we have

Theorem 1 *In a Weyl spacetime suppose that $\lambda_0 > 0$ is such that (i) $\nabla\psi \neq 0$ everywhere on $\{\, p \mid \psi(p) \geq -\lambda_0 \,\}$, and (ii) the coordinate function ρ has only one local maximum on each curve D_λ corresponding to S_λ for $\lambda \leq \lambda_0$. Then $L_e(S) \geq 4\pi m$ for all axisymmetric surfaces S of spherical topology outside of and enclosing S_{λ_0} if and only if $L_e(S_\lambda) \geq 4\pi m$ for all S_λ outside S_{λ_0}.*

Note that conditions (i) and (ii) will be fulfilled for surfaces S_{λ_0} sufficiently far from the singular source, i.e., for sufficiently small λ_0. The precise distance required will depend on the sizes of the dipole and higher order multipole mass moments of the fictitious Newtonian source compared to that of the monopole moment.

Proof: We first show that each surface S_λ for $\lambda \leq \lambda_0$ is of spherical topology. If any one of these surfaces is not connected, put $\bar{\lambda} = \inf\{\, \lambda \mid S_\lambda$ has more than one connected component$\}$, which is strictly positive as $\psi \approx -m/r$ as $r \to \infty$. Then it can be seen that there is a point p in $S_{\bar{\lambda}}$ with $\nabla\psi(p) = 0$, which contradicts assumption (i). Hence each S_λ is a connected, compact, orientable two-dimensional manifold, and so is topologically a sphere with n handles. An argument similar to that just given shows that the genus n must be zero. Also, the outward normal derivative $\partial\psi/\partial n$ is positive everywhere on each S_λ by condition (i), and so the region exterior to S_λ is the union of the S_σ for $\sigma < \lambda$.

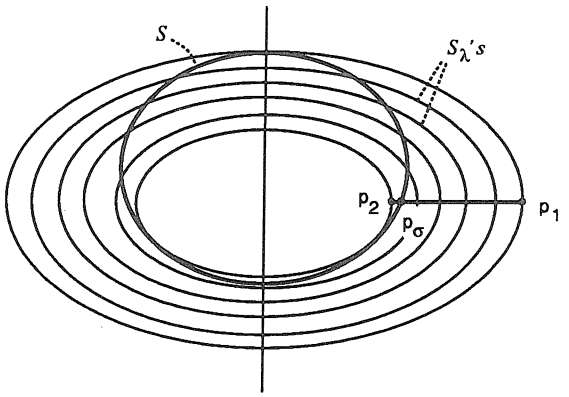

Figure 2.6: An illustration of the situation in the theorem. The ellipses represent level surfaces of the lapse function $e^{2\psi}$.

We now prove the 'if' part of the theorem, as the 'only if' part is obvious. Suppose that we are given a surface S as in the statement of the theorem. Define $\lambda_1 = \inf_S(-\psi)$, $\lambda_2 = \sup_S(-\psi)$ (see Fig. 2.6), and for λ between λ_1 and λ_2 let p_λ be the unique point on D_λ furthest from the z axis. Then we have that $\eta(p_\lambda) = \sup\{\, \eta(p) \mid p \in S_\lambda \,\}$, where η is the function $\rho e^{-\psi}/(2m)$. Hence

$$\eta(p_\lambda) \geq 1, \quad \lambda_1 \leq \lambda \leq \lambda_2, \tag{2.31}$$

by Eq. (2.19). Let Γ be the smooth curve generated by the p_λ's and let S_i, S_e denote the regions interior to and exterior to S. We claim that $p_2 \equiv p_{\lambda_2}$ lies in $S_i \cup S$. Otherwise there would exist a neighbourhood of p_2 in S_e, and as $\nabla\psi(p_2) \neq 0$, there would exist a point $q \in S_e$ with $\psi(q) < \psi(p_2) = \inf_S \psi = \inf_{S_e} \psi$ (using the fact that ψ is harmonic) which is a contradiction. Similarly $p_1 \equiv p_{\lambda_1} \in S_e \cup S$, and so it follows that the curve Γ cuts S at some point, say p_σ. It follows from Eqs. (2.19) and (2.31) that

$$\frac{L_e(S)}{4\pi m} = \sup_S \eta \;\geq \eta(p_\sigma) \geq 1. \tag{2.32}$$

This concludes the proof.

We now turn to an analysis of the inequality (2.30) under the simplifying assumption that $\psi_{|D}$ is constant. First we introduce the following generalised notion of capacity which is a geometric measure of the size of a region. For Ω any connected open region in a Riemannian manifold Σ , let u be the unique function satisfying $\nabla^2 u = 0$ on the complement Ω_e of Ω in Σ, $u|_{\partial\Omega} = -1$, and $u \to 0$ at infinity. Then the capacity of Ω is

$$R_o(\Omega) \equiv \frac{1}{4\pi} \int_{\partial\Omega} n^a \nabla_a u, \tag{2.33}$$

where n^a is the outward pointing unit normal to $\partial\Omega$. It can be shown[40] that

$$R_o(\Omega) = \inf \ \{ \ \int_{\Omega_e} g^{ab} \nabla_a u \ \nabla_b u \mid u \in C^\infty(\Omega_e), \\ u_{|\partial\Omega} = -1, u \to 0 \text{ at } \infty\}, \tag{2.34}$$

and it follows that the capacity function R_o is monotone in the sense that

$$\Omega \subset \Omega' \Rightarrow R_o(\Omega) \leq R_o(\Omega'). \tag{2.35}$$

For Ω a connected region, we define $R_o(\partial\Omega) = R_o(\Omega)$.

Suppose now that we are given a curve D and we specify $\psi_{|D}$. Then from Eqs. (2.14) and (2.17) the mass is given by $m(D, \psi_{|D}) = -\psi_{|D} \ R_o(S)$, as m is a linear function of the number $\psi_{|D}$. Hence to obtain $m > 0$ we must take $\psi_{|D} = -\lambda$, where $\lambda > 0$. Here the capacity is calculated with respect to ${}^{(F)}ds^2$, the flat three-dimensional metric. (In terms of the physical curved 3-metric we have $m = (1 - e^{-\nu})R_o(S_\nu)$ for any $\nu > 0$.) We now let ψ_o be the solution of the boundary value problem with the boundary condition $\psi_{o|D} = -1$, with the mass being m_o and γ_o being the corresponding function obtained from Eqs. (2.15). Then $\psi = \lambda\psi_o$ and $\gamma = \lambda^2\gamma_o$, and Eqs. (2.18) and (2.19) yield that

$$L_e = \sup_D \ 2\pi\rho e^\lambda \tag{2.36}$$

and

$$m = \lambda m_o = \lambda R_o(S). \tag{2.37}$$

Now if we use the monotonicity property (2.35) together the fact that the capacity R_o of a sphere is just its ordinary radius, we obtain that $R_o(S) \leq r_m \equiv \sup_D r$, where $r = \sqrt{\rho^2 + z^2}$. Also if we define $\rho_m = \sup_D \rho$, then from Eqs. (2.36) and (2.37),

$$\frac{L_e}{4\pi m} = \frac{\rho_m}{2R_o(S)} \frac{e^\lambda}{\lambda} \geq \left(\frac{e}{2}\right) \frac{\rho_m}{r_m}. \tag{2.38}$$

Thus for curves D for which $\rho_m \approx r_m$, L_e is approximately equal to m and the HC for these surfaces is approximately satisfied. Only in cases where $\rho_m \ll r_m$ can it be violated, and we expect that in such cases $L_p > 4\pi m$ instead, so that by Eq. (2.21) the inequality $\mathcal{C}(S) > 4\pi m$ is still maintained.

More generally, if we define the 'eccentricity' of a curve D via

$$\epsilon(D) \equiv \frac{\rho_m}{R_o(D)}, \tag{2.39}$$

then we see from the inequality (2.38) that $L_e(S) \geq 4\pi m$ if and only if $\epsilon(D) \geq 2\lambda e^{-\lambda}$. Combining this with theorem 1 we obtain

Theorem 2 *Suppose in a Weyl spacetime (i) $\nabla\psi \neq 0$ everywhere, and (ii) the level surfaces of ψ are convex with respect to the fictitious flat 3-geometry. Then $L_e(S) \geq 4\pi m$ for all axisymmetric surfaces S of spherical topology enclosing the singularity if and only if $\epsilon(D_\lambda) \geq 2\lambda e^{-\lambda}$ for every $\lambda > 0$.*

The condition on the eccentricity will be satisfied in particular when $\rho_m > (2/e)r_m$ for all curves D on which ψ is constant. As an example we apply this theorem to the 'Γ-metrics' discussed earlier[cf. Eq. (2.24)] and rederive the result that the hoop conjecture is satisfied for $\Gamma > 1$. Using $\rho_m = a\,\mathrm{Sinh}u$, $R_o(D) = \Gamma a/\lambda$ and $\lambda = -\Gamma \ln\tanh(u/2)$ we obtain that

$$\inf_\lambda \epsilon(D_\lambda)\frac{e^\lambda}{2\lambda} = \inf_\lambda \frac{\exp\left[\lambda(1-1/\Gamma)\right]}{\Gamma\left(1-e^{-2\lambda/\Gamma}\right)}$$

$$= \frac{\Gamma+1}{2\Gamma}\left(\frac{\Gamma-1}{\Gamma+1}\right)^{(1-\Gamma)/2} \quad \geq 1 \quad \forall\ \Gamma > 1, \tag{2.40}$$

where the last expression is the same as that obtained previously in Eq. (2.27).

3.3 Prolate Weyl spacetimes

We now turn to a consideration of the inequality (2.30) in the case when the surface S is prolate. We again restrict attention to equipotential surfaces, although in this case we have not been able to show that it is sufficient to consider these surfaces only. Our result is as follows:

Theorem 3 *In a Weyl spacetime, let D be a curve in the ρz half plane with $\psi_{|D} = -\lambda$. Suppose that (i) D is convex, and (ii) $\lambda \leq \lambda_{\mathrm{crit}}(D)$, where*

$$\lambda_{\mathrm{crit}}^{-1} = 2\int_0^{\rho_m}\left(\frac{\partial\psi_o}{\partial n}\right)^2 \rho\, d\rho$$

and $\psi_o \equiv \lambda^{-1}\psi$. Then

$$\frac{L_p(S)}{4\pi m} \geq \frac{e}{\pi}\left(1+\frac{\pi^2}{4}\right)^{-\frac{1}{2}} \approx \frac{1}{2}.$$

Thus the spirit, if not the letter, of the hoop conjecture is satisfied for sufficiently small λ in the special case of convex D. To prove this result, we have from Eq. (2.20) that

$$L_p = 2\int_0^{L(D)} d\xi\; e^{\lambda+\lambda^2\gamma_o(\xi)}. \tag{2.41}$$

Here $L(D)$ is the length of D with respect to ${}^{(2)}ds^2$, and ξ is the proper length parameter. Now from Eqs. (2.15) we calculate that $\gamma_o' = -\psi_{o,n}^2\rho\rho'$, where the prime denotes differentiation with respect to ξ, and the n denotes normal derivative. If $\mu \equiv -\gamma_o$, then it follows that $\mu_m \equiv \sup_D \mu = \int_0^{\rho_m} \psi_{0,n}^2 \rho d\rho$, and so by (ii) above $1/\lambda \geq 2\mu_m \geq -2\gamma_o(\xi)$ for all ξ. Hence

$$e^{\lambda+\lambda^2\gamma_o} > e^{\lambda/2}, \tag{2.42}$$

and combining this with Eqs. (2.37) and (2.41) yields that

$$\frac{L_p}{4\pi m} \geq \frac{e^{\lambda/2}}{\lambda}\frac{L(D)}{2\pi m_o} \geq \frac{e}{4\pi}\frac{L(D)}{R_o(S)}. \tag{2.43}$$

To obtain an estimate of the capacity of the surface S, we use the result[40] that

$$R_o(S) \leq \frac{1}{4\pi}\int_S \bar{\kappa}\, d^2S, \tag{2.44}$$

where $\bar{\kappa}$ is the mean curvature of the surface. If we take D to be specified by the equation $\rho = R(z)$ for $z_0 \leq z \leq z_1$, with $R(z_0) = R(z_1) = 0$, then we obtain

$$\bar{\kappa} = \frac{1}{2}\left(\frac{1/R}{(1+R'^2)^{\frac{1}{2}}} - \frac{R''}{(1+R'^2)^{\frac{3}{2}}}\right). \tag{2.45}$$

In this expression the second term in brackets is the curvature κ of the curve D in the ρz plane, and primes denote differentiation with respect to z. Inserting this into the bound (2.44) gives

$$R_o(S) \leq \frac{1}{4}\Delta z + \frac{1}{4}\int_D \rho\kappa\, d\ell \tag{2.46}$$

where $\Delta z \equiv z_1 - z_0$, so that from Eq. (2.43)

$$\frac{L_p}{4\pi m} \geq \frac{e}{\pi}\left(\frac{\Delta z}{L(D)} + \langle\rho\kappa\rangle\right)^{-1} \geq \frac{e}{\pi}\frac{1}{1+\langle\rho\kappa\rangle}, \tag{2.47}$$

where

$$\langle\rho\kappa\rangle \equiv \frac{1}{L(D)}\int_D \rho\kappa\, d\ell\,. \tag{2.48}$$

Now for a general curve D, the quantity $\langle\rho\kappa\rangle$ may be arbitrarily large, but when D is convex it is possible to show that it is bounded above. As $R'' \leq 0$ for D convex, we have

$$\langle\rho\kappa\rangle = \frac{1}{L(D)}\int \mathrm{dz}\ \frac{-R''\rho}{1+R'^2} \leq \frac{\rho_m}{L(D)}\int \mathrm{dz}\ \frac{-R''}{1+R'^2}$$

$$= -\frac{\rho_m}{L(D)}\tan^{-1}(R')|_{z_0}^{z_1} = \frac{\rho_m}{L(D)}\pi. \tag{2.49}$$

But it is easy to see that $L(D) \geq 2\rho_m$ so that from Eqs. (2.47) and (2.49) we finally obtain

$$\frac{L_p}{4\pi m} \geq \frac{e}{\pi}\frac{1}{1+\pi/2} \approx \frac{1}{3}. \tag{2.50}$$

It is possible to improve this bound to give the one quoted in the theorem by combining Eq. (2.49) with the first inequality in (2.47) and considering the geometric relationships between Δz, ρ_m and $L(D)$. [As indicated by Fig. 2.7, the length $L(D)$ of the curve satisfies $L(D) \geq \sqrt{(\Delta z - \alpha)^2 + \rho_m^2} + \sqrt{\alpha^2 + \rho_m^2}$ for some α.]

In the course of the above proof we showed that condition (ii) in the theorem is equivalent to $\lambda^{-1} \geq 2\mu_m$, where $\mu = -\gamma_o$ and $\mu_m = \sup_D \mu$. By using the inequality $\int_0^1 e^f \geq \exp\int_0^1 f$ it is possible to weaken this condition to $\lambda^{-1} \geq 2\langle\mu\rangle$, where $\langle\mu\rangle \equiv \int_0^{L(D)} d\xi\, \mu(\xi)/L(D)$.

3.4 Future directions for Weyl spacetimes

In this section we have considered the ratio $\Theta \equiv \mathcal{C}(S)/4\pi m$ for convex equipotential surfaces S in Weyl geometries as a function of (i) the curve D that generates S by a rotation, and (ii) the value $-\lambda$ of the potential ψ on this surface. We found that $\Theta \geq 1$ for all positive values of λ whenever the eccentricity of the curve is greater than $2/e$. For smaller values of the eccentricity we found that the ratio Θ is bounded below by a positive constant of the order of a half when $\lambda \geq \lambda_1(\epsilon(D))$ and when $\lambda \leq (2\langle\mu\rangle)^{-1}$, where $\lambda_1(x)$ is the larger of the two roots of $2\lambda e^{-\lambda} = x$. Now in general $(2\langle\mu\rangle)^{-1}$ is not greater than $\lambda_1(\epsilon(D))$, and thus there is a range of values of λ for which none of the bounds obtained for Θ apply. For example for ellipses whose ratio of semiminor axis to semimajor axis is $t \ll 1$, asymptotically $\lambda_1(\epsilon(D)) \approx |\ln t|$ and $(2\langle\mu\rangle)^{-1} \approx \frac{1}{2}|\ln t|$. Further progress towards showing $\Theta \gtrsim 1$ generically would necessitate finding better estimates for the lengths of polar curves with λ in this intermediate range.

Also, we have restricted attention to Weyl spacetimes with isolated singular sources. If one considers non-isolated sources, one can obtain spacetimes with non-

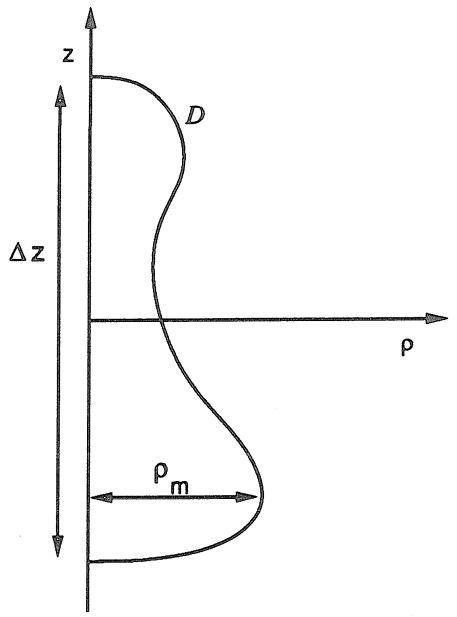

Figure 2.7: An illustration of the quantities $L(D)$, ρ_m, and Δz.

Schwarzschild event horizons. A complete classification of such 'distorted black holes' in static, axisymmetric spacetimes has been given by Geroch and Hartle[41]. It might be interesting to investigate the circumferences of the distorted horizons.

4 CONCLUSION

In this paper we have reviewed some of the evidence in favor of the HC, and presented some tentative but suggestive results which tend to support it. We have also advocated the following two points of view: (i) that the conjecture can be interpreted as a quasi-local statement in the spirit of Schoen and Yau's theorem, and (ii) that the geometric constraints embodied in the conjecture may very well be consequences of the exterior vacuum field equations and independent of the complicated interior physics.

The dynamical collapse simulations of Shapiro and Teukolksy[16] apparently exhibit violations of cosmic censorship, violations which are in accordance with the HC. A proof of some criterion along the lines of the HC would both bolster our faith in those calculations, and also possibly increase our understanding of when such violations can occur.

ACKNOWLEDGEMENTS

The author's thanks go to Kip Thorne for many helpful and detailed discussions about aspects of this work, and about it's presentation.

APPENDIX A: DEFINITIONS OF CIRCUMFERENCE

In this appendix we show that for axisymmetric surfaces S, the definition (2.2) of circumference satisfies

$$C_2(S) = L_p, \tag{2.51}$$

where L_p is twice the distance from the north pole to the south pole. In particular we have that $C_2(S) \neq C_1(S) \equiv \max(L_e, L_p)$, which is the quantity that seems to be appropriate for the HC in axisymmetric spacetimes. Here L_e denotes the maximum of the lengths of closed azimuthal curves as in Eq. (2.19).

An axisymmetric surface S can be described by a line element of the form

$$ds^2 = \alpha(\theta)^2 d\theta^2 + \beta(\theta)^2 \sin^2\theta d\phi^2.$$

Given points $\mathcal{P}$, $\mathcal{Q}$ in S, let Γ_1 be the curve joining $\mathcal{P}$ to the north pole $\mathcal{N}$ along a line of longitude ($\phi = \text{const}$). Let Γ_2 be a similar curve joining $\mathcal{N}$ to $\mathcal{Q}$, and let $\Gamma_{\mathcal{N}}$ be Γ_2 joined onto Γ_1. Similarly construct $\Gamma_{\mathcal{S}}$ joining $\mathcal{P}$ to $\mathcal{Q}$ via the south pole $\mathcal{S}$. Then the distance from $\mathcal{P}$ to $\mathcal{Q}$ satisfies $d(\mathcal{P}, \mathcal{Q}) \leq L(\Gamma_{\mathcal{N}})$, and similarly for the curve $\Gamma_{\mathcal{S}}$. However it is easy to see that $L(\Gamma_{\mathcal{N}}) + L(\Gamma_{\mathcal{S}}) = L_p$, so that $2\, d(\mathcal{P}, \mathcal{Q}) \leq L_p$. Now taking the maximum over all points $\mathcal{P}$ and $\mathcal{Q}$ and using the definition (2.2) yields that $C_2(S) \leq L_p$, and Eq. (2.51) then follows.

Now consider a surface of constant lapse in the spacetime given by Eq. (2.24). From Eq. (2.20) we obtain that

$$\begin{aligned} L_p(S) &= 4\sinh^{\Gamma^2}(u)\tanh^{-\Gamma}(u/2) \\ &\quad \int_0^\pi dv(\sinh^2 u + \sin^2 v)^{-\Gamma^2} \\ &\leq 4\pi \tanh^{-\Gamma}(u/2)\sinh^{\Gamma^2}(u), \end{aligned} \tag{2.52}$$

which tends to zero as u tends to zero if $\Gamma > 1$. Hence $C_2(S)/m$ can be arbitrarily small.

APPENDIX B: WORLD TUBE CIRCUMFERENCE PROOF

In this appendix we show that the definition (2.5) of the circumference of a world tube reduces to the usual definition in the case of a static spacetime. Such a spacetime can be described by a line element of the form

$$ds^2 = g_{00}(x^k)dt^2 + g_{ij}(x^k)dx^i dx^j \tag{2.53}$$

where i, j and k range from 1 to 3, and $g_{00}(x^k) < 0$. Any spacelike hypersurface is given (not just locally) by an equation of the form

$$t = F(x^1, x^2, x^3), \tag{2.54}$$

and the induced metric on Σ is

$${}^{(\Sigma)}ds^2 = (g_{ij} + g_{00}F_{,i}F_{,j})dx^i dx^j. \tag{2.55}$$

If we define Σ_o to be the hypersurface $t = 0$, then the diffeomorphism from Σ_o to Σ obtained by identifying the coordinates x^1, x^2, and x^3 will be a contraction, i.e., lengths of curves on Σ_o will always be longer than the lengths of the corresponding curves on Σ. This is because g_{ij} is positive definite and $g_{00} < 0$. A similar statement applies to distances between points. This shows that the maximum over all Σ of $C_e(\Sigma \cap T)$ will be achieved by Σ_o, which establishes the desired result.

Bibliography

[1] K.S. Thorne, in *Magic Without Magic : John Archibald Wheeler*, edited by J. Klauder (Freeman, San Francisco, 1972), p. 231.

[2] R. Penrose, Riv. Nuovo. Ciment. **1**, 252 (1969).

[3] S.W. Hawking, J. Gen. Relativ. Gravit. **10**, 1047 (1979).

[4] C.W. Misner, K.S. Thorne, and J.A. Wheeler, *Gravitation* (Freeman, San Francisco, 1973), p. 867.

[5] T. Nakamura and H. Sato, Prog. Theor. Phys. **67**, 1396 (1982).

[6] R.F. Stark and T. Piran, Phys. Rev. Lett. **55**, 891 (1985).

[7] T. Nakamura, S.L. Shapiro, and S.A. Teukolsky, Phys. Rev. D **38**, 2972 (1988).

[8] S.L. Shapiro and S.A. Teukolsky, Phys. Rev. Lett. **66**, 994 (1991).

[9] I.H.Redmount, Phys. Rev. D **27**, 710 (1983).

[10] D. Papadopoulos, B. Stewart and L. Witten, Phys. Rev. D **24**, 320 (1981).

[11] R. Bach and H. Weyl, Math. Z. **13**, 134 (1922).

[12] W.B. Bonnor, Phys. Lett. **99A**, 424 (1983).

[13] W.B. Bonnor, Phys. Lett. **102A**, 347 (1984).

[14] A. Chommoro, R. Gregory, and J.M. Stewart, Proc. R. Soc. London **A413**, 251 (1987).

[15] P.W. Lamberti and V.H. Hamity, Gen. Relativ. Gravit. **21**, 869 (1989).

[16] P.Bizon, E. Malec, and N. O'Murchadha, Phys. Rev. Lett. **61**, 1147 (1988).

[17] J.B. Hartle and D.C. Wilkins, Phys. Rev. Lett. **31**, 60 (1973).

[18] P.N. Demmie and A.I. Janis, J. Math. Phys. **14**, 793 (1973).

[19] R. Schoen and S.T. Yau, Commun. Math. Phys. **90**, 575 (1983). An improved definition of radius is given in N. O'Murchadha, Phys. Rev. Lett. **57**, 2466 (1986).

[20] P. Bizon, E. Malec, and N. O'Murchadha, Class. Quant. Grav. **6**, 961 (1989).

[21] R. Arnowitt, S. Deser, and C.W. Misner, "The Dynamics of General Relativity" in *Gravitation: An Introduction to Current Research*, edited by L. Witten (John Wiley, New York, 1962).

[22] S.W. Hawking and G.F.R. Ellis, *The large scale structure of spacetime* (Cambridge University Press, 1983).

[23] W. Israel, Can. J. Phys. **64**, 120 (1986).

[24] R. Penrose, Phys. Rev. Lett. **14**, 57 (1965).

[25] Specifically, the radius $\mathcal{R}(\Omega)$ of a region Ω is defined to be the largest number r such that there is some closed curve Γ in Ω for which the set $\{x \mid d(x,y) \leq r$ for some y in $\Gamma\}$ satisfies two conditions: (i) it forms a torus, i.e., it is not simply connected, and (ii) it lies completely inside Ω.

[26] M. Ludvigsen and J.A. Vickers, J. Phys. A. **16**, 3349 (1983).

[27] This is a consequence of the fact that such a portion of a hypersurface will be a local maximum of a volume functional.

[28] S.W. Hawking, J. Math. Phys. **9**, 598 (1968).

[29] R. Penrose, Proc. R. Soc. London **A381**, 53 (1982). See also R. Penrose and W. Rindler, *Spinors and Spacetime* (Cambridge University Press, 1984), Vol. 2, p. 395.

[30] A. Komar, Phys. Rev. **113**, 934 (1959).

[31] R. Wald, *General Relativity* (University of Chicago press, Chicago, 1984), p. 289.

[32] K. Eppley, Phys. Rev. D **16**, 1609 (1977); S.M. Miyama, Prog. Theor. Phys. **65** 894 (1981). A recent rigorous proof of the fact that black holes can form in purely vacuum spacetimes has been given by R. Beig and N. O'Murchadadh, *Trapped Surfaces due to Concentration of Gravitational Radiation* (to be published).

[33] Ponce de Leon, J. Gen. Relativ. Gravit. (USA) **19**, 289 (1987).

[34] The mass function $m(r,t)$ is defined by the line element $ds^2 = g_{tt}(r,t)dt^2 + [1-2m(r,t)/r]^{-1}dr^2 + r^2 d\Omega^2$.

[35] C.W. Misner, K.S. Thorne, and J.A. Wheeler, *Gravitation* (Freeman, San Francisco, 1973), p. 603.

[36] G.T. Horowitz and B.G. Schmidt, Proc. R. Soc. London **A381**, 215 (1982) [Eq. (1.5) with $\rho\mu \geq 0$].

[37] W. Israel, Phys. Rev. **164**, 1776 (1967).

[38] H. Weyl, Ann. Phys. (Leipzig) **54**, 117 (1917).

[39] J.L. Synge, *Relativity: The General Theory* (North Holland, Amsterdam, 1966), p. 312.

[40] G. Szego, Bull. Am. Math. Soc. **51**, 325 (1945).

[41] R. Geroch and J.B. Hartle, J. Math. Phys. **23** (4) 680 (1982).

Addendum to Chapter 2

In this addendum (written after the body of the chapter was published) we extend slightly the results obtained in chapter 2, and more importantly clarify their physical interpretation. Essentially we show that there are large classes of Weyl spacetimes in which the hoop conjecture is satisfied.

We start by describing the *fibered structure* of the space $\mathcal{W}$ of Weyl spacetimes. We define a real valued function or coordinate Γ on $\mathcal{W}$ in the following way. For a given spacetime M, consider the multipole expansion of the potential function ψ on the fictitious Euclidean 3-space. If the first non-vanishing mass multipole moment beyond the monopole is the lth moment, then at at large r,

$$\psi(\mathrm{x}) = -m/r + \frac{Q^{(l)}_{a\ldots b}\hat{x}^a \ldots \hat{x}^b}{r^{l+1}} + O(1/r^{l+2}). \tag{2.56}$$

Here $r = ||\mathrm{x}||$ and $\hat{\mathrm{x}} = \mathrm{x}/r$. Then Γ is given by

$$\Gamma^{-l} = \frac{|Q^{(l)}|}{m^{l+1}}, \tag{2.57}$$

where $|Q^{(l)}|$ is the square root of the contraction of the traceless symmetric lth rank tensor $Q^{(l)}_{a\ldots b}$ with itself. In the usual case $l = 2$, then $\Gamma^2 \propto m^3/Q$, where Q is the quadrupole moment.

Roughly speaking, Γ parameterizes the "asphericity" of the potential, in the following sense. At large distances from the source, the monopole part of ψ is dominant, and the potential is approximately spherically symmetric. The non-spherically-symmetric nature of the potential becomes apparent only at radii satisfying $|Q^{(l)}|/r^{l+1} \gtrsim m/r$, i.e.,

$$\frac{r}{m} \lesssim \Gamma. \tag{2.58}$$

Thus, for $\Gamma \gg 1$, the spacetime is aspherical in the Newtonian regime at large distances from the source. When $\Gamma \ll 1$, on the other hand, the potential ψ and also the spacetime is spherically symmetric except in the very relativistic regime. Note that the correspondence between the spherical symmetry of ψ and that of the spacetime is valid only in the Newtonian regime; e.g., the Curzon spacetime is not spherically symmetric in the strong field region. Hence the quantity Γ does not represent the *physical* sphericity of the spacetime. We note that Eq. (2.58) will not be valid if the first non-vanishving multipole is small compared to higher order multipoles, but the qualitative interpretation of Γ that we have described, as given by the nature of the regimes $\Gamma \to 0$ and $\Gamma \to \infty$, is nonetheless valid.

Now consider for each positive real number α the map $f_\alpha : \mathcal{W} \to \mathcal{W}$ given by $\psi \to \alpha\psi$ (and correspondingly $\gamma \to \alpha^2\gamma$). It is easy to see that under this transformation, $\Gamma \to \alpha\Gamma$, that is, $\Gamma(f_\alpha(M)) = \alpha\Gamma(M)$ for any spacetime M. Let us call two Weyl spacetimes *equivalent* when they are related by the action of f_α for some α. Then, the partition of the space $\mathcal{W}$ of Weyl spacetimes into disjoint equivalence classes gives $\mathcal{W}$ a fibered structure. Each fiber (or equivalence class) contains one spacetime M with $\Gamma(M) = 1$, and any other spacetime M' in the same fiber can be specified by giving its value of Γ. (We ignore the degenerate fiber corresponding to the Curzon solution.) The fibers can be subdivided into various types in the following way. Consider in a given Weyl spacetime the foliation of level surfaces S_λ of the potential ψ, in the notation of theorem 1. For small λ these surfaces will be of spherical topology, but they may not be so for large λ, i.e., near to the source. We will call a Weyl spacetime a "type I" spacetime if all the level surfaces *are* of spherical topology, and "type II" otherwise. For example, the spacetime (2.24) is of type I, but the spacetime generated by a fictitious Newtonian source consisting of two separated point masses would be of type II. A similar division clearly applies to the fibers; we analyse the two types of fiber separately.

Consider first the type II case. Our result can be stated as follows.

Theorem 4 *For a given fiber of type II, let $\mathcal{A}$ denote the region of the flat background space in which the level surfaces of ψ (which are common to the whole fiber) have spherical topology, and in which the coordinate function ρ has only one local maximum on each level surface. Then there exist numbers Γ_1 and Γ_2 such that all spacetimes in the fiber with either $\Gamma < \Gamma_1$ or $\Gamma > \Gamma_2$ have the property that all axisymmetric surfaces S of spherical topology in the region $\mathcal{A}$ which enclose the singularity satisfy $\mathcal{C}(S) \geq 4\pi m$.*

Fibers of type I are in some sense more interesting, because theorem 1 allows use to deduce results that apply all the way down to the source, at $\lambda \to \infty$. We restrict attention to fibers that do not have the property that $\epsilon(S_\lambda) \to 0$ faster than any power of $e^{-\lambda}$ as $\lambda \to \infty$, where the eccentricity function ϵ is defined in Eq. (2.39). (If this property is satisfied by any spacetime in a given fiber, it will be satisfied by all of them). Although it seems likely that generic fibers of type II will satisfy this rather weak condition, we have not been able to prove this and so instead take it as an assumption. For this type of fiber we show the following.

Theorem 5 *Suppose a fiber of type I has the property that the coordinate function ρ has only one local maximum on each level surface of ψ. Then there exists a*

number Γ_2 such that all spacetimes in the fiber with $\Gamma > \Gamma_2$ have the property that all axisymmetric surfaces of spherical topology enclosing the singularity satisfy $C(S) \geq 4\pi m$.

This is a somewhat trivial result because the $\Gamma \to \infty$ limit of any fiber is (roughly) just the Curzon spacetime.

It is straightforward to derive these results from those in the body of this chapter; we now sketch the proofs. Define for a Weyl spacetime M the function

$$\Theta(\lambda; M) = \epsilon(S_\lambda) \frac{e^{2\lambda}}{\lambda}. \tag{2.59}$$

From theorem 2 the HC will be satisfied in M if $\Theta(\lambda; M) \geq 1$ for all λ. Consider now a fiber $\mathcal{F}$ of type I. For a given spacetime M in $\mathcal{F}$, it may happen that $\Theta(\lambda; M) \to 0$ as $\lambda \to \infty$, as in the case of the metric (2.24) when $\Gamma < 1$. However, because of our assumption that $\epsilon(S_\lambda)$ does not go to zero faster than any power of $e^{-\lambda}$ as $\lambda \to \infty$, spacetimes M' in $\mathcal{F}$ of sufficiently high Γ values will instead have the property that $\Theta(\lambda; M') \to \infty$ as $\lambda \to \infty$. This is because

$$\Theta(\alpha\lambda, f_\alpha(M)) = \frac{e^{\lambda(\alpha-1)}}{\alpha} \Theta(\lambda; M). \tag{2.60}$$

Moreover, in the Newtonian limit $\lambda \to 0$ it is easy to see that $\Theta(\lambda; M) \sim e^\lambda/(2\lambda) \to \infty$. Hence, for a suitable choice of M' in $\mathcal{F}$, $\Theta(\lambda; M')$ diverges at both 0 and ∞, and hence is bounded away from zero because it is a positive, continuous function. The idea now is to find a number α^* such that $\Theta(\lambda, f_\alpha(M'))$ is bounded below by 1 when $\alpha > \alpha^*$, then the HC will be satisfied by all spacetimes M in $\mathcal{F}$ with $\Gamma(M) > \alpha^* \Gamma(M')$.

Pick numbers λ_1, λ_2 such that $\lambda_1 < 1 < \lambda_2$ and that $\Theta(\lambda; M') \geq 1$ when $\lambda < \lambda_1$ or $\lambda > \lambda_2$. Let

$$\Theta^*(\lambda) = \Theta(\alpha\lambda; f_\alpha(M')) = \frac{e^{\lambda(\alpha-1)}}{\alpha} \Theta(\lambda; M'). \tag{2.61}$$

Clearly $\Theta^*(\lambda) \geq 1$ for $\lambda \geq \lambda_2$ for all $\alpha \geq 1$. But in the Newtonian limit $\lambda \to 0$,

$$\Theta^*(\lambda) \sim \frac{e^{\alpha\lambda}}{2\alpha\lambda}, \tag{2.62}$$

so in particular we can choose λ_1 small enough that $\Theta^*(\lambda) > (2/e)e^{\alpha\lambda}/(2\alpha\lambda) \geq 1$ for $\lambda \leq \lambda_1$. With this choice of λ_1 and λ_2, let

$$\delta = \min_{\lambda_1 \leq \lambda \leq \lambda_2} \Theta(\lambda; M'), \tag{2.63}$$

and let α^* be the largest solution of the equation

$$\frac{e^{\lambda_1(\alpha-1)}}{\alpha} = \frac{1}{\delta}. \tag{2.64}$$

Then the multiplicative factor $\exp[\lambda(\alpha-1)]/\alpha$ appearing in Eq. (2.61) will be bounded below by 1 on the interval $[\lambda_1, \lambda_2]$ for all $\alpha \geq \alpha^*$. Hence $\Theta^*(\lambda) \geq 1$ for all λ when $\alpha \geq \alpha^*$, which proves the "large Γ" portion of theorem 5. The proof also applies with obvious modifications to fibers of type II, giving the "large Γ" portion of theorem 4.

We now conside the small Γ limit for a fiber $\mathcal{F}'$ of type II. Fix a spacetime M in $\mathcal{F}'$. Then there is some number $\lambda_{\max}$ corresponding to the last level surface of spherical topology, and we want to show that for sufficiently *small* α,

$$\Theta^*(\lambda) \equiv \Theta(\alpha\lambda; f_\alpha(M)) \geq 1, \tag{2.65}$$

for all $\lambda \leq \lambda_{\max}$. The proof uses the fact that

$$\min_{\lambda_1 \leq \lambda \leq \lambda_2} \frac{e^{\lambda(\alpha-1)}}{\alpha} \to \infty \qquad \text{as } \alpha \to 0 \tag{2.66}$$

for any finite interval $[\lambda_1, \lambda_2]$, and otherwise proceeds exactly as previously.

Finally, suppose that a fiber of type I has convex level surfaces of ψ, and that the quantity $\lambda_{\text{crit}}(S_\lambda)/\lambda$ is bounded above as $\lambda \to \infty$. Then it is similarly straightforward to show using theorems 2 and 3 that all spacetimes in the fiber of sufficiently small Γ have the property that

$$\mathcal{C}(S) \gtrsim 2\pi M \tag{2.67}$$

for all axisymmetric surfaces S enclosing the singularity. This applies in particular to the fiber corresponding to the metric (2.24), since for this case $\lambda_{\text{crit}}(D_\lambda) \sim \lambda/(2\Gamma)$ as $\lambda \to \infty$.

Chapter 3

Trapped surfaces in nonspherical initial data sets and the hoop conjecture

(Originally appeared in Phys. Rev. D 46, 1429 (1992).)

Abstract

The existence of outer trapped surfaces in conformally flat, axisymmetric, momentarily static initial data sets for Einstein's equations is investigated. It is shown that none of the level surfaces of the conformal factor can be outer trapped, whenever the minimum value of the circumferences (or of the square roots of the areas) of all the surfaces surrounding the source region is greater than a constant times the ADM mass. This result is along the lines of the hoop conjecture. It also provides evidence in favor of the conclusion of Shapiro and Teukolsky, drawn from recent numerical relativity calculations, that the gravitational field on a spacelike hypersurface can be arbitrarily singular without an apparent horizon being present.

1 INTRODUCTION AND SUMMARY

The concept of a closed trapped surface (CTS) has been a crucial tool in furthering our understanding of gravitational collapse. Thanks to the celebrated singularity theorems of Hawking and Penrose [1] we know that if locally measured energy densities are positive, then the appearance of a CTS signifies that a point of no return has been passed: classical general relativity dictates that a singularity must form, independently of the equation of state of the collapsing matter. If one assumes that cosmic censorship is true, then the existence of a CTS also implies that an event horizon is present [2]. Even in the absence of this assumption, Israel [3] has established a gravitational confinement theorem which roughly states that "if a closed trapped surface forms, it can be extended into a spacelike 3-cylinder on which the future directed light cones are always inward pointing." This suggests that the singularity which is formed is non-naked.

Thus there is considerable motivation for finding necessary and sufficient conditions for the formation of CTS's. Such conditions would justify and make precise the popular belief that if enough matter is compacted into a small enough region then a black hole must be formed. Many efforts have been made in this direction [4, 5, 6, 7]. Simple dimensional considerations tell us that a suitable sufficient condition is that $m \lesssim \ell$, where m is a typical mass scale and ℓ is a typical length scale of the collapsing configuration. (We set Newton's gravitational constant and the speed of light to unity). Attempts to make this condition more precise must face up to the following problem: in extreme, strong field situations, the masses and lengths that are measured by internal and by external observers may differ by large factors. Specifically, for an isolated collapsing body the ADM mass [8] may be small compared to the total proper mass [9], and internally measured radii may be large compared to surface measures of size [10]. So which mass and length are appropriate for a criterion of the type $m/\ell \lesssim 1$?

For spherically symmetric spacetimes, which are relatively well understood, these questions have been resolved [11]. Let m_p denote the total proper mass inside a spherical surface S, and m_H the Hawking mass of S, which coincides with the ADM mass when the exterior to S is vacuum. Let r_p denote the proper radius of the sphere and r_s the Schwarschild radius, so that $4\pi r_s^2$ is the area. Then sufficient conditions for the existence of CTS's are [12] (i) $m_p/r_p > 1$ (ii) $m_H/r_s > \frac{1}{2}$, while necessary conditions for S to be outer trapped are (i) $m_p/r_p > \frac{1}{2}$ (ii) $m_p/r_s > 1$, and (iii) $m_H/r_s > \frac{1}{2}$.

Strongly aspherical spacetimes are less well understood. For criteria involving internally measurable quantities, Schoen and Yau have proved a very general sufficient condition for the existence of CTC's of the form (minimum density) x (radius squared) $\geq$ constant [6]. In terms of externally measurable quantities, there is some evidence in favor of Thorne's (1972) hoop conjecture (HC): *Black holes with horizons form when and only when a mass M gets compacted into a region whose circumference in every direction is $\mathcal{C} \lesssim 4\pi M$* [13, 14, 15].

Recent numerical relativity calculations of gravitational collapse by Shapiro and Teukolsky [16] provide strong evidence in favor of the HC. For collapsing prolate and oblate ellipsoids, apparent horizons (marginally outer trapped surfaces) appear in a particular time slice as soon as the condition $\mathcal{C}_{\rm min} \lesssim 4\pi m_\infty$ is satisfied. Here m_∞ is the ADM mass and $\mathcal{C}_{\rm min}$ is the minimum of the circumferences of axisymmetric surfaces surrounding the spheroid. The circumference of an axisymmetric surface S is defined as

$$\mathcal{C}(S) = \max(L_e, L_p), \tag{3.1}$$

where L_e is the maximum of the lengths of closed azimuthal curves, and L_p is twice the distance from the north pole to the south pole. For sufficiently elongated prolate spheroids which collapse down to a spindle, $\mathcal{C}_{\rm min} = L_p$ does not change appreciably during the collapse and so the HC predicts that no trapped surfaces should be formed. This is precisely what Shapiro and Teukolsky find, and they cite this and an apparent singularity at the spindle's end as evidence that cosmic censorship is violated. Analytic models by Barrabes, Israel and Letelier [18] of thin shells collapsing with the speed of light show qualitatively similar features to these numerically generated spacetimes and reinforce these conclusions.

The purpose of this paper is to investigate the occurrence of outer trapped surfaces in axisymmetric initial data sets, and to present a proof of the 'only when' part of the HC, interpreted in the sense described above, under some restrictive limitations and assumptions. Our approach is to try to find constraints that must be satisfied by quantities of the form $m(S)/r(S)$, when the surface S is, or is not, trapped. Here $m(S)$ is a measure of the mass inside S, and $r(S)$ is a measure of the size of S.

This work was in part inspired by a recent paper of Malec's [19], where using similar assumptions and a similar approach, he finds conditions for the existence of closed, outer-trapped surfaces in momentarily static, conformally flat initial data sets. Malec's conditions are expressed in terms of the internal quantities r_p (proper radius) and m_p (proper mass). In this paper, we focus instead on the following

external quantities: the circumferential radius of a surface S

$$r_c(S) \equiv \frac{\mathcal{C}}{2\pi} = \frac{1}{2\pi}\max(L_e, L_p), \tag{3.2}$$

the Schwarschild radius $r_s(S)$ defined so that $4\pi r_s^2$ is the area of S (also considered by Malec), and the asymptotic ADM mass m_∞.

We restrict attention to asymptotically flat, axisymmetric initial value hypersurfaces, that are conformally flat and momentarily static outside a compact source region in which the matter density is nonvanishing. We need not assume anything about the interior of this source region. With these assumptions we can write the 3-metric of the hypersurface in the external region in the form $h_{ab} = \Phi^4 \bar{h}_{ab}$, where the metric $\bar{h}_{ab}$ is flat, and Φ is a conformal factor. We also restrict attention to surfaces S which lie outside of and surround the source region.

The first of our two main conclusions is as follows.

Theorem 6 *Let S be a level surface of the conformal factor Φ in the external region, and be convex with respect to $\bar{h}_{ab}$. Then*

$$\frac{m_\infty}{r_c(S)} \leq \frac{\pi}{8}\sqrt{1+\frac{\pi^2}{4}} \approx 0.73. \tag{3.3}$$

An examination of various examples (see appendix C) indicates that the least possible upper bound for the quantity m_∞/r_c is probably 1/2. Also in appendix C we give an example of an initial data set which shows that no analogous upper bound applies to the quantity m_∞/r_s.

The physical interpretation of Theorem 6 is that if a body has passed a certain critical degree of compression (as measured by m_∞/r_c), then it cannot be momentarily static, i.e., it must be collapsing. A similar result of the form $m_p/r_p \leq$ constant is established in Ref. [19], with roughly the same physical interpretation.

To motivate our second result, we briefly review the general behavior of our chosen type of initial data set. Because of time symmetry, there can be no trapped surfaces present, only outer trapped ones. If these are present, then in the spherically symmetric case the ratio $m_\infty/r_c = m_\infty/r_s$ varies with radius as shown in Fig. 3.1. We see that deep inside the trapped region the ratio can be arbitrarily small. This behavior persists in strongly aspherical initial data sets. In Sec. 2.2 we show that if S is a convex, level surface of the conformal factor, then

$$\frac{m_\infty}{r_c} = f_1(\Phi_{|S}) f_2(S), \tag{3.4}$$

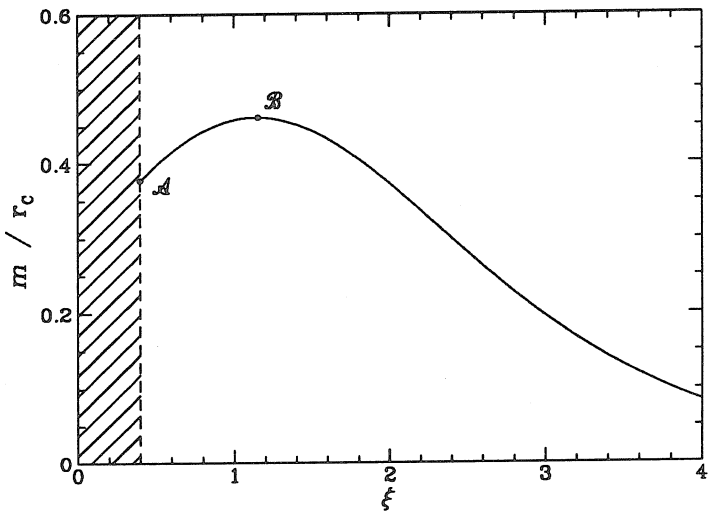

Figure 3.1: The ratio m_∞/r_c as a function of some radial coordinate ξ outside the source region (shaded), in a typical momentarily static, conformally flat initial data set. The turnaround seems to always occur when there are outer trapped surfaces present, and these are then found in the region between points $\mathcal{A}$ and $\mathcal{B}$. For some other data sets, as one decreases ξ, the matter surface is reached before the ratio comes to a local maximum.

where the function f_2 is bounded above and $f_1(x) \equiv 4(x-1)/x^2$. Now if the source is sufficiently compact that just outside the source the conformal factor satisfies $\Phi \gg 1$, then we see from this equation that that the ratio m_∞/r_c will be $\ll 1$ there. The ratio will also be $\ll 1$, of course, at large distances from the source. Only in some intermediate region, where $\Phi \sim 2$, will it become of order unity. See Ref. [20] and also appendix C for some examples.

Because of this behavior we cannot hope to establish a necessary condition of the form $m_\infty/r_c(S) \geq$ constant for a surface S to be outer trapped. (This is in contrast the situation in Ref. [19] where Malec does find such a condition for the ratio m_p/r_p). However a necessary condition which does work is that if S is outer trapped, then there must exist *some* surface S' outside S for which the ratio $m_\infty/r_c(S')$ is of order unity. This is essentially the interpretation of the HC for which Shapiro and Teukolsky find strong evidence [16], and which we shall make precise in our second theorem.

Our second theorem depends on a property [Eq. (3.45) below] of the foliation of the external region by level surfaces of the conformal factor. This property holds for a large class of foliations, and we conjecture that it is always satisfied.

Theorem 7 *Suppose that all the level surfaces of Φ in the external, source free region are convex with respect to $\bar{h}_{ab}$ and satisfy Eq.* (3.45), *and that some level surface in the external region is outer trapped. Then there exists another level surface S' such that*

$$\frac{m_\infty}{r_c(S')} \geq \frac{\pi}{4}\left(1 - \frac{1}{\sqrt{2}}\right), \tag{3.5}$$

and

$$\frac{m_\infty}{r_s(S')} \geq 1 - \frac{1}{\sqrt{2}}. \tag{3.6}$$

The above results are derived in Sec. 2. Some technical details are relegated to appendices A and B. In appendix C we give an analysis of a class of initial data sets whose sources are ellipsoidal thin shells of matter, in order to motivate and illustrate the general results. Our notation and conventions follow those of Ref. [21].

2 AXISYMMETRIC, CONFORMALLY FLAT, MOMENTARILY STATIC INITIAL DATA SETS

2.1 Governing equations

In this section we write down the initial value equations and define the various measures of mass and radius that we use. An initial data set for Einstein's equations consists of a 3-manifold Σ with 3-metric h_{ab}, extrinsic curvature tensor K_{ab}, matter density ρ_M, and momentum density j^a. These must satisfy the initial value equations [21]

$$^{(3)}R = \mathrm{tr}(K^2) - (\mathrm{tr}K)^2 + 16\pi\rho_M \tag{3.7}$$

and

$$D_a K^{ab} - D^b \mathrm{tr}\, K = 8\pi j^b, \tag{3.8}$$

where $^{(3)}R$ is the Ricci scalar and D^a the covariant derivative operator associated with the metric h_{ab}. If we specialize to maximal slices ($\mathrm{Tr}K = K_a{}^a = 0$), then these equations can be simplified by making a conformal transformation [22] to new variables $\bar{h}_{ab} = \Phi^{-4} h_{ab}$, $\bar{K}_{ab} = \Phi^2 K_{ab}$. This gives

$$\left[\bar{D}_a \bar{D}^a - \frac{1}{8}{}^{(3)}\bar{R}\right]\Phi = -\frac{1}{8}\Phi^{-7}\mathrm{tr}(\bar{K}^2) - 2\pi\rho_M \Phi^5, \tag{3.9}$$

and

$$\bar{D}_a \bar{K}^{ab} = 8\pi\Phi^{10} j^b. \tag{3.10}$$

Here $\bar{D}_a$ is the derivative operator associated with the unphysical metric $\bar{h}_{ab}$.

Consider now closed 2-surfaces S of spherical topology in the slice Σ. If n^a is the unit outward normal to S, the expansions of the future directed, inward and outward directed, null geodesic congruences normal to S are

$$\theta_{\mathrm{in}} = -D_a n^a + (h_{ab} - n_a n_b) K^{ab} \tag{3.11}$$

and

$$\theta_{\mathrm{out}} = D_a n^a + (h_{ab} - n_a n_b) K^{ab}. \tag{3.12}$$

In terms of the conformally transformed metric $\bar{h}_{ab}$ and normal $\bar{n}^a$ (normalized by $\bar{h}_{ab}\bar{n}^a\bar{n}^b = 1$), we get

$$\theta_{\mathrm{out,in}} = \pm\Phi^{-2}\left[\bar{D}_a \bar{n}^a + 4\bar{n}^a \bar{D}_a \ln\Phi\right] - \Phi^{-6}\bar{K}_{ab}\bar{n}^a\bar{n}^b, \tag{3.13}$$

where the upper sign refers to the the outwards expansion. The surface S will be trapped if $\theta_{\text{in}} < 0$ and $\theta_{\text{out}} < 0$ everywhere, and outer trapped if $\theta_{\text{out}} < 0$. The property of being outer trapped is sufficient for the singularity theorems to hold [23], and to guarantee that an apparent horizon is present.

We now specialize to the following type of initial data set. Divide Σ into a compact interior region Σ_i, and an exterior region Σ_e which has the topology of Euclidean 3-space with a ball removed. Suppose that all the sources are contained in Σ_i, so that $\rho_M = j^a = 0$ in Σ_e, and that all the level surfaces of the coformal factor Φ in Σ_e have spherical topology [24]. Suppose also that the exterior region is axisymmetric, conformally flat and momentarily static, then $K_{ab} = 0$ and $\bar{h}_{ab}$ is flat in Σ_e [25]. The metric h_{ab} is given in cylindrical coordinates by

$$ds^2 = \Phi^4(\rho, z)(d\rho^2 + dz^2 + \rho^2 d\varphi^2), \tag{3.14}$$

where from Eq. (3.9) the conformal factor Φ satisfies Laplace's equation

$$\bar{D}_a \bar{D}^a \Phi = 0. \tag{3.15}$$

The measures of mass and of size that we will use are as follows. The ADM mass of Σ is given by [8]

$$m_\infty = -\frac{1}{2\pi} \oint_S \bar{n}^a \bar{D}_a \Phi \; d^2\bar{S}, \tag{3.16}$$

where S is any surface enclosing the source region Σ_i. The Schwarschild radius of a surface S is defined by

$$4\pi r_s^2 = \mathcal{A}(S) = \oint_S \Phi^4 d^2\bar{S}, \tag{3.17}$$

where $\mathcal{A}(S)$ is the area of S. Let D be the curve where S intersects the half plane $\varphi = 0$. The circumferential radius is

$$r_c = C/2\pi = \frac{1}{2\pi} \max(L_e, L_p), \tag{3.18}$$

where the length of the longest closed azimuthal curve on S is

$$L_e = \sup_{x \in D} \; 2\pi\rho(x)\Phi(x)^2, \tag{3.19}$$

and twice the distance from the north pole to the south pole is

$$L_p = 2 \int_D \Phi^2 dl. \tag{3.20}$$

Note that it follows from these definitions that

$$r_s^2 = \frac{1}{2}\int_D \rho\Phi^4 dl \;\leq\; \left(\sup_{x\in D}\rho(x)\Phi(x)^2\right)\frac{1}{2}\int_D \Phi^2 dl, \tag{3.21}$$

so that

$$r_s^2 \leq (\pi/2)r_c^2 \tag{3.22}$$

for all surfaces S.

We also introduce some definitions of the 'radius' of S with respect to the unphysical flat geometry determined by the metric $\bar{h}_{ab}$. These measures of radius will be useful later in the proof of theorems 6 and 7, and their various properties that we shall need are derived in appendix A. The first measure is the 'flat' Schwarschild radius $\bar{r}_s$ defined by

$$\bar{r}_s = \sqrt{\frac{\bar{\mathcal{A}}(S)}{4\pi}}, \tag{3.23}$$

where $\bar{\mathcal{A}}(S)$ is the area computed in the flat geometry. This is to be distinguished from the physical Schwarschild radius r_s introduced in Eq. (3.17). The capacity of S is [27]

$$r_o = \frac{1}{4\pi}\oint_S \bar{n}^a \bar{D}_a\psi \; d^2\bar{S} \tag{3.24}$$

where ψ is the unique function satisfying $\bar{D}^a\bar{D}_a\psi = 0$ outside S, $\psi = -1$ on S, and $\psi \to 0$ at infinity. Finally we define the quantities

$$r_* = \frac{1}{8\pi}\oint_S p \; d^2\bar{S}, \tag{3.25}$$

where $p \equiv \bar{D}_a\bar{n}^a$ is twice the mean curvature of S, and

$$r_e = \frac{1}{4\pi}\oint_S (\kappa_g/\psi_n) \; d^2\bar{S}, \tag{3.26}$$

where κ_g is the Gauss curvature of S and $\psi_n \equiv \bar{n}^a\bar{D}_a\psi$. It is known [27] that

$$\bar{r}_s \leq r_* \tag{3.27}$$

and that

$$r_o \leq r_*, \tag{3.28}$$

for all convex surfaces S.

2.2 Compact bodies cannot be static

We now turn to a proof of theorem 6. Suppose that S is a level surface of Φ, so that $\Phi = A$ on S, where A is a constant. Suppose also (in accordance with the statement of Theorem 6) that S is convex with respect to the flat 3-geometry. Then

$$r_c = A^2 \max[\rho_m, L(D)/\pi], \tag{3.29}$$

where $\rho_m = \max_{x \in D} \rho(x)$ and $L(D)$ is the length of the curve D. Also from Eqs. (3.15), (3.16), and (3.24) we have that $m_\infty = 2(A-1)r_o(S)$. This implies from the positive energy theorems that $A \geq 1$. Combining these yields that

$$\frac{m_\infty}{r_c} = f_1(A) f_2(S), \tag{3.30}$$

where $f_1(A) \equiv 4(A-1)/A^2$ which is bounded above by 1 for $A \geq 1$, and

$$f_2(S) \equiv \min\left\{\frac{r_o}{2\rho_m}, \frac{\pi r_o}{2L(D)}\right\}. \tag{3.31}$$

Now in Ref. [14], Sec. III.C it is shown that when S is convex, then

$$\frac{r_o}{L(D)} \leq \frac{1}{4}\sqrt{1+\pi^2/4}. \tag{3.32}$$

Thus we finally obtain

$$m_\infty / r_c \leq \alpha, \tag{3.33}$$

where $\alpha \equiv \pi(1+\pi^2/4)^{\frac{1}{2}}/8 \approx 0.73$. This completes the proof.

2.3 Outer trapped surfaces

In this section, we carry through the proof of theorem 7, in stages. First of all, in lemma 1, we show that if S is an averaged trapped surface, then $m_\infty / r_s(S) \gtrsim 1/\Phi_{|S}$. A similar lower bound is found in lemma 2 for the ratio $m_\infty / r_c(S)$. Then in lemma 3, we show that with certain assumptions the conformal factor Φ cannot be large on the outermost averaged trapped surface. Finally we combine these three lemmas with Eq. (3.45) to arrive at the theorem.

Suppose that S is an arbitrary surface in Σ_e which encloses the source. Let $\Phi_{\min}$ and $\Phi_{\max}$ be the minimum and maximum values of the conformal factor Φ on S. By combining Eqs. (3.13) and (3.16) one gets

$$m_\infty = \frac{1}{8\pi}\oint_S p\Phi \; d^2\bar{S} - \frac{1}{8\pi}\oint_S \theta_{\text{out}}\Phi^3 \; d^2\bar{S}. \tag{3.34}$$

We will call S an averaged trapped surface if the last term on the right-hand side above is positive. Note that this differs from the conventional definition of averaged trapped [4] in that the weighting factor is chosen to be Φ^3 instead of Φ^4. Now if S is convex with respect to $\bar{h}_{ab}$ so that the mean curvature $2p$ is positive, and if also S is averaged trapped, then from Eqs. (3.34) and (3.25) it follows that $m_\infty \geq \Phi_{\min} r_*$. Combining this with Eqs. (3.27), (3.17) and (3.23) proves the following.

Lemma 1 *Let S be a closed surface enclosing the source region Σ_i which is convex with respect to $\bar{h}_{ab}$. If S is averaged trapped then*

$$\frac{m_\infty}{r_s(S)} \geq \frac{\Phi_{\min}}{\Phi^2_{\max}}. \tag{3.35}$$

A similar result holds for the circumferential radius r_c. If we assume that S is a convex, axisymmetric, averaged trapped surface, then Eqs. (3.18) - (3.20) similarly yield that

$$\frac{m_\infty}{r_c} \geq \frac{\Phi_{\min}}{\Phi^2_{\max}}\, r_*\, \max\left(\frac{L(D)}{\pi}, \rho_m\right)^{-1}. \tag{3.36}$$

We claim that $r_* \geq L(D)/4$. To see this, suppose that the surface is defined by the equation $\rho = R(z)$, for $z_0 \leq z \leq z_1$. Then from Eq. (3.25),

$$r_* = \frac{1}{4}\int_D pR\, dl, \tag{3.37}$$

where $p = 1/(Rv) - R''/v^3$, $v^2 = 1 + R'^2$, and primes denote differentiation with respect to z. Now integrating by parts and using the inequality

$$1 + R' \tan^{-1} R' \;\geq\; \sqrt{1 + R'^2}$$

proves the claim.

From Eq. (3.36) it is clear that we also need to find a lower bound for the quantity r_*/ρ_m. Using the fact that $L(D) \geq 2\rho_m$ (which is apparent from a diagram), we see that $r_*/\rho_m \geq 1/2$. In fact in appendix A we show that this can be improved to $r_*/\rho_m \geq \pi/4$. Inserting these results into Eq. (3.36) gives

Lemma 2 *Let S be a closed, axisymmetric surface enclosing the source region Σ_i, which is convex with respect to $\bar{h}_{ab}$. If S is averaged trapped then*

$$\frac{m_\infty}{r_c(S)} \geq \frac{\pi}{4}\,\frac{\Phi_{\min}}{\Phi^2_{\max}}. \tag{3.38}$$

As the next step in our proof of theorem 7, suppose that there is some outer-trapped, level surface S in the external region Σ_e. Then in particular there will be averaged trapped, level surfaces. For these surfaces, the lower bounds derived in lemmas 1 and 2 will get better as Φ gets smaller. The optimum lower bound will occur at the outermost, level, averaged trapped surface, for which the average value of θ_{out} vanishes. Such a surface will exist because Σ is asymptotically flat. We now show that the value of the conformal factor Φ on this particular surface (call it S_{outer}) is bounded above:

Lemma 3 *Let Φ_{outer} be the value of Φ on the outermost, averaged trapped, level surface S_{outer}. Then*

$$1/\Phi_{\text{outer}} \geq 1 - \sqrt{\frac{r_e}{2r_o}}. \tag{3.39}$$

Here r_e and r_o are the radius functions introduced in Sec. 2.1, and are evaluated at S_{outer}.

To derive this bound, suppose that S is a level surface of Φ. Then combining Eqs. (3.25), (3.34) and (3.69) yields that

$$\frac{1}{8\pi m_\infty r_*(S)} \oint_S \Phi^3 \theta_{\text{out}} \, d^2\bar{S} = \frac{1}{m_\infty} + \frac{1}{2r_o(S)} - \frac{1}{r_*(S)}. \tag{3.40}$$

This provides us with a necessary and sufficient condition for S to be averaged trapped, namely that the right hand side above be negative. (For spherical space-times $r_o = r_*$ and we recover the well known condition $m > 2r$.) Evaluating Eq. (3.40) at S_{outer} and using Eq. (3.69), one finds that

$$r_*(S_{\text{outer}}) = m_\infty/\Phi_{\text{outer}}. \tag{3.41}$$

Now both sides of Eq. (3.40) can be considered as functions of the parameter r_o, which increases monotonically as one moves outward through the foliation of level surfaces (see appendix A). If $r_{\text{crit}} \equiv r_o(S_{\text{outer}})$ and $\langle\theta_{\text{out}}\rangle \equiv \oint \Phi^3 \theta_{\text{out}} \, d^2S$, then the equation can be written as

$$f(r_o)\, \langle\theta_{\text{out}}\rangle\,(r_o) = g(r_o)$$

where f is a positive function. Since S_{outer} is the outermost averaged trapped surface, we must have $\langle\theta_{\text{out}}\rangle\,(r_{\text{crit}}) = 0$ and $\partial_{r_o} \langle\theta_{\text{out}}\rangle\,(r_{\text{crit}}) \geq 0$. This implies that $g'(r_{\text{crit}}) \geq 0$, or

$$\frac{-1}{2r_o^2} + \frac{1}{r_*^2} \frac{\partial r_*}{\partial r_o} \geq 0. \tag{3.42}$$

Using Eqs. (3.41), (3.69) and (3.70) we can write this as

$$\frac{\Phi^2_{\text{outer}}}{(\Phi_{\text{outer}}-1)^2} \geq \frac{2r_o}{r_e}, \tag{3.43}$$

which establishes lemma 3.

Now from Eq. (3.39) it is clear that we would like to show that $r_e \lesssim r_o$ always. Unfortunately we have not been able to prove this. However we have evaluated the ratio r_e/r_o for prolate and oblate spheroids, and for level surfaces of the function

$$\Phi = 1 + \frac{m}{2r} + \alpha \left(\frac{m}{2r}\right)^{l+1} P_l(\cos\theta) \tag{3.44}$$

with $\alpha \ll 1$, to second order in α. In all cases we find that r_e/r_o decreases away from unity as the surface becomes less spherical. See appendix B for details. This leads us to conjecture that all surfaces S embedded in flat 3-dimensional space probably do satisfy the property

$$r_e(S) \leq r_o(S). \tag{3.45}$$

For initial data sets with the property that all the level surfaces in the external region satisfy the property (3.45), by combining the three lemmas we deduce theorem 7 as quoted in the introduction.

3 CONCLUSION

In this paper we have have found conditions for outer trapped surfaces *not* to be present in an initial data set. This work supports the conclusion of Shapiro and Teukolsky that the matter and gravitational field configurations on a particular time slice can become arbitrarily singular without the appearance of an apparent horizon. However it is not clear that this tells one anything about cosmic censorship, as Wald has shown that there are non spherically-symmetric partial Cauchy evolutions of initial data sets in standard black-hole spacetimes which approach arbitrarily close to the singularity and yet which contain no apparent horizons (on any spacelike slices) in their interiors [30]. It would be useful to find out just when can a spacelike hypersurface fail to register the presence of an event horizon by an apparent horizon.

ACKNOWLEDGMENTS

The author would like to acknowledge the inspiration gained from reading the papers of Edward Malec, and also to thank him for helpful correspondence. Thanks are also due to Eric Poisson, Curt Cutler and Richard Price for some useful discussions, and especially to Kip Thorne for his encouragement and comments. This work was supported in part by NSF grants AST-8817792 and AST-9114925.

APPENDIX A: MEASURES OF RADIUS IN FLAT SPACE

Several different definitions of "radius" are possible for a surface in flat, three-dimensional space. In Sec. 2.1 we defined for a closed surface S the capacity $r_o(S)$ [Eq. (3.24)], the schwarschild radius $\bar{r}_s(S)$ [Eq. (3.23)], the quantity $r_*(S)$ [Eq. (3.25)], and the quantity $r_e(S)$ [Eq. (3.26)]. The properties of these measures and the relationships between them form a crucial underpinning to our analysis of trapped surfaces. In this appendix we derive some of the properties which are quoted and used in the body of the paper.

It turns out that, in the derivation of these properties, it is useful not to consider a single closed surface S, but instead a foliation of surfaces. Accordingly, let S_o be a 2-surface with the topology of a sphere, and fix a foliation by similar surfaces of the region outside S_o. Then we can find coordinates σ, x^A $(A = 1, 2)$ such that (i) the line element of the flat 3-geometry takes the form

$$ds^2 = e^{2F(\sigma,x^A)}d\sigma^2 + h_{BC}(\sigma, x^A)dx^B dx^C, \tag{3.46}$$

and (ii) the surfaces of the foliation are the surfaces of constant σ, such that σ increases monotonically as one moves outwards towards infinity. The extrinsic curvature tensor of a typical surface S_σ is given by

$$K_{AB} = \frac{1}{2}e^{-F}\dot{h}_{AB} \tag{3.47}$$

where the dot denotes differentiation with respect to σ. Its trace (twice the mean curvature of S) is

$$p = \frac{1}{2}e^{-F}h^{AB}\dot{h}_{AB}, \tag{3.48}$$

which appears in the definition of the radius function $r_*(S)$. The Gauss curvature is the product of the eigenvalues of K_{AB} with respect to h_{AB}, which is

$$\begin{aligned}\kappa_g = & \quad \tfrac{1}{2}\left[(\mathrm{tr}K)^2 - \mathrm{tr}K^2\right] \\ = & \quad \tfrac{1}{8}e^{-2F}\left[(h^{AB}\dot{h}_{AB})^2 - \dot{h}_{AB}\dot{h}_{CD}h^{AC}h^{BD}\right]. \end{aligned} \tag{3.49}$$

Now we make use of the fact that the 3-geometry is flat. The Riemann tensor computed from the metric (3.46) has components

$$\begin{aligned} R_{\sigma A\sigma B} = & \quad \tfrac{1}{4}\left\{\dot{h}_A{}^C\dot{h}_{CB} + 2\dot{F}\dot{h}_{AB} - 2\ddot{h}_{AB}\right\} \\ & \quad -e^F\nabla_A\nabla_B e^F. \end{aligned} \tag{3.50}$$

$$R_{\sigma ABC} = \quad e^F\nabla_{[C}e^{-F}\dot{h}_{B]A} \tag{3.51}$$

$$R_{ABCD} = \quad {}^{(2)}R_{ABCD} - \tfrac{1}{2}e^{-2F}\dot{h}_{A[C}\dot{h}_{D]B}. \tag{3.52}$$

Here ∇_A denotes the covariant derivative associated with the 2-metric h_{AB}, the two-dimensional Riemann tensor of S_σ is ${}^{(2)}R_{ABCD}$, and $\dot{h}_{AB}$, $\ddot{h}_{AB}$, and F are regarded as tensor fields on S_σ. By equating these Riemann tensor components to zero, we obtain necessary and sufficient conditions for the functions F and h_{AB} to describe foliations of flat space. Since in two dimensions there is only one independent component of the Riemann tensor, these conditions are

$${}^{(2)}R = 2\kappa_g, \tag{3.53}$$

$$\dot{h}_A{}^C\dot{h}_{CB} + 2\dot{F}\dot{h}_{AB} - 2\ddot{h}_{AB} = 4e^F\nabla_A\nabla_B e^F, \tag{3.54}$$

and

$$\nabla_{[A}e^{-F}\dot{h}_{B]C} = 0. \tag{3.55}$$

Next we derive a useful formula for the rate of change with respect to σ of the integral of any function over the surface S_σ. Using the fact that the area element of the surface is

$$d^2S = \sqrt{\det h_{AB}}\, dx^1 dx^2,$$

we get

$$\begin{aligned}\partial_\sigma \oint_{S_\sigma} f\, d^2S &= \oint_{S_\sigma} \left(\partial_\sigma f + f\partial_\sigma \ln\sqrt{\det h_{AB}}\right) d^2S \\ &= \oint_{S_\sigma} \left(\partial_\sigma f + e^F p f\right) d^2S. \end{aligned} \tag{3.56}$$

The second equality here follows from Eq. (3.48). In these equations and throughout this appendix, the symbol d^2S means the surface area element with respect to the flat background geometry, which was denoted $d^2\bar{S}$ in the body of the paper.

The radius functions $\bar{r}_s$, r_*, and r_o are defined in Eqs. (3.23), (3.25), and (3.24). Evaluated on the surfaces S_σ these produce functions $\bar{r}_s(\sigma)$, $r_*(\sigma)$ etc. Using the formula (3.56) we can find how these functions vary through the foliation. We find that

$$\partial_\sigma \bar{r}_s^2 = \frac{1}{4\pi} \oint e^F p \, d^2S \tag{3.57}$$

and

$$\partial_\sigma r_* = \frac{1}{8\pi} \oint (\dot{p} + e^F p^2) \, d^2S. \tag{3.58}$$

Now using Eqs. (3.48), (3.49), and (3.54) after some manipulation we obtain

$$\dot{p} + e^F p^2 = 2e^F \kappa_g - \nabla^2 e^F, \tag{3.59}$$

which when inserted in Eq. (3.58) gives [26]

$$\partial_\sigma r_* = \frac{1}{4\pi} \oint e^F \kappa_g \, d^2S. \tag{3.60}$$

To calculate $\partial_\sigma r_o$ is a little more complicated. Let $\psi_{(\tau)}(\sigma, x^A)$ be that harmonic function which takes the value -1 on S_τ and which vanishes at infinity. Then from Eq. (3.24)

$$r_o(\sigma) = \frac{1}{4\pi} \left[\oint e^{-F} \partial_\sigma \psi_{(\tau)} \, d^2S \right]_{\tau=\sigma}, \tag{3.61}$$

since $e^{-F}\partial_\sigma = \partial_n$ is the unit outward normal derivative. Now using Eq. (3.56) gives

$$\begin{aligned} \dot{r}_o(\sigma) = \frac{1}{4\pi} \oint [&\partial_\sigma \partial_n \psi_{(\tau)} + \partial_\tau \partial_n \psi_{(\tau)} \\ &+ e^F p \, \partial_n \psi_{(\tau)}] \, d^2S \, \big|_{\tau=\sigma}. \end{aligned} \tag{3.62}$$

From the equation $D_a D^a \psi = 0$ and using the metric (3.46) we find that

$$\partial_\sigma (e^{-F} \dot{\psi}) = -\dot{\psi} p - \nabla_A (e^F \nabla^A \psi). \tag{3.63}$$

When this expression for $\partial_\sigma \partial_n \psi_{(\tau)}$ is inserted above, the second term is a total derivative which vanishes when integrated, and the first term cancels with the last term in Eq. (3.62), so we get

$$\dot{r}_o(\sigma) = \frac{1}{4\pi} \left[\oint \partial_\tau \partial_n \psi_{(\tau)} \, d^2S \right]_{\tau=\sigma}. \tag{3.64}$$

To evaluate this we find an approximate expression for $\psi_{(\tau)}$. Let $\tau = \sigma_o + \varepsilon$, and suppose that $\psi_{(\tau)} = \psi_{(\sigma_o)} + \varepsilon f + O(\varepsilon^2)$. Then by demanding that $\psi_{(\tau)} = -1 + O(\varepsilon^2)$

on S_τ, we find that the function f is determined by the requirements $f(\sigma_o, x^A) = -\dot{\psi}(\sigma_o, x^A)$, $D^a D_a f = 0$, and $f \to 0$ at infinity. Also it follows that

$$\partial_\tau \psi_{(\tau)}(\sigma, x^A)\big|_{\tau=\sigma_o} = f(\sigma, x^A), \tag{3.65}$$

and so from Eq. (3.64), $\dot{r}_o = \oint \partial_n f \, d^2S/4\pi$. Now by using Greens theorem $\oint \psi \partial_n f = \oint f \partial_n \psi$ we finally get

$$\dot{r}_o(\sigma) = \frac{1}{4\pi} \oint_{S_\sigma} e^{-F} \dot{\psi}^2_{(\sigma)} \, d^2S, \tag{3.66}$$

where $\dot{\psi}_{(\sigma)} \equiv \partial_\sigma \psi_{(\tau)}(\sigma, x^A)\big|_{\tau=\sigma}$.

The rate of change equations (3.57), (3.60) and (3.66), together with the freedom to choose a particular foliation of surfaces S_σ starting from a given surface S_o, comprise powerful tools for deriving properties of the radius functions. By using these equations specialized to the foliation in which $F = 0$, Szego [27] shows that $\bar{r}_s \leq r_*$ and $r_o \leq r_*$ always. It might be possible, using these tools, to prove the conjecture in Sec. 2.3 [Eq. (3.45) above], although we have not been able to do so.

The results we need for this paper can be obtained by choosing the foliation to be the set of level surfaces of a harmonic function. In the notation introduced above, let S_o be a given initial surface corresponding to $\sigma = \sigma_o$, put $\chi = \psi_{(\sigma_o)}$, and choose the foliation to be the level surfaces of χ. It follows that $\chi = \chi(\sigma)$, i.e., that χ is independent of the coordinates x^A, and also that

$$\psi_{(\tau)} = -\chi/\chi(\tau). \tag{3.67}$$

Now using Eqs. (3.24), (3.66), (3.67), and the fact that $\partial_n \psi_{(\tau)} = -e^{-F}\dot{\chi}/\chi(\tau)$, we get

$$\dot{r}_o(\sigma) = -\frac{\dot{\chi}(\sigma)}{\chi(\sigma)} r_o(\sigma). \tag{3.68}$$

This means that χ must be of the form $\chi(\sigma) = A + B/r_o(\sigma)$ for some constants A and B. The conformal factor Φ of this paper clearly must also be of this form, and from Eq. (3.16) and the boundary condition at infinity it follows that

$$\Phi(\sigma) = 1 + \frac{m_\infty}{2r_o(\sigma)}, \tag{3.69}$$

which is one of the results used in Sec. 2.3.

Next, if we combine Eqs. (3.60), (3.26) and (3.68) we find that $\dot{r}_* = \dot{r}_o r_e/r_o$. Hence if we consider r_* as a function of r_o instead of σ [r_o increases monotonically with σ, cf. Eq. (3.66)], then we get

$$\frac{\partial r_*}{\partial r_o} = \frac{r_e}{r_o}. \tag{3.70}$$

This is the quantity that we conjecture to be always less than 1, and that we use in the derivation of lemma 3.

The final result concerns a convex axisymmetric surface S, defined by an equation of the form $\rho = R(z)$ for $z_0 \leq z \leq z_1$. Here (z, ρ, φ) are standard cylindrical coordinates, and $R(z_0) = R(z_1) = 0$. In Sec. 2.3 we claimed that $r_*(S) \geq (\pi/4)\rho_m$ always, where $\rho_m \equiv \max_z R(z)$. This can be derived by means of the following trick. We can find a surface S' inside S which is a pancake shaped ellipsoid of revolution, of the form

$$\frac{(z-\bar{z})^2}{z_m^2} + \frac{\rho^2}{\rho_m^2} = 1,$$

where $\bar{z}$ is such that $R(\bar{z}) = \rho_m$, and we choose z_m to be small enough so that S' fits inside S. Now clearly we can find a foliation of convex surfaces interpolating between S' and S. Hence by Eq. (3.60) we see that

$$r_*(S) \geq r_*(S'). \tag{3.71}$$

But a straightforward calculation gives that, in the limit where $z_m \to 0$, $r_*(S') = \pi\rho_m/4$ [cf. Eq. (3.86) below]. This proves the claim.

APPENDIX B: THE CONJECTURE $r_e \leq r_o$

In this appendix we calculate the ratio r_e/r_o for several classes of surfaces using the formalism described in appendix A. Consider firstly prolate ellipsoids. The appropriate form of the metric (3.46) describing flat space is

$$\begin{aligned} ds^2 = a^2(\sinh^2 u + \sin^2 v)(du^2 + dv^2) \\ + a^2 \sinh^2 u \sin^2 v \, d\varphi^2 \end{aligned} \tag{3.72}$$

where the $u =$ constant surfaces surfaces are prolate ellipsoids of eccentricity $\varepsilon = \operatorname{sech} u$. If we define

$$\chi = -\log \tanh(u/2) \tag{3.73}$$

and $\Delta^2 = \sinh^2 u + \sin^2 v$, we find from Eqs. (3.48) and (3.49) that

$$p = \frac{2\sinh^2 u + 1 - \cos^2 v}{a\Delta^3 \tanh u} \tag{3.74}$$

and

$$\kappa_g = \frac{\cosh^2 u}{a^2\Delta^4}. \tag{3.75}$$

Also since χ is harmonic, $\psi_n = -e^{-F}\dot{\chi}/\chi$, and it follows that

$$\psi_n = [a\chi\Delta \sinh u]^{-1}\,. \tag{3.76}$$

Using the definitions of the radius functions, we calculate that

$$r_o = a/\chi, \tag{3.77}$$

$$r_* = \frac{1}{2}a\cosh u\,[1 + \chi \sinh u \tanh u]\,, \tag{3.78}$$

and

$$r_e = a\chi^2 \cosh u \sinh^2 u. \tag{3.79}$$

The ratio r_e/r_o is plotted as a function of the eccentricity $\varepsilon = \operatorname{sech} u$ in Fig. 3.2 (lower curve); it is always smaller than unity.

For oblate ellipsoids the discussion is exactly analogous so we merely list the equations:

$$\begin{aligned} ds^2 = {} & a^2(\sinh^2 u + \sin^2 v)(du^2 + dv^2) \\ & + a^2 \cosh^2 u \cos^2 v\, d\varphi^2, \end{aligned} \tag{3.80}$$

$$\chi = 2\tan^{-1} e^{-u}, \tag{3.81}$$

$$p = \frac{2\sinh^2 u + 1 + \sin^2 v}{a\Delta^3 \coth u}, \tag{3.82}$$

$$\kappa_g = \frac{\sinh^2 u}{a^2\Delta^4}, \tag{3.83}$$

$$\psi_n = [a\chi\Delta \cosh u]^{-1}\,, \tag{3.84}$$

$$r_o = a/\chi, \tag{3.85}$$

$$r_* = \frac{1}{2}a\sinh u\,[1 + \chi \cosh u \coth u]\,, \tag{3.86}$$

$$r_e = a\chi^2 \cosh^2 u \sinh u; \tag{3.87}$$

see the upper curve in Fig. 3.2.

Finally consider level surfaces of the function

$$\Phi = 1 + \frac{m}{2r} + \alpha\left(\frac{m}{2r}\right)^{l+1} P_l(\cos\theta), \tag{3.88}$$

where $\alpha \ll 1$, P_l is the l^{th} Legendre polynomial, and (r, θ, φ) are standard spherical polar coordinates. A straightforward calculation shows that for the surface $\Phi = A$,

$$\frac{r_e}{r_o} = 1 - c_l\alpha^2 + O(\alpha^3), \tag{3.89}$$

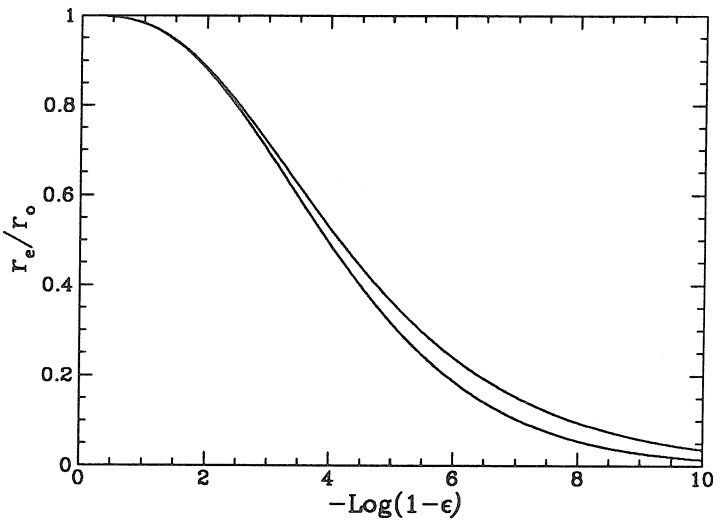

Figure 3.2: The ratio r_e/r_o plotted as a function of eccentricity ε for prolate (lower curve) and oblate (upper curve) ellipsoids. Notice that it decreases away from unity as the surfaces become less spherical.

where $c_l = (A-1)^{2l}2l^2(2l-1)/(2l+1)$. The ratio decreases away from unity as α is increased for all values of l.

We remark that our conjecture $r_e \leq r_o$ is similar to a conjecture of Malec's [Eq. (16) of Ref. [19]], which in our notation reads $r_e r_o \leq r_*^2$. By Eq. (3.28), this would be a consequence of $r_e \leq r_o$. Also it is known that the the corresponding pointwise inequality $\kappa_g \leq \psi_n^2$ is not always true.

APPENDIX C: THIN ELLIPSOIDAL SHELLS

In this appendix we examine a class of initial data sets which contain momentarily static, ellipsoidal, thin shells of matter. The distribution of surface matter density that we assume is non-uniform, but is chosen to make the calculations simple. We analytically determine when and where outer trapped and averaged outer trapped level surfaces occur in these data sets, and calculate the ratios m_∞/r_c and m_∞/r_s. The conclusions are that (i) the qualitative behavior of the ratio m_∞/r_c is in accordance with Fig. 3.1, and (ii) whenever outer trapped level surfaces occur, the quantity $\Theta_{\max} \equiv \max_S m_\infty/r_c(S)$ is larger than some critical value Θ_c. For prolate initial data sets $\Theta_c = 0.4889$, and for oblate ones $\Theta_c = 0.4799$.

A closely related class of initial data sets was examined by Nakamura, Shapiro and Teukolsky in Ref. [15], where they numerically calculated $\Theta_{\max}$ for various matter configurations, and related its value to the presence of apparent horizons. Here we obtain similar results by analytic methods.

To describe the results in more detail we now discuss the parameters used to describe the shell. A shell will be determined by (i) the semi-major axis α of the ellipse that generates the ellipsoid by a rotation, (ii) the eccentricity ε of this ellipse, and (iii) the proper mass m_p of the shell. This is defined as

$$m_p = \int \rho_M \, d^3V = \int \rho_M \Phi^6 \, d^3\bar{V}. \tag{3.90}$$

Now sometimes two different shells will give rise to the same external 3-geometry [28]. This will be the case if the values for each shell of the following two combinations of the above parameters

$$m_\infty = m_p \left[1 - \frac{m_p}{2\alpha}\frac{\chi(\varepsilon)}{\varepsilon}\right], \tag{3.91}$$

and

$$\Gamma = \left[\frac{2\alpha\varepsilon}{m_p} - \chi(\varepsilon)\right]^{-1} \tag{3.92}$$

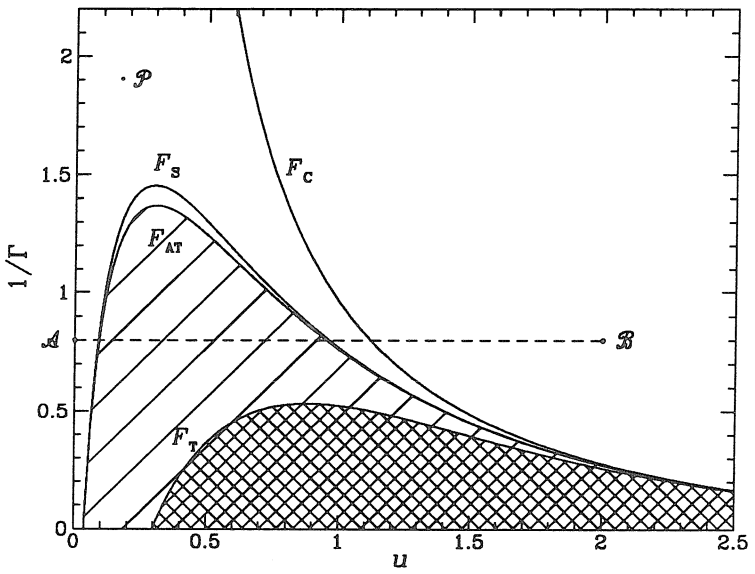

Figure 3.3: The behavior of prolate initial data sets. Each point $(u_o, 1/\Gamma)$ in this diagram corresponds to a shell, and all the points $(u, 1/\Gamma)$ with $u \geq u_o$ correspond to the level surfaces in the 3-geometry outside the shell. (The value of u_o can be anything one wishes and thus is not shown explicitly here.) The hatched region contains outer trapped surfaces, and the region shaded by lines contains averaged outer trapped surfaces. The curves F_C and F_S show where the level surfaces of minimum circumference and of extremal area occur.

are the same. Here $\chi = \log\left[(1+\varepsilon)/(1-\varepsilon)\right]/2$ in the prolate case, and $\chi = 2\tan^{-1}\left[(1-\sqrt{1-\varepsilon^2})/\varepsilon\right]$ in the oblate case. The dimensionless parameter Γ^{-2} is essentially the ratio of the asymptotic mass of the shell cubed to its quadrupole moment, and m_∞ is the asymptotic mass [29].

We also introduce a dimensionless radial coordinate u (see below) with the properties that (i) the shell is the surface $u = u_o$, with $\varepsilon = \operatorname{sech} u_o$, (ii) the level surfaces of the conformal factor Φ and of u coincide, and (iii) u increases monotonically as one goes outwards from the shell towards infinity. The parameters Γ, m_∞ and u_o turn out to be a more convenient set to use to describe the shell than α, ε, and m_p. Now any level surface in any of these data sets may be specified by giving values of u and Γ, since it does not matter at which $u_o < u$ the shell is

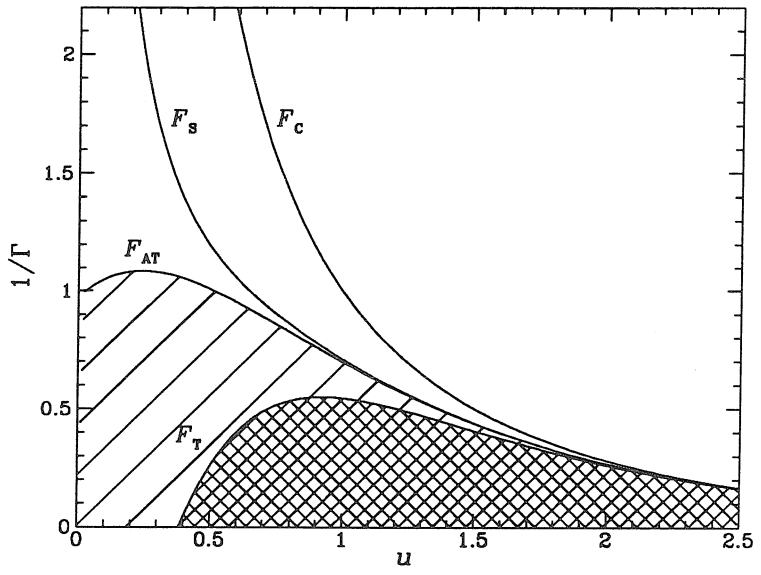

Figure 3.4: The behavior of oblate initial data sets; see caption of Fig. 3.3

located, and without loss of generality we can take $m_\infty = 1$.

The results we obtain [Eqs. (3.95), (3.97), (3.101) and (3.103) below] are summarized graphically in Figs. 3.3 and 3.4, which are diagrams of this parameter space of level surfaces. They show where outer trapped and averaged outer trapped level surfaces occur, and where the ratios m_∞/r_c and m_∞/r_s have local maxima or minima. These ratios as a function of u along the line $\mathcal{AB}$ in Fig. 3.3 are shown in Fig. 3.5. We see that at shells such as that corresponding to the point $\mathcal{P}$ in Fig. 3.3, the ratio m_∞/r_s can be arbitrarily large, even though there are no trapped level surfaces or averaged trapped level surfaces anywhere outside these shells. This shows that area is not as useful a measure of size as circumference, at least for prolate geometries. Notice that the behaviour of m_∞/r_s is quite different in the oblate case.

Also we see that if one imagines traveling inwards from infinity in an initial data set, one encounters first the level surface of minimum circumference, then the one of minimum area, then the outermost, outer averaged trapped level surface, and finally the outermost outer trapped level surface. These all coincide in the

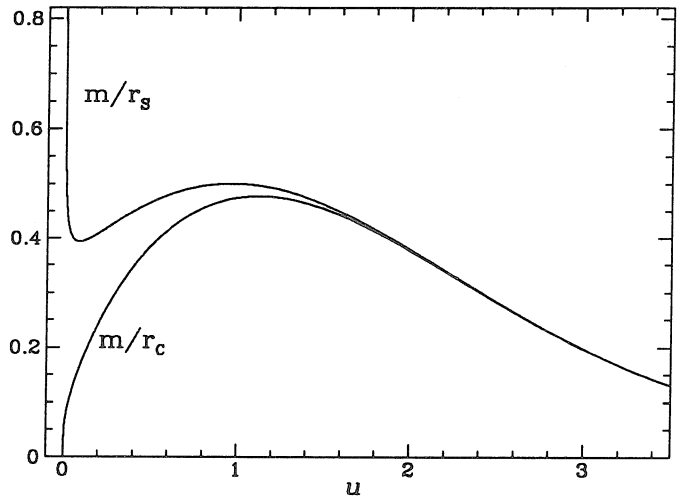

Figure 3.5: The shape of the functions $m_\infty/r_c(u,\Gamma)$ and $m_\infty/r_s(u,\Gamma)$ can be visualized easily be combining this figure with Fig. 3.3. This plot shows how these quantities vary with u in the prolate case when $\Gamma = 1.25$, i.e., along the line $\mathcal{AB}$ above.

limit $\Gamma \to \infty$, i.e., in the limit of spherical symmetry. In the prolate case, the plot suggests (but does not prove) that there is an anti-trapped region at small u values containing no averaged outer trapped surfaces, such as is found inside the inner horizon of a Reissner-Nordstrom black hole.

It is also apparent that outer trapped level surfaces are present if and only if Γ is greater than some critical value Γ_c, where $\Gamma_c = 1.876$ (prolate case), or $\Gamma_c = 1.819$ (oblate case). The quantity $\max_u m_\infty/r_c(u)$ can be calculated numerically and increases monotonically with Γ, asymptoting to the value of $1/2$. Therefore outer trapped level surfaces are present only when $\max_u m_\infty/r_c(u)$ is large enough, in accordance with theorem 7

We now turn to a derivation of these results. The starting point is the line element (3.14), where the base metric $\bar{h}_{ab}$ is described in coordinates (u, v, φ) according to Eq. (3.72) [Eq. (3.80) in the oblate case]. The conformal factor we use

is

$$\Phi = \begin{cases} 1+\Gamma\chi(u) & u \geq u_o \\ 1+\Gamma\chi(u_o) & u < u_o, \end{cases} \tag{3.93}$$

where χ is the harmonic function defined in Eq. (3.73) [Eq. (3.81)]. From the Lichnerowicz equation (3.9) it is apparent that this describes a thin shell of matter, with surface density proportional to $e^{-2F} = 1/\Delta^2$. Using Eqs. (3.69), (3.93), (3.77) and (3.85), we find that $m_\infty = 2\Gamma a$. But from Eqs. (3.90) and (3.16) we obtain

$$m_\infty = \frac{m_p}{\Phi(u_o)}. \tag{3.94}$$

Equations (3.91) and (3.92) can be derived from this, using also that $\alpha = \Phi(u_o)^2 a \cosh u_o$ and $\varepsilon = \operatorname{sech} u_o$.

Consider now a level surface S_u which is in the external region, so that $u \geq u_o$. From Eqs. (3.40) and (3.69) we see that it will be averaged trapped iff $1/\Phi_{|S} \leq 1 - r_*/(2r_0)$. By Eq. (3.93) this occurs if and only if $1/\Gamma \leq F_{AT}(u)$, where

$$F_{AT}(u) = \chi(u)(2r_o/r_* - 1). \tag{3.95}$$

This function was evaluated using the expressions for χ, r_o and r_* in appendix B to produce the plots in Figs. 3.3 and 3.4. It is similarly straightforward to find when will the surface S_u be pointwise outer trapped. From Eq. (3.13) with $\bar{K}_{ab} = 0$, we find that

$$\Phi^2\theta_{\text{out}} = p + \frac{4}{\Phi}\partial_n\Phi.$$

But if $A \equiv \Phi_{|S}$ and $\psi \equiv \psi_{(u)}$ in the notation of appendix A, then $\Phi = 1+(1-A)\psi$, and so $A^2\theta_{\text{out}} = p - 4(1-1/A)\psi_n$. Hence S_u will be outer trapped if and only if

$$1 - \frac{1}{\Phi_{|S}} \geq \max_S \frac{p}{4\psi_n}, \tag{3.96}$$

which from Eq. (3.93) is equivalent to $1/\Gamma \leq F_T(u)$, where

$$F_T(u) = \chi(u)\left[\min_S \frac{4\psi_n}{p} - 1\right]. \tag{3.97}$$

Using Eqs. (3.73),(3.74), (3.76) etc. we find that

$$F_T(u) = \begin{cases} 2\operatorname{sech} u + \log[\tanh u/2] & \text{prolate case} \\ \frac{4\sinh u}{1+2\sinh^2 u} - 2\tan^{-1} e^{-u} & \text{oblate case.} \end{cases} \tag{3.98}$$

Next we find where the surfaces of extremal area occur. Now the physical Schwarschild radius r_s is related to the flat space Schwarschild radius $\bar{r}_s$ by $r_s = \Phi^2 \bar{r}_s$. Also from the metrics (3.72) and (3.80), it follows that

$$\bar{r}_s^2 = \frac{1}{2} a^2 \sinh^2 u \left[1 + \cosh u \coth u \sin^{-1}(\operatorname{sech} u)\right] \tag{3.99}$$

in the prolate case, and

$$\bar{r}_s^2 = \frac{1}{2} a^2 \cosh^2 u \left[1 + \sinh u \tanh u \sinh^{-1}(\operatorname{cosech} u)\right] \tag{3.100}$$

in the oblate case. If S_u is a surface of extremal area, then $\dot{r}_s = 0$, i.e., $2\dot{\Phi}\bar{r}_s + \Phi\dot{\bar{r}}_s = 0$. From Eq. (3.93), this is equivalent to $1/\Gamma = F_S(u)$, where

$$F_S = -\chi - \dot{\chi}\bar{r}_s/\dot{\bar{r}}_s. \tag{3.101}$$

A similar method can be used to find the surfaces of minimum circumference. If we define the quantity $\bar{r}_c = \Phi^{-2} r_c$, then we find that

$$\bar{r}_c = \begin{cases} \frac{2a}{\pi} \cosh u \, E(\operatorname{sech}^2 u) & \text{prolate case} \\ a \cosh u & \text{oblate case.} \end{cases} \tag{3.102}$$

Then the function

$$F_C = -\chi - \dot{\chi}\bar{r}_c/\dot{\bar{r}}_c \tag{3.103}$$

satisfies $F_C(u) = 1/\Gamma$ when $\dot{r}_c(u) = 0$. These equations determine the functions F_C and F_S which are plotted in Figs. 3.3 and 3.4.

Finally the ratio $\Theta = m_\infty / r_c$ is given by

$$\Theta = \frac{2\Gamma a}{[1 + \Gamma\chi(u)]^2 \, \bar{r}_c(u)}. \tag{3.104}$$

Evaluating this along the curves F_C in Figs. 3.3 and 3.4 produces in each case a function of Γ, $\Theta_{\max}(\Gamma)$, which turns out to be monotonically increasing. Evaluated at the critical value Γ_c below which there are no trapped level surfaces yields the value $\Theta_{\max}(\Gamma_c) = 0.4889$ in the prolate case, and $\Theta_{\max}(\Gamma_c) = 0.4799$ in the oblate case. Outer trapped level surfaces will be present only when $\Theta_{\max}$ is greater than these critical values.

Bibliography

[1] R. Penrose, Ann. N.Y. Acad. Sci. **224** (1973).

[2] R. Wald, *General Relativity* (University of Chicago press, Chicago, 1984), p. 310.

[3] W. Israel, Can. J. Phys. **64**, 120 (1986).

[4] J.B. Hartle and D.C. Wilkins, Phys. Rev. Lett. **31**, 60 (1973).

[5] P.N. Demmie and A.I. Janis, J. Math. Phys. **14**, 793 (1973).

[6] R. Schoen and S.T. Yau, Commun. Math. Phys. **90**, 575 (1983).

[7] P.Bizon, E. Malec, and N. O'Murchadha, Phys. Rev. Lett. **61**, 1147 (1988).

[8] R. Arnowitt, S. Deser, and C.W. Misner, "The Dynamics of General Relativity" in *Gravitation: An Introduction to Current Research*, edited by L. Witten (John Wiley, New York, 1962).

[9] By proper mass we mean the integral over a region in a spacelike hypersurface of the stress energy tensor doubly contracted with the normal to that hypersurface.

[10] For an example of this effect, see N. O'Murchadha, Class. Quant. Grav. **7** (1990), Eq. (1.18) in the limit where $M \to 2L$.

[11] This has come about largely through a series of papers by Bizon, Malec and O'Murchadha. See Ref. [17] for a review.

[12] See Ref. [7] above. The conditions involving the proper mass m_p also require the assumption that the unique conformally flat spacelike hypersurface containing S be momentarily static, and the proper mass is defined using this hypersurface.

[13] K.S. Thorne, in *Magic Without Magic : John Archibald Wheeler*, edited by J. Klauder (Freeman, San Francisco, 1972), p. 231.

[14] E. Flanagan, Phys. Rev. D. 44, 2409 (1991); chapter 2 of this thesis.

[15] T. Nakamura, S.L. Shapiro, and S.A. Teukolsky, Phys. Rev. D **38**, 2972 (1988).

[16] S.L. Shapiro and S.A. Teukolsky, Phys. Rev. Lett. **66**, 994 (1991), Am. Scientist **79** 330 (1991).

[17] E. Malec, Acta Phys. Pol. B **22**, 829 (1991).

[18] C. Barrabes, W. Israel, P.S. Letelier, Phys. Lett. A **160**, 41 (1991); erratum Phys. Lett. A **161**, 562 (1992).

[19] E. Malec, Phys. Rev. Lett. **67**, 949 (1991). See also Ref. [17] for a comprehensive review of this and related work.

[20] J.A. Wheeler, in *Relativity, Groups, and Topology*, eds. Bryce and Cecile DeWitt (Gordon and Breach, New York, 1964).

[21] C.W. Misner, K.S. Thorne, and J.A. Wheeler, *Gravitation* (Freeman, San Francisco, 1973), p. 515.

[22] J. York in *Gravitational Radiation*, edited by T. Piran and N. Deruelle (North Holland, Amsterdam, 1982).

[23] N. O'Murchadha, in *Proceedings of the Center for Mathematical Analysis*, edited by R. Bartnick, (Australian National University, Canberra), **19**, 137 (1989). See also Ref. [2] for a proof that outer trapped surfaces must lie inside event horizons in asymptotically predictable spacetimes (modulo a topological condition which is satisfied in the case considered in this paper).

[24] This will be the case if Σ_i is large enough to include all the points at which the gradient of Φ vanishes, see Ref. [14].

[25] In fact it is only necessary to assume that the extrinsic curvature tensor K_{ab} is a pure trace, then the rest of our assumptions imply that it must vanish in the external region. The author is grateful to J. Eisenberg for bringing up this point.

[26] This formula was previously established using a different method by E. Malec in Acta. Phys. Pol. B22, 347 (1991).

[27] G. Szego and G. Polya, Amer. J. Math. 67, 1 (1945).

[28] In the sense that region external to one shell will be iosmetric to a submanifold of the region external to another one.

[29] Notice that the negative, gravitational potential energy term in m_∞ increases with increasing eccentricity.

[30] R. Wald, Phys. Rev. D 44, 3719 (1992).

Chapter 4

Sensitivity of the Laser Interferometer Gravitational Wave Observatory (LIGO) to a stochastic background, and its dependence on the detector orientations

(Originally appeared in Phys. Rev. D 48, 2389 (1993).)

Abstract

We analyze the sensitivity of a network of interferometer gravitational wave detectors to the gravitational wave stochastic background, and derive the dependence of this sensitivity on the orientations of the detector arms. We build on and extend the recent work of Christensen, but our conclusion for the optimal choice of orientations of a pair of detectors differs from his. For a pair of detectors (such as LIGO) that subtends an angle at the center of the Earth of $\lesssim 70°$, we find that the optimal configuration is for each detector to have its arms make an angle of 45° (modulo 90°) with the arc of the great circle that joins them. For detectors that are farther separated, each detector should instead have one arm aligned with this arc. We show that the broadband sensitivity to the stochastic background of a detector pair which are $\lesssim 3000$ km apart is essentially determined by their relative rotation. Their average rotation with respect to the arc joining them is unimportant. We also describe in detail the optimal data-analysis algorithm for searching for the stochastic background with a detector network, which is implicit in earlier work of Michelson. The LIGO pair of detectors will be separated by ~ 3000 km. The minimum detectable stochastic energy-density for these detectors with their currently planned orientations is $\sim 3\%$ greater than what it would be if the orientations were optimal, and ~ 4 times what it would be if their separation were $\lesssim$ a few kilometers. [The detectors are chosen to be far apart so that their sources of noise will be uncorrelated, and in order to improve the angular resolution of the determinations of positions of burst sources.]

1 INTRODUCTION AND SUMMARY

1.1 Background and motivation

Construction will begin soon on the American Laser Interferometer Gravitational Wave Observatory (LIGO) [1], and on its French-Italian counterpart, VIRGO [4]. Early in the next century there will likely be in operation a worldwide network of detectors, with sites in America, Europe, and possibly Japan and Australia [3]. It is important at this stage for physicists to look ahead and identify the types of science that the community might focus on using this network when it reaches a mature stage, perhaps a decade after the first gravitational waves are detected. One of the reasons for doing so is that some properties and parameters of the network, which ultimately will constrain what it can accomplish in the future, are being finalized today. The orientation of the detector arms is one example.

One of the long term aims of this detector network will be to place upper limits on (or perhaps detect) the energy density of a stochastic background (SB) of gravitational waves. This background would be analogous to the relic 3° K electromagnetic background, except that its spectrum is not expected to be thermal. The spectrum is usually characterized by a quantity $\Omega_g(f)$ which is the gravitational-wave energy density per unit logarithmic frequency, divided by the critical energy density ρ_c to close the Universe:

$$\Omega_g(f) = \frac{1}{\rho_c} \frac{dE}{d^3x\, d(\ln f)}. \tag{4.1}$$

Some possible sources of a SB include (i) random superposition of many weak signals from binary-star systems [4], (ii) decaying cosmic strings [5] and first-order phase transitions [6] in the early Universe, and (iii) parametric amplification of quantum mechanical zero-point fluctuations in the metric tensor during inflation [7, 8, 9]. See Refs. [12, 11, 12] for reviews. The predicted wave strengths from all of these stochastic sources are highly uncertain, reflecting our relative ignorance of the relevant physics and/or astrophysics. Hence, detecting or placing upper limits on the SB can bring us valuable information, particularly about the very early Universe.

Relic gravitational waves produced during inflation are particularly interesting, because, as Grishchuk has shown [13], the energy spectrum for these waves contains a unique imprint of the time evolution of the Universe's scale factor $a(t)$. We now discuss what is known about the magnitude of the contribution to $\Omega_g(f)$ from these

waves, at frequencies relevant to LIGO and/or VIRGO. The predictions for Ω_g from cosmological models are not very firm: they can vary between ~ 1 and $\sim 10^{-14}$ or less. However, observational upper bounds on $\Omega_g(f)$ in various frequency bands give interesting constraints on the models [8]. In turn these constraints can be used, within the context of particular inflation models, to place upper bounds on the contribution of relic gravitons to the value of $\Omega_g(f)$ in the LIGO/VIRGO wave band, see, e.g., Ref. [14]. The strongest such upper bound comes from matching the normalization of the scalar and tensor fluctuations produced during inflation to the recent COBE measurement of the microwave background anisotropy [9, 15]. The result of this matching is somewhat discouraging: standard exponential inflation models predict that $\Omega_g(f) \leq 3 \times 10^{-14}$ at the 95% confidence level [9], far too small to be detected by LIGO/VIRGO [cf. Eq. (4.50) below]. While it is far from certain that exponential inflation is correct, it seems unlikely that the expansion during the inflationary era was so much faster than exponential as to tilt the gravitational wave spectrum enough to give a detectable signal at high, LIGO/VIRGO frequencies. It is also possible, of course, that the observed microwave anisotropy was caused by physical processes of structure formation other than inflation.

Despite these pessimistic prospects for the detection of relic gravitons by the LIGO/VIRGO network, it is certainly possible that there will be a detectable signal from other sources such as cosmic strings [5]. Hence, it is important to determine how the detector arm orientations, which will not be changeable in the future, affect the sensitivity of the detector network to the SB. To do so is the first of the two principal purposes of this paper. This issue was first considered by Michelson [16], and has been extensively discussed by Christensen [12, 17]. Essentially we build on and extend slightly their analyses. Our conclusions are also slightly different from those of Christensen.

The second principal purpose of this paper is to spell out the optimal data-processing procedure for searching for the SB with a network of detectors. The algorithm for two detectors is implicit in Michelson [16] (and is incorrectly treated in Ref. [17]); we give a more detailed description and a generalization to a network of detectors, taking into account the possible effect of correlated sources of noise. We now turn to a description of our results and an explanation of how they relate to earlier work.

1.2 Detection of the stochastic background

The effect of the SB on a gravitational wave detector is essentially to produce a small contribution to the random, Gaussian noise in its output. For one detector this contribution will be swamped by the detector's own sources of noise, unless the SB strength is implausibly large ($\Omega_g \sim 10^{-6}$; see Sec. 2). For two detectors which have no common sources of noise, however, the only contribution to the correlated fluctuations in the detector outputs will be the SB. By cross correlating the outputs of the detectors, the SB can in principle be measured. If one had identical, LIGO-type detectors at the same site, oriented in same way so that they respond in exactly the same way to the SB, and with levels of intrinsic noise corresponding to the "advanced detectors" of Ref. [1], then cross correlating would give a sensitivity to Ω_g of the order of 10^{-10} in the frequency band $10\,\mathrm{Hz} \lesssim f \lesssim 1000\,\mathrm{Hz}$ [12].

For a pair of separated, nonaligned detectors, two new physical effects complicate the analysis [12, 16, 17]. First, if the detectors are not aligned the same way, they will respond to different polarization components of the SB. Orthogonal polarization components of the SB are expected to be statistically independent, and so the cross correlation will be reduced. Second, for each mode there will be a time lag between exciting the first detector and the second detector, and hence phase lags in the cross correlation. For the LIGO detectors separated by $\sim 3000\,\mathrm{km}$ and having maximum sensitivity at a frequency of $f \sim 70\,\mathrm{Hz}$, a typical phase lag will be of order unity. Hence, there will be some destructive interference between parts of the cross correlation that are due to modes which propagate in different directions. Thus we expect a reduction in the sensitivity of the detector pair to the SB.

To analyze this reduction, it is necessary to (i) determine how to *optimally process* the output from the detectors, and (ii) find the signal-to-noise ratio (SNR) that results from this method of filtering. We also want to (iii) determine how the optimal SNR depends on the detector orientations, and (iv) find those orientations that maximize the SNR. Steps (i) and (ii) were analyzed in Refs. [16, 17]. They found that, when optimal signal processing is used, the square of the signal-to-noise ratio for a broadband measurement of the SB is [18]

$$\frac{S^2}{N^2} = \left(\frac{4G\rho_c}{5\pi c^2}\right)^2 2\hat{\tau}\int_0^\infty df\,\frac{\Omega_g(f)^2\gamma(f)^2}{f^6 S_n(f)^2}. \tag{4.2}$$

Here $\hat{\tau}$ is the duration of the measurement, and $S_n(f)$ is the spectral noise density in either detector. The key quantity appearing in this equation is the dimensionless

function $\gamma(f)$, which we call the *overlap reduction function.* It characterizes the reduction in sensitivity to the SB of the detector pair at frequency f that is due to their separation and nonoptimal orientations, and its value is unity for coincident, aligned detectors. In Refs. [16, 17] a formula for the overlap reduction function was derived, which expresses it as an integral over all solid angles of the complex phase lag between the detectors, weighted by combinations of the detector beam pattern functions [cf. Eq. (4.16) below]. Christensen [12, 17] numerically calculated this function for various detector configurations and discussed some of its properties. However its dependence on the detector orientations was not apparent.

In this paper we derive an analytic formula for the overlap reduction function. Using this formula we are able to carry through steps (iii) and (iv) outlined above. We also determine how good are the choices that have been made for the orientations of the detectors in LIGO, VIRGO, and GEO (an as-yet-unfunded British/German collaboration); i.e., we determine how their sensitivity to the SB compares to the sensitivity they would have if they were optimally oriented.

1.3 Effect of detector orientations

Our results are as follows. Call σ_1 the angle between the bisector of the arms of the first detector and the arc of the great circle that joins the detectors, and similarly define σ_2 for the second detector. Let $\delta = (\sigma_1 - \sigma_2)/2$ and $\Delta = (\sigma_1 + \sigma_2)/2$, so that δ describes the relative rotation of the detector pair, and Δ describes their average rotation with respect to the line joining them. Then in Sec. 5 below we show that the optimum SNR (4.2) is given by

$$\frac{S^2}{N^2} = A\cos^2(4\delta) + 2B\cos(4\delta)\cos(4\Delta) + C\cos^2(4\Delta), \tag{4.3}$$

where the quantities A, B, and C are independent of δ and Δ, and A and C are positive. There are thus two possibilities for the optimum detector orientation, depending on the sign of B: (I) $\cos(4\delta) = -\cos(4\Delta) = \pm 1$, corresponding to each detector having an arm along the line joining them, and (II) $\cos(4\delta) = \cos(4\Delta) = \pm 1$, corresponding to each detector arm being at an angle of 45° (mod 90°) to this line. In Fig. 4.1 we plot the SNR for both of these choices of orientation, as a function of the angle β subtended between the detectors at the center of the Earth. Configuration II is optimal for $\beta \lesssim 70°$, while configuration I is optimal for detectors which are further apart. Figure 4.1 shows that detectors which are close together are the most sensitive; the sensitivity of LIGO is roughly $\sim 25\%$ of what

it would be if its detectors were coincident. It also shows that detectors whose planes are roughly perpendicular ($\beta \sim 90°$) have poor sensitivity, as we would expect.

We also show in Sec. 5 that the narrow band sensitivity of the detector pair near a given frequency f, which is proportional to $|\gamma(f)|$, is also always optimized at either configuration I or II. For example, at very low frequencies, $|\gamma(f)|$ becomes essentially the overlap of the polarization tensors of the two detectors [cf. Eq. (4.107) below with $\rho_2(0) = \rho_3(0) = 0$], which is maximized in configuration I. This low frequency limit was previously derived by Christensen [17]. Motivated by this, he suggested that configuration I was always the best orientation to choose. Figure 4.1 shows that, though this is not true for some values of the separation angle β, the amount lost by choosing I rather than II is never more than a few percent in SNR.

We now discuss the orientations that have been chosen for the detector systems that are under construction or that have been proposed. The relative rotation angle δ for a pair of detectors essentially determines whether the detectors respond to different polarization components, or to the same polarization component, of the gravitational wave field. The advantage in responding to different components ($2\delta \sim 45°$) is that more information can be extracted from incoming burst signals. On the other hand, if the detectors respond to the same component ($\delta \sim 0°$) then the detection signal-to-noise threshold is reduced, i.e., the fact that the same waveform is seen in both detectors means that one can be more confident that a candidate event is not due to detector noise. These considerations guided the choices of the presently planned values of δ for the detector pairs LIGO/LIGO (there will be two LIGO detectors) and VIRGO/GEO, which are $\delta \approx 0°$ and $2\delta \approx 45°$, respectively [23].

Within the context of these constraints, a key issue that we wanted to understand was the following: given the above values of δ, how much does the broadband sensitivity of the detector pair depend on Δ, i.e., by how much can the SNR be reduced if Δ is chosen arbitrarily instead of being optimally chosen? The answer we obtain [Secs. 4 and 5 below] is that for relatively close detectors with $\beta \lesssim 30°$, the dependence on Δ is very weak; but the dependence is strong for detectors on different continents. Hence for LIGO's parallel detectors, the sensitivity will be close to optimal irrespective of the value of Δ; the present choice of $\Delta = 28.2°$ implies that the SNR for LIGO is $\sim 97\%$ of the sensitivity at optimal orientation. The VIRGO/GEO orthogonal detector pair, however, will have a SNR of less than

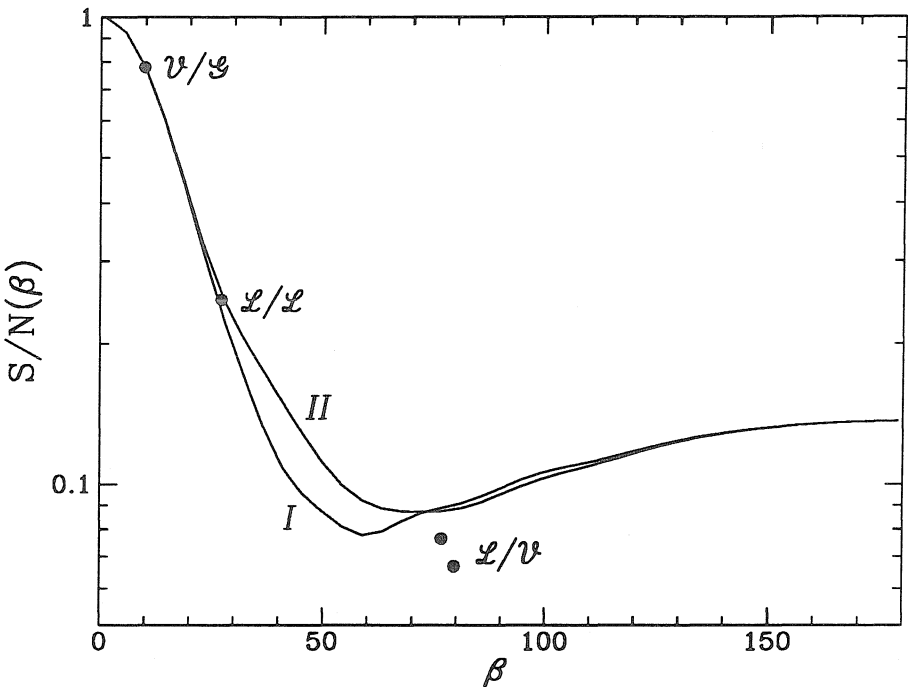

Figure 4.1: The broadband signal-to-noise ratio for a pair of detectors as a function of the angle β subtended between them at the center of the Earth, normalized to unity for coincident detectors. Curve I corresponds to each detector having an arm along the arc of the great circle that joins them, and curve II corresponds to each one having an arm at 45° to this arc. The optimal configuration is II for $\beta \lesssim 70°$ (except very close to $\beta = 0$), and I for larger values of β. The point $\mathcal{L}/\mathcal{L}$ and the two points marked $\mathcal{L}/\mathcal{V}$ show the expected sensitivities of the LIGO detector pair and of both LIGO-VIRGO detector pairs, with their planned orientations. The point $\mathcal{V}/\mathcal{G}$ shows the sensitivity the detector pair VIRGO-GEO would have if the orientations were chosen optimally for the stochastic background (which will probably not be the case, since optimization for the stochastic background implies sensitivity to only one of the waves' two polarizations, and a corresponding loss of information when studying nonstochastic waves).

10^{-3} times the optimal value, irrespective of the value of Δ, if 2δ is chosen to be 45° (as is planned, so as to optimize the information obtainable from burst sources).

Finally, we estimate the 90% upper confidence limit that can be placed on $\Omega_g(f)$ by the so-called "advanced detectors" in LIGO [1], in a broadband measurement using a one third of a year integration time, to be $\sim 5 \times 10^{-10}$ in the frequency band $20\,\mathrm{Hz} \lesssim f \lesssim 70\,\mathrm{Hz}$ [cf. Eq. (4.49) below]. This is a little worse than earlier estimates which assume that the detectors are coincident and aligned [12, 11].

1.4 Organization of this chapter

The layout of this chapter is as follows. In Sec. 2 we define the cross correlation matrix for a network of detectors and give the formula for the contribution to this quantity from the SB. In Sec. 3 we describe the general optimal data-processing strategy, the justification of which is given in Appendix A. In this appendix we also derive the generalization of the signal-to-noise formula for optimal signal processing (4.2), to a network of more than two detectors, but more importantly to a network that has more than one interferometer per site: we show how to take into account the effect of correlated noise in detectors at the same site by introducing the concept of the *effective spectral noise density* of a detector site. In Appendix B we derive the formula for the overlap reduction function, and we describe some of its properties in Sec. 4.

Next, in Sec. 5, we show how to optimize the orientations of a pair of detectors, both for narrow band and for broadband measurements of the SB. Section 6 describes the implications of our results for the LIGO, VIRGO, and GEO detector facilities. Finally in Sec. 7 we summarize our main results.

We use units throughout in which the speed of light c and Newton's gravitational constant G are unity.

2 DETECTOR CROSS CORRELATION MATRIX

The effect of a stochastic background on a detector network will be essentially to produce statistical correlations between the outputs of the various detectors. A key result which we will need is an expression for these correlations in terms of the spectrum $\Omega_g(f)$ of the gravitational background. This was first given by Christensen [12, 17], although it is implicit in the work of Michelson[16]. We briefly

describe the derivation in this section, and we lay the foundations for our analysis of Appendix A and Sec. 3.

A detector network with N detectors will have outputs

$$h_a(t) = h_a^{\text{signal}}(t) + n_a(t) + s_a(t), \tag{4.4}$$

for $1 \leq a \leq N$. Here h_a is the strain amplitude that we read out from the ath detector; it consists of an intrinsic detector noise n_a, a contribution from the SB s_a, and possibly a contribution h_a^{signal} from nonstochastic gravitational waves (bursts and periodic waves). The noise n_a and the SB induced strain s_a are independent random processes, which we assume to be Gaussian and stationary.

The detector correlations can be described by the correlation matrix

$$C_h(\tau)_{ab} = \langle h_a(t+\tau) h_b(t) \rangle - \langle h_a(t+\tau) \rangle \langle h_b(t) \rangle, \tag{4.5}$$

where angular brackets mean an ensemble average or a time average. The Fourier transform of the correlation matrix, multiplied by two, is the power spectral density matrix:

$$S_h(f)_{ab} = 2 \int_{-\infty}^{\infty} d\tau \, e^{2\pi i f \tau} C_h(\tau)_{ab}. \tag{4.6}$$

This is a positive definite Hermitian matrix which satisfies the equations

$$\langle \tilde{h}_a(f) \tilde{h}_b(f')^* \rangle = \frac{1}{2} \delta(f - f') S_h(f)_{ab}, \tag{4.7}$$

and

$$\left\langle e^{i \int dt \, w_a(t) h_a(t)} \right\rangle = \exp\left\{ -\frac{1}{2} \int_0^{\infty} df \, \tilde{\mathbf{w}}^{\dagger} \cdot \mathbf{S}_h \cdot \tilde{\mathbf{w}} \right\}, \tag{4.8}$$

for any functions $w_a(t)$. Here tildes denote Fourier transforms, according to the convention that

$$\tilde{h}(f) = \int e^{2\pi i f t} h(t) dt.$$

Since the random processes $n_a(t)$ and $s_a(t)$ are uncorrelated, the spectral density matrix of the detector outputs is just the sum of those for the detector noise and for the background:

$$\mathbf{S}_h(f) = \mathbf{S}_n(f) + \mathbf{S}_s(f). \tag{4.9}$$

To derive an expression for $\mathbf{S}_s(f)$, two key ingredients are needed. The first is a mode expansion for the metric perturbation for an isotropic, stationary SB. Expressed in frequency space, this is

$${}^{(\text{SB})}\tilde{h}_{ij}(\mathbf{x}, f) = \int d^2\Omega_n \sum_{A=+,\times} s_{A,\mathbf{n}}(f) \, e^{2\pi i f \mathbf{n}\cdot\mathbf{x}} \, e_{ij}^{A,\mathbf{n}} \tag{4.10}$$

for $f \geq 0$, and ${}^{(\mathrm{SB})}\tilde{h}_{ij}(\mathrm{x}, f) = {}^{(\mathrm{SB})}\tilde{h}_{ij}(\mathrm{x}, -f)^*$ for $f < 0$. Here the tensors $\mathrm{e}^{A,\mathrm{n}}$ are the usual transverse traceless polarization tensors, normalized according to $e_{ij}^{A,\mathrm{n}} e_{ij}^{B,\mathrm{n}} = 2\delta_{AB}$, and $\int d^2\Omega_n$ denotes the integral over solid angles parametrized by the unit vector n. The coefficients $s_{A,\mathrm{n}}$ are random processes which satisfy [20]

$$\begin{aligned} \langle\, s_{A,\mathrm{n}}(f)\, s_{B,\mathrm{m}}(f')^*\,\rangle &= \delta_{AB}\,\delta^2(\mathrm{n},\mathrm{m}) \\ &\quad \times \delta(f-f')\,\frac{\rho_c}{4\pi f^3}\,\Omega_g(f) \end{aligned} \tag{4.11}$$

and

$$\langle\, s_{A,\mathrm{n}}(f)\, s_{B,\mathrm{m}}(f')\,\rangle = 0, \tag{4.12}$$

for $f, f' \geq 0$ [21]. Here $\delta^2(\mathrm{n},\mathrm{m})$ is the δ function on the unit sphere.

The second ingredient is the expression for the response of the ath detector to the background. This is

$$s_a(t) = \mathrm{d}_a : {}^{(\mathrm{SB})}\mathrm{h}(\mathrm{x}_a, t), \tag{4.13}$$

where x_a is the position of the detector, the colon denotes a double contraction, and d_a is a symmetric tensor that characterizes the detector's orientation (its polarization tensor). If the arms of the detector are in the directions of the unit vectors l and m, then $\mathrm{d}_a = (l \otimes l - \mathrm{m} \otimes \mathrm{m})/2$ [45]. From Eqs. (4.10) and (4.13) we obtain that

$$\tilde{s}_a(f) = \sum_A \int d^2\Omega_n\, F_a^A(\mathrm{n})\, s_{A,\mathrm{n}}\, e^{2\pi i f \mathrm{n}\cdot\mathrm{x}_a}, \tag{4.14}$$

where $F_a^A(\mathrm{n}) \equiv \mathrm{d}_a : \mathrm{e}^{A,\mathrm{n}}$ are the detector beam pattern functions. Inserting this response function into an equation analogous to Eq. (4.7), and using Eqs. (4.11) and (4.12), we obtain

$$S_s(f)_{ab} = \frac{4\rho_c\Omega_g(f)}{5\pi f^3}\,\gamma_{ab}(f), \tag{4.15}$$

where [23]

$$\begin{aligned} \gamma_{ab}(f) = \frac{5}{8\pi}\int d^2\Omega_n\,(F_a^+ F_b^+ + F_a^\times F_b^\times) \\ \times \exp\left[2\pi i f \mathrm{n}\cdot(\mathrm{x}_a - \mathrm{x}_b)\right]. \end{aligned} \tag{4.16}$$

The functions γ_{ab} are the overlap reduction functions discussed in Sec. 1. It can be seen that their value is unity for coincident, aligned detectors. Below when considering a single pair of detectors we shall write $\gamma_{ab}(f)$ simply as $\gamma(f)$.

3 THE OPTIMAL PROCESSING STRATEGY

In this section we describe the optimal method for filtering the detector outputs when searching for the SB. We discuss the two- detector case in Sec. 3.1; the filtering method in this subsection is implicit in the formulae of Ref. [16]. A detailed proof that the method is optimal is given in Appendix A. In Sec. 3.2 we discuss the effects of correlated sources of noise, and explain why correlation measurements between detectors at widely separated sites yield much better upper bounds on $\Omega_g(f)$ than correlation measurements between detectors at one site. Next we describe the modifications to the filtering method necessitated by correlated noise, in Sec. 3.3.

3.1 General description

To measure the stochastic background one really needs to measure the spectral density matrix of the detector outputs $\mathbf{S}_h(f)$. Now there is no way in principle to separate out the portions of $\mathbf{S}_h(f)$ due to detector noise $\mathbf{S}_n(f)$, and due to the SB $\mathbf{S}_s(f)$. If we had only one detector, we could only conclude that $S_s(f) \leq S_h(f)$. From Eq. (4.15) and using $\gamma_{aa}(f) = 1$, this would give an upper bound on Ω_g of

$$\Omega_g(f) \lesssim 2.5 \times 10^{-6} \left(\frac{h_n(f)}{10^{-23}}\right) \left(\frac{f}{100\,\mathrm{Hz}}\right) h_{75}^{-2}. \tag{4.17}$$

Here $h_n = \sqrt{f S_h(f)}$, which is projected to be $\gtrsim 10^{-23}$ for LIGO, even at an advanced stage [1]. The quantity h_{75} is the Hubble constant scaled to the value of 75 km secs^{-1} Mpc^{-1}.

It is unlikely that Ω_g will be as large as the value in Eq. (4.17). However, if it does happen that $\Omega_g \gtrsim 10^{-5}$ in the LIGO/VIRGO wave band, then the SB-induced noise may dominate over the other sources of detector noise at some frequencies, and may ultimately constrain the amount of information that we can extract from burst gravitational waves. In this paper we shall from now on assume that Ω_g is small, and restrict attention to measurements made using two or more detectors.

With two or more detectors, one takes advantage of the fact that the sources of noise in each detector will be independent. This will be the case for detectors at widely separated sites, because sources of noise that are correlated between the detectors on time scales of the order of the light travel time between them are expected to be insignificant, or if not they can be monitored and compensated for [17]. When correlated noise is unimportant, then the off-diagonal elements of

$S_n(f)$ will be very small, so that

$$S_s(f)_{ab} \approx S_h(f)_{ab} \quad \text{for } a \neq b. \tag{4.18}$$

By measuring these components we can gain information about the SB. One does this by cross correlating the two output streams [12]. One takes each detector output $h_a(t)$, $a = 1, 2$, and constructs, using an optimizing linear filter $K(t)$, the quantity $\tilde{H}_a(f) = \tilde{K}(f)\tilde{h}_a(f)$. The purpose of this filter is essentially to suppress the signal at those frequencies at which the detector noise is strong, and it is given by [cf. Eq. (4.101) below]

$$\tilde{K}(f) = \frac{1}{f^{3/2}S_h(f)}. \tag{4.19}$$

For coincident, aligned detectors the next step is simply to integrate $H_1(t)$ against $H_2(t)$, see, e.g., Ref. [12]. For noncoincident detectors, however, a different strategy is necessary. One first constructs the correlation with time delay τ,

$$Y(\tau) = \int_{-\hat{\tau}/2}^{\hat{\tau}/2} dt\, H_1(t+\tau)H_2(t), \tag{4.20}$$

where $\hat{\tau}$ is the observation time, typically of the order of 1 yr. Then one calculates the weighted average

$$Y = \int_{-\tau_1}^{\tau_1} d\tau\, L(\tau)Y(\tau), \tag{4.21}$$

where τ_1 is the light travel time between the detectors, and $L(\tau)$ is a weighting function which must be carefully chosen for each detector pair in order to maximize the sensitivity. Roughly speaking, this smearing of the cross correlation compensates in some measure for the phase lags between the detectors which were discussed in Sec. 1. The quantity Y will then have a truncated Gaussian distribution (i.e., Gaussian but restricted to positive values) with signal-to-noise ratio given by Eq. (4.2) [18].

In fact the sliding delay function $L(\tau)$ is just the Fourier transform of the overlap reduction function [see Eqs. (4.100) and (4.101)]. In Appendix B we give an analytic formula for $L(\tau)$, and we show in Fig. 4.2 the sliding delay function that will need to be used for the LIGO pair of detectors.

In order of magnitude, the 90% confidence upper limit that can be placed on Ω_g by cross correlating between the detectors is [12]

$$\Omega_g^{\max} \approx \frac{\Omega_0}{\sqrt{\hat{\tau}\Delta f}}. \tag{4.22}$$

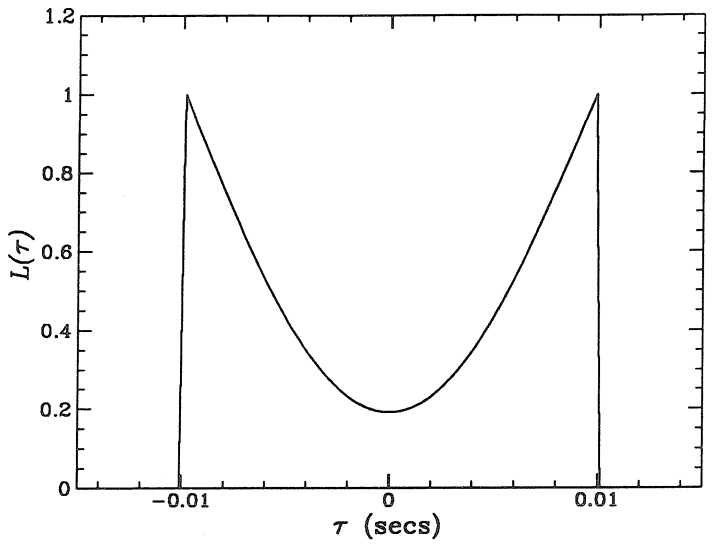

Figure 4.2: The "sliding delay function" $L(\tau)$ for the LIGO pair of interferometers. To maximize the broadband sensitivity to the stochastic background, the cross correlation with a time delay τ between the detector pair must be integrated against this function; see text.

Here $\Omega_0 \sim 10^{-6}$ is the upper bound (4.17) obtainable from one detector, and Δf is the bandwidth of the measurement. [If no bandpass filtering of the data is carried out, Δf will be roughly the width of the peak of the function $1/(f^3 S_n)$; and if filtering with a bandwidth Δf is used, then the domain of integration in Eq. (4.2) must be suitably restricted].

3.2 Effects of correlated noise

Up to this point we have assumed that the intrinsic detector noise is uncorrelated between different detectors, i.e., that the matrix $\mathbf{S}_n(f)$ is diagonal. We now relax this assumption and consider the effects of correlated noise. It is planned for LIGO/VIRGO to ultimately have two or three detectors per detector site, perhaps optimized for different types of gravitational wave sources. Thus, there will be two possible types of correlation measurements: *intrasite* measurements at one site, and *intersite* measurements between detectors at different sites. As previously mentioned, it seems very unlikely that there will be any significant correlated noise in intersite measurements, and so it will only be important for intrasite measurements.

We now consider what information can be extracted from intrasite correlations. This issue has been previously discussed by Christensen [17], who indicates that intrasite upper bounds on the SB will be competitive with those from intersite measurements. As we now discuss, we disagree with this conclusion. The quantity we can measure is the sum $\mathbf{S}_n(f) + \mathbf{S}_s(f)$, the two terms of which are in principle indistinguishable [24]. Hence, we can draw inferences about $\mathbf{S}_s(f)$ *only* if we have some information about the correlated noise. The most obvious such *a priori* information is the fact that $\mathbf{S}_n$ is a positive Hermitian matrix. It follows that if we measure the total power spectral density matrix to be $\hat{\mathbf{S}}_h$, then $\mathbf{S}_s < \hat{\mathbf{S}}_h$. However, this only tells us that $\Omega_g \gtrsim 10^{-6}$ [cf. Eq. (4.17) above], since the inequality applies to the total matrix, and the off-diagonal elements are small compared to the diagonal elements. In particular, it is not true without further assumptions that

$$S_s(f)_{ab} \leq |\, \hat{S}_h(f)_{ab} \,| \qquad \text{for } a \neq b \tag{4.23}$$

(as is implicitly assumed in Ref. [17]), since $S_n(f)_{ab}$ may be negative (or complex). A complex value of $S_n(f)_{ab}$ corresponds physically to sources of noise that excite two detectors with a certain preferred phase lag between them.

In Appendix A, we derive the 90% confidence upper limit that one can place on Ω_g in a bandwidth Δf using intrasite correlations, which generalizes Eq. (4.22). If we define the noise correlation coefficients by

$$\mathcal{C}_{ab} \equiv \frac{S_n(f)_{ab}}{\sqrt{S_n(f)_{aa}\, S_n(f)_{bb}}}, \tag{4.24}$$

then the result depends on (i) the measured value $\hat{\mathcal{C}}$ of $\mathcal{C}$ (determined from $\hat{\mathbf{S}}_h$), and (ii) the assumed *a priori* maximum value $\mathcal{C}_{\max}$ of $|\mathcal{C}|$. In order of magnitude we find [cf. Eqs. (4.86) and (4.90) below]

$$\Omega_g^{\max} \approx \Omega_0 \left[\hat{\mathcal{C}} + \sqrt{\frac{1}{\hat{\tau}\Delta f} + \mathcal{C}_{\max}^2} \right]. \tag{4.25}$$

Since there will be various unknown sources of weak correlated noise, it is not appropriate to choose a very small value of $\mathcal{C}_{\max}$. Hence, the upper bound (4.25) will be much worse than the bound (4.22) obtained from intersite correlations.

We also consider the assumption that the correlated detector noise always excites different detectors in phase, but can be arbitrarily large in magnitude, so that

$$S_n(f)_{ab} \geq 0 \text{ for } a \neq b. \tag{4.26}$$

In this case intrasite correlation measurements cannot be used to *detect* the SB, but can only be used to place upper bounds on its magnitude. The resulting upper limit [cf. Eq. (4.88)] is given by Eq. (4.25) with $\mathcal{C}_{\max} = 0$. Thus, the intersite correlations will still give better bounds unless the actual amount of correlated noise in the detectors satisfies

$$\hat{\mathcal{C}} \lesssim \frac{1}{\sqrt{\hat{\tau}\Delta f}}, \tag{4.27}$$

which is $\sim 10^{-4}$ for a year-long measurement with a bandwidth of $\sim 50\,\mathrm{Hz}$. Since it is not clear that either of the conditions (4.26) or (4.27) will be appropriate, we henceforth consider only intersite correlations.

3.3 Filtering intersite correlation measurements

In Appendix A we show how to optimally filter the intersite data when there is a detector network with several interferometers per detector site. In this case the detector noise matrix $\mathbf{S}_n(f)$ will have a block diagonal form, with each block corresponding to a site. Let $\mathbf{S}_A$ be the subblock corresponding to the Ath site. The strategy is essentially to measure the off-diagonal blocks of $\mathbf{S}_h(f)$ (i.e., the intersite correlations), and to use these to obtain information about the SB. The resulting SNR squared is then given [cf. Eq. (4.102) below] by a simple generalization of Eq. (4.2):

$$\frac{S^2}{N^2} = \left(\frac{4\rho_c}{5\pi}\right)^2 2\hat{\tau}\int_0^\infty df\,\frac{\Omega_g(f)^2}{f^6}\sum_{A<B}\frac{\gamma_{AB}(f)^2}{S_A^{(\mathrm{eff})}(f)S_B^{(\mathrm{eff})}(f)}. \tag{4.28}$$

Here the sum is over the pairs of sites, and γ_{AB} is the overlap reduction function for any detector at site A together with any detector at site B. The quantities $S_A^{(\mathrm{eff})}(f)$, which we call the effective site spectral noise densities for correlations between sites, are given by

$$S_A^{(\mathrm{eff})}(f) = \left[\sum_{ab}\left(\mathbf{S}_A^{-1}\right)_{ab}\right]^{-1}. \tag{4.29}$$

They will be real since the matrices $\mathbf{S}_A$ are Hermitian. In the case where the off-diagonal elements of $\mathbf{S}_A$ are all equal to $S_n'(f)$, and the common value of the diagonal elements is $S_n(f)$, then we obtain that

$$S_A^{(\mathrm{eff})}(f) = \frac{1}{N}S_n(f) + \left(1 - \frac{1}{N}\right)S_n'(f), \tag{4.30}$$

where N is the number of detectors. This formula shows that the use of N detectors instead of a single detector at one site reduces that sites effective noise density by

a factor of $1/N$, *if* the detectors noise sources are independent ($S_n' \approx 0$). If the noise sources are strongly correlated, however, so that $S_n' \approx S_n$, then there is no significant reduction in the effective noise.

4 THE OVERLAP REDUCTION FUNCTION

In the preceding sections we have seen that for a pair of interferometric detectors, the overlap reduction function $\gamma(f)$ characterizes the dependence on the detector separation and orientations of both the correlation matrix (4.15), and the broad-band sensitivity to the SB (4.2). We now give an analytic formula for this function and discuss some of its properties.

4.1 The general formula for $\gamma(f)$

We first define the variables which describe the orientations and separation of a pair of detectors. Let L be the line joining the two detectors and P_1 (P_2) be the plane formed by the arms of the first (second) detector; see Fig. 4.3. The variables we will use are (i) the distance d between the detectors (ii) the acute angle β_1 between L and P_1 (iii) the angle σ_1 between the projection of L onto P_1 and the bisector of the two arms of the first detector (iv) the corresponding angles β_2 and σ_2, and (v) the angle χ between L and and the intersection of P_1 and P_2. The directions (clockwise or anticlockwise) in which σ_1 and σ_2 are chosen to be positive are unimportant, as long as the conventions for σ_1 and for σ_2 coincide as $\beta_1, \beta_2 \to 0$. Let $\delta \equiv (\sigma_1 - \sigma_2)/2$ and $\Delta = (\sigma_1 + \sigma_2)/2$. In Sec. 1 we have called these the *relative rotation* and *total rotation* angles, respectively, since for $\beta_1 = \beta_2 = 0$, the angle δ is half of the relative rotation of the detectors while Δ measures the average rotation with respect to the line joining them [25].

In general the overlap reduction function as given in Eq. (4.16) will depend on all of the variables β_1, β_2, δ, Δ, χ, and on the phase lag $\alpha = 2\pi f d$ between the detectors, where f is the frequency. Now for terrestrial detectors $\chi = \pi/2$ and $\beta_1 = \beta_2$ ($= \beta$ say), which is also the angle subtended at the center of the Earth by the detector pair. For this case we derive in Appendix B the formula

$$\gamma(f) = \cos(4\delta)\Theta_1(\alpha, \beta) + \cos(4\Delta)\Theta_2(\alpha, \beta), \tag{4.31}$$

where the functions Θ_1 and Θ_2 are

$$\Theta_1(\alpha, \beta) = \cos^4(\beta/2) g_1(\alpha) \tag{4.32}$$

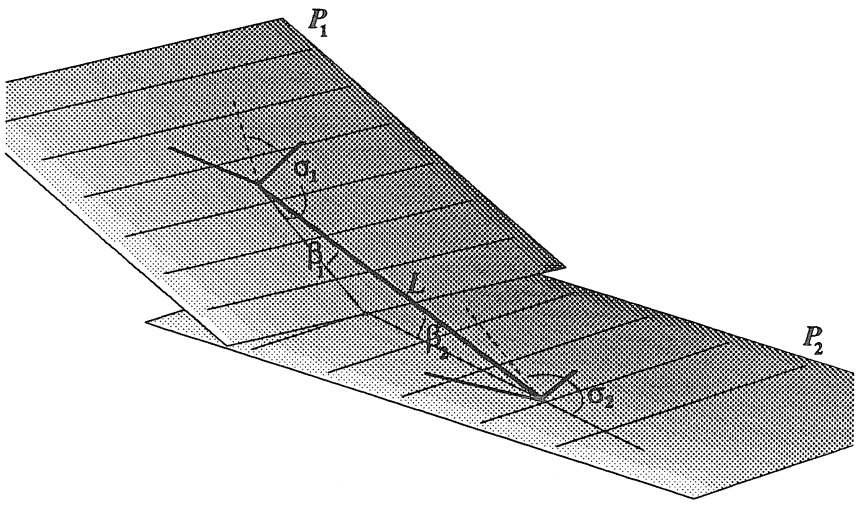

Figure 4.3: The angles σ_1, σ_2, β_1, and β_2 formed by a pair of interferometric detectors and the line L which joins them.

and

$$\Theta_2(\alpha,\beta) = \cos^4(\beta/2)g_2(\alpha) + g_3(\alpha) - \sin^4(\beta/2)\left[g_2(\alpha) + g_1(\alpha)\right]. \qquad (4.33)$$

The functions $g_j(\alpha)$ are given in Eqs. (4.113), (4.114), and (4.115) of Appendix B, and are all linear combinations of the functions $\sin(\alpha)/\alpha^n$ and $\cos(\alpha)/\alpha^n$ where $1 \leq n \leq 5$.

Several properties of the overlap reduction function $\gamma(f)$, which were discovered by Christensen and others from numerical calculations[12, 16, 17], can be read off the formula (4.31). First, there will always be frequencies f for which $\gamma(f)$ vanishes, and correspondingly near which the narrow-band sensitivity of the detector pair to the SB is very poor. For detectors that are less than a few thousand kilometers apart, the first null frequency is at $f_1 \sim (70\,\mathrm{Hz})(3000\,\mathrm{km}/d)$, irrespective of the detector orientations (see below). Second, the reduction function falls off like $1/f$ when $\alpha \gg 1$, or equivalently when $f \gg f_1$. Hence the 90% confidence limit that we can place on $\Omega_g(f)$ scales like $1/(fd)$ for large d. However for detectors which are $\sim 3000\,\mathrm{km}$ apart, the phase lag α is of order unity for typical detector frequencies, and hence the variation of the sensitivity with distance is more complex than simply scaling like $1/d$ (see Sec. 6 below and also Fig. 4.1 above).

4.2 Some special cases

To understand the behavior of $\gamma(f)$ as a function of δ, Δ, and β, it is useful to consider some limiting cases. For coplanar, coincident detectors, $d = \beta = 0$, and using $g_1(0) = 1$ and $g_2(0) = g_3(0) = 0$ we find that $\gamma = \cos(4\delta)$. This is just what we would expect physically. Consider, for instance, detectors which are rotated with respect to one another by 45°. Vertically incident gravitational waves will couple to the two detectors via polarization components that are orthogonal and hence statistically independent; thus these waves give no contribution to the cross correlation. Waves which are incident from non-vertical directions do give rise to correlations between the detectors, but when we average over all incident directions the total correlation vanishes [26]. It is also clear from rotational symmetry that there should be no dependence on the total rotation angle Δ.

Now suppose that the detectors are still coincident but no longer coplanar, so that $\beta \neq 0$. Equivalently, suppose the detectors are separated by a distance d but evaluate $\gamma(f)$ at frequencies $f \ll 1/d$. The result is

$$\gamma(f) = \cos^4(\beta/2)\cos(4\delta) - \sin^4(\beta/2)\cos(4\Delta). \tag{4.34}$$

This equation agrees with Eq. (3.9) of Ref. [17] after making an appropriate change of variables. As we would expect, the dependence on Δ is small when β is small; it is smaller than the dependence on the relative rotation angle δ by a factor of $\tan^4(\beta/2)$ ($\sim 3 \times 10^{-3}$ for the planned LIGO detectors; see below).

A third limiting case is when $\beta = 0$ but $d \gtrsim 1/f$, so that the detectors are coplanar but effectively separated. In this case,

$$\gamma(f) = \cos(4\delta)g_1(\alpha) + \cos(4\Delta)\left\{g_2(\alpha) + g_3(\alpha)\right\}. \tag{4.35}$$

Plots of the functions $g_1(\alpha)$ and $g_2(\alpha)+g_3(\alpha)$ are shown in Fig. 4.4. We see that for $\alpha \lesssim 4$, the $\cos(4\delta)$ term dominates, just as above for coincident detectors for small β. When the phase lag α is large, the functions in Eq. (4.35) can be approximated as $g_0(\alpha) \approx 5\sin\alpha/(16\alpha)$ and $g_2(\alpha) + g_3(\alpha) \approx -g_0(\alpha)$, so we obtain

$$\gamma(f) \approx -\frac{5\sin\alpha}{8\alpha}\sin(2\sigma_1)\sin(2\sigma_2). \tag{4.36}$$

What is happening physically here is that the cross correlation is dominated by modes whose propagation vectors are nearly parallel to the line joining the detectors. This can be seen by applying a stationary phase argument to the integral (4.16). Hence it is reasonable that the overlap reduction function should have separate factors for each detector that depend on how they are oriented with respect to

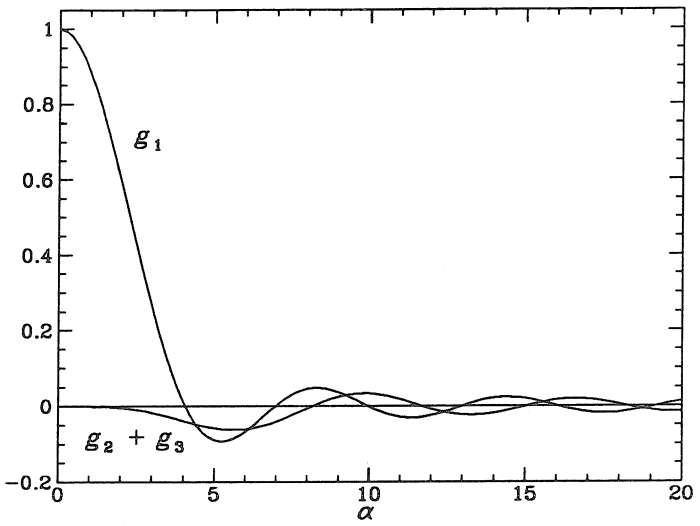

Figure 4.4: For coplanar detectors the overlap reduction function is of the form $\gamma(f) = \cos(4\delta)g_1(\alpha) + \cos(4\Delta)\,[g_2(\alpha) + g_3(\alpha)]$, where δ and Δ are the relative and total rotation angles, and α is the phase lag between the detectors at frequency f; see text. Here we plot the functions $g_1(\alpha)$ and $g_2(\alpha) + g_3(\alpha)$.

the line joining the detectors. In this case the dependence of the overlap reduction function γ on the total rotation angle Δ is strong.

In summary, the dependence on the relative rotation angle δ will dominate over the dependence on the total rotation angle Δ unless two conditions are satisfied: (i) $\beta \gtrsim \pi/4$, and (ii) $\alpha \gtrsim 1$, i.e., $d \gtrsim c/f_n$, where $f_n \sim 100\,\mathrm{Hz}$ is a typical frequency at which the detector is sensitive. In reality of course β and d are not independent; they are related by

$$d = 2\sin(\beta/2)r_E, \tag{4.37}$$

where r_E is the radius of the Earth. Because of the coincidence that the quantity $f_n r_E/c$ is of order unity, conditions (i) and (ii) above become satisfied at approximately the same value of β.

For a pair of terrestrial detectors, as β and d are increased from zero, the following three effects occur: (i) $\gamma(f)$ decreases because d is increasing, as discussed above; (ii) $\gamma(f)$ decreases because β is increasing. From Eq. (4.34) we see that the maximum over all orientations of the value of $\gamma(0)$ is $1 - \sin^2\beta/2$. Hence the effect of increasing β contributes typically a factor of at most $1/2$ to the decrease in $\gamma(f)$. (iii) The dependence of $\gamma(f)$ on Δ increases to become as strong as the

dependence on δ.

5 OPTIMIZATION OF DETECTOR ORIENTATIONS

We now turn to the issue of how to *optimize* the orientations of a single pair of detectors so as to detect or measure the SB. We assume that the detector's noise curves are the same, so that $S_n(f)_{aa} = S_n(f)_{bb} = S_n(f)$. We consider separately the cases of maximizing the narrow band sensitivity to the SB in the vicinity of some frequency f, and of maximizing the overall broadband sensitivity.

Now if we rotate a detector through 90°, then its polarization tensor d [cf. Eq. (4.13) above] will have its sign flipped. Hence $|\gamma(f)|$ is a periodic function of both of the angles σ_1, σ_1 (or δ, Δ) with period 90°. In the following discussion, all values of these angles and all equations involving them should be treated modulo 90°.

5.1 Narrow band sensitivity

From Eq. (4.2) we see that the 90% confidence limit that we can place on $\Omega_g(f)$ in a small interval of frequency of width Δf centered about f, using a measurement of duration $\hat{\tau}$, is [18]

$$\Omega_g^{(90\%)}(f;\Delta f) = \left(\frac{5\pi}{4\rho_c}\right)\frac{f^3 S_n(f)}{|\gamma(f)|}\frac{1.65}{\sqrt{2\hat{\tau}\Delta f}}. \tag{4.38}$$

To minimize this we need to maximize the quantity $|\gamma(f)|$. From Eq. (4.31) it follows that the maximum value over all orientations of $|\gamma(f)|$ is $|\Theta_1(f)| + |\Theta_2(f)|$.

Now if the signs of Θ_1 and Θ_2 are different, then this maximum will be achieved at $\sigma_1 = \sigma_2 = 45°$ (i.e., either $\delta = 45°$, $\Delta = 0°$ or $\delta = 0°$, $\Delta = 45°$). This corresponds to each detector having one arm parallel to the line which joins them. We will call this type of orientation *configuration I*. This will be the optimal orientation at zero frequency, since $\Theta_1(f = 0) = \cos^4(\beta/2) > 0$, and $\Theta_2(f = 0) = -\sin^4(\beta/2) < 0$. It will also be optimal at high frequencies ($fd \gg 1$), since from from Eqs. (4.31) and (4.113) - (4.116) we see that $\Theta_1(\alpha) \approx -\Theta_2(\alpha)$ for $\alpha \gg 1$.

If, on the other hand, the signs of Θ_1 and Θ_2 are the same, then we see from Eq. (4.31) that $|\gamma(f)|$ will be maximized at $\sigma_1 = \sigma_2 = 0°$ (i.e. either $\delta = \Delta = 0°$ or $\delta = \Delta = 45°$). In this case, which we will call *configuration II*, each detector

arm makes an angle of 45° (mod 90°) to the line joining the detectors. This will be optimal, e.g., for $10\,\mathrm{Hz} \lesssim f \lesssim 40\,\mathrm{Hz}$ when $\beta = 29°$ (the LIGO value; see below).

Now suppose that the detector pair is in either configuration I or configuration II. Then for some frequencies the orientations will be optimal, while for some other frequencies they will not be. It is useful to calculate, for a given frequency f, the factor $\mathcal{R}(f)$ by which $|\gamma(f)|$ is reduced if the wrong configuration out of I and II is chosen. Note that choosing between I and II is equivalent to fixing the relative rotation angle δ to be zero, and then choosing Δ to be either 0° or 45°. Hence $\mathcal{R}$ measures the sensitivity of $\gamma(f)$ to the total rotation angle Δ when the detectors are parallel. From Eq. (4.31), we obtain

$$\mathcal{R} = \frac{\big||\Theta_1| - |\Theta_2|\big|}{|\Theta_1| + |\Theta_2|}. \tag{4.39}$$

At low frequencies ($\alpha = 2\pi f d \ll 1$) this is approximately

$$\mathcal{R}(f \to 0) \approx \left(1 + \frac{2\nu^4}{1 - 2\nu^2}\right)^{-1}, \tag{4.40}$$

where $\nu = \sin(\beta/2)$. Thus for small values of β we have $\mathcal{R}(f \to 0) \approx 1$, and whether configuration I or II is chosen is relatively unimportant.

At high frequencies ($\alpha \gg 1$), however, we find that $\mathcal{R}(f)$ asymptotes to a constant $\mathcal{R}_\infty$ independent of frequency, where

$$\mathcal{R}_\infty \approx \left(\frac{2\nu}{\nu^2 + 1}\right)^2, \tag{4.41}$$

which can be quite small. [$\mathcal{R}_\infty \approx 0.2$ for the LIGO detectors; see below.] Hence the choice of Δ will have a large effect on the high frequency sensitivity to the SB, especially for detectors which are close together for which ν is small.

5.2 Broadband sensitivity

It is quite likely that the SB will be so weak that it will only be detectable (if at all) by integrating over a broad range of frequencies, e.g., from $\sim 20\,\mathrm{Hz}$ to $\sim 70\,\mathrm{Hz}$. Hence it is more important to optimize the overall broadband response (4.2) of the pair of detectors than to optimize the narrow-band sensitivity at some frequency. We now determine how to do this if we assume that the spectrum $\Omega_g(f)$ is approximately constant over the relevant frequency range – the so-called "Zel'dovich spectrum."

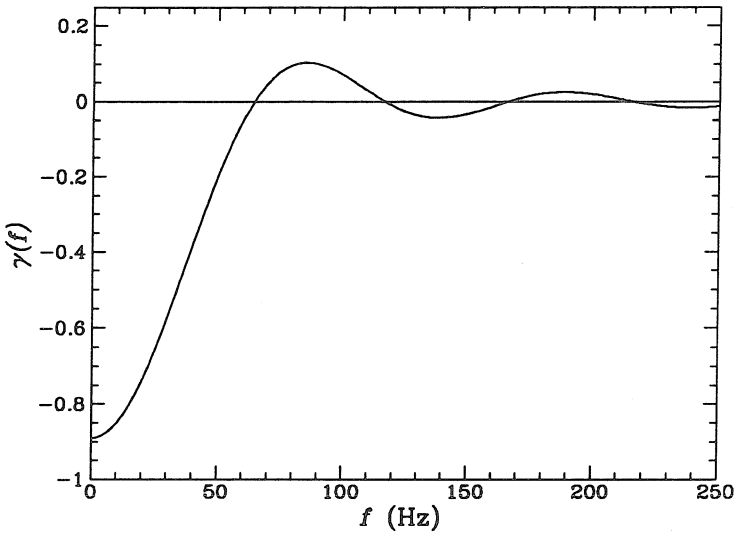

Figure 4.5: The overlap reduction function for the LIGO detectors using their planned orientations.

By inserting Eq. (4.31) into Eq. (4.2), we find that the SNR squared after optimal filtering is

$$\frac{S^2}{N^2} = A(\beta)\cos^2(4\delta) + 2B(\beta)\cos(4\delta)\cos(4\Delta) + C(\beta)\cos^2(4\Delta), \tag{4.42}$$

where

$$B(\beta) = \left(\frac{4\rho_c}{5\pi}\right)^2 2\hat{\tau}\int_0^\infty df\,\frac{\Omega_g^2\Theta_1\Theta_2}{f^6 S_n^2}, \tag{4.43}$$

and A and C are given by similar formulae with $\Theta_1\Theta_2$ replaced by Θ_1^2 and Θ_2^2, respectively. Note that A, B, and C depend on β in two distinct ways, since from Eq. (4.37),

$$\Theta_{1,2}(f) = \Theta_{1,2}\left[\alpha = 4\pi f r_E \sin(\beta/2), \beta\right]. \tag{4.44}$$

The explicit formula (4.42) makes it easy to determine how to optimally orient the detectors at a fixed value of β, and also how the SNR at the optimal orientation varies with β. The SNR (4.42) is maximized at $|\cos(4\delta)| = |\cos(2\Delta)| = 1$, and the optimum orientations are just configurations I and II again, applying when $B < 0$ and $B > 0$, respectively.

6 IMPLICATIONS FOR LIGO AND VIRGO

The planned LIGO detectors in Hanford, Washington and Livingston, Louisiana will have $\beta = 27.2°$, $\delta = 44.9°$, and $\Delta = 28.2°$ (the last two mod 90°) [27]. A graph of $\gamma(f)$ for this configuration is shown in Fig. 4.5. In Fig. 4.6 we show what the functions Θ_1 and Θ_2 look like at the value $\beta = 27.2°$ appropriate for LIGO. For any possible LIGO orientations, $\gamma(f)$ will be a linear combination of these two functions as in Eq. (4.31). From Fig. 4.6 we can see that there will be a zero of $\gamma(f)$ at $f \sim 70\,\mathrm{Hz}$, whose position is relatively insensitive to the orientations chosen.

The noise power spectral density in the LIGO detectors after some years of operation might be roughly

$$S_n(f) = \max\left[S_m(f/f_m)^{-4}, S_m(f/f_m)^2\right], \tag{4.45}$$

where $S_m = 10^{-48}\,\mathrm{Hz}^{-1}$ and $f_m = 70\,\mathrm{Hz}$. For frequencies less than $\sim 10\,\mathrm{Hz}$ the noise will be effectively infinite. Equation (4.45) is a crude analytic fit to the noise curve estimate for the "advanced detectors" given by the LIGO team in Ref. [1]. A more detailed model of the noise is unnecessary because of the uncertainty as to what the actual noise levels might be.

We now estimate what the effective site noise level $S_n^{(\mathrm{eff})}$ [cf. Eq. (4.30)] might be if, after an upgrade of the LIGO facility, there are eventually two or three interferometers at each site, as is planned. The noise spectral density $S_n(f)$ in each detector will be a sum of the form [1, 12]

$$S_n = S_{\mathrm{seismic}} + S_{\mathrm{thermal}} + S_{\mathrm{shot}} + S_{\mathrm{gas}} + \cdots, \tag{4.46}$$

including contributions due to seismic noise, thermal noise, photon shot noise, and residual gas noise, among others. By contrast, the typical value S'_n of the off-diagonal elements of the spectral density matrix will be approximately a sum of terms that are due to sources of noise which are strongly correlated between different interferometers at the same site:

$$S'_n \lesssim S_{\mathrm{seismic}} + S_{\mathrm{gas}}. \tag{4.47}$$

Since $S_{\mathrm{seismic}} + S_{\mathrm{gas}} \ll S_n$ when $f \gtrsim 10\,\mathrm{Hz}$ for the advanced detectors of Ref. [1], we find from Eq. (4.29) that to a good approximation for LIGO,

$$S_n^{(\mathrm{eff})}(f)^{-1} \approx \sum_a S_n(f)^{-1}_{aa}. \tag{4.48}$$

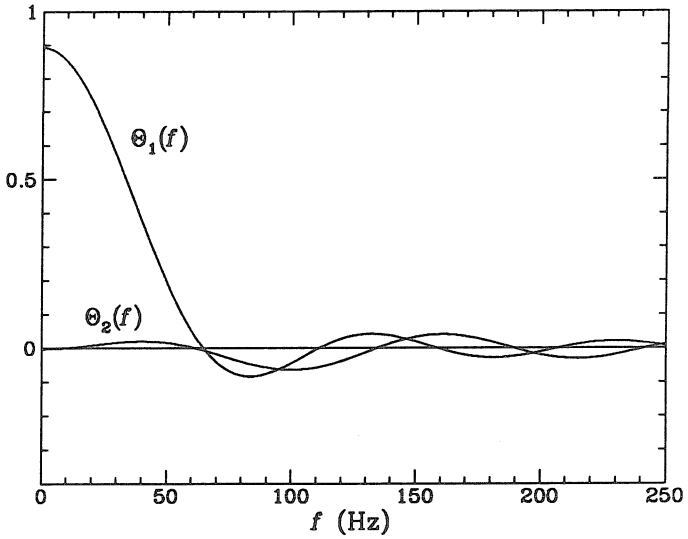

Figure 4.6: For *any* orientation angles δ, Δ of the LIGO detectors, the overlap reduction function will be given in terms of two functions of frequency $\Theta_1(f)$ and $\Theta_2(f)$ by $\gamma(f) = \cos(4\delta)\Theta_1(f) + \cos(4\Delta)\Theta_2(f)$. Here we show the functions $\Theta_1(f)$ and $\Theta_2(f)$.

Here the sum is over the different detectors, and $a = 1$ corresponds to the primary, broadband interferometer with noise curve (4.45). Now the second and/or third detectors at each site will most likely be specialized ones such as dual-recycled detectors [29], which have high sensitivity only in some narrow frequency band. Thus in the relevant frequency band of $20\,\mathrm{Hz} \lesssim f \lesssim 70\,\mathrm{Hz}$ [cf. Fig. 4.9 below], it is likely that $S_n^{(\mathrm{eff})}(f) \approx S_n(f)_{11}$. If, instead, three identical broadband detectors are operated at each site (which is unlikely initially), then $S_n^{(\mathrm{eff})}(f) \approx S_n(f)_{11}/3$, and the 90% confidence upper limit estimated below should be divided by 3.

If we now make the plausible assumption that the SB has approximately constant $\Omega_g(f)$ over the above wave band, then by inserting Eq. (4.45) into Eq. (4.28) we can calculate the 90% confidence upper limit that we can place on Ω_g. Using the planned LIGO positions and orientations we thus obtain

$$
\begin{aligned}
{}^{(\mathrm{B})}\Omega_g^{(90\%)} &= 1.65\,\frac{5\pi}{4\rho_c}\left[2\hat{\tau}\int_0^\infty df\,\frac{\gamma(f)^2}{f^6 S_n^{(\mathrm{eff})}(f)^2}\right]^{-1/2} \\
&= 5.1\times 10^{-10}\,h_{75}^{-2}\,N\left(\frac{\hat{\tau}}{10^7\,\mathrm{s}}\right)^{-1/2}, \qquad (4.49)
\end{aligned}
$$

where h_{75} is the Hubble constant scaled to the value $75\ \mathrm{km\,sec^{-1}\,Mpc^{-1}}$, $\hat{\tau}$ is the

observation time, the prefix (B) indicates broadband, and $N = S_m/10^{-48}\ \mathrm{Hz}^{-1}$. Note that this is the upper bound obtained from intersite cross correlations, since as argued in Sec. 3.2, it will not help much to include the information from intrasite correlations.

This bound (4.49) is a reasonably conservative estimate of what the LIGO sensitivity might be when the advanced detectors are operating. However the ultimate noise levels are largely unknown. This is because the experimental techniques and technology, which are presently somewhat far from the advanced level, will be steadily improving. To obtain an upper limit to ${}^{(\mathrm{B})}\Omega_g^{(90\%)}$ we take $S_n^{(\mathrm{eff})}(f) \approx S_{\mathrm{gas}}(f)$, which is a source of correlated noise that cannot be changed once the beam tube is built. Using $S_{\mathrm{gas}} \approx 2.2 \times 10^{-50}\,\mathrm{Hz}^{-1}$ [28] gives as a rather firm upper limit for the LIGO sensitivity:

$$ {}^{(\mathrm{B})}\Omega_g^{(90\%)} \geq 2 \times 10^{-13} N h_{75}^{-2} \left(\frac{\hat{\tau}}{10^7\,\mathrm{sec}} \right)^{-1/2} . \tag{4.50} $$

We now consider how ${}^{(\mathrm{B})}\Omega_g^{(90\%)}$ would change if we were to vary the angles β, δ, and Δ. The integral (4.43) is positive for $\beta = 27.2°$ with the noise power spectral density (4.45). Hence the optimal configuration of the detectors is configuration II, i.e., at $\delta = \Delta = 0°$ or 45°. However LIGO already has $\delta \approx 45°$ (corresponding to parallel detectors because $\sigma_1 - \sigma_2 = 2\delta \approx 90°$). Also, as we have discussed in Sec. 4, the dependence of $\gamma(f)$ on Δ is very weak for $f \lesssim 100\,\mathrm{Hz}$ and at $\beta = 27°$, see Eq. (4.31) and Fig. 4.6. Because of these two facts the expected LIGO sensitivity at its planned configuration of $\delta = 44.9°$ and $\Delta = 28.2°$ is only $\sim 3\%$ less than the optimal sensitivity which would be attained at $\delta = \Delta = 45°$. This follows from Eq. (4.42) where we find that $B/A = 0.045$ and $C/A = 7.8 \times 10^{-3}$.

The European VIRGO and GEO detectors, however, are currently planned to have $2\delta = \sigma_1 - \sigma_2 \approx 45°$. Such a configuration will allow VIRGO and GEO to extract information from both polarization components of burst and periodic gravitational waves, but will severely reduce the sensitivity to the SB. For these detectors $\beta = 9.75°$, and we find from Eq. (4.43) that $B/A = 4.0 \times 10^{-4}$ and $C/A = 1.7 \times 10^{-6}$. In Fig. 4.7 we plot the broadband signal-to-noise ratio (4.42) as a function of δ (assuming that Δ is optimally chosen); it can be seen that at $\delta = 45°$, the sensitivity to the SB is reduced by about 3 orders of magnitude. An intermediate choice of $\delta \sim 40°$ would give a broadband sensitivity to the SB comparable to that of LIGO, while still allowing the detectors to access two polarization components of the gravitational-wave field that are largely independent.

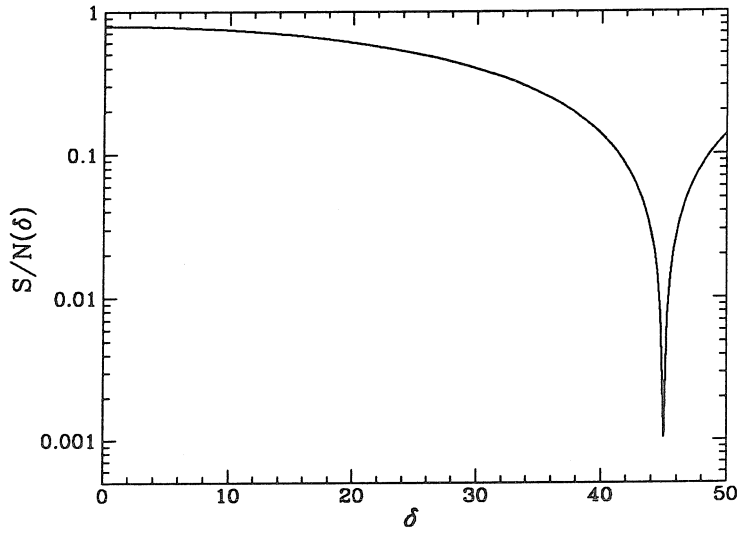

Figure 4.7: The broadband signal-to-noise ratio for the VIRGO/GEO detector pair as a function of the relative rotation angle δ, assuming (i) that the total rotation angle Δ is optimally chosen, and (ii) the advanced detector noise curve of Ref. [1]. The normalization is to unity for coincident, aligned detectors.

The total rotation angle Δ is unimportant for the broadband sensitivity to the SB in the case of detectors which are sufficiently close to each other [but *not* unimportant for the narrow-band sensitivity, cf. Eq. (4.41) above]. However, for detectors which are on separate continents, Δ will become important. For example in Fig. 4.8 we show the functions $\Theta_1(f)$ and $\Theta_2(f)$ for $\beta = 79.5°$, the value appropriate for one of the two LIGO-VIRGO cross correlations. Since Θ_2 is typically large compared to Θ_1 in this case, varying Δ will have a large effect on the sensitivity. This is confirmed by Eq. (4.42), where we find $B/A = -0.22$ and $C/A = 18.3$.

Next we consider how the broadband sensitivity to the SB varies with the angle β, assuming that the orientations are optimally chosen. Recall (cf. Sec. 5) that this means either configuration I or II is chosen. In Fig. 4.1 we plot the SNR (4.42) as a function of β, for both configurations I and II, again assuming the noise curve (4.45). It can be seen that the sensitivity falls off rapidly when the detectors become more than a few thousand kilometers apart. The sensitivity for the LIGO separation is already a factor of ~ 4 worse than that for coincident detectors. Hence if there is ultimately a worldwide network of detectors in America, Europe,

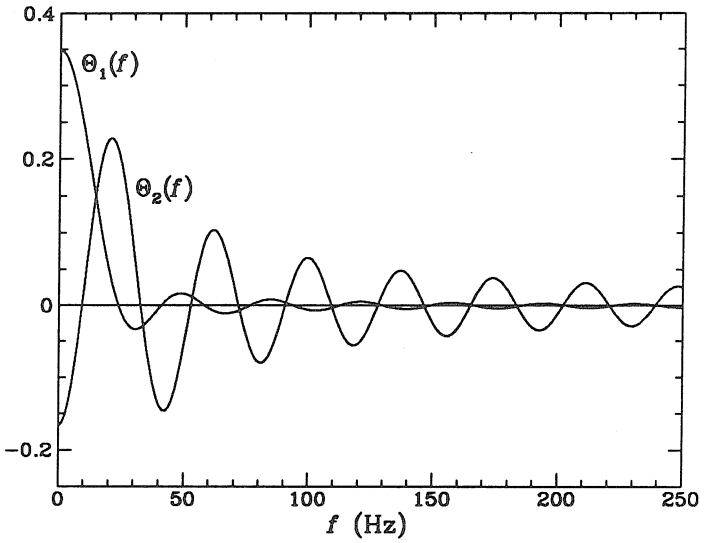

Figure 4.8: The functions $\Theta_1(f)$ and $\Theta_2(f)$ appropriate for the LIGO detector in Hanford, Washington together with the VIRGO detector in Pisa, Italy. The fact that $\Theta_2(f)$ is large compared to $\Theta_1(f)$ for most frequencies implies that the sensitivity of the detector pair to the SB depends strongly in this case on the total rotation angle Δ of the two detectors with respect to the line joining them; see text.

Japan and Australia, only the cross-correlations between proximate detector pairs like LIGO-LIGO or VIRGO-GEO will be important.

The various conclusions that we have drawn are relatively insensitive to the detailed properties of the detector noise curve (4.45) that we have assumed (except for the value of the minimum frequency). This is because the integral (4.2) is dominated by contributions in the narrow frequency band $20\,\mathrm{Hz} \lesssim f \lesssim 70\,\mathrm{Hz}$; see Fig. 4.9. At these frequencies thermal noise dominates over photon shot noise [1], so using sophisticated optical configurations of the interferometer such as dual recycling [29] to reduce the shot noise will not help much. It thus will be important for the detectors to have good low frequency sensitivity for the purposes of placing upper limits on the SB.

7 CONCLUSION

To place upper bounds on the strength of the gravitational stochastic background, or perhaps to detect it, is but one of the aims of LIGO and other detector systems. Moreover, this background may well be very weak compared to waves from astrophysical sources; consider by analogy the weakness of the electromagnetic stochastic background in the visible region of the spectrum. However, these waves if detected would be amongst the most interesting that the detectors would see.

The sensitivity to these waves is therefore just one of various factors that need to be taken into account when choosing the fixed orientations of interferometric detectors. Nevertheless, in order to be able to make a wise choice, it is important to know the effect for the sensitivity of choosing this or that orientation. One of the main results of this paper is the simple expression (4.107) describing this dependence. In particular, for frequencies such that the phase lag between the detectors is $\lesssim 1$, the sensitivity is determined solely by the overlap of the polarization tensors of the two detectors. At higher frequencies the direction of the vector which joins the detectors also becomes important.

We also determine the orientation of a pair of interferometers that will optimize the sensitivity of the pair to the SB, and show that the orientations which have been chosen for the LIGO detectors are close to optimal.

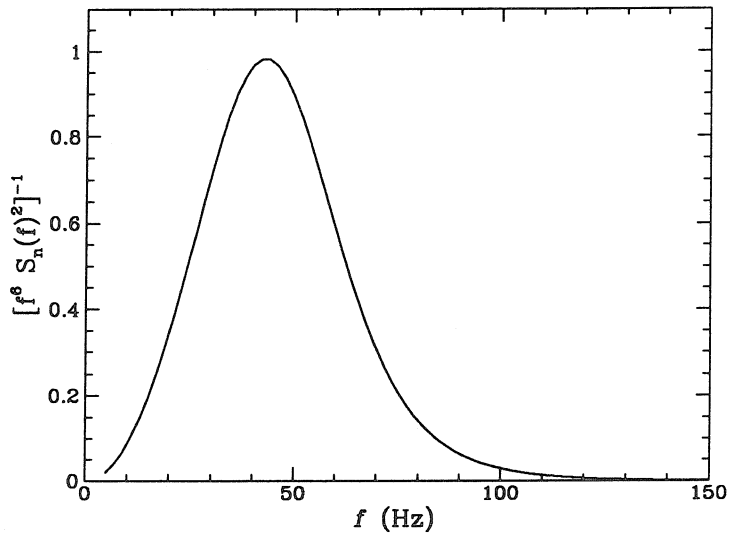

Figure 4.9: A plot of the quantity $f^{-6}S_n(f)^{-2}$ with arbitrary normalization as a function of frequency. It is this quantity that must be integrated against the square of the overlap reduction function to determine the broadband response of a detector pair to the stochastic background, when one assumes a constant, Harrison-Zel'dovich spectrum. It is clear that the highest sensitivity is limited to a narrow band of frequency between ~ 20 Hz and ~ 70 Hz.

ACKNOWLEDGMENTS

The author is grateful to Kip Thorne for an introduction to the issue of detector orientations, for many helpful discussions and comments on the presentation, and also for the foresight of guessing, roughly, what the optimal filtering method and implications for LIGO/VIRGO might be, which to a large extent motivated and guided this papers analysis. Thanks are also due to Eric Poisson for some helpful and detailed comments. This work was supported in part by NSF grant PHY-9213508.

APPENDIX A: STATISTICAL FOUNDATIONS

7.1 Overview

In this appendix we justify the method of optimal filtering described in Sec. 3 and the resulting signal-to-noise ratio (4.28). We do this by deriving the probability distribution for the spectrum Ω_g given the detectors' output $\mathrm{h}(t)$, $p[\Omega_g|\mathrm{h}(t)]$.

First we transform from a continuous to a discrete description of the measured data. In the body of this paper we have treated the output of the detector network as a continuous vector random process $\mathrm{h}(t)$. However, a real, discrete measurement will be of a finite duration $\hat{\tau}$, and will contain frequencies only up to some maximum frequency determined by the time resolution of the sampling. In other words the output of the detectors will consist of the numbers $h_{aj} = h_a(t_j = t_{\rm start} + j\Delta)$ for $1 \le a \le n_d$ and $0 \le j \le N$, where n_d is the number of detectors, $t_{\rm start}$ is the starting time, and Δ is the time resolution, of the order of 10^{-4} sec. The number of samples per interferometer is $N = \hat{\tau}/\Delta$. We denote by $\mathbf{X}$ the vector of numbers h_{aj}, which we assume to have a multivariate Gaussian distribution with some variance-covariance matrix $\mathbf{\Sigma}'$. This matrix is essentially the correlation matrix (4.5):

$$\Sigma'_{ai\,bj} = C_h(t_i - t_j)_{ab}. \tag{4.51}$$

However if we take a finite Fourier transform, which amounts to making a change of basis in the space of vectors $\mathbf{X}$, then $\mathbf{\Sigma}'$ corresponds instead to the spectral density matrix (4.6).

Now from Eq. (4.9), we have $\mathbf{\Sigma}' = \mathbf{\Sigma}'_n + \mathbf{\Sigma}'_s(\Omega)$, where the contribution $\mathbf{\Sigma}'_s$ from the SB depends on the spectrum $\Omega_g(f)$ as in Eq. (4.15). [Because of the finite frequency resolution of order $\sim 1/\hat{\tau}$, we represent the function $\Omega_g(f)$ as a

finite vector Ω.] What we want to do is extract information about Ω from a measurement of X.

There are two general approaches to the task of quantifying the information obtained, in situations of this sort. First, one can in principle compute the probability distribution function (PDF) for Ω given the measurement X, $p(\Omega|\mathrm{X})$. This PDF then contains complete information about the measurement. However, the calculation of the PDF $p(\Omega|\mathrm{X})$ is frequently difficult in practice; and so one has to resort to instead calculating estimators (statistics) $\hat{\Omega}(\mathrm{X})$ which are functions of X, chosen so that the PDF for their values given some value of Ω, $p(\hat{\Omega}|\Omega)$, is peaked near $\hat{\Omega} = \Omega$. There are standard criteria for choosing such estimators, see, for example, Refs. [21, 56].

Now suppose that, instead of one measurement of X, we have n measurements $\mathrm{X}_1, \ldots, \mathrm{X}_n$. A standard statistical result is that in the Cramer-Frechet-Rao limit of $n \rightarrow \infty$ [56, 32], the two approaches discussed above yield the same unique result. More precisely, the PDF $p(\Omega|\mathrm{X}_j)$ becomes a Gaussian centered at $\hat{\Omega}_{\mathrm{ml}}(\mathrm{X}_j)$, where $\hat{\Omega}_{\mathrm{ml}}$ is the so-called maximum likelihood estimator of Ω. The variance-covariance matrix Σ_Ω of this probability distribution depends on the X_j only through $\hat{\Omega}_{\mathrm{ml}}(\mathrm{X}_j)$, $\Sigma_\Omega = \Sigma_\Omega(\hat{\Omega}_{\mathrm{ml}})$. Conversely, the PDF $p(\hat{\Omega}_{\mathrm{ml}}|\Omega)$ of the estimator $\hat{\Omega}_{\mathrm{ml}}$ given some value of Ω becomes a Gaussian centered at Ω with width $\Sigma_\Omega(\Omega)$. Thus the two probability distributions, which are conceptually very different objects, become effectively the same, and all one really needs to calculate is the variance-covariance matrix $\Sigma_\Omega(\Omega)$.

However, this simplifying Cramer-Frechet-Rao (CFR) limit does not apply in a straightforward manner to the calculation of $p(\Omega|\mathrm{X})$ for measurements of the SB; there are a number of subtleties and differences from the usual situations discussed in Refs. [56, 32]. First, we have only one measurement of X instead of a large number n of measurements. Nevertheless, something like a "large number of measurements limit" does apply, which we discuss further below. Second, one needs to address the issue of distinguishing between the contributions to Σ' from the detector noise and from the SB, since both are unknown *a priori*. Third, the CFR limit only applies to the extent that our *a priori* knowledge of the variables being measured is unimportant. However, our *a priori* knowledge about the correlated detector noise in intrasite correlations *is* important in the calculation of $p(\Omega|\mathrm{X})$, and consequently this PDF is not approximately Gaussian [cf. Eqs. (4.71) and (4.83) below].

To resolve these complications, we now derive from first principles an approx-

imate expression for $p(\Omega|\mathrm{X})$. We also identify the conditions under which the approximations we make are valid, and show that they will all be satisfied in the LIGO/VIRGO context. We assume throughout that the effect of the SB on the detectors is small compared to the detectors intrinsic noise, so that from Eq. (4.17), $\Omega_g(f) \ll 10^{-6}$.

7.2 Calculation of $p(\Omega|\mathrm{X})$

We start by considering the *frequency resolution* of the measurement of $\Omega_g(f)$. In a finite measurement of length $\hat{\tau}$ there are roughly $N = \hat{\tau}/\Delta$ independent frequencies f_j, and we get what amounts to one measurement of each $\Omega_j = \Omega_g(f_j)$. Now if $\hat{\tau}$ is doubled, we double the number of measurements, but we also double the number of variables measured. Clearly, the Cramer-Frechet-Rao limit of repeated measurements of the same variables cannot be attained in this context without further assumptions. Below we shall argue that in the LIGO/VIRGO context, to a good approximation,

$$\mathrm{C}_h(\tau) \approx 0 \quad \text{for } \tau > \tau_c, \tag{4.52}$$

for some correlation time $\tau_c \ll \hat{\tau}$ [33]. In this case the unknown quantities to be measured are $\mathrm{C}_h(j\Delta)$ for $0 \le j \le n = \tau_c/\Delta$, or equivalently $\mathrm{S}_h(f)$ at n different frequencies; and the number of measurements of each of these variables is $\sim N/n = \hat{\tau}/\tau_c \gg 1$.

In order to explain Eq. (4.52), we fix a value of τ_c, and decompose $\mathrm{C}_h(\tau)$ into

$$\mathrm{C}_h(\tau) = \mathrm{C}_h(\tau)\Theta(\tau_c - |\tau|) + \mathrm{C}_h(\tau)\Theta(|\tau| - \tau_c), \tag{4.53}$$

where Θ is the step function. Let $\mathrm{S}_h = \mathrm{S}_h^< + \mathrm{S}_h^>$ be the corresponding decomposition in frequency space, so that $\mathrm{S}_h^<(f)$ is $\mathrm{S}_h(f)$ averaged over frequency scales of the order of $1/\tau_c$. Then from Eq. (4.9) there will be two contributions to $\mathrm{S}_h^>(f)$:

$$\mathrm{S}_h^>(f) = \mathrm{S}_s^>(f) + \mathrm{S}_n^>(f). \tag{4.54}$$

The first term here will be small if $\Omega_g(f)$ is smooth over frequency scales $\sim 1/\tau_c$ [cf. Eq. (4.15)], which will be the case for currently conceived of SB sources when $\tau_c = 100\,\mathrm{sec}$, for example. The second term in Eq. (4.54) will also be small for this value of τ_c, except near isolated frequencies corresponding to high-Q resonances [34], the effect of which can be neglected.

We now calculate the PDF for Ω using Baye's rule; by virtue of the condition (4.52), something like the CFR limit will apply. Let $\hat{\Sigma}' = \mathrm{X} \otimes \mathrm{X}$, which is the

maximum likelihood estimator of Σ'. This is an $Nn_d \times Nn_d$ matrix, where n_d is the number of detectors. Similarly the matrices Σ'_n and Σ'_s are of dimension Nn_d, and are given by formulae analogous to (4.51). However because of the condition (4.52) the independent variables in Σ' can be formed into a smaller matrix Σ, which is given by

$$\Sigma_{ai\,bj} = C_h[(i-j)\Delta]_{ab} \tag{4.55}$$

for $0 \leq i,j \leq n = \tau_c/\Delta$. Note that since $\mathrm{C}_h(-\tau) = \mathrm{C}_h(\tau)^{\mathrm{T}}$, the matrix Σ contains only $n\,n_d^2$ independent variables. We define the matrices Σ_n, Σ_s, and $\hat{\Sigma}$ analogously in terms of $\mathrm{C}_n(\tau)$, $\mathrm{C}_s(\tau)$, and the estimator

$$\hat{C}_h(\tau)_{ab} \equiv \frac{1}{\hat{\tau}} \int_{t_{start}}^{t_{start}+\hat{\tau}} dt\; h_a(t+\tau) h_b(t), \tag{4.56}$$

which is defined for $|\tau| < \tau_c$. The estimator $\hat{\mathrm{C}}_h$ is the quantity that will be measured; it is a sufficient statistic for Ω, and moreover its discrete counterpart $\hat{\Sigma}(\mathrm{X})$ is the maximum likelihood estimator of Σ.

The joint PDF for Σ_n and Σ_s given X is

$$p(\Sigma_n, \Sigma_s|\mathrm{X}) \;\propto\; p_n^{(0)}(\Sigma_n)\, p_s^{(0)}(\Sigma_s) \exp\left[-\frac{1}{2}\Lambda'(\Sigma')\right], \tag{4.57}$$

where

$$\Lambda'(\Sigma') = \ln\det\Sigma' + \hat{\Sigma}' : \Sigma'^{-1}, \tag{4.58}$$

and $p_n^{(0)}$ and $p_s^{(0)}$ are the PDF's that represent our *a priori* knowledge. From the distribution (4.57) we obtain the PDF $p(\Omega|\mathrm{X})$ for Ω given X by integrating over Σ_n:

$$p(\Omega|\mathrm{X}) = \mathcal{N} \int d\Sigma_n\, p(\Sigma_n, \Sigma_s(\Omega)|\mathrm{X}), \tag{4.59}$$

where $\mathcal{N}$ is a normalization constant.

The above formulae involve primed, $Nn_d \times Nn_d$ matrices. We now express them in terms of the corresponding, unprimed, $nn_d \times nn_d$ matrices, by using the fact that all the matrices will be approximately diagonal in frequency space. That is, they will be approximately diagonal in the indices i,j after a finite Fourier transform change of basis, but not in the indices a,b. For example, on a suitable basis,

$$(\Sigma_n)_{aI,bJ} \approx \delta_{IJ}\, S_n(f_I)_{ab}, \tag{4.60}$$

where $f_I = I/\tau_c$ for $1 \leq I \leq n$. It is straightforward to verify using Eqs. (4.52) and (4.56) that [60]

$$\Lambda'(\Sigma') \approx k\,\Lambda(\Sigma), \tag{4.61}$$

where $k = \hat{\tau}/\tau_c = N/n$ is the effective number of measurements, and

$$\Lambda(\Sigma) = \ln\det\Sigma + \hat{\Sigma} : \Sigma^{-1}. \tag{4.62}$$

For example, the second term in $\Lambda'(\Sigma')$ can be written as

$$\begin{aligned}\hat{\Sigma}' : \Sigma'^{-1} &= \left(\Sigma'^{-1}\right)^{\alpha\beta} X_\alpha X_\beta \\ &= 2\int_{-\infty}^{\infty} df\ \tilde{\mathbf{h}}(f)^\dagger \cdot \mathbf{S}_h(f)^{-1} \cdot \tilde{\mathbf{h}}(f) \\ &= \hat{\tau}\int_{-\infty}^{\infty} df\ \mathrm{tr}\left[\mathbf{S}_h(f)^{-1} \cdot \hat{\mathbf{S}}_h(f)\right]. \end{aligned} \tag{4.63}$$

Here we have used Eq. (4.8), switched into the time domain, used Eq. (4.56), and switched back [60]. The result is just $k\hat{\Sigma} : \Sigma^{-1}$, and the first term in Eq. (4.58) transforms analogously.

Now Eqs. (4.57), (4.59), (4.61), and (4.62) together yield a formal expression for $p(\Omega|\mathrm{X})$. To proceed further we need to invoke some approximations. The first of these is the quadratic approximation: we expand the likelihood function (4.62) to give

$$\begin{aligned}\Lambda(\Sigma) &= \ln\det\hat{\Sigma} + n\,n_d \\ &\quad + \frac{1}{2}\mathrm{tr}\left[\hat{\Sigma}^{-1} \cdot \delta\Sigma \cdot \hat{\Sigma}^{-1} \cdot \delta\Sigma\right] + \mathcal{O}(\delta\Sigma^3), \end{aligned} \tag{4.64}$$

where $\delta\Sigma = \Sigma - \hat{\Sigma} = \Sigma_n + \Sigma_s(\Omega) - \hat{\Sigma}$. Clearly this approximation will be good only for certain values of Σ_n and of Ω; we discuss below the implications of this restriction. First we derive the conditions under which most of the probability of the PDF

$$p(\Sigma|\mathrm{X}) \propto \exp\left[-\frac{k}{2}\Lambda(\Sigma)\right] \tag{4.65}$$

will be concentrated in the region $\mathcal{Q}$ where the quadratic approximation (4.64) is valid, in which case the normalization of the PDF (4.65) can be calculated correctly using Eq. (4.64). If we let $\lambda_1, \ldots, \lambda_n$ be the eigenvalues of $\Sigma \cdot \hat{\Sigma}^{-1} - 1$, then, up to an additive constant,

$$\Lambda(\Sigma) = -\sum_j \left[\ln(1+\lambda_j) + \frac{1}{1+\lambda_j}\right]. \tag{4.66}$$

From this formula it can be seen that the quadratic regime $\mathcal{Q}$ is given by $\max_j |\lambda_j| < \varepsilon$ where ε is some small number. If we demand that the total probability in $\mathcal{Q}$ be

$1-\delta$ for some $\delta \ll 1$, and assume that the *a priori* distribution $p_n^{(0)}$ is not sharply peaked, then we find the condition

$$N \gtrsim \frac{4}{\varepsilon^2}\left(\ln n + |\ln \delta|\right). \tag{4.67}$$

This condition will be just barely satisfied for, e.g, $\varepsilon = \delta = 0.01$, $\hat{\tau} = 10^7\,\mathrm{sec}$, $\tau_c = 100\,\mathrm{sec}$, and $\Delta = 10^{-4}\,\mathrm{sec}$, which are values that are appropriate for LIGO and/or VIRGO. Now if $\Omega \ll 10^{-6}$, then the intgeral over Σ_n in Eq. (4.59) will be dominated by contributions from the region $\mathcal{Q}$, and so the approximation is valid. For $\Omega \gtrsim 10^{-6}$, the exact probability $p(\Omega \,|\, \mathbf{X})$ is very small, and so the quadratic approximation will still give a qualitatively correct result. In particular, the normalization of the PDF $p(\Omega \,|\, \mathbf{X})$ resulting from Eq. (4.64) will be approximately correct.

The next approximation involves consideration of the relative magnitudes of various components of the measured autocorrelation matrix $\hat{\mathbf{\Sigma}}$ [cf. Eq. (4.56) above]. We introduce the following notation: for any matrix $\mathbf{A}$, $\mathbf{A}^{\|}$ denotes the matrix consisting of the diagonal subblocks (in the indices a, b) of $\mathbf{A}$ corresponding to intrasite correlations, and $\mathbf{A}^{\perp} = \mathbf{A} - \mathbf{A}^{\|}$ consists of the off-diagonal subblocks. We also define $\mathbf{A}^{D}$ to be the matrix of diagonal elements (in the indices a, b) of $\mathbf{A}$ and $\mathbf{A}^{O} = \mathbf{A}^{\|} - \mathbf{A}^{D}$. Thus, the estimator $\hat{\mathbf{\Sigma}}$ decomposes into $\hat{\mathbf{\Sigma}}^{D} + \hat{\mathbf{\Sigma}}^{O} + \hat{\mathbf{\Sigma}}^{\perp}$, where $\hat{\mathbf{\Sigma}}^{D}$ contains the detector noises $\hat{\mathbf{C}}_h(\tau)_{aa}$, $\hat{\mathbf{\Sigma}}^{O}$ contains the measured intrasite correlations, and $\hat{\mathbf{\Sigma}}^{\perp}$ the measured intersite correlations. Now we expect the contribution of correlated detector noise to $\hat{\mathbf{\Sigma}}^{\perp}$ to be very small, cf. the discussion in Sec. 3.3 above. Hence from Eq. (4.17), $\hat{\mathbf{\Sigma}}^{\perp} \sim \varepsilon\, \hat{\mathbf{\Sigma}}^{D}$, where

$$\varepsilon \approx \frac{\Omega_g}{10^{-6}}. \tag{4.68}$$

For example, if the SB is just barely detectable, then $\varepsilon \sim 10^{-4}$. We similarly define in order of magnitude the small parameter $\tilde{\varepsilon}$ by

$$\hat{\mathbf{\Sigma}}^{O} \sim \tilde{\varepsilon}\, \hat{\mathbf{\Sigma}}^{D}, \tag{4.69}$$

which we expect to be of the order of $S_{\mathrm{gas}}(f)/S_n(f) \sim 10^{-2}$ or smaller if $\Omega_g \lesssim 10^{-8}$; see Eq. (4.47).

In the expression (4.64) for the likelihood function, to leading order in ε we can replace the factors of $\hat{\mathbf{\Sigma}}^{-1}$ by $(\hat{\mathbf{\Sigma}}^{\|})^{-1}$, so that the cross terms between $\delta\mathbf{\Sigma}^{\perp}$ and $\delta\mathbf{\Sigma}^{\|}$ vanish. Note that to this order $(\hat{\mathbf{\Sigma}}^{-1})^{\|} = (\hat{\mathbf{\Sigma}}^{\|})^{-1}$. Hence, the PDF (4.57) splits into a product of two factors which incorporate the measured intersite and

the intrasite correlations. The *a priori* PDF for the detector noise in Eq. (4.57) can be written as

$$p_n^{(0)}(\Sigma_n) \approx \delta(\Sigma_n^{\perp}) p_{n,\|}^{(0)}(\Sigma_n^{\|}), \tag{4.70}$$

since we expect $\Sigma_n^{\perp} \approx 0$. Using Eqs. (4.57), (4.59), (4.61), (4.64), and (4.70) we obtain

$$\begin{aligned} p(\ \ \Omega\ \ |\mathrm{X}) \approx\ & \mathcal{N}_1 p_s^{(0)}(\Omega) p_C(\Omega) \\ & \times \exp \mathrm{tr} \left\{ -\frac{k}{4} \left[(\hat{\Sigma}^{\|})^{-1} \cdot \left(\Sigma_s(\Omega)^{\perp} - \hat{\Sigma}^{\perp} \right) \right]^2 \right\}, \end{aligned} \tag{4.71}$$

where $\mathcal{N}_1$ is a normalization constant. Here

$$\begin{aligned} p_C(\Omega) \ \equiv\ & \int d\Sigma_n^{\|}\, p_{n,\|}^{(0)}(\Sigma_n^{\|}) \\ & \times \exp \mathrm{tr} \left\{ -\frac{k}{4} \left[(\hat{\Sigma}^{\|})^{-1} \cdot \delta\Sigma^{\|} \right]^2 \right\} \end{aligned} \tag{4.72}$$

is a function representing the information from intrasite correlations, and $\delta\Sigma^{\|} = \Sigma_n^{\|} + \Sigma_s(\Omega)^{\|} - \hat{\Sigma}^{\|}$.

Now if $\tilde{\varepsilon} \gg \varepsilon$ as estimated above, then most of the information we obtain from the SB will come from the intersite correlation measurements. In this case the factor $p_C(\Omega)$ in Eq. (4.71) can be approximated to be constant [see Eq. (4.83) below]. We discuss the implications of the resulting PDF for data processing in Sec. 7.4. However it may turn out that $\tilde{\varepsilon} \lesssim \varepsilon$, which from Eqs. (4.68) and (4.69) will be the case if $\Omega_g \gtrsim 10^{-8}$. Even if $\Omega_g \ll 10^{-8}$, it may happen that the correlation coefficient between different detectors for residual gas noise in the beam tube will be small compared to unity, so that in the notation of Eq. (4.47), $S_n' \ll S_{\mathrm{gas}}$ and again $\tilde{\varepsilon} \lesssim \epsilon$. Alternatively, it may be possible to detect and take account of bursts of outgassing from the beam tube walls. More detailed discussions of the possible magnitude of intrasite correlated noise can be found in Ref. [17]. Because of the possibility that $\tilde{\varepsilon} \lesssim \varepsilon$, we now derive an approximate expression for $p_C(\Omega)$.

7.3 Information from intrasite correlations

To evaluate the expression (4.72) we first make a change of variables. Let $\hat{\mathcal{C}}$ be the matrix of correlation coefficients,

$$\hat{\mathcal{C}} = (\hat{\Sigma}^D)^{-1/2} \cdot \hat{\Sigma}^O \cdot (\hat{\Sigma}^D)^{-1/2}, \tag{4.73}$$

and similarly define matrices $\mathbf{N}$ and $\mathbf{G}$ by replacing $\hat{\Sigma}^O$ in Eq. (4.73) by Σ_n^D and $\Sigma_s(\Omega)^{\|}$, respectively. Also let

$$\mathcal{C} = (\Sigma_n^D)^{-1/2} \cdot \Sigma_n^O \cdot (\Sigma_n^D)^{-1/2}. \tag{4.74}$$

We assume that the volume element in Eq. (4.72) can be written as

$$p_{n,\|}^{(0)}(\Sigma_n^{\|})\, d\Sigma_n^{\|} \propto p_{\rm noise}(\Sigma_n^D)\, p_{\rm corr}(\mathcal{C})\, d\mathbf{N}\, d\mathcal{C}. \tag{4.75}$$

To leading order in $\tilde{\varepsilon}$ the cross term between $\delta\Sigma^D$ and $\delta\Sigma^O$ in the argument of the exponential in Eq. (4.72) vanishes, and so it becomes proportional to

$$\mathrm{tr}\left[\left(\mathbf{N} + \mathbf{G}^D - 1\right)^2 + \left(\mathbf{N}^{1/2} \cdot \mathcal{C} \cdot \mathbf{N}^{1/2} + \mathbf{G}^O - \hat{\mathcal{C}}\right)^2\right]. \tag{4.76}$$

Using the relations $k \gg 1$, $\hat{\mathcal{C}} \sim \tilde{\varepsilon} \ll 1$, $\mathbf{G} \sim \Omega_g/10^{-6} \ll 1$, and $|\mathcal{C}| \lesssim 1$, and assuming that the PDF $p_{\rm noise}(\Sigma_n^D)$ is slowly varying, we can approximately carry out the integral over $\mathbf{N}$. From Eqs. (4.72), (4.75), and (4.76), the result is

$$p_C(\Omega) \approx \mathcal{N}_2 \int d\mathcal{C}\; p_{\rm corr}(\mathcal{C})\; \exp \mathrm{tr}\left\{-\frac{k}{4}\left[\mathcal{C} + \mathbf{G}^O - \hat{\mathcal{C}}\right]^2\right\}, \tag{4.77}$$

where $\mathcal{N}_2$ is a constant. This expression is actually only a good approximation when $|\mathcal{C}| \ll 1$, but the integral (4.77) is dominated by values of $\mathcal{C}$ close to $\hat{\mathcal{C}} - \mathbf{G}^O$ which is $\ll 1$.

Now the behavior of the function (4.77) depends strongly on our *a priori* information about the correlation matrix $\mathcal{C}$. As in Eq. (4.60), this matrix will be approximately diagonal on a frequency basis:

$$\mathcal{C}_{aI,bJ} \approx \delta_{IJ}\, \mathcal{C}_{abI}, \tag{4.78}$$

where from Eq. (4.74),

$$\mathcal{C}_{abI} = \frac{S_n(f_I)_{ab}^O}{\sqrt{S_n(f_I)_{aa}\, S_n(f_I)_{bb}}}. \tag{4.79}$$

Since $\mathbf{S}_h(f)$ is positive definite, we have $|\mathcal{C}_{abI}| < 1$. Moreover, the variables $\mathcal{C}_{abI}$ will be real whenever

$$\langle n_a(t+\tau)\, n_b(t)\rangle = \langle n_a(t)\, n_b(t+\tau)\rangle \tag{4.80}$$

for all t and τ, and thus in particular they will be real if there are no sources of noise that preferentially excite one detector later than another one. If we assume that such sources of noise are negligible, then by inserting into Eq. (4.77) the PDF,

$$p_{\rm corr}(\mathcal{C}) = \delta(\mathrm{Im}\,\mathcal{C})\, p'_{\rm corr}(\mathrm{Re}\,\mathcal{C}), \tag{4.81}$$

we obtain an equation again of the form (4.77), but where C and $\hat{C}$ are now understood to be real. [A factor of $\exp\left[-k\,\mathrm{tr}\,(\mathrm{Im}\,\hat{C})^2/4\right]$ is absorbed into $\mathcal{N}_2$.]

Next we assume that our *a priori* information about the correlation coefficients C_{abI} is of the form $C_{\min} \le C_{abI} \le C_{\max}$, so that we can take [36]

$$p_{\mathrm{corr}}(C)dC = \prod_{I=1}^{n} \prod_{a<b} \Theta(C_{\max} - C_{abI})\,\Theta(C_{abI} - C_{\min})\,dC_{abI}, \tag{4.82}$$

where Θ is the step function. Using Eqs. (4.77) and (4.82) and the replacement $\mathrm{tr} \to 2\sum_{I=1}^{n}$ [cf. Eq. (4.63)], gives

$$p_C(\Omega) \propto \prod_{I=1}^{n} \prod_{a<b} \left[\mathrm{erf}\left(C_{\max}\sqrt{k} - \beta_{abI}\right) - \mathrm{erf}\left(C_{\min}\sqrt{k} - \beta_{abI}\right)\right], \tag{4.83}$$

where

$$\beta_{abI} = \sqrt{k}\left(\hat{C}_{abI} - G^{o}_{abI}\right). \tag{4.84}$$

If we define $\hat{\mathrm{S}}_h(f)$ to be twice the Fourier transform of the estimator (4.56) as in Eq. (4.6), and put

$$\hat{\Omega}_{abI} = \frac{5\pi f^3}{4\rho_c}\,\hat{S}_h(f_I)^{o}_{ab}, \tag{4.85}$$

then we find from Eq. (4.17) that

$$\begin{aligned}\beta_{abI} &= \frac{4\rho_c}{5\pi f^3}\sqrt{\frac{k}{\hat{S}_h(f_I)_{aa}\hat{S}_h(f_I)_{bb}}}\left(\hat{\Omega}_{abI} - \Omega_I\right) \\ &\approx \frac{\sqrt{k}}{10^{-6}}\left(\hat{\Omega}_{abI} - \Omega_I\right),\end{aligned} \tag{4.86}$$

where $\Omega_I \equiv \Omega_g(f_I)$.

We now discuss the content of Eqs. (4.83)–(4.86). If we make no assumption about the amount of correlated noise present, and so take $C_{\min} = -1$ and $C_{\max} = 1$, then we see using $k \approx 10^5$ that $p_C(\Omega)$ is roughly constant for $0 \le \Omega_I \lesssim 10^{-6}$. Thus we obtain little information. More information about the correlated noise needs to be input in order to constrain the strength of the SB. One assumption which may be valid is that

$$S_n(f)_{ab} \ge 0, \tag{4.87}$$

which can be enforced by setting $C_{\min} = 0$ in Eq. (4.82). Equation (4.87) will hold if there are no sources of noise $\hat{n}(t)$ which contribute an amount $+\hat{n}(t)$ to the output of one detector, and an amount $-\hat{n}(t)$ to the output of another. An example of such a source of noise could be a mode of vibration of a suspension system that

couples in a suitable way the vibrations of mirrors in two different interferometers. It may be a valid assumption that all such sources of noise will be negligible. In this case we can use in Eq. (4.83) the values $\mathcal{C}_{\min} = 0$ and $\mathcal{C}_{\max} = 1$. (The value chosen for $\mathcal{C}_{\max}$ is unimportant as long as $\mathcal{C}_{\max} \gg 1/\sqrt{k}$.) Then from Eq. (4.86) we see that $\beta_{abI} \ll \mathcal{C}_{\max}\sqrt{k}$ as $\hat{\Omega} \ll 10^{-6}$, and so, to a good approximation,

$$p_{\mathcal{C}}(\Omega) \propto \prod_{I=1}^{n} \prod_{a<b} \left[\frac{1}{2} - \operatorname{erf}(-\beta_{abI})\right]. \tag{4.88}$$

Essentially this PDF gives an upper bound on each $\Omega_I = \Omega_g(f_I)$ of $\Omega_{I,\max} = \min_{a,b} \hat{\Omega}_{abI}$, which is of the order of $\sim 10^{-6}\tilde{\varepsilon}$ if $\Omega_g \lesssim 10^{-8}$. As already mentioned, this upper bound will be much worse than that obtained from intersite correlations, unless the dimensionless correlation coefficient $\tilde{\varepsilon}$ is $\lesssim 10^{-4}$. Moreover, the bound is only obtained by making the specific assumptions (4.80) and (4.87) about sources of correlated noise at the individual sites. For these reasons, in the following subsection on data analysis we consider only intersite correlations and take $p_{\mathcal{C}}(\Omega) \approx$ const.

We now show in more detail that very little information about the SB is obtained if the assumptions (4.80) and (4.87) are dropped. As a simple model, we consider the opposite extreme of assuming equal probability for all relative phases in the contributions to the outputs of different detectors from correlated sources of noise. Thus, we take the *a priori* PDF to be of the form [36]

$$p_{\text{corr}}(\mathcal{C})d\mathcal{C} = \prod_{I=1}^{n} \prod_{a<b} \exp\left[-\frac{|\mathcal{C}_{abI}|^2}{2\mathcal{C}_{\max}^2}\right] d(\operatorname{Re}\mathcal{C}_{abI})\, d(\operatorname{Im}\mathcal{C}_{abI}), \tag{4.89}$$

where $\mathcal{C}_{\max}$ is the *a priori* maximum correlation. Then from Eq. (4.77) we obtain

$$p_{\mathcal{C}}(\Omega) \propto \prod_{I=1}^{n} \prod_{a<b} \exp\left[-\frac{(\operatorname{Re}\beta_{abI})^2}{1 + k\mathcal{C}_{\max}^2}\right]. \tag{4.90}$$

This function is of the form of Eq. (4.92) below, where, from Eq. (4.86),

$$\sigma_I \approx 10^{-6}\sqrt{\frac{1 + k\,\mathcal{C}_{\max}^2}{k}}. \tag{4.91}$$

This is roughly the minimum detectable value of Ω_g that can be detected in a bandwidth of $\sim 1/\tau_c$. Thus, the function (4.90) is qualitatively similar to the PDF (4.92) obtained from intersite correlations, with the simple change that the minimum detectable value of Ω_g in any frequency band is increased by a factor of $\sqrt{1 + k\,\mathcal{C}_{\max}^2}$. If we take $\mathcal{C}_{\max}$ to be of order unity and so make no assumption

about the amount of correlated noise present, then the upper bounds on Ω_g from intrasite correlations will be worse by a factor of $\sqrt{k} \sim 300$ than those obtained from intersite correlations. Only if $C_{\max} \approx 1/\sqrt{k}$ will the two be comparable. However, because of the possibility of weak, unknown sources of noise, it is probably inappropriate to make such a strong assumption.

7.4 Implications for data processing

The distribution (4.71) with $p_C = \text{const}$ is of the form

$$p(\Omega_I) = \mathcal{N}_3\, p_s^{(0)}(\Omega_I)\, \exp\left\{-\sum_{I=1}^{n} \frac{(\Omega_I - \hat{\Omega}_I)^2}{2\sigma_I^2}\right\}, \tag{4.92}$$

where $\Omega_I = \Omega_g(f_I = I/\tau_c)$, because the matrices are all approximately diagonal in frequency. Using Eq. (4.15), we find that the argument of the exponential in Eq. (4.92) becomes

$$-\frac{\hat{\tau}}{2}\int_0^\infty df\, \mathrm{tr}\left\{\left[\hat{\mathbf{S}}_h^{-1\parallel}\cdot\left(\Omega\bar{\gamma}^\perp - \hat{\mathbf{S}}_h^\perp\right)\right]^2\right\}, \tag{4.93}$$

where $\bar{\gamma}_{ab} = 4\rho_c\gamma_{ab}/(5\pi f^3)$. Hence we find, using $\int_0^\infty df \to (1/\tau_c)\sum_I$, that

$$\frac{1}{\sigma_I^2} = k\,\mathrm{tr}\left[\left(\hat{\mathbf{S}}_h^{\parallel\,-1}(f_I)\cdot\bar{\gamma}\right)^2\right], \tag{4.94}$$

and

$$\hat{\Omega}_I = k\,\sigma_I^2\,\mathrm{tr}\left[\hat{\mathbf{S}}_h^{\parallel\,-1}(f_I)\cdot\bar{\gamma}\cdot\hat{\mathbf{S}}_h^{\parallel\,-1}(f_I)\cdot\hat{\mathbf{S}}_h^\perp(f_I)\right]. \tag{4.95}$$

One would like to summarize the information contained in Eq. (4.92) by calculating some kind of signal-to-noise ratio. There are various, inequivalent ways of doing this. For example, one could calculate probability distributions for the quantities $\Omega_{\max} = \max_I \Omega_I$ or $\bar{\Omega} = \sum_I \Omega_I/n$; it is clear that the SNR for $\Omega_{\max}$ would be worse than that for $\bar{\Omega}$. What we shall in fact do is calculate the probability distribution $p(\Omega|\Omega_I = \Omega)$ of Ω assuming that $\Omega_1 = \cdots = \Omega_n = \Omega$, as this is the easiest to calculate. Now if we ignore the *a priori* information represented by $p_s^{(0)}$ in Eq. (4.92) [so that $p(\Omega_I)$ is a multivariate Gaussian], then this is equivalent to calculating the PDF for the weighted average

$$\bar{\Omega}_1 = \sum_I \frac{\Omega_I}{\sigma_I^2} \Big/ \sum_I \frac{1}{\sigma_I^2}. \tag{4.96}$$

However when we include the information contained in $p_s^{(0)}$, the main effect is to truncate and renormalize [18] the PDF's for each Ω_I, since all the Ω's must

be positive. Hence a simple interpretation of the PDF $p(\Omega|\Omega_I = \Omega)$ and the corresponding SNR in terms of the average (4.96) not possible. Nevertheless we suspect that $p(\Omega|\Omega_I = \Omega)$ approximately represents the probability distribution of some type of average of $\Omega_g(f)$.

We now insert the assumption $\Omega_I = \Omega$ (const) into Eq. (4.92), which gives a PDF of the form

$$p(\Omega \,|\, \Omega_I = \Omega) \propto \Theta(\Omega) \exp\left[\frac{(\Omega - \Omega_M)^2}{(2\sigma^2)}\right]. \tag{4.97}$$

Here the quantity

$$\Omega_M = \sum_I \frac{\hat{\Omega}_I}{\sigma_I^2} \Big/ \sum_I \frac{1}{\sigma_I^2} \tag{4.98}$$

is the statistic that should be calculated to estimate the value of Ω. We obtain

$$\Omega_M \propto \int_0^\infty df \,\mathrm{tr}\, \left[\hat{\mathbf{S}}_h^{\perp} \cdot \hat{\mathbf{S}}_h^{-1\parallel} \cdot \bar{\gamma}^{\perp} \cdot \hat{\mathbf{S}}_h^{-1\parallel}\right]. \tag{4.99}$$

This can be written in the time domain as

$$\Omega_M \propto \int dt \int d\tau \, H_a(t+\tau) L_{ab}(\tau) H_b(t), \tag{4.100}$$

where $\tilde{\mathrm{L}}(f) = \gamma(f)^{\perp}$, and

$$\tilde{\mathbf{H}}(f) = \frac{1}{f^{3/2}} \hat{\mathbf{S}}_h^{-1}(f)^{\parallel} \cdot \tilde{\mathbf{h}}(f). \tag{4.101}$$

The functions $L_{ab}(\tau)$ are the sliding delay functions discussed in Sec. 3. Note that Ω_M is constructed from the measured correlations in the following way: the intrasite correlations are used only to estimate the detector noise matrix $\mathbf{S}_n^{\parallel}$, and then this noise matrix is used together with the measured inter-site correlations to estimate Ω_M. However, the matrix $\mathbf{S}_n^{\parallel}$ will typically be approximately diagonal, and so neglecting the intrasite correlations will give only a negligible error.

Finally the intersite SNR Ω_M/σ can be obtained from Eq. (4.93) [18]. If we assume that $\hat{\mathbf{S}}_h(f)^{\perp} = \Omega_{\mathrm{real}}(f)\bar{\gamma}(f)^{\perp}$, so that all the intersite correlations we measure come from the SB, then the SNR takes the form

$$\frac{S^2}{N^2} = \hat{\tau}\left(\frac{4\rho_c}{5\pi}\right)^2 \int_0^\infty df \, \frac{\Omega_{\mathrm{real}}(f)^2}{f^6} \,\mathrm{tr}\left[\left(\gamma(f)^{\perp} \cdot \hat{\mathbf{S}}_h^{-1}(f)^{\parallel}\right)^2\right]. \tag{4.102}$$

Using the fact that the matrix $\gamma(f)_{ab}$ will be constant on each subblock corresponding to two detector sites, one can derive Eqs. (4.28) and (4.29) from Eq. (4.102).

APPENDIX B: CALCULATION OF THE OVERLAP REDUCTION FUNCTION

The ath detector is characterized by its position $\mathbf{x}_a$ and by the tensor $\mathbf{d} = (\mathbf{u} \otimes \mathbf{u} - \mathbf{v} \otimes \mathbf{v})/2$, where $\mathbf{u}$ and $\mathbf{v}$ are unit vectors in the direction of its arms. In terms of these quantities, the overlap reduction function is given, from Eq. (4.16), by

$$\gamma_{ab}(f) = \frac{5}{8\pi} \sum_A \int d^2\Omega \, (\mathbf{d}_a : \mathbf{e}^{A,\mathbf{n}}) \, (\mathbf{d}_b : \mathbf{e}^{A,\mathbf{n}}) \times \exp\left[2\pi i f \mathbf{n} \cdot (\mathbf{x}_a - \mathbf{x}_b)\right]. \tag{4.103}$$

If we write $\mathbf{x}_a - \mathbf{x}_b = d\,\mathbf{m}$ where $\mathbf{m}$ is a unit vector, and put $\alpha = 2\pi f d$ (in units in which $c = 1$), then we obtain

$$\gamma_{ab}(f) = d_{a\,ij} \, \Gamma_{ijkl}(\alpha, \mathbf{m}) \, d_{b\,kl}, \tag{4.104}$$

where

$$\Gamma_{ijkl}(\alpha, \mathbf{m}) = \frac{5}{8\pi} \sum_A \int d^2\Omega \, e^{A,\mathbf{n}}_{ij} e^{A,\mathbf{n}}_{kl} \, e^{i\alpha \mathbf{n}\cdot\mathbf{m}}. \tag{4.105}$$

This integral can be evaluated by the standard method of writing down the most general possible answer:

$$\begin{aligned} \Gamma_{ijkl}(\ \alpha\ , \mathbf{m}) &= A(\alpha)\delta_{ij}\delta_{kl} + B(\alpha)\left[\delta_{ik}\delta_{jl} + \delta_{il}\delta_{jk}\right] \\ &+ C(\alpha)\left[\delta_{ij}m_k m_l + \delta_{kl}m_i m_j\right] + D(\alpha) m_i m_j m_k m_l \\ &+ E(\alpha)\left[\delta_{ik}m_j m_l + \ldots + \delta_{jl}m_i m_k\right]. \end{aligned} \tag{4.106}$$

One might expect to have to include a term proportional to $w_{il}w_{jk} + w_{ik}w_{jl}$ where $w_{ij} = \varepsilon_{ijk}m^k$, but in fact this tensor is a linear combination of the five tensors included above. Contracting Eq. (4.106) with the five different tensorial expressions that appear on its right-hand side yields a system of linear equations for $A(\alpha) \cdots E(\alpha)$ which involves scalar integrals that are straightforward to evaluate. Solving these equations and substituting the results back into Eqs. (4.104) and (4.106) gives

$$\begin{aligned} \gamma_{ab}(f) \ &= \ \rho_1(\alpha)\mathbf{d}_a : \mathbf{d}_b + \rho_2(\alpha)\mathbf{m}\cdot\mathbf{d}_a\cdot\mathbf{d}_b\cdot\mathbf{m} \\ &\quad + \rho_3(\alpha)(\mathbf{m}\cdot\mathbf{d}_a\cdot\mathbf{m})(\mathbf{m}\cdot\mathbf{d}_b\cdot\mathbf{m}). \end{aligned} \tag{4.107}$$

The functions $\rho_j(\alpha)$ are linear combinations of the spherical Bessel functions:

$$\rho_1(\alpha) = 5j_0(\alpha) - 2j_1(\alpha)/\alpha + 5j_2(\alpha)/\alpha^2, \tag{4.108}$$

$$\rho_2(\alpha) = -10j_0(\alpha) + 40j_1(\alpha)/\alpha - 50j_2(\alpha)/\alpha^2, \tag{4.109}$$

and

$$\rho_3(\alpha) = 5j_0(\alpha)/2 - 25j_1(\alpha)/\alpha + 175j_2(\alpha)/(2\alpha^2). \tag{4.110}$$

The result (4.107) applies to any gravitational wave antennas, such as interferometers with nonperpendicular arms and arbitrary orientations, or resonant bar antennas. The special case of two resonant bar antennas, for which each $\mathbf{d}_a \propto 1 - 3\mathbf{n}_a \otimes \mathbf{n}_a$ for some vector $\mathbf{n}_a$, has been previously derived by Michelson [16]. As can be seen from Fig. 4.10, the first term in Eq. (4.107) dominates for $\alpha \lesssim 1$ (unless $\mathbf{d}_a : \mathbf{d}_b \approx 0$). A similar simplification applies for $\alpha \gg 1$: we have

$$\gamma_{ab}(f) = 5j_0(\alpha)\, \mathbf{d}_a^\perp : \mathbf{d}_b^\perp + \mathcal{O}(\alpha^{-2}), \tag{4.111}$$

where $\mathbf{d}_a^\perp$ denotes the trace-free part of the projection $(\delta_{ik} - m_i m_k)(\delta_{jl} - m_j m_l) d_{a\,kl}$ of $\mathbf{d}_a$ perpendicular to $\mathbf{m}$. The fact that $\gamma(f)$ does not depend on the components of $\mathbf{d}_a$ and $\mathbf{d}_b$ parallel to $\mathbf{m}$ is due to the fact that the cross correlation at $\alpha \gg 1$ is dominated by modes whose wave vectors are nearly parallel to $\mathbf{m}$, as discussed in Sec. 4.2.

To apply Eq. (4.107) to terrestrial detectors, we need to choose a coordinate system and express the tensors $\mathbf{d}_1$, $\mathbf{d}_2$ and $\mathbf{m}$ in terms of the angles δ, Δ, and β defined in Sec. 4. A convenient choice is to take the detectors to be located at $\theta = \pi/2 \pm \beta/2$ and $\phi = 0$, where r, θ, ϕ are spherical polar coordinates with origin at the Earth's center, so that the unit vector in the direction joining the detectors is $\mathbf{m} = \mathbf{e}_z$. If we let $\mathbf{e}_{\hat{r}}$, $\mathbf{e}_{\hat{\theta}}$, and $\mathbf{e}_{\hat{\phi}}$ be the usual basis of orthonormal vectors, and define

$$\begin{aligned} \mathbf{d}(\sigma, \theta, \phi) \;=\; & \sin(2\sigma)(\mathbf{e}_{\hat{\theta}} \otimes \mathbf{e}_{\hat{\theta}} - \mathbf{e}_{\hat{\phi}} \otimes \mathbf{e}_{\hat{\phi}})/2 \\ & - \cos(2\sigma)(\mathbf{e}_{\hat{\theta}} \otimes \mathbf{e}_{\hat{\phi}} + \mathbf{e}_{\hat{\phi}} \otimes \mathbf{e}_{\hat{\theta}})/2, \end{aligned} \tag{4.112}$$

then we can take $\mathbf{d}_1 = \mathbf{d}(\Delta + \delta, \pi/2 + \beta/2, 0)$ and $\mathbf{d}_2 = \mathbf{d}(\Delta - \delta, \pi/2 - \beta/2, 0)$. Inserting these expressions into the formula (4.107) yields, after some manipulation, the result (4.31), where the functions $g_j(\alpha)$ are

$$g_1(\alpha) = \frac{5}{16} f(\alpha) \cdot (-9, -6, 9, 3, 1), \tag{4.113}$$

$$g_2(\alpha) = \frac{5}{16} f(\alpha) \cdot (45, 6, -45, 9, 3), \tag{4.114}$$

$$g_3(\alpha) = \frac{5}{4} f(\alpha) \cdot (15, -4, -15, 9, -1), \tag{4.115}$$

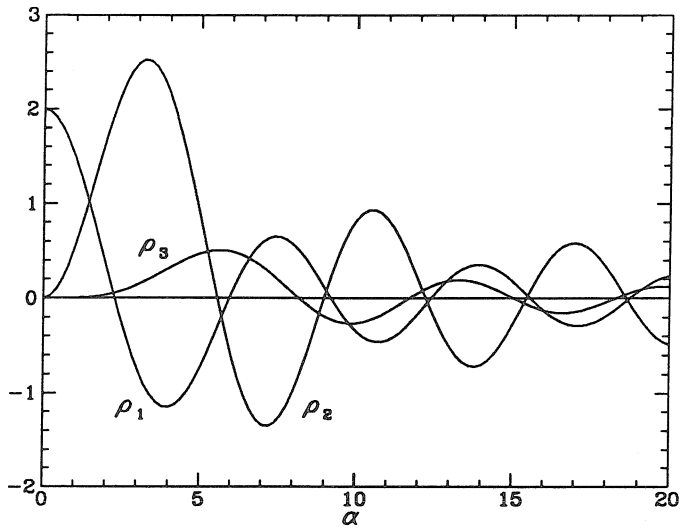

Figure 4.10: A graph of the functions $\rho_1(\alpha)$, $\rho_2(\alpha)$, and $\rho_3(\alpha)$.

and

$$f(\alpha) = (\alpha\cos\alpha, \alpha^3\cos\alpha, \sin\alpha, \alpha^2\sin\alpha, \alpha^4\sin\alpha)/\alpha^5. \tag{4.116}$$

From Eq. (4.31) it is straightforward to evaluate the Fourier transform of the overlap reduction function, which gives the sliding delay function discussed in Sec. 3,

$$L_{ab}(\tau) = \int_{-\infty}^{\infty} df\, e^{-2\pi i f\tau}\gamma_{ab}(f). \tag{4.117}$$

The function $L_{ab}(\tau)$ vanishes for $|\tau| > d = 2r_E\sin(\beta/2)$. For $|\tau| < d$, $L_{ab}(\tau)$ is given by Eqs. (4.31)–(4.33), where the functions g_j are now

$$g_1(\tau) = \frac{5}{32d}\left(1 + 3v + \frac{3}{8}v^2\right), \tag{4.118}$$

$$g_2(\tau) = \frac{5}{32d}\left(3 - 3v - \frac{15}{8}v^2\right), \tag{4.119}$$

$$g_3(\tau) = \frac{5}{32d}\left(-4 + 8v - \frac{5}{2}v^2\right), \tag{4.120}$$

and $v = 1 - \tau^2/d^2$.

Bibliography

[1] A. Abrmovici, W.E. Althouse, R.W.P. Drever, Y. Gürsel, S. Kawamura, F.J. Raab, D. Shoemaker, L. Sievers, R.E. Spero, K.S. Thorne, R.E. Vogt, R. Weiss, S.E. Whitcomb, and M.E. Zucker, Science **256**, 325 (1992).

[2] C. Bradaschia *et al.*, Nucl. Instrum. Methods **A 289**, 518 (1990); also in *Gravitation 1990*, Proceedings of the Banff Summer Institute, Banff, Alberta, 1990, edited by R. Mann and P. Wesson (World Scientific, Singapore, 1991).

[3] *The Detection of Gravitational Waves*, edited by D.G. Blair (Cambridge University Press, Cambridge, England, 1991).

[4] L.A. Rosi and R.L. Zimmerman, Astrophys. Space. Sci. **45**, 447 (1976); D. Hils, P.L. Bender, and R.F. Webbink, Astrophys. J. **360**, 75 (1990).

[5] T. Vachaspati and A. Vilenkin, Phys. Rev. D **31**, 3502 (1985); F.R. Bouchet and D.B. Bennett, *ibid.* 720 (1990).

[6] C.J. Hogan, Mon. Not. R. Astron. Soc. **218**, 629 (1986); M.S. Turner and F. Wilczek, Phys. Rev. Lett. **65**, 3080 (1990); A. Kosowsky, M.S. Turner, and R. Watkins, Phys. Rev. D **45**, 4514 (1992), also Phys. Rev. Lett. **69**, 2026 (1992); A. Kosowsky and M.S. Turner, Phys. Rev. D **47**, 4372 (1993); M. Kamionkowski, A. Kosowsky, and M.S. Turner (unpublished).

[7] L.P. Grishchuk, Zh. Eksp. Teor. Fiz. **67**, 825 (1974) [Sov. Phys. JETP **40**, 409 (1975)]; E.W. Kolb and M.S. Turner, *The Early Universe* (Addison-Wesley, Redwood, CA, 1990), and references therein.

[8] L. Abbott and M. Wise, Nucl. Phys. **B224**, 541 (1984).

[9] L.M. Krauss and M. White, Phys. Rev. Lett. **69**, 869 (1992).

[10] K.S. Thorne, in *300 Years of Gravitation*, edited by S.W. Hawking and W. Israel (Cambridge University Press, Cambridge, England, 1987), pp. 330–458.

[11] K.S. Thorne, in *Recent Advances in General Relativity*, edited by A. Janis and J. Porter (Birkhauser, Boston, 1991).

[12] N.L. Christensen, Ph. D. thesis, Massachusetts Institute of Technology, 1990 (unpublished).

[13] L.P. Grishchuk and M. Solokhin, Phys. Rev. D **43**, 2566 (1991).

[14] A.A. Starobinsky, Pis'ma Astron. Zh. **11**, 223 (1985) [Sov. Astr. Lett. **11**, 133 (1985)].

[15] R.L. Davies *et al.*, Phys. Rev. Lett. **69**, 1856 (1992).

[16] R.F. Michelson, Mon. Not. R. Astron. Soc. **227**, 933 (1987).

[17] N.L. Christensen, Phys. Rev. D **46**, 5250, (1992).

[18] The phrase *signal-to-noise ratio* usually means the following: From the measured data one can compute a number Y which has to a good approximation a Gaussian statistical distribution, and SNR is just the expected value of Y divided by the square root of its variance. In this paper we frequently encounter quantities Y whose distributions are *truncated* Gaussians:

$$p_Y(y) = \frac{N}{\sqrt{2\pi}\sigma} \exp\left[\frac{(y-\mu)^2}{2\sigma^2}\right] \Theta(y),$$

where Θ is the step function, and the normalization factor N depends on μ/σ. In this case we still use SNR to mean just μ/σ. The use of truncated Gaussian distributions affects the constants appearing in Eqs. (4.38) and (4.49) (where we assume $\mu \ll \sigma$).

[19] K.S. Thorne (private communication).

[20] The coefficients $s_{A,\mathrm{n}}(f)$ are related to the variables $\tilde{h}_A$ of Ref. [17] by $s_{A,\mathrm{n}}(f) = 2\pi^2 f \tilde{h}_A(\mathrm{n}, 2\pi f)$; Eqs. (4.11) and (4.12) correct Eq. (4.1) of that reference.

[21] For relic gravitational waves from the big bang, Grishchuk [13] has shown that Eq. (4.12) must be replaced by

$$\langle\, s_{A,\mathrm{n}}(f)\, s_{B,\mathrm{m}}(f')\,\rangle = \delta_{AB}\, \delta^2(\mathrm{n},\mathrm{m})\, \delta(f-f') D(f),$$

for $f, f' > 0$, where $D(f)$ is a complex function satisfying $|D(f)| \approx$ the corresponding term in Eq. (4.11). This is because the relic background is phase

squeezed. However, Eq. (4.12) remains an adequate approximation for our purposes, since $D(f)$ is a rapidly oscillating function of f with a period of order H_0, the Hubble constant [13]. Observations of the SB by the methods discussed in this paper will have a frequency resolution $\gg H_0 \sim 10^{-18}$ Hz, and consequently will "average out" the effects of the phase squeezing.

[22] R.L. Forward, Phys. Rev. D **17**, 379 (1978).

[23] Equations (4.15) and (4.16) are essentially equivalent to Eqs. (4.5) and (4.6) of Ref. [17], and can be obtained from those by (i) taking a Fourier transform, (ii) dividing by the square of the transfer function $|\tilde{B}(f)|$ to convert from correlations of light intensities to correlations of strain amplitudes, (iii) replacing the cosine with a complex exponential, and (iv) correcting for the difference in normalization convention for $\gamma(f)$ between Ref. [17] and this paper.

[24] It is not quite true that the contributions $\mathbf{S}_n(f)$ and $\mathbf{S}_s(f)$ are indistinguishable. The structure of the matrix $\mathbf{S}_s(f)$ at a fixed frequency is tightly constrained by Eq. (4.15), so the whole (off-diagonal) matrix can be determined from just one element. Moreover all the off-diagonal elements must be real. If we measure the off-diagonal part of $\mathbf{S}_h(f)$ to be nonzero and it does not have the form (4.15), then we know that we are seeing noise that is not due to the SB. This fact will be helpful in identifying noise in intersite correlations (if there is any intersite correlated noise). It will not be as useful for identifying noise in intrasite correlations, because in this case the constraint is just that all the off-diagonal elements of $\mathbf{S}_A(f)$ be equal and positive, and this is likely to be satisfied by some sources of correlated noise.

[25] These designations must not be taken too literally, however, since for $\beta = 180°$, the angle Δ is what would normally be called the relative rotation; see Eq. (4.112).

[26] Using Eq. (4.107) and the fact that $\rho_1(0) = \rho_2(0) = 0$, we see that for *any* symmetric traceless tensors $\mathbf{e}_1$ and $\mathbf{e}_2$, the metric perturbation $\mathbf{h}(\mathbf{x}, t)$ due to the SB satisfies

$$\langle \mathbf{e}_1 : \mathbf{h}(\mathbf{0}, t)\ \mathbf{e}_2 : \mathbf{h}(\mathbf{0}, t') \rangle \propto \mathbf{e}_1 : \mathbf{e}_2.$$

This is a precise expression of the fact that orthogonal components of the strain tensor at a fixed point in space are statistically independent.

[27] LIGO team (private communication).

[28] S. Whitcomb (private communication).

[29] B.J. Meers, Phys. Rev. D **38**, 2317 (1988); K.A. Strain and B.J. Meers, Phys. Rev. Lett. **66**, 1391 (1991); A. Krolak, J.A. Lobo, and B.J. Meers Phys. Rev. D **43**, 2470 (1991).

[30] L.A. Wainstein and V.D. Zubakov, *Extraction of Signals from Noise* (Dover Publications, Inc., New York, 1962).

[31] C.W. Helstrom, *Statistical Theory of Signal Detection*, 2nd ed. (Pergamon Press, New York, 1968).

[32] H. Cramer, *Mathematical Methods of Statistics* (Princeton University Press, Princeton, 1946).

[33] If the condition (4.52) were not valid, one could still in principle integrate over $\Omega_g^>(f)$ to derive the reduced PDF for $\Omega_g^<(f)$ [in the notation of Eq. (4.54)]. However, in this case the CFR limit need not apply.

[34] A. Gillespie and F. Rabb, LIGO Report No. 93-2 (unpublished).

[35] There will be corrections due to aliasing which can be made small by increasing τ_c by a factor of a few, so that $\mathbb{C}_h(\tau) \approx 0$ for $|\tau| > \tau_c/(\text{a few})$.

[36] Strictly speaking $p_{\text{corr}}(\mathcal{C})$ should have support only on positive definite matrices $\mathcal{C}$. However, this will be approximately true if $1/\mathcal{C}_{\max} + 1 \geq$ (number of detectors per site).

Chapter 5

Gravitational waves from merging compact binaries: How accurately can the binary's parameters be extracted from the inspiral waveform? [Co-authored with Curt Cutler]

(submitted to Phys. Rev. D.)

Abstract

The most promising source of gravitational waves for the planned kilometer-size laser-interferometer detectors LIGO and VIRGO are merging compact binaries, i.e., neutron star/neutron star (NS/NS), neutron star/black hole (NS/BH), and black hole/black-hole (BH/BH) binaries. We investigate how accurately the distance to the source and the masses and spins of the two bodies will be measured from the inspiral gravity-wave signals by the three detector LIGO/VIRGO network using "advanced detectors" (those present a few years after initial operation).

The large number of cycles in the observable waveform increase our sensitivity to those parameters that affect the inspiral rate, and thereby the evolution of the waveform's phase. These parameters are thus measured much more accurately than parameters which affect the waveform's polarization or amplitude. To lowest order in a post-Newtonian expansion, the evolution of the waveform's phase depends only on the combination $\mathcal{M} \equiv (M_1 M_2)^{3/5}(M_1 + M_2)^{-1/5}$ of the masses M_1 and M_2 of the two bodies, which is known as the "chirp mass." To post-1-Newtonian order, the waveform's phase also depends sensitively on the binary's reduced mass $\mu \equiv M_1 M_2/(M_1 + M_2)$, allowing, in principle, a measurement of both M_1 and M_2 with high accuracy. We show that the principal obstruction to measuring M_1 and M_2 is the post-1.5-Newtonian effect of the bodies' spins on the waveform's phase, which can mimic the effects that allow μ to be determined.

The chirp mass is measurable with an accuracy $\Delta\mathcal{M}/\mathcal{M} \approx 0.1\% - 1\%$. Although this is a remarkably small error bar, it is ~ 10 times larger than previous estimates of $\Delta\mathcal{M}/\mathcal{M}$ which neglected post-Newtonian effects. The reduced mass is measurable to $\sim 10\% - 15\%$ for NS/NS and NS/BH binaries, and $\sim 50\%$ for BH/BH binaries (assuming $10M_\odot$ BH's). Measurements of the masses and spins are strongly correlated; there is a combination of μ and the spin angular momenta that is measured to within $\sim 1\%$. Moreover, *if* both spins were somehow known to be small ($\lesssim 0.01M_1^2$ and $\lesssim 0.01M_2^2$, respectively), then μ could be determined to within $\sim 1\%$.

Finally, building on earlier work of Marković, we derive an approximate, analytic expression for the accuracy ΔD of measurements of the distance D to the binary, for an arbitrary network of detectors. This expression is accurate to linear order in $1/\rho$, where ρ is the signal-to-noise ratio. We also show that, contrary to previous expectations, contributions to $\Delta D/D$ that are nonlinear in $1/\rho$ are significant, and we develop an approximation scheme for including the dominant of these non-linear effects. Using a Monte-Carlo simulation, we estimate that dis-

tance measurement accuracies will be $\leq 15\%$ for $\sim 8\%$ of the detected signals, and $\leq 30\%$ for $\sim 60\%$ of the signals, for the LIGO/VIRGO 3-detector network.

1 INTRODUCTION

Neutron star-neutron star (NS-NS) binaries with orbital periods of less than half a day will spiral together and merge in less than a Hubble time, due to gravitational radiation reaction. Three such short-period NS-NS binaries have been observed in our galaxy; when extrapolated to the rest of the universe these observations result in an estimated NS-NS merger rate in the universe of $\sim 10^2$ yr^{-1}Gpc^{-3} [1, 2]. A strong gravitational wave signal is emitted during the last few minutes of inspiral, before the tidal-disruption/coalescence stage begins. If the Laser Interferometer Gravitational Wave Observatory (LIGO) [3], and its French-Italian counterpart VIRGO [4], achieve the so-called "advanced detector" sensitivity level of Ref. [3], then they will detect gravitational waves from the last few minutes of NS-NS inspirals out to distances of order ~ 1 Gpc [3]. Hence, event rates of order 10^2 yr^{-1} may be achieved. While there is no direct observational evidence relevant to the merger rates for neutron star-black hole (NS-BH) and black hole-black hole (BH-BH) binaries, arguments based on progenitor evolution scenarios suggest that these merger rates may also be on the order of 10^2 yr^{-1}Gpc^{-3} [2, 5]. The merger of two $10M_\odot$ black holes would be detectable by LIGO/VIRGO out to cosmological distances at redshifts of $\sim 2-3$.

The gravitational waveform arriving at the Earth depends on the inspiraling bodies' masses and spins, the orientation of their orbit when the waves enter the LIGO waveband, the distance to the binary, and the binary's location on the sky. By comparing the observed waveforms with theoretically derived templates, the observers will extract these parameters to a level of accuracy that is determined by the noise in the detectors, and by the detectors' relative positions and orientations. The output of a single detector is sufficient information to determine the masses of the two bodies, but not their distance or their location on the sky. By combining the outputs of the three LIGO/VIRGO detectors, it should be possible to determine the location of the binary on the sky to within ~one degree [6, 7], and the distance to the binary to within $\sim 30\%$.

There are many potential applications of such measurements, as has been emphasized by Schutz [6]. For example, coalescing binaries are potentially very useful standard candles for astronomical distance measurements — it has been estimated that from $\sim 10^2$ detected NS-NS events it will be possible to determine the Hubble constant H_0 to within $\sim 10\%$ [8, 9, 10, 11]. It may also be possible to measure NS radii, and thus constrain the NS equation of state, by measuring the frequency

at which the tidal disruption of the neutron star causes the waves to shut off [8]. And from gravity-wave observations of the final coalescence of two black holes, there may follow new insights into gravitational dynamics in the highly nonlinear regime. The effectiveness of these and other applications depends on the accuracy with which parameters such as the distance to the binary and the masses of its two components can be measured.

The purpose of this paper is to estimate the limits on measurement accuracies that arise from sources of noise that are intrinsic to the detectors. These sources of noise include, for example, thermal vibrations in the interferometers' suspended test masses, and randomness in the arrival times of individual photons at the interferometers' mirrors (photon shot-noise), which simulate in the interferometers' output the effects of gravitational waves [3]. Intrinsic detector noise is expected to be the dominant source of error in the determination of coalescing binary parameters, in part because gravitational waves interact very weakly with matter through which they pass, so that processes such as absorbtion, scattering and redenning are negligible [12]. Other possible sources of error which we do not consider here include (i) systematic errors due to insufficiently accurate theoretical modeling of the gravitational waveforms, which will be important primarily for mass and spin measurements [8, 13]; and (ii) amplification/deamplification of the wave amplitudes by gravitational lensing effects, which will be important primarily for distance measurements. See Marković [9] for a detailed discussion of this issue.

Many of our conclusions have already been summarized in Cutler et al. [8]. Initial measurement accuracy analyses have been carried out by Finn and Chernoff [14], and by Jaranowski and Krolak [15], using a simplified, "Newtonian" model of the waveform. Newtonian waveforms are adequate for predicting the accuracy of distance measurements , but they do not allow one to calculate how accurately the individual masses can be measured, as we explain below. For this purpose, one must include post-Newtonian corrections to the waveform.

Much of our work was guided by the following sequence of considerations. These considerations introduce some of the issues addressed in this paper, motivate a number of approximations that we make in our analysis, and give a preview of our main conclusions.

First, coalescing binaries are very "clean" sources of gravitational waves: the waveform is determined to high accuracy by a relatively small number of parameters [6]. These parameters are the source's location, orientation, and time of coalescence, as well as the bodies' masses and spin angular momenta. Various

other complicating physical effects, not described by these parameters, are unimportant. We can generally assume, for instance, that the orbits are circular. This is because radiation reaction causes the orbit's eccentricity ε to decrease during the inspiral, according to $\varepsilon^2 \propto P^{19/9}$, where P is the orbital period [16]. (The effect of a small eccentricity on the phase of the waveform scales like ε^2.) The emitted gravitational waves are in the frequency band accessible to LIGO only for the last few minutes of inspiral, when $P < 0.2\,\mathrm{sec}$. Thus a binary born with ε of order unity and $P > 1$ hour will have $\varepsilon^2 < 10^{-9}$ by the time it becomes "visible" to LIGO [17]. Also, tidal interactions between the bodies have been shown to be negligible [18, 19] (except for the last few orbits), so for our purposes the bodies can be treated as structureless, spinning point masses [20].

Second, the technique of matched filtering will be used to extract the gravitational waveforms from the considerably larger instrumental noise in which they will be imbedded. This will work as follows. The measured strain amplitude in each detector

$$s(t) = h(t) + n(t) \tag{5.1}$$

will consist of a (possibly present) signal $h(t)$, and the detector noise $n(t)$, which we assume is Gaussian. To detect any imbedded signal, one first suppresses those frequency components of the signal at which the detector noise is largest, by convolving with Wiener's optimal filter $w(t)$: thus, $s(t) \to \int w(t-\tau)s(\tau)d\tau$ [21]. Then, for each inspiral waveform $\hat{h}(t)$ in a large set of theoretical template waveforms, one computes the signal-to-noise ratio S/N, defined by

$$\frac{S}{N}[\hat{h}] = \frac{\int \hat{h}(t)\, w(t-\tau)\, s(\tau)\, d\tau dt}{\mathrm{rms} \int \hat{h}(t)\, w(t-\tau)\, n(\tau)\, d\tau dt}. \tag{5.2}$$

In Eq. (5.2), the denominator is what *would* be the root-mean-square value of the numerator, *if* the detector output (5.1) consisted of noise alone. Thus, when no gravitational wave is present, each $S/N[\hat{h}]$ is a random variable with Gaussian distribution and root-mean-square equal to 1. On the other hand, if $S/N[\hat{h}]$ is sufficiently large, then one can assert with high confidence that a gravitational wave h has been detected, and that h is close to $\hat{h}$. Cutler et al. [8] have estimated that if, for some $\hat{h}$, $S/N[\hat{h}] \geq 6.0$ in each of two detectors, then one can assert with greater than 99% confidence that a gravitational wave has been detected. Defining the combined signal-to-noise ratio ρ of a network of detectors by

$$\rho \equiv \sqrt{\sum_a \rho_a^2}, \tag{5.3}$$

where ρ_a is the S/N in the ath detector, we see that $\rho \approx 8.5$ represents the "detection threshold" for two detectors. For a three-detector network, the detection threshold is still $\rho \approx 8.5$, corresponding to $S/N \gtrsim 4.9$ in each detector. Since detections at threshold represent the most distant coalescences that one can observe (given the binary's masses, its orientation, and its angular position on the sky), and since coalescing binaries are presumably distributed roughly uniformly on large scales, the mean value of ρ for detected events will be roughly 1.5 times the threshold value [22]. Thus "typical" detections will have $\rho \approx 12.7$. Similarly, the strongest 1% of signals should have $\rho \gtrsim 40$; i.e., $(100)^{1/3}$ times the threshold value.

Third, much more information is obtainable from the waveform than one might naively expect, for the following reason. The LIGO and VIRGO detectors will be broad-band detectors, with good sensitivity in the frequency range 10−500 Hz. The gravitational wave trains from inspiraling stellar-mass binaries typically contain $\sim 10^3$ cycles in this range. Now, if the signal $h(t)$ and template $\hat{h}(t)$ lose phase with each other by just one cycle out of thousands, as they sweep upwards in frequency from ~ 10 Hz to ~ 500 Hz, then the integral $\int \hat{h}(\tau)h(t)w(t-\tau)d\tau dt$ will be significantly diminished. Consequently from Eq. (5.2) above the S/N is very sensitive to having the phase of the template waveform be "just right" throughout the inspiral. Since the evolution of the waveform's phase is largely determined by the masses of the two bodies (through their influence on the inspiral rate), one might expect to measure the masses of the bodies with fractional error $\sim 1/\mathcal{N}_{\rm cyc}$, where $\mathcal{N}_{\rm cyc}$ is the total number of cycles in the observed waveform. This fractional error of $\sim 10^{-3}$ contrasts with the $\sim 20\%$ accuracy with which one can determine parameters, such as the distance to the source, that do not affect the phase evolution. This idea that sensitivity to the accumulated phase of the waveform might allow very accurate mass and spin measurements, despite the only modest signal-to-noise ratio, was first pointed out by Cutler et al. [8] and by Chernoff and Finn [14].

Fourth, our extension of the measurement-error analysis to include post-Newtonian effects introduces the following new features. To Newtonian order, the gravitational-wave signal depends on the two masses *only* through the particular combination $\mathcal{M} \equiv \mu^{3/5}M^{2/5}$, where μ is the reduced mass and M is the total mass of the system. This combination is referred to as the "chirp mass." The degeneracy in the dependence on the masses is broken, however, by post-Newtonian effects that in principle allow one to determine M_1 and M_2 individually. In the equation govern-

ing the evolution of the waveform's phase [Eq. (5.42) below], the post-Newtonian terms are $\sim M/r$ times smaller than the Newtonian terms, where r is the orbital separation. Since $M/r \approx 1/20$ when the signal is strongest, one might expect to determine each of the two masses ~ 20 times less accurately than $\mathcal{M}$. We show in Sec. 3 that this expectation is correct, *provided* the spins of the bodies are known to be small.

Now, black holes and neutron stars in merging binaries may or may not be rapidly spinning. However if we cannot assume *a priori* that their spin angular momenta are very small, then in attempting to find the best fit to the data, we must allow for the possibility that the spin angular momenta are of order their maximum possible values. We show in Sec. 3.2 that the extra "confusion" introduced by the spin-dependence of the waveform worsens the accuracy of individual mass measurements by more than an order of magnitude. This is easy to understand: the leading order spin terms in the orbital evolution equation [Eq. (5.59) below] are only one-half post-Newtonian order higher than the leading terms responsible for splitting the mass degeneracy. Therefore the effect on the gravitational waveform of small changes in a binary's masses can be approximately masked by somewhat larger, compensating changes in its spins. Hence the measured values of masses and spins will have strongly correlated errors [cf. Fig. 5.3 below], thereby increasing mass-measurement errors [40]. Our results for meaurement accuracies are summarized in Tables 1 and 2 and Fig. 5.4 below.

The rest of the paper is organized as follows. In Sec. 2 we review the anticipated detector noise levels, the basic elements of signal processing, and the lowest-order, "Newtonian" waveforms. In Sec. 3 we calculate expected mass-measurement accuracies, taking post-Newtonian effects into account. We do this in two stages: first neglecting spin effects in Sec. 3.1, then including them in Sec. 3.2. Our emphasis is on learning *roughly* what accuracies can be expected—in part because to treat the parameter-estimation problem in full generality would be extremely complicated. Therefore, we focus on a somewhat simplified "model" of the gravitational waveform, which nevertheless incorporates the effects that are most important for determining the mass-extraction accuracy. A further approximation which we make is to use a linear error-estimation formalism, which is valid when the errors are small (or equivalently, when the signal-to-noise ratio is large).

Most of the information that allows a measurement of the binary masses is contained in the phase evolution of the waveform (rather than in its amplitude or polarization). Since all detectors in a detector network measure very nearly the

same phase evolution, for the purpose of estimating mass measurement accuracies, to a good approximation it should be adequate to model measurements made by single detector. Modelling a network of detectors, with their various orientations, would be a needless complication in Sec. 3.

When measuring the distance D to the binary, on the other hand, one must also determine the position of the source on the sky and the amplitude and polarization of the waveform. Hence, to estimate distance measurement accuracies, we must model measurements by a entire detector network. However in this case it is a needless complication to use post-Newtonian waveforms; as we show in Sec. 4 and Appendix C below, to a good approximation it is adequate to use Newtonian waveforms in the analysis. This is our approach in Sec. 4, where we estimate the distance measurement accuracy ΔD attainable by an arbitrary network of detectors. Krolak has already developed a formalism with which he has numerically calculated the distance measurement accuracy one can achieve with the LIGO/VIRGO network [15]. We provide a greatly simplified, analytic solution to the distance estimation problem, using an approximation due to Marković [9]. The approximation consists in neglecting the effect on distance measurement errors of the relatively small uncertainty in the angular position of the source on the sky. Making this approximation, we derive a relatively simple formula for the rms distance error ΔD, which applies to any number of detectors, with arbitrary orientations.

This formula is derived using the linear error-estimation formalism mentioned above, and consequently is accurate only to linear order in $1/D$. We show that, contrary to previous expectations, effects which are nonlinear in $1/D$ have a significant effect (i.e., factors $\gtrsim 2$) on the predicted distance measurement accuracies, and develop an approximate method of calculation which gives rough estimates of these nonlinear effects. This method is based on a Bayesian derivation of the (non-Gaussian) probability distribution for the distance D, which incorporates our *a priori* knowledge as well as the information obtained from a gravitational wave measurement. The method also allows us to estimate values of ΔD for binaries that are seen nearly face-on, for which, as pointed out by Marković [9], the linear error-estimation method breaks down. Our results for nearly face-on binaries are typically factors of order 2 to 3 smaller than the upper-limit estimates given by Marković [9].

In Appendix A we extend the treatment of signal processing given in Sec. 2, to incorporate (i) an arbitrary number of detectors, (ii) the effects of *a priori*

knowledge, and (iii) estimation of measurement errors beyond the leading-order, Gaussian approximation. These extensions are required in Secs. 3.2 and 4. We also develop other tools which should be useful in future analyses of LIGO/VIRGO measurement accuracies: we derive an expression for the minimum signal-to-noise ratio $(S/N)_{\rm min}$ necessary in order that the Gaussian approximation for estimation of measurement accuracy be valid, and explain how to treat degenerate points in parameter space at which the Gaussian approximation breaks down.

In this paper we will focus on three fidiucal types of binary— NS-NS, BH-NS, and BH-BH— where unless otherwise specified all black hole masses are assumed to be $10M_\odot$, and all neutron star masses to be $1.4M_\odot$. Throughout we use units where $G = c = 1$. Thus all quantities are measured in units of seconds, except where, for convenience, we use units of solar masses. The conversion factor is $1M_\odot = 4.926 \times 10^{-6}$sec.

2 DETECTION AND MEASUREMENT OF GRAVITATIONAL WAVEFORMS

2.1 Detector characteristics

In order to decide what information can be extracted from gravitational waveforms, one must have a realistic model of the detector noise $n(t)$. This noise will have both Gaussian and non-Gaussian components. We will restrict our analysis to statistical errors due to Gaussian noise. It is likely that the effects of the non-Gaussian components will be unimportant due to (i) the rejection of events that are not simultaneously detected in two or more detectors, and (ii) the filtering of the detector outputs with theoretical waveform templates; however this issue needs further study.

The remaining Gaussian noise can be described by its spectral density $S_n(f)$, where f is frequency. The LIGO team has published an estimate of the noise spectrum that might be attained a few years after LIGO comes on line — the so-called "advanced detector" noise spectral density [3]. We use the following rough analytic fit to their noise curve:

$$S_n(f) = \begin{cases} \infty & f < 10\,\mathrm{Hz}, \\ S_0\left[(f_0/f)^4 + 2\left(1 + (f^2/f_0^2)\right)\right] & f > 10\,\mathrm{Hz} \end{cases} \tag{5.4}$$

where $S_0 = 3 \times 10^{-48}\,\mathrm{Hz}^{-1}$ and $f_0 = 70\,\mathrm{Hz}$. For frequencies $f < 10$ Hz, the

noise due to seismic vibrations is so large that we take it to be effectively infinite. Thermal noise dominates in the frequency band $10\text{Hz} \lesssim f \lesssim 50\text{Hz}$, and photon shot noise dominates for $f \gtrsim 50$ Hz. We refer the reader to Refs. [3, 12] for more details on the sources of noise.

The amount of detector noise determines the strength of the weakest signals that can be detected, and thus the distance to which a given type of source can be seen. The noise level (5.4) will permit the detection of NS-NS mergers out to $\sim 1\,\text{Gpc}$ [3, 14, 22], probably giving a detection rate of $\sim 10^2\ \text{yr}^{-1}$ [2]. In this paper we are principally concerned with the accuracy of parameter estimation rather than with detection issues. The accuracy of parameter estimation depends only on the shape of the noise spectrum and the signal-to-noise (S/N) of the detection; e.g., simultaneously doubling both the noise levels and the signal strength leaves measurement accuracy unchanged. Because we normalize our results to a fixed S/N, our results are insensitive to the parameter S_0 appearing in the noise spectrum (5.4) which sets the overall scale of the noise; all that influences them is the *shape* of the spectrum.

Since the LIGO team's publication [3] of their estimate of the advanced detector's noise curve, there have been new developments in the understanding of the detector's thermal noise which indicate that the advanced thermal noise spectrum may be flatter than previously thought [23]. A modified noise-curve estimate, reflecting this new understanding, has not yet been published. Like the noise spectrum in Ref. [3] on which our simplified model (5.4) is based, such a modified noise curve will depend on the values of advanced detector parameters (such as the quality-factors of modes of vibration and oscillation of the suspension wires and suspended masses) for which only rough estimates of what might be attainable are available. An approximate analytic formula describing the modified advanced detector noise curve, for one choice of detector parameters, is

$$S_n(f) = \begin{cases} \infty & f < 10\,\text{Hz}, \\ S_m\,\alpha^{-4}\,(f/f_m)^{-5} & 10\,\text{Hz} \le f \le f_m/\alpha \\ S_m (f/f_m)^{-1} & f_m/\alpha \le f \le \alpha f_m \\ S_m\,\alpha^{-3}\,(f/f_m)^{2} & f \ge \alpha f_m \end{cases} \tag{5.5}$$

where $S_m = 2.7 \times 10^{-47}\,\text{Hz}^{-1}$, $f_m = 74$ Hz, and $\alpha = 3.8$ [24]. We chose the particular detector parameters underlying Eq. (5.5) in part to accentuate the difference between Eqs. (5.5) and (5.4). Since the ultimate shape of the noise curve is not yet well known, we calculate the attainable measurement accuracies for both noise

spectra. The flatter spectrum (5.5) gives a modest improvement in how accurately the binary's masses can be measured, for fixed signal-to-noise [cf. Tables II and III below] that.

2.2 Review of parameter estimation

In this section we give a concise summary of those elements of signal processing that are necessary for parameter estimation. The basic concepts of detection and measurement have also been reviewed recently by Finn [26] and Krolak et al. [27]. In Appendix A we give give a more detailed treatment, and give an extensive discussion of the ways in which the simplified linear formalism described in this section can break down: (i) when the signal-to-noise of the detection is low, and (ii) when our *a priori* knowledge of some of the binary parameters is not negligible compared to the information obtained from the measurement.

We start by assuming that an inspiraling binary gravitational wave *has* been observed; i.e, that the appropriate detection criterion has been met by the detector outputs. We now discuss how to determine the parameters of an inspiraling binary system that best fit the measured signal.

The basic framework for addressing this question is illustrated in Fig. 5.1. The set of all gravitational waveforms from two inspiraling bodies can be characterized by a relatively small number of parameters (the distance to the source; the time of merger; five angles specifying the position of the source on the sky, the plane of the orbit, and the orbital phase at some given time; and the masses and spin angular momenta of the two bodies—fifteen parameters in all, assuming that the eccentricity of the orbit is negligible). We regard this set of waveforms as a fifteen-dimensional surface embedded in the vector space of all possible measured signals. In the absence of any noise, all measured signals from inspiraling binaries would lie on this submanifold; in practice, of course, the measured signal consisting of waveform plus noise is displaced off the submanifold.

The statistical properties of the noise determine a natural inner product on the vector space of signals. Given two signals $h_1(t)$ and $h_2(t)$, we define $(h_1 \mid h_2)$ by [28]

$$(h_1 \mid h_2) = 2 \int_0^\infty \frac{\tilde{h}_1^*(f)\tilde{h}_2(f) + \tilde{h}_1(f)\tilde{h}_2^*(f)}{S_n(f)}\, df, \tag{5.6}$$

where $\tilde{h}_1$ and $\tilde{h}_2$ are the fourier transforms of h_1 and h_2. This definition is chosen

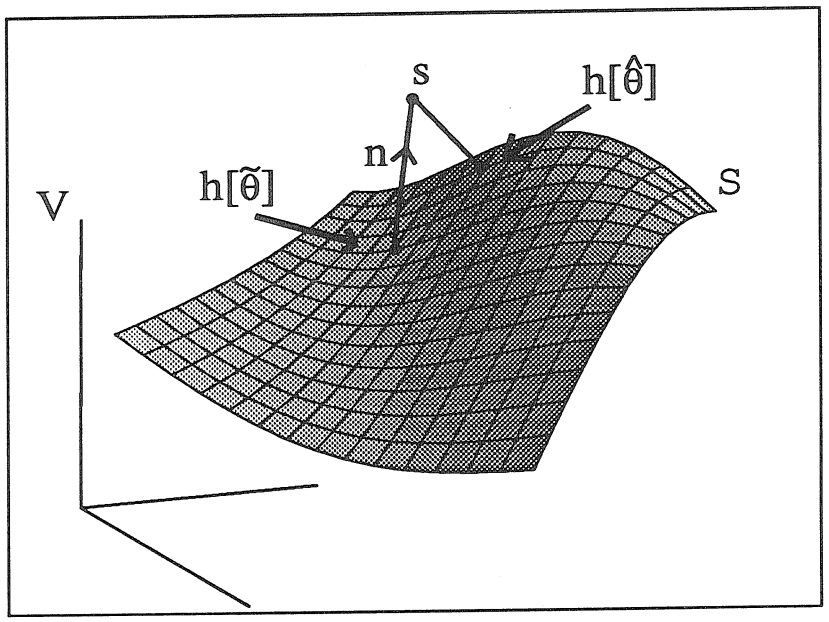

Figure 5.1: Gravitational waveforms from coalescing compact binaries are completely specified by a finite number of parameters $\theta = (\theta^1, \ldots, \theta^k)$, and so form a surface $\mathcal{S}$ in the vector space V of all possible measured detector outputs $s = s(t)$. The statistical properties of the detector noise endow V with the structure of a infinite-dimensional Euclidean space. This figure illustrates the relationships between the true gravitational wave signal $h(\tilde{\theta})$, the measured signal s, and the "best-fit" signal $h(\hat{\theta})$. Given a measured detector output s, of the form "true signal" $h(\tilde{\theta})$ plus noise n, the most likely values $\hat{\theta}$ of the binaries parameters are just those that correspond to the point $h(\hat{\theta})$ on the surface $\mathcal{S}$ which is closest [in the Euclidean distance $(s - h \,|\, s - h)$] to y.

so that the probability for the noise to have some realization $n_0(t)$ is

$$p(n = n_0) \propto e^{-(n_0 \,|\, n_0)/2}. \tag{5.7}$$

Hence if the actual incident waveform is $h(t)$, then from Eq. (5.1) the probability of measuring a signal s in the detector output is proportional to $e^{-(s-h \,|\, s-h)/2}$. Correspondingly, given a measured signal s, the gravitational waveform h that "best fits" the data is the one that minimizes the quantity $(s-h \,|\, s-h)$; see Fig. 5.1.

It also follows from Eq. (5.6) that for any functions $g(t)$ and $k(t)$, the expectation value of $(g|n)(k|n)$, for an ensemble of realizations of the detector noise $n(t)$, is just $(g|k)$. Hence the signal-to-noise (5.2) of the detection will be approximately given by

$$\frac{S}{N}[h] = \frac{(h|h)}{\text{rms } (h|n)} = (h|h)^{1/2}. \tag{5.8}$$

The kernel $w(t)$ of Wiener's optimal filter appearing in Eq. (5.2) is just the Fourier transform of $1/S_n(f)$.

For a given incident gravitational wave, different realizations of the noise will of give rise to somewhat different best-fit parameters. For large S/N, the best-fit parameters will have a Gaussian distribution centered on the correct values. Specifically, let $\tilde{\theta}^i$ be the "correct" values of the parameters on which the waveforms depend, and let $\tilde{\theta}^i + \Delta\theta^i$ be the best fit parameters in the presence of some realization of the noise. Then for large S/N, the parameter-estimation errors $\Delta\theta^i$ have the Gaussian probability distribution [26]

$$p(\Delta\theta^i) = \mathcal{N} e^{-\frac{1}{2}\Gamma_{ij}\Delta\theta^i\Delta\theta^j}. \tag{5.9}$$

Here Γ_{ij} is the so-called Fisher information matrix defined by

$$\Gamma_{ij} \equiv \left(\frac{\partial h}{\partial\theta^i} \,\middle|\, \frac{\partial h}{\partial\theta^j}\right), \tag{5.10}$$

and $\mathcal{N} = \sqrt{\det(\Gamma/2\pi)}$ is the appropriate normalization factor. It follows that the root-mean-square error in θ^i is

$$\sqrt{\langle(\Delta\theta^i)^2\rangle} = \sqrt{\Sigma^{ii}} \tag{5.11}$$

where $\Sigma \equiv \Gamma^{-1}$.

The above discussion applies to measurements made by a single detector. The (straightforward) generalization to a network of detectors, which will be required in Sec. 4, is given in Appendix A.

This discussion also neglects the effects of any *a priori* constraints on the parameters that may be available. The incorporation of such *a priori* information can have a significant effect on the predicted parameter-extraction accuracies (and also on the best-fit parameter values themselves), not only for those parameters to which the constraints apply, but also (because of correlations) for the remaining parameters. The effect is significant whenever, for a given parameter, the *a priori* information is comparable with the information contained in the measured signal. Hence, *a priori* constraints are usually important whenever we include in an error-estimation analysis parameters which are *weakly determined* by the detected gravitational wave signal. In Appendix A we derive a generalization of Eq. (5.10) [cf. Eq. (5.172) below] which roughly incorporates the effect of *a priori* information. This generalization will be used in Sec. 3.2, where we consider the (somewhat weak) dependence of the inspiral waveform h on the spins of the two bodies.

2.3 The gravitational wave signal in the Newtonian approximation

Inspiraling compact binaries can be described, to lowest order, as two Newtonian point particles whose orbital parameters evolve secularly due to gravitational radiation, where the gravitational waves and corresponding energy loss rate are given by the Newtonian quadrupole formula. That is, the orbital angular frequency Ω is given by

$$\Omega = \frac{M^{1/2}}{r^{3/2}}, \tag{5.12}$$

where $M \equiv M_1 + M_2$ is the total mass of the system and r is the orbital separation. The inspiral rate, for circular orbits, is given by

$$\frac{dr}{dt} = -\frac{r}{E}\frac{dE}{dt} = -\frac{64}{5}\frac{\mu M^2}{r^3}, \tag{5.13}$$

where $\mu \equiv M_1 M_2/M$ is the reduced mass. Integrating Eq. (5.13) we obtain

$$r = \left(\tfrac{256}{5}\mu M^2\right)^{1/4} (t_c - t)^{1/4}, \tag{5.14}$$

where t_c is the "collision time" at which (formally) $r \to 0$. Since the emitted gravitational waves are quadrupolar, their frequency f (cycles/sec) is equal to Ω/π. The gravitational waves induce a measured strain $h(t)$ at the detector which is given by (see, e.g., Ref. [12])

$$h(t) = \frac{(24/5)^{1/2}\pi^{2/3} Q(\theta, \varphi, \psi, \iota)\mu M}{D\, r(t)} \cos\left(\int 2\pi f dt\right), \tag{5.15}$$

where D is the distance to the source, and Q is a function of the angles $(\theta, \varphi, \psi, \iota)$ that describe the position of the source on the sky and the orientation of the orbital plane (with respect to axes aligned with the detector arms). The exact form of Q is given in Sec. 4 below.

Because both the amplitude and frequency of the signal increase as $t \to t_c$, the signal is referred to as a "chirp." From Eqs. (5.12) and (5.13), the frequency evolves according to

$$\frac{df}{dt} = \frac{96}{5}\pi^{8/3}\,\mathcal{M}^{5/3}\,f^{11/3}, \tag{5.16}$$

where $\mathcal{M} \equiv \mu^{3/5}M^{2/5}$ is the chirp mass parameter discussed in Sec. 1. The phase $\phi(t) = \int^t 2\pi f(t')dt'$ is thus given by

$$\phi(t) = -2\left[\tfrac{1}{5}\mathcal{M}^{-1}(t_c - t)\right]^{5/8} + \phi_c, \tag{5.17}$$

where the constant of integration ϕ_c is defined by $\phi \to \phi_c$ as $t \to t_c$.

In Eqs. (5.15)–(5.17) we have omitted the (obvious) time delay between signal emission and detection, and we have implicitly assumed that the detector and the binary's center-of-mass are at rest with respect to each other. The latter requires some explanation. If the detector and binary are in relative motion, the detected signal is Doppler-shifted with respect to the emitted signal. One cannot determine this Doppler-shift from the detected signal, since $h(t)$, as defined by Eqs. (5.15)–(5.16), is invariant under the transformation

$$(f, \mathcal{M}, \mu, r, D, t) \to (f/\lambda, \mathcal{M}\lambda, \mu\lambda, r\lambda, D\lambda, t\lambda)\,. \tag{5.18}$$

Thus, strictly speaking, one can extract from the signal only the "Doppler-shifted" mass and distance parameters $\lambda\mathcal{M}$, $\lambda\mu$, and λD, where λ is the Doppler-shift factor. This is not just a feature of our simplified, Newtonian waveform; it also holds for the true, general-relativistic waveforms, as can be seen on purely dimensional grounds and from the fact that general relativity does not define any preferred mass/length scales.

Similarly, for binary sources at cosmological distances, the waves will depend on and reveal the redshifted masses

$$\mathcal{M} = (1+z)\mathcal{M}_{\rm true}, \quad \mu = (1+z)\mu_{\rm true}, \tag{5.19}$$

where z is the source's cosmological redshift, and also depend on and reveal its so-called luminosity distance D_L [6, 9, 26]. Our measurement-accuracy analysis applies to these *redshifted* masses and to the luminosity distance; the determination

of the true masses for very distant binaries will require some method of estimating redshifts [9].

It is most convenient to work directly with the Fourier transform of $h(t)$,

$$\tilde{h}(f) \equiv \int_{-\infty}^{\infty} e^{2\pi i f t} h(t)\, dt, \tag{5.20}$$

which is easily computed using the stationary phase approximation [12]. Given a function $B(t) = A(t)\cos\phi(t)$, where $d\ln A/dt \ll d\phi(t)/dt$ and $d^2\phi/dt^2 \ll (d\phi/dt)^2$, the stationary phase approximation provides the following estimate of the Fourier transform $\tilde{B}(f)$ for $f \geq 0$:

$$\tilde{B}(f) \approx \frac{1}{2} A(t) \left(\frac{df}{dt}\right)^{-1/2} \exp\left[i\left(2\pi f t - \phi(f) - \pi/4\right)\right]. \tag{5.21}$$

In this equation, t is defined as the time at which $d\phi(t)/dt = 2\pi f$, and (in a slight abuse of notation) $\phi(f)$ is defined as $\phi(t(f))$. Using Eqs. (5.16) and (5.17) we obtain

$$\begin{aligned} t(f) &= t_c - 5(8\pi f)^{-8/3}\mathcal{M}^{-5/3} \\ \phi(f) &= \phi_c - 2\left[8\pi\mathcal{M}f\right]^{-5/3}. \end{aligned} \tag{5.22}$$

Hence from Eq. (5.21), the Fourier transform of the Newtonian waveform is

$$\tilde{h}(f) = \frac{Q}{D}\mathcal{M}^{5/6} f^{-7/6} \exp\left[i\Psi(f)\right] \tag{5.23}$$

for $f \geq 0$, where the phase $\Psi(f)$ is

$$\Psi(f) = 2\pi f t_c - \phi_c - \frac{\pi}{4} + \frac{3}{4}(8\pi\mathcal{M}f)^{-5/3}. \tag{5.24}$$

Equation (5.23) for $\tilde{h}(f)$ is clearly invalid at very high frequencies, because the real inspiral will terminate at some finite orbital frequency. For BH-BH and BH-NS mergers, there will be a transition from inspiral to a final plunge [29] near the location of the last stable circular orbit, which is roughly at $r = 6M$ for non-spinning bodies [30]. The final plunge will last roughly one orbital period. [Neutron stars merging with rapidly spinning black holes may instead tidally disrupt, thereby shutting off the waves, outside the horizon [8].] For NS-NS mergers, the two bodies will collide and coalesce at roughly $r = 6M$. Generally therefore the inspiral gravitational wave $h(t)$ will "shut off" at roughly $r = 6M$, and correspondingly $\tilde{h}(f)$ will shut off at roughly $f = (6^{3/2}\pi M)^{-1}$. We therefore "correct" the waveform (5.23) by setting $\tilde{h}(f) = 0$ for $f > (6^{3/2}\pi M)^{-1}$. We note that when $r > 6M$,

$$\frac{|r^{-1}dr/dt|}{d\phi/dt} = \frac{2}{3}\frac{d^2\phi/dt^2}{(d\phi/dt)^2} < \frac{1}{55}\left(\frac{4\mu}{M}\right), \tag{5.25}$$

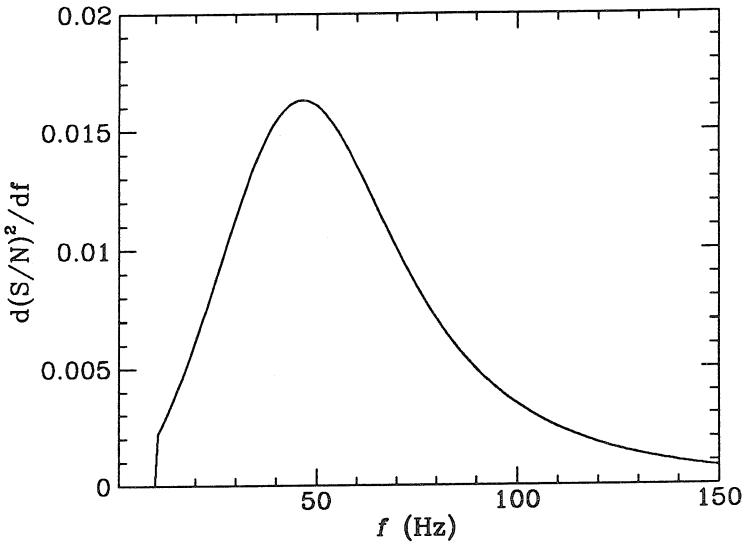

Figure 5.2: This plot shows how the total signal-to-noise squared S^2/N^2 for a detected coalescing-binary waveform is distributed in frequency f. Most of the signal-to-noise ratio comes not near 70 Hz where the detector sensitivity $S_n(f)^{-1}$ is highest, but rather at a somewhat lower frequency of $\sim$ 50 Hz, because more cycles per unit frequency are received at lower frequencies.

so the stationary phase approximation should reproduce the Fourier transform of $h(t)$ with good accuracy throughout the inspiral. Note that, as advertised in Sec. 1, in the Newtonian approximation the signal (5.23) depends on M_1 and M_2 only through the chirp mass $\mathcal{M}$.

Using Eqs. (5.4) and (5.23), we can see how the signal-to-noise squared accumulates as the frequency sweeps upwards:

$$\begin{aligned}(S/N)^2(f) &\equiv 4\int_0^f \frac{|\tilde{h}(f')|^2}{S_n(f')}\,df' \\ &= 4\frac{Q^2}{D^2}\mathcal{M}^{5/3}\int_0^f \frac{(f')^{-7/3}}{S_n(f')}\,df'. \end{aligned} \tag{5.26}$$

In Fig. 5.2 we plot the integrand $d(S/N)^2/df = 4|\tilde{h}(f)|^2/S_n(f)$, using the advanced detector noise spectrum (5.4). The shape of this curve is universal once the noise spectrum is given: the masses, the relative angles, the distance to the source, etc. affect only the overall amplitude. (This is strictly true only for the

"Newtonian" signal, but will remain true to a good approximation when post-Newtonian effects are taken into account.) While 90% of the cycles come between 10 and 40 Hz, and while most of the energy is released in the last few orbits at $f > 200\,\mathrm{Hz}$, we find that $\sim 60\%$ of the total signal-to-noise squared accumulates between 40 and 100 Hz, the frequency band in which LIGO is most sensitive.

We now evaluate the Fisher information matrix (5.10). For measurements using a single detector, there are only four parameters on which the Newtonian signal depends: an overall amplitude $\mathcal{A} \equiv (Q/D)\mathcal{M}^{5/6}$, and $\mathcal{M}$, t_c, and ϕ_c. The derivatives of $\tilde{h}(f)$ with respect to these parameters (for $f > 0$) are given by

$$\frac{\partial \tilde{h}}{\partial \ln \mathcal{A}} = \tilde{h}, \qquad \frac{\partial \tilde{h}}{\partial t_c} = 2\pi i f \tilde{h}, \tag{5.27}$$

$$\frac{\partial \tilde{h}}{\partial \phi_c} = -i\tilde{h}, \qquad \frac{\partial \tilde{h}}{\partial \ln \mathcal{M}} = -\frac{5i}{4}(8\pi \mathcal{M} f)^{-5/3}\tilde{h}. \tag{5.28}$$

From Eqs. (2.3) and the noise spectrum (5.4), it is straightforward to evaluate the Fisher information matrix (5.10) and its inverse Σ^{ij} [31]. General expressions for the elements of Γ_{ij} using Newtonian waveforms, valid for any detector noise spectrum, are given in Ref. [14]. We will not reproduce them here. However, for purposes of comparison to our post-Newtonian results in Sec. 3, we list the rms errors $\Delta\mathcal{A}$, $\Delta\mathcal{M}$, Δt_c and $\Delta\phi_c$ for the case of low-mass (e.g., NS-NS) binaries, assuming the approximate waveform (5.23) and the detector noise spectrum (5.4):

$$\Delta(\ln \mathcal{A}) = 0.10\left(\frac{10}{S/N}\right) \tag{5.29}$$

$$\Delta t_c = 0.40\left(\frac{10}{S/N}\right)\,\mathrm{msec}, \tag{5.30}$$

$$\Delta\phi_c = 0.25\left(\frac{10}{S/N}\right)\,\mathrm{rad} \tag{5.31}$$

$$\Delta(\ln \mathcal{M}) = 1.2\times 10^{-5}\left(\frac{10}{S/N}\right)\left(\frac{\mathcal{M}}{M_\odot}\right)^{5/3}. \tag{5.32}$$

For low-mass binaries, the fact that we "cut off" the waveform $\tilde{h}(f)$ for $f > (6^{3/2}\pi M)^{-1}$ has little effect on the rms errors (2.3), due to the sharp rise in $S_n(f)$ at high frequency. The exact scaling of $\Delta(\ln \mathcal{M})$ as $\mathcal{M}^{5/3}$, and the fact that Δt_c and $\Delta\phi_c$ are independent of M, strictly hold only when the cut-off is unimportant. For BH-BH binaries with $S/N = 10$, one has $\Delta t_c = 0.60\,\mathrm{msec}$, $\Delta\phi_c = 0.32\,\mathrm{rad}$, and $\Delta(\ln \mathcal{M}) = 1.3\times 10^{-5}\,(\mathcal{M}/M_\odot)^{5/3}$.

The rather phenomenal accuracy attainable for the chirp mass $\mathcal{M}$ is due to the large number $\mathcal{N}_{\rm cyc}$ of cycles in the detectable portion of the gravitational waveform. We see from Eq. (5.16) that $\mathcal{N}_{\rm cyc}$ scales like $\mathcal{M}^{-5/3}$, so $\Delta(\ln \mathcal{M})$ is proportional $1/\mathcal{N}_{\rm cyc}$, as one would expect.

The rms errors (2.3) apply to single-detector measurements. In practice, one will have a network of detectors, with different locations and orientations. For a network, $\Delta(\ln \mathcal{M})$, will be roughly given by Eq. (5.32), but with S/N replaced by the combined signal-to-noise ρ of the detector network, defined by Eq. (5.3) above. This is because each detector, by itself, yields an estimate of $\mathcal{M}$, and the rms error in the (weighted) average of those estimates is reduced from the error in a single detector by the factor $\rho^{-1}\,(S/N)$. The same argument does *not* apply to the rms errors in t_c, $\mathcal{A}$, and ϕ_c, because the gravitational waves will arrive at the different detectors at different times, and because detectors with different orientations measure different values of $\mathcal{A}$ and ϕ_c [cf. Sec. 4 below].

We conclude this section by noting that from the measured value of the chirp mass $\mathcal{M}$ alone, one already obtains a lower limit on the larger of the individual masses, and upper limits on the smaller mass and on the reduced mass. We adopt the convention that $M_1 \geq M_2$; i.e., M_1 always refers to the *larger* of the two masses. Then it follows by definition that

$$M_1 \geq 2^{1/5}\mathcal{M}, \quad M_2 \leq 2^{1/5}\mathcal{M}, \quad \mu \leq 2^{-4/5}\mathcal{M}. \tag{5.33}$$

However, if μ is unknown, then the mass ratio M_1/M_2 is unconstrained. The bounds (5.33) that follow from measuring $\mathcal{M}$ may themselves be of astrophysical interest. For instance, if one determines using (5.33) that $M_1 \geq 3M_\odot$, then one may conclude that the heavier body is a black hole (assuming the redshift is small, cf. Eq. (5.19) above and associated discussion). Also, it has been suggested [8] that from LIGO/VIRGO measurements of NS-BH coalescences where the BH is rapidly spinning, it may be possible to constrain the neutron-star equation of state by measuring the frequency at which the NS's tidal disruption causes the waves to shut off. Knowledge of this tidal-disruption frequency, coupled with an upper limit on the neutron star mass M_2 determined from the inspiral waveform, would allow one to place an upper limit on the stiffness of the equation of state.

3 POST-NEWTONIAN EFFECTS AND PARAMETER ESTIMATION

We now extend the analysis of the previous section to include post-Newtonian effects. We continue to treat the bodies as point masses, since tidal interactions have a negligible effect. Also, for the moment we will neglect the effects of the bodies' spin angular momenta.

The post-Newtonian approximation provides the most accurate description currently available of the gravitational radiation from inspiraling, stellar-mass binaries. Corrections of order M/r (P^1N corrections) to the lowest-order, Newtonian waveform (5.15) were calculated almost twenty years ago by Wagoner and Will [32]. Calculations of the inspiral rate have recently been extended to $P^{1.5}N$ order, for the case of non-spinning bodies, by Wiseman [33] (after Cutler *et al.* [13] and Poisson [34] had determined the form of the $P^{1.5}N$ correction for the case $\mu/M \ll 1$). By "P^xN order" we mean that corrections to the quadrupole-formula radiation field and corresponding inspiral rate that are of order $(M/r)^x$ have been taken into account, along with order $(M/r)^x$ corrections to the non-radiative orbital equations which determine, e.g., the orbital frequency at a given separation. [There is no standard convention for "counting" post-Newtonian orders in calculations involving radiation; e.g., some authors refer to the lowest-order radiation field as $P^{2.5}N$. Our own terminology is motivated by the application considered here: since radiation reaction effects *cause* the inspiral, $O(M/r)$ corrections to the quadrupole formula accumulate secularly and have just as large an effect on the phase of the orbit $\phi(f)$ as do $O(M/r)$ corrections to the orbital frequency at a given radius.]

The post-Newtonian waveforms improve upon their Newtonian counterparts in three respects [35, 36]. First, they include contributions from higher-order multipoles of the stress-energy tensor (e.g., mass-octupole and current-quadrupole radiation in addition to the mass-quadrupole term), whose frequencies are different harmonics of the orbital frequency. Second, they include post-Newtonian corrections to the lowest-order expressions for the amplitude of each multipole component. And, most importantly for our purposes, post-Newtonian corrections to the energy $E(r)$ and gravitational wave luminosity $dE/dt(r)$ modify the inspiral rate and thereby the accumulated orbital phase $\Phi(t)$. We can write $h(t)$ schematically

as

$$h(t) = \Re\left\{\sum_{x,m} h^x_m(t) e^{im\Phi(t)}\right\} \tag{5.34}$$

where "$\Re$" means "the real part of", x indicates the term's post-Newtonian order, the integer m labels the different harmonics, and $\Phi(t)$ is the orbital phase. Each amplitude h^x_m has the form

$$h^x_m(t) \equiv \frac{\mu M}{D\, r(t)}\, g^x_m(M_1/M_2)\, Q^x_m(\theta, \varphi, \psi, \iota) \tag{5.35}$$

where $r(t)$ is the orbital separation, g^x_m is some function of the mass ratio, and Q^x_m is a function of the source's position on the sky and the orientation of the orbital plane. To connect with the notation of Sec. 2 and below, we note that the phase $\phi(t)$ of the quadrupole part of the waveform is essentially twice the orbital phase: $\phi(t) = 2\Phi(t) + k$, for some constant k that depends on the relative positions and orientations of the detector and the binary [37]. Thus, the expansion for $h(t)$ through $P^{1.5}N$ order is given by

$$\begin{aligned} h(t) \;=\; & \Re[\,(h^0_2 + h^1_2 + h^{1.5}_2)e^{2i\Phi} + (h^{0.5}_1 + h^{1.5}_1)e^{i\Phi} \\ & + (h^{0.5}_3 + h^{1.5}_3)e^{3i\Phi} + h^1_4 e^{4i\Phi} + h^{1.5}_5 e^{5i\Phi}\,] \end{aligned} \tag{5.36}$$

where $\Phi(t)$ has the post-Newtonian expansion

$$\Phi(t) = \Phi^0 + \Phi^1 + \Phi^{1.5} + O(M/r)^2. \tag{5.37}$$

In Eq. (5.37), Φ^x refers to the P^xN order contribution to the orbital phase. As indicated by Eq. (5.37), the term $\Phi^{0.5}$ vanishes identically, as do several omitted terms in Eq. (5.36). The term $h^0_2 e^{2i\Phi^0}$ is just the Newtonian, mass-quadrupole waveform given by Eq. (5.15), while the terms $h^{0.5}_1 e^{i\Phi^0(t)}$ and $h^{0.5}_3 e^{3i\Phi^0(t)}$ are the lowest order current-quadrupole pieces of the waveform. The term $h^{1.5}_2\, e^{2i\Phi}$ is the so-called "hereditary" or "tail" term produced by the interaction of the outgoing wave with the binary's gravitational potential [34, 38]. The interested reader can find explicit expressions for the amplitudes h^x_m through P^1N order in Krolak [35].

In Sec. 1 we argued that the waveform's accumulated phase Φ contains most of the "information" that allows sensitive measurement of the masses of the bodies. Since this paper aims at only an approximate calculation of parameter-estimation accuracies, rather than use the full $P^{1.5}N$ waveform (5.36), we calculate the Fisher information matrix (5.10) using the following "model" waveform:

$$h(t) = \Re\Big\{h^0_2\, e^{2i\left[\Phi^0 + \Phi^1 + \Phi^{1.5}\right]}\Big\}. \tag{5.38}$$

That is, we include P^1N and $P^{1.5}N$ corrections to the phase of the waveform, since these are decisive for extracting the mass and spin parameters of the binary, but we neglect the other post-Newtonian effects that are nominally of the same order. We expect that the Fisher information matrix Γ_{ij} calculated using Eq. (5.38) will be reasonably close to what one would obtain using the full $P^{1.5}N$ waveform, which would in turn be reasonably close to the Γ_{ij} one would obtain for the true, general relativistic waveforms.

There is another, practical, reason for the use of the truncated waveform (5.38). As explained in Sec. 2, we can simplify the error-estimation analysis by considering only single-detector measurements, and still obtain a reasonable estimate of the accuracies attainable for mass and spin measurements. However, as stated above, each of the amplitudes h^x_m has a different dependence on the angles $(\theta, \varphi, \psi, \iota)$. These angles cannot be measured using one detector alone. The position of the source θ, φ is determined from differences in signal arrival times at (at least) three widely separated detectors [6]. Moreover at least two of the detectors must have different orientations to obtain even a crude estimate of the angles ψ, ι (which describe the principal polarization axis of the wave and the angle between the line of sight and the normal to the orbital plane). Thus, to make use of the extra information contained in the post-Newtonian terms that we are omitting in Eq. (5.38), a full detector network would have to be modeled. Hence, for simplicity, in our model waveform (5.38) we omit all of the terms in Eq. (5.36) except for the largest one. [Although we do analyze a general network of detectors in Sec. 4 below, that analysis takes advantage of the fact that the phase-evolution information and the amplitude/polarization information in the measured waveforms are largely independent, and — complementary to this section's analysis — focuses on the amplitude/polarization information alone.]

3.1 Parameter estimation neglecting spin effects

In this section we estimate how well the masses M_1 and M_2 could be determined, if we knew *a priori* (or *a posteriori* by some independent means), that the spins of the bodies were negligible. This is different from the situation where the spins *happen* to be zero, but where we have no knowledge of this fact apart from the information contained in the gravity waveform.

It is probably not justified to assume *a priori* that compact objects in close binaries have negligible spins, since they have typically experienced a period of

mass transfer and spin-up. The three known NS-NS binaries in our galaxy that will merge within a Hubble time all contain pulsars whose spin angular momenta are roughly 2% of their maximum possible values [2]. We show in Sec. 3.2 below that allowing for spins of this magnitude increases the predicted error bars for mass measurements by roughly a factor of two, compared to errors obtained if the spins are assumed to vanish. Nevertheless, we feel it is instructive to calculate the Fisher information matrix neglecting spin effects (i.e., assuming the spins are negligible *a priori*), both to illustrate the inclusion of post-Newtonian terms and to compare with the results obtained when we include spins.

We now briefly derive the $P^{1.5}N$ corrections to the phase of the waveform, for non-spinning bodies. Through $P^{1.5}N$ order, the orbital frequency, energy, and energy-loss rates are [32, 33]:

$$\Omega(r) = \frac{M^{1/2}}{r^{3/2}}\left[1+\left(\frac{-3}{2}+\frac{\mu}{2M}\right)\frac{M}{r}+O\left(\frac{M}{r}\right)^2\right] \tag{5.39}$$

$$E(r) = \frac{-\mu M}{2r}\left[1+\left(\frac{-7}{4}+\frac{\mu}{4M}\right)\frac{M}{r}+O\left(\frac{M}{r}\right)^2\right] \tag{5.40}$$

$$\begin{aligned}\frac{dE}{dt}(r) &= -\frac{32}{5}(\mathcal{M}\Omega)^{10/3}\left[1+\left(\frac{-1247}{336}+\frac{35\mu}{12M}\right)\left(\frac{M}{r}\right)\right.\\ &\left.+4\pi\left(\frac{M}{r}\right)^{3/2}+O\left(\frac{M}{r}\right)^2\right],\end{aligned} \tag{5.41}$$

where r is the orbital separation in DeDonder gauge (the standard gauge choice for post-Newtonian calculations), and t refers to time measured at infinity.

Defining $f \equiv \Omega/\pi$, the frequency (in cycles/sec) of the quadrupolar part of the gravitational waves, we combine Eqs. (5.39)–(5.41) to obtain

$$\begin{aligned}df/dt &= \frac{96}{5}\pi^{8/3}\mathcal{M}^{5/3}f^{11/3}\left[1-\left(\frac{743}{336}+\frac{11\mu}{4M}\right)(\pi Mf)^{2/3}\right.\\ &\left.+4\pi(\pi Mf)+O(\pi Mf)^{4/3}\right].\end{aligned} \tag{5.42}$$

In Eq. (5.42) and below, we use $(\pi Mf)^{1/3}$ as our post-Newtonian expansion parameter, instead of $(M/r)^{1/2}$. We note that $(\pi Mf)^{1/3}$ equals $(M/r)^{1/2}$ up to but not including terms of order $(M/r)^{3/2}$. This change of variables is advantageous because the frequency of the wave is a directly measurable, gauge-independent quantity (unlike the radius of the orbit). Equation (5.42) can be easily integrated to obtain $t(f)$ and $\phi(f)$, where $\phi \equiv \pi \int f dt$ is the phase of the waveform. Defining $x \equiv (\pi Mf)^{2/3}$, we find that

$$t(f) = t_c - 5(8\pi f)^{-8/3}\mathcal{M}^{-5/3}\left[1+\frac{4}{3}\left(\frac{743}{336}+\frac{11\mu}{4M}\right)x\right.$$

$$-\frac{32\pi}{5}x^{3/2}+O(x^2)\Big], \tag{5.43}$$

$$\phi(f) = \phi_c - 2\left[8\pi\mathcal{M}f\right]^{-5/3}\Big[1+\frac{5}{3}\left(\frac{743}{336}+\frac{11\mu}{4M}\right)x$$
$$-10\pi\, x^{3/2}+O(x^2)\Big], \tag{5.44}$$

where, as in Sec. 2, we define t_c and ϕ_c by $t \to t_c$ and $\phi \to \phi_c$ as $f \to \infty$.

Using Eqs. (5.43) and (5.44) and the stationary phase approximation, we can repeat the analysis of Sec. 2 to obtain $\tilde{h}(f)$. As before, we (crudely) model the end of the inspiral at $r \approx 6M$ by setting $\tilde{h}(f) = 0$ for $f > (6^{3/2}\pi M)^{-1}$. The stationary phase result then becomes

$$\tilde{h}(f) = \begin{cases} \mathcal{A}\, f^{-7/6}\, e^{i\Psi} & 0 < f < (6^{3/2}\pi M)^{-1} \\ 0 & (6^{3/2}\pi M)^{-1} < f, \end{cases} \tag{5.45}$$

where $\mathcal{A} = (Q/D)\,\mathcal{M}^{5/6}$ and

$$\Psi(f) = 2\pi f t_c - \phi_c - \pi/4 + \frac{3}{4}(8\pi\mathcal{M}f)^{-5/3}$$
$$\times\left[1+\frac{20}{9}\left(\frac{743}{336}+\frac{11\mu}{4M}\right)x - 16\pi x^{3/2}\right]. \tag{5.46}$$

Note that the post-Newtonian correction terms in square brackets in Eq. (5.46) have their greatest effect on the phase of $\tilde{h}(f)$ at *low* frequencies, because they are multiplied by the overall factor $f^{-5/3}$. This may seem counterintuitive, since the post-Newtonian corrections to the inspiral rate are largest at small r, or high f; however the high-frequency portion of the waveform contains far fewer cycles, so the cumulative effect of PN corrections on the waveform's phase is smaller there.

Our model waveform (5.46) for non-spinning bodies depends on five parameters: $\mathcal{A}$, ϕ_c, $\mathcal{M}$, μ, and t_c. It is actually somewhat simpler to compute and interpret the Fisher information matrix Γ_{ij} in terms of the following modified parameters for which the rms errors are rescaled: $\ln\mathcal{A}$, ϕ_c, $\ln\mathcal{M}$, $\ln\mu$, and $f_0 t_c$, where f_0 is some fiducial frequency. With respect to these parameters, the derivatives of $\tilde{h}(f)$ are [39]

$$\frac{\partial\tilde{h}(f)}{\partial\ln\mathcal{A}} = \tilde{h}(f) \tag{5.47}$$

$$\frac{\partial\tilde{h}(f)}{\partial f_0 t_c} = 2\pi i\,(f/f_0)\tilde{h}(f) \tag{5.48}$$

$$\frac{\partial\tilde{h}(f)}{\partial\phi_c} = -i\tilde{h}(f) \tag{5.49}$$

$$\frac{\partial\tilde{h}(f)}{\partial\ln\mathcal{M}} = -\frac{5i}{4}(8\pi\mathcal{M}f)^{-5/3}\tilde{h}(f) \times\left[1+\frac{55\mu}{6M}x+8\pi x^{3/2}\right] \tag{5.50}$$

$$\frac{\partial\tilde{h}(f)}{\partial\ln\mu} = \frac{3i}{4}(8\pi\mathcal{M}f)^{-5/3}\tilde{h}(f) \times\left[(\frac{-3715}{756}+\frac{55\mu}{6M})x+24\pi x^{3/2}\right]. \tag{5.51}$$

Using Eqs. (3.1) and the noise spectrum (5.4), we have numerically computed Γ_{ij}, its inverse Σ^{ij}, and the corresponding errors $\Delta\phi_c = \left(\Sigma^{\phi_c\,\phi_c}\right)^{1/2}$, etc. Since our model waveform includes post-Newtonian corrections to the phase but not to the amplitude, Σ^{ij} is block diagonal: $\Sigma^{\ln\mathcal{A}\,j} = 0$ for $j = \phi_c$, $\ln\mathcal{M}$, $\ln\mu$, or $f_0 t_c$. Hence, $\Delta\mathcal{A}/\mathcal{A} = (S/N)^{-1}$, while errors in $\mathcal{A}$ are uncorrelated with errors in the other parameters. Table 1 lists $\Delta\phi_c$, Δt_c, $\Delta\mathcal{M}/\mathcal{M}$, and $\Delta\mu/\mu$ for a range of values of M_1 and M_2. The results in Table 1 are for a single detector and are normalized to $S/N = 10$. For measurements by a detector network, the rms errors $\Delta\mathcal{M}/\mathcal{M}$, and $\Delta\mu/\mu$ will be approximately those given Table 1, but with S/N replaced by ρ, the combined signal-to-noise (5.3) of the network. As explained in Sec. 2, this is because each detector provides almost-independent estimates of $\mathcal{M}$ and μ. The result we particularly wish to draw attention to is: *if spins can be treated as negligible then μ can typically be measured to* $\sim 1\%$, while $\mathcal{M}$ can be determined to $\sim 0.01 - 0.1\%$

Table 1 also lists the correlation coefficient $c_{\mathcal{M}\mu} \equiv \Sigma^{\mathcal{M}\mu}/(\Sigma^{\mathcal{M}\mathcal{M}}\,\Sigma^{\mu\mu})^{1/2}$, a dimensionless ratio indicating the degree to which errors in $\mathcal{M}$ and μ are correlated. The quantity $c_{\mathcal{M}\mu}$ is independent of S/N, and by definition satisfies $c_{\mathcal{M}\mu} \in [-1, 1]$. We find that typically $|c_{\mathcal{M}\mu}| > 0.90$, indicating that the errors in $\mathcal{M}$ and μ are strongly correlated. This strong correlation implies that there is some linear combination of $\mathcal{M}$ and μ which can is much more accurately than either one of them [40]. In particular, $\Delta\left(\mathcal{M} - (\Sigma^{\mathcal{M}\mu}/\Sigma^{\mu\mu})\,\mu\right)$ is smaller than $\Delta\mathcal{M}$ by a factor of $\sim (1 - c^2_{\mathcal{M}\mu})^{-1/2}$. Hence, the combination $\mathcal{M} - \sqrt{\Sigma^{\mathcal{M}\mathcal{M}}/\Sigma^{\mu\mu}}\,\mu$ can be determined with approximately the same accuracy [cf. Eqs. (2.3) above] with which one *could* determine $\mathcal{M}$, *if* the waveform were given by the Newtonian expression (5.23) [40].

How accurately can the individual masses M_1 and M_2 be determined? While it is straightforward to answer this question when the mass ratio is large, we shall see that some care is required when M_1 and M_2 are comparable, since in this case the distribution of errors in M_1, M_2 is non-Gaussian. Recall that we have adopted

the convention that $M_1 \geq M_2$. Then we have

$$M_{1,2} = \frac{1}{2}\left[\mathcal{M}^{5/2}\,\mu^{-3/2} \pm \left(\mathcal{M}^5\,\mu^{-3} - 4\mathcal{M}^{5/2}\,\mu^{-1/2}\right)^{1/2}\right]. \tag{5.52}$$

Using Eq. (5.52), $\Sigma^{M_1M_1}$ and $\Sigma^{M_2M_2}$ can be expressed as linear combinations of $\Sigma^{\mathcal{M}\mathcal{M}}$, $\Sigma^{\mathcal{M}\mu}$, and $\Sigma^{\mu\mu}$. However it is clear from Table 1 that in practice the $\Sigma^{\mu\mu}$ term will give the dominant contribution. Neglecting the terms proportional to $\Sigma^{\mathcal{M}\mathcal{M}}$ and $\Sigma^{\mathcal{M}\mu}$, we find that

$$\Sigma^{M_1M_1} = \Sigma^{\mu\mu}\left[\frac{M(\mu - 3M_1)}{2\mu(M_1 - M_2)}\right]^2 \tag{5.53}$$

$$\Sigma^{M_2M_2} = \Sigma^{\mu\mu}\left[\frac{M(\mu - 3M_2)}{2\mu(M_1 - M_2)}\right]^2. \tag{5.54}$$

For example, if $M_1 = 10M_\odot$ and $M_2 = 1.4M_\odot$, Eqs. (3.1) imply that $\Delta M_1/M_1 \approx 1.9\Delta\mu/\mu$ and $\Delta M_2/M_2 \approx 1.4\Delta\mu/\mu$.

While the expressions (3.1) for $\Sigma^{M_1M_1}$ and $\Sigma^{M_2M_2}$ should be adequate for estimating the distribution of errors when $M_1 \gg M_2$, these expressions unfortunately diverge when $M_1 = M_2$. This divergence is due to the fact that the Jacobian of the transformation $(M_1, M_2) \to (\mathcal{M}, \mu)$ vanishes when $M_1 = M_2$. Of course, the rms mass measurement errors do not actually become infinite. Rather, the *linear* approximation that one typically uses to estimate rms errors loses its validity. That is, the approximation that

$$\begin{aligned}\Delta\tilde{h} \approx\ & \frac{\partial\tilde{h}}{\partial\mathcal{A}}\Delta\mathcal{A} + \frac{\partial\tilde{h}}{\partial\phi_c}\Delta\phi_c + \frac{\partial\tilde{h}}{\partial t_c}\Delta t_c \\ & + \frac{\partial\tilde{h}}{\partial M_1}\Delta M_1 + \frac{\partial\tilde{h}}{\partial M_2}\Delta M_2,\end{aligned} \tag{5.55}$$

for variations $\Delta\tilde{h}$ of a size determined by typical realizations of the noise, becomes inaccurate when $M_1 - M_2 \to 0$, as $\partial\tilde{h}/\partial M_1 + \partial\tilde{h}/\partial M_2 \to 0$ in this limit.

To overcome this problem we proceed as explained in Sec. 5.7 below, and use the PDF for the best-fit values $\hat{\mathcal{M}}$, $\hat{\mu}$ of the parameters $\mathcal{M}$, μ, which is a simply a Gaussian centered on the true parameters $\tilde{\mathcal{M}}$, $\tilde{\mu}$. [Thus, we are considering so-called frequentist errors, cf. Sec. 5.2 below]. Let $\hat{M}_1$ and $\hat{M}_2$ be the corresponding best-fit values for the individual masses. Substituting into this PDF the transformation $\hat{\mathcal{M}} = \mathcal{M}(\hat{M}_1, \hat{M}_2)$ and $\hat{\mu} = \mu(\hat{M}_1, \hat{M}_2)$ yields a non-Gaussian PDF for $\hat{M}_1, \hat{M}_2$, from which we can calculate the 95% confidence limits for $\hat{M}_1$ and $\hat{M}_2$. The use of confidence limits is somewhat crude, in the sense that it leaves out

much of the information contained in the PDF, but it is suitable for our purpose of determining *roughly* how accurately these quantities can be measured. Since $\Delta\mathcal{M}$ is very small, for the purposes of this discussion we can assume $\mathcal{M}$ has been measured exactly. Let $\tilde{\mu}$ is the true value of the binary's reduced mass. Then with 95% confidence $\hat{\mu}$ lies in the interval

$$\tilde{\mu} - 2\Delta\mu < \hat{\mu} < \tilde{\mu} + 2\Delta\mu \tag{5.56}$$

where $\Delta\mu \equiv (\Sigma^{\mu\mu})^{1/2}$ is determined from the variance-covariance matrix. Roughly speaking, a necessary condition for the distribution of $\hat{M}_1$ and $\hat{M}_2$ to be Gaussian is that $\tilde{\mu} + 2\Delta\mu < 2^{-4/5}\,\mathcal{M}$ (so that the μ's 95% confidence interval does not include the equal-mass case).

From Eqs. (5.52) and (5.56) we obtain the following 95% confidence limits on $\hat{M}_1$ and $\hat{M}_2$:

$$M_1(\mathcal{M}, \tilde{\mu} + 2\Delta\mu) < \hat{M}_1 < M_1(\mathcal{M}, \tilde{\mu} - 2\Delta\mu) \tag{5.57}$$

$$M_2(\mathcal{M}, \tilde{\mu} - 2\Delta\mu) < \hat{M}_2 < M_2(\mathcal{M}, \tilde{\mu} + 2\Delta\mu) \tag{5.58}$$

where the functions M_1 and M_2 are given by Eq. (5.52) above. If $\tilde{\mu}+2\Delta\mu$ is greater than the maximum allowed value of μ, then one should replace $\tilde{\mu}+2\Delta\mu$ by $2^{-4/5}\mathcal{M}$ in Eqs. (3.1). For example, if $\mathcal{M} = 1.219M_\odot$, $\tilde{\mu} = 0.7M_\odot$, and $\Delta\mu/\tilde{\mu} = 0.004$ (the NS-NS case), then one can state with 95% confidence that $\hat{M}_1$ and $\hat{M}_2$ lie in the ranges $1.4M_\odot < \hat{M}_1 < 1.65M_\odot$ and $1.2M_\odot < \hat{M}_2 < 1.4M_\odot$. Thus the individual masses are determined with much less accuracy than μ when they are roughly equal.

3.2 Parameter estimation including spin effects

As explained in the Introduction, the high accuracy with which the masses could be extracted from the gravitational waveform, if the spins of the bodies were known to be negligible, is considerably degraded by correlations with the extra parameters for which one must fit when the spins are included. This section represents a rough attempt at calculating these degraded measurement accuracies. For the same reasons as in Sec. 3.1, we incorporate the effects of spins on the phase of the waveform, but neglect their effects on the waveform amplitude.

Let $\vec{S}_1$ and $\vec{S}_2$ be the spin angular momenta of the two bodies, and let $\vec{L}$ be the total orbital angular momentum. We define the unit vector $\hat{L}$ by $\hat{L} \equiv \vec{L}/|\vec{L}|$. Then Kidder, Will, and Wiseman [41] have shown that, due to an "$\vec{L}\cdot\vec{S}$" term in the

two-body force law as well as spin corrections to the expressions for the system's mass-quadrupole and current-quadrupole moments, Eq. (5.42) becomes modified at $P^{1.5}N$ order as follows:

$$\begin{aligned} df/dt &= \frac{96}{5}\pi^{8/3}\mathcal{M}^{5/3}f^{11/3}\Big[1-\Big(\frac{743}{336}+\frac{11\mu}{4M}\Big)x \\ &\quad +(4\pi-\beta)x^{3/2}+O(x^2)\Big] \end{aligned} \tag{5.59}$$

where again $x \equiv (\pi M f)^{2/3}$, and where

$$\beta \equiv M^{-2}\hat{L}\cdot\Big[\Big(\frac{113}{12}+\frac{25}{4}\frac{M_2}{M_1}\Big)\vec{S}_1+\Big(\frac{113}{12}+\frac{25}{4}\frac{M_1}{M_2}\Big)\vec{S}_2\Big]. \tag{5.60}$$

Through $P^{1.5}N$ order, the six components of $\vec{S}_1$ and $\vec{S}_2$ affect the waveform's phase only via the particular combination (5.60). (Of course, other combinations appear at higher order.)

We now discuss the magnitude of the correction due to β. For black holes, one has a strict upper limit on the magnitude of the spins: $|\vec{S}_i| \leq M_i^2$. This is also roughly the upper limit for neutron stars, though the actual upper limit depends on the (uncertain) nuclear equation of state. We can therefore estimate the maximum size of β by considering the case where the spins are aligned with $\vec{L}$, and where $|\vec{S}_1|/M_1^2 = |\vec{S}_2|/M_2^2 = 1$. In this case $\beta = \frac{113}{12} - \frac{19}{12}(4\mu/M)$. This maximum value β_{max} is always within 10% of 8.5, regardless of the mass ratio.

The $P^{1.5}N$ order equations of motion also contain "$\vec{L}\times\vec{S}$" terms, which do not directly affect df/dt, but do so indirectly by causing the directions of $\hat{L}$, $\vec{S}_1$ and $\vec{S}_2$ to precess during the inspiral. One can think of this precession as an example of the Lense-Thirring effect. The following equations describe the secular evolution of $\hat{L}$, $\vec{S}_1$ and $\vec{S}_2$ through P^2N order [42]:

$$\frac{d\hat{L}}{dt} = r^{-3}\Big[a_1\vec{S}_1+a_2\vec{S}_2-\frac{3}{2}\frac{(\vec{S}_2\cdot\hat{L})\vec{S}_1+(\vec{S}_1\cdot\hat{L})\vec{S}_2}{L}\Big]\times\hat{L} \tag{5.61}$$

$$\frac{d\vec{S}_1}{dt} = r^{-3}\Big[a_1 L\hat{L}+\frac{1}{2}\vec{S}_2-\frac{3}{2}(\vec{S}_2\cdot\hat{L})\hat{L}\Big]\times\vec{S}_1 \tag{5.62}$$

$$\frac{d\vec{S}_2}{dt} = r^{-3}\Big[a_2 L\hat{L}+\frac{1}{2}\vec{S}_1-\frac{3}{2}(\vec{S}_1\cdot\hat{L})\hat{L}\Big]\times\vec{S}_2, \tag{5.63}$$

where $a_1 = 2+(3M_2)/(2M_1)$, $a_2 = 2+(3M_1)/(2M_2)$, $L = |\vec{L}| = \mu\sqrt{Mr}$, and where we use the expression (5.14) for $r(t)$.

The precession of $\hat{L}$, $\vec{S}_1$ and $\vec{S}_2$ causes β to evolve; $d\beta/dt$ as calculated from Eqs. (3.2) does not vanish identically. Fortuitously, however, β is *almost* conserved

by Eqs. (3.2), in the following sense. We have integrated these equations numerically from $f = 10\text{Hz}$ to $f = (6^{3/2}\pi M)^{-1}$, for a wide variety of spin magnitudes, initial spin directions, and mass ratios; we found that β never deviates from its average value by more than ~ 0.25 (or $\sim 0.03\beta_{max}$). Moreover, the non-constant part of β is oscillatory, which further diminishes its integrated effect on the waveform's phase. These properties of the evolution of β are explored analytically and numerically in Appendix B.

The near-constancy of β allows a considerable simplification of our model waveform: in Eq. (5.59), we simply take β to be a constant. That is, we treat β as just another parameter, like $\mathcal{M}$ and μ, on which the signal depends. The Fourier transform of our model waveform, including spin effects, is therefore given by

$$\tilde{h}(f) = \begin{cases} \mathcal{A} f^{-7/6} e^{i\Psi} & 0 < f < (6^{3/2}\pi M)^{-1} \\ 0 & (6^{3/2}\pi M)^{-1} < f \end{cases} \tag{5.64}$$

where now

$$\begin{aligned} \Psi(f) &= 2\pi f t_c - \phi_c - \pi/4 + \frac{3}{4}(8\pi\mathcal{M}f)^{-5/3} \\ &\quad \times \left[1 + \frac{20}{9}\left(\frac{743}{336} + \frac{11\mu}{4M}\right)x + (4\beta - 16\pi)\,x^{3/2}\right]. \end{aligned} \tag{5.65}$$

Now, for spinning bodies it is not really correct to treat the amplitude $\mathcal{A} \equiv Q(\theta,\phi,\psi,\iota)D^{-1}\mathcal{M}^{5/6}$ as constant. The precession of the orbital plane described by Eqs. (3.2) causes the angles ψ and ι and to vary—and hence $Q(\theta,\varphi,\psi,\iota)$ to vary—throughout the inspiral. Typically, the orbital plane precesses around the total angular momentum vector $\vec{J} \equiv \vec{L} + \vec{S}_1 + \vec{S}_2$ roughly 20 times during the observable portion of the inspiral. The result is a sinusoidal modulation of the waveform envelope [8, 43], and the amplitude of the modulation can be large when $|\vec{S}_1|$ or $|\vec{S}_2|$ is comparable to $|\vec{L}|$. Nevertheless, in the interest of simplifying the calculation, *in our model waveform* (5.64) *we take* $\mathcal{A}$ *to be a constant.* We discuss futher below the implications of this simplification.

The derivatives $\partial\tilde{h}/\partial\ln\mathcal{A}$, $\partial\tilde{h}/\partial(f_0 t_c)$, and $\partial\tilde{h}/\partial\phi_c$ of the signal (5.64) are given by the same expressions as in Eqs. (3.1). The derivatives of $\tilde{h}(f)$ with respect to $\ln\mathcal{M}$, $\ln\mu$, and β are:

$$\begin{aligned} \frac{\partial\tilde{h}(f)}{\partial\ln\mathcal{M}} &= -\frac{5i}{4}(8\pi\mathcal{M}f)^{-5/3}\tilde{h}(f)\left[1 + \frac{55\mu}{6M}x\right. \\ &\quad \left. + (8\pi - 2\beta)\,x^{3/2}\right] \end{aligned} \tag{5.66}$$

$$\frac{\partial\tilde{h}(f)}{\partial\ln\mu} = \frac{3i}{4}(8\pi\mathcal{M}f)^{-5/3}\,\tilde{h}(f)\left[\left(\frac{-3715}{756}+\frac{55\mu}{6M}\right)x + (24\pi-6\beta)\,x^{3/2}\right] \tag{5.67}$$

$$\frac{\partial\tilde{h}(f)}{\partial\beta} = 3i\,(8\pi\mathcal{M}f)^{-5/3}(\pi Mf)\,\tilde{h}(f). \tag{5.68}$$

Using Eqs. (3.2) we again compute the variance-covariance matrix Σ^{ij} for a range of values of M_1 and M_2. One can show that $\Delta\phi_c$, Δt_c, $\Delta\mathcal{M}/\mathcal{M}$, and $\Delta\mu/\mu$ do not depend the value of β. The simple way to prove this is to make a change of variables from $(\mathcal{A},\phi_c,t_c,\mathcal{M},\mu,\beta)$ to $(\mathcal{A},\phi_c,t_c,\mathcal{M},\mu,\beta')$, where

$$\beta' \equiv (4\beta-16\pi)\,\mathcal{M}^{5/6}\mu^{-3/2}. \tag{5.69}$$

Since the waveform phase $\Psi(f)$ [Eq. (5.65)] depends linearly on $\beta' f^{-2/3}$, the Fisher information matrix calculated with respect to the new variables is independent of β'. This implies that the rms errors in the *other* parameters, and their correlation coefficients, are independent of the value of β. The values of $\Delta\beta$, $c_{\mathcal{M}\beta}$ and $c_{\mu\beta}$ do depend on β, however.

In Table 2 we list the rms errors $\Delta\phi_c$, Δt_c, $\Delta\mathcal{M}/\mathcal{M}$, $\Delta\mu/\mu$, and $\Delta\beta$ for the same fiducial binaries that appear in Table 1. In computing the results in Table 2 we use the model of the advanced detector noise curve given by Eq. (2.1). Since we are principally concerned with how our lack of knowledge of the bodies' spins affects how well we can determine the *other* parameters, we take the "true" value of β to be zero in all cases. As in Table 1, the results in Table 2 are for a single detector and are normalized to $S/N = 10$; for a detector network, the rms errors $\Delta\mathcal{M}/\mathcal{M}$, and $\Delta\mu/\mu$ and $\Delta\beta$ will be approximately those given in Table 2, but with S/N replaced by the combined signal-to-noise ratio ρ.

Summarizing the results of Table 2, we find that $\Delta\mathcal{M}/\mathcal{M}$ is roughly an order of magnitude larger than predicted by the Newtonian analysis of Sec. 2. Nevertheless, we find that $\Delta\mathcal{M}/\mathcal{M}$ is typically less than 0.1%. Thus, despite the "confusion" introduced by the extra parameters that enter at post-Newtonian order, we conclude that $\mathcal{M}$ can still be measured with remarkable accuracy. However, compared to the case where the bodies are assumed to have negligible spin *a priori*, we see that $\Delta\mu$ has increased by a factor which ranges from 20 to 60!

Table 2 also reveals the "reason" for this loss of accuracy: the correlation coefficient $c_{\mu\beta}$ is extremely close to -1 [40]. Clearly the strong correlation is due to the fact that the frequency dependence of the "$\vec{L}\cdot\vec{S}$" term in the expression

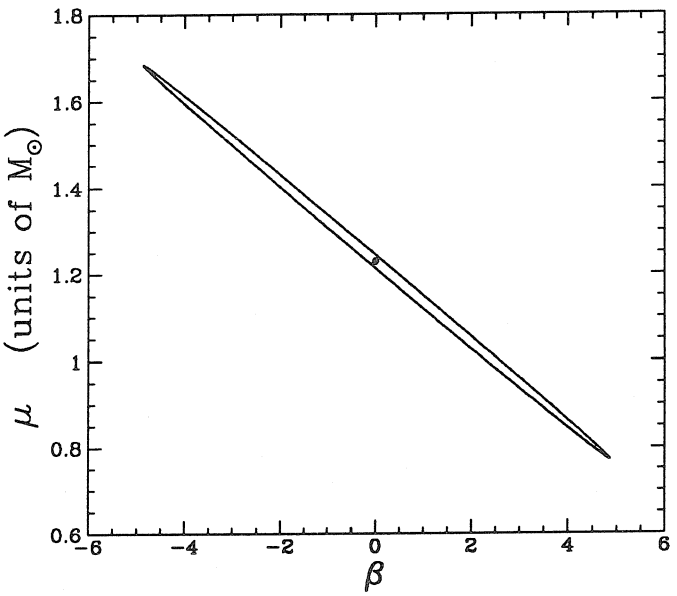

Figure 5.3: This plot shows the curve of constant probability on the $\mu\beta$ plane for a NS-BH binary, where μ is the binary's reduced mass and β is a dimensionsless spin-related parameter, such that the true values of these parameters lie inside the ellipse with 95% confidence. The strong correlation between possible values of μ and β is evident. To a good approximation, the chirp mass $\mathcal{M}$ is measured to arbitrarily high accuracy. Hence in the three-dimensional space of the parameters $(\mathcal{M}, \mu, \beta)$, the true values of these parameters are confined with high confidence to a thin strip of the above ellipsoidal shape in a plane of constant $\mathcal{M}$.

(5.65) for the waveform phase $\Psi(f)$ is very similar to the frequency dependence of the other post-Newtonian terms in Eq. (5.65). This strong correlation implies that there is a combination of μ and β which can be determined to much higher accuracy than μ itself [40]. Specifically, $\Delta\left(\mu - (\Sigma^{\mu\beta}/\Sigma^{\beta\beta})\,\beta\right)$ is smaller than $\Delta\mu$ by a factor of $\sim (1 - c_{\mu\beta}^2)^{-1/2}$, which is approximately $20 - 60$ for the cases in Table 2. Thus the combination $\mu + \sqrt{\Sigma^{\mu\mu}/\Sigma^{\beta\beta}}\,\beta$ can be determined with approximately the same accuracy that one *could* achieve for μ, *if* spin effects could be neglected [cf. Table 1]. Since both $\mathcal{M}$ and this particular combination of μ and β can be determined to high accuracy, the inspiral gravitational wave measurement essentially constrains the parameters to lie near a thin two-dimensional strip in $(\mathcal{M}, \mu, \beta)$ space. This is illustrated in Fig. 5.3, for the case of a BH-NS binary.

Up to this point, the formalism we have been using to calculate measurement accuracies neglects *a priori* constraints on the parameters, and thus implicitly assumes that β can take on arbitrary values. This assumption should be adequate as long as the 95% confidence intervals determined from $\Sigma^{\beta\beta}$ are well within the "allowed" range: $|\beta| \leq \beta_{max} \approx 8.5$. However we see from Table 2 that this criterion is not satisfied when both bodies are heavier than a few solar masses. For example, when $M_1 = M_2 = 10M_\odot$ we calculate $\Delta\beta = 19.5$. We can (somewhat crudely) incorporate the restricted range of β into our formalism, as follows. We replace the *a priori* information $|\beta| < \beta_{\max}$ at hand by an assumed Gaussian distribution $p^{(0)}(\beta) \propto e^{-\frac{1}{2}(\beta/5)^2}$ for β. In Appendix A we derive an expression for the variance-covariance matrix which incorporates the effect of an (assumed Gaussian) *a priori* probability distribution for the signal parameters. We have used this result [Eq. (5.172) below] to re-evaluate the variance-covariance matrix for the two high-mass binaries shown in Table 2. (Taking the restricted range of β into account makes little difference to the other cases in Table 2.) These re-evaluated results are marked in Table 2 with a dagger (†). Again, the rms errors listed are for $S/N = 10$; note however that since $p^{(0)}(\beta)$ is fixed, the rms errors no longer scale simply as $(S/N)^{-1}$. We see that taking the restricted range of β into account leads to the improved estimate $\Delta\mu/\mu \approx 50\%$ in both the high-mass cases.

We mentioned above that in the three known NS-NS binaries that will merge in a Hubble time, the radio pulsars all have spin angular momenta that are $\sim 2\%$ of their maximum possible values. We feel it is an interesting exercise to calculate what

We now calculate the measurement accuracies that could be attained if we knew that NS's in nature were slowly spinning in general, e.g., if we knew *a priori* that

$\beta < .02\beta_{max}$. Repeating the procedure used above, we take $p^{(0)}(\beta) \propto e^{-\frac{1}{2}(\beta/0.1)^2}$, and we use Eq. (5.172) to calculate the variance-covariance matrix for the NS-NS case, for $S/N = 10$. We find $\Delta\mu/\mu \approx 0.9\%$, which is roughly twice the value obtained in Sec. 3.1, where spin effects were taken to be completely negligible.

We turn again to the question of how accurately the individual masses can be measured. The procedure for calculating ΔM_1 and ΔM_2 in terms of $\Delta\mathcal{M}$ and $\Delta\mu$ is of course the same as described in Sec. 3.1. Thus for the BH-NS case, using the fact that $\Delta\mu/\mu \approx 15\%$, we find from Eqs. (3.1) that $\Delta M_1/M_1 \approx 30\%$ and $\Delta M_2/M_2 \approx 20\%$. In Sec. 3.1 we explained that the distribution of errors in M_1 and M_2 will be non-Gaussian if $\mu + 2\Delta\mu > 2^{-4/5}\,\mathcal{M}$. By this criterion, if $\Delta\mu/\mu \approx 15\%$, then we can reliably estimate ΔM_1 and ΔM_2 by using Eqs. (3.1) only if $M_1/M_2 \geq 5.5$

Again, even when the Gaussian approximation is invalid, one can still use Eqs. (3.1) to place 95% confidence limits on M_1 and M_2. Consider again the NS-NS case, which we looked at in this context in Sec. 3.1, with the *true* values of the masses being $M_1 = M_2 = 1.4M_\odot$. Then $\mathcal{M} = 1.22M_\odot$, and, using the 2σ error bar indicated by Table 2 (for $S/N = 10$) we see that, 95% of the time, the observers would measure μ to be between $0.56M_\odot$ and $0.70M_\odot$. Correspondingly, the measured values of M_1 and M_2 would lie in the ranges $1.4M_\odot < \hat{M}_1 < 3.2M_\odot$ and $0.7M_\odot < \hat{M}_2 < 1.4M_\odot$. Thus, in the NS-NS case, measuring μ to within 20% means determining the individual masses only to within a factor of ~ 2. The constraints obtained on M_1 and M_2, for this case and the BH-NS case, are illustrated in Fig. 5.4.

Finally, we repeat these calculations using the flatter spectrum (5.5) instead of (5.4) as our model of the advanced detector noise. The results are shown in table 3. We see that the main conclusions which we drew from table 2 are unchanged, but that (for fixed signal-to-noise) the relative errors $\Delta\mathcal{M}/\mathcal{M}$ and $\Delta\mu/\mu$ are a factor of ~ 1.5 times smaller with the flatter noise spectrum (5.5). This is presumably due to the fact that noise spectrum (5.5) exhibits better sensitivity at low frequencies, where most of the gravitational wave cycles (and hence most of the sensitivity) come from.

3.3 Caveats

Since the results in Tables 1–3 were obtained using several approximations and simplifying assumptions, we feel that it is useful to collect the most important of

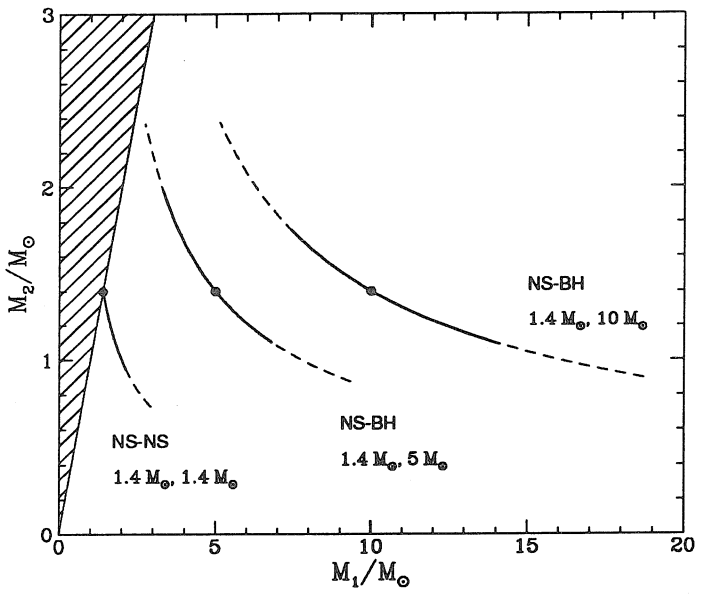

Figure 5.4: A diagram showing the information obtained from the gravity wave signal, constraining the individual masses M_1 and M_2 of the binary components, in various cases. Because of the highly accurate measurement of the chirp mass $\mathcal{M}$ in each case, the individual masses are essentially constrained to lie on a curve of constant $\mathcal{M}$ in the $M_1\,M_2$ plane. It can be seen that the measured value of $\mathcal{M}$ provides a sharp lower bound for the larger mass M_1, and a sharp upper bound for the smaller mass M_2, since the constant-$\mathcal{M}$ curves terminate sharply at the forbidden, hatched region. The measurement of the reduced mass μ gives some (but not much) information about where along the constant $\mathcal{M}$ curve the binary is most likely to be located. In each case, the solid circles show the true values of M_1 and M_2, the solid curve denotes the 68% (1 sigma) confidence interval, and the dashed extension denotes the 95% (2 sigma) confidence interval. The detector noise spectrum (5.4) was assumed.

these in one place. They are as follows:

First, we restricted attention to statistical errors arising from detector noise. In practice, theoretical template waveforms will be quite difficult to compute accurately [8, 13]. Hence some systematic error may also arise from fitting the data to imperfect template waveforms.

Second, we assumed the "advanced LIGO" noise-curve shape, for which we have used two estimates: Eq. (5.4) and Eq. (5.5). As emphasized above, these are only rough estimates of the spectral shape that the LIGO/VIRGO detectors will actually achieve. We have seen, however, that our results do not depend very sensitively on the exact shape of the noise spectrum.

Third, we have used the approximate, linearized error-estimation formalism described in Sec. 2.2 and Appendix A; the rms errors so calculated are guaranteed to be accurate only in the limit that the errors are small. When the errors are so large that the linearized approach is invalid, then our approach will probably generally underestimate the true variances. To avoid the limitations of the linearized error analysis, we are currently performing a Monte-Carlo simulation of the parameter extraction process.

Fourth, we calculated the variance-covariance matrix Σ^{ij} using the simplified model waveform (5.64), which is qualitatively inaccurate in a number of respects. In particular, our model waveform depends on the spins of the two bodies only through a single parameter, β. We have neglected the spin-induced precession of the orbital plane, which also arises at $P^{1.5}N$ order, and we have neglected the effect of the spin-spin coupling on inspiral rate, which arises at P^2N order. Besides neglecting these other spin components we have neglected higher-order multipole radiation (except insofar as the energy carried away by the higher multipoles affects the inspiral rate). And we have only crudely modeled the cut-off of the waveform during the bodies' final tidal-disruption, plunge, or coalescence. [In particular, we have made no attempt to model the spin dependence of the cut-off. It is possible that with dual-recycling detectors, which can be tuned to have good sensitivity in a narrow, high-frequency band [44], one could use the last few cycles of the gravity wave signal to help disentangle the μ and β parameters.]

It is unclear to us whether the inadequacies of our model waveform have led us to underestimate or overestimate parameter-extraction accuracies. On the one hand, the P^2N spin-spin interaction term that we have neglected would, if included, inevitably lead to some degradation of parameter-extraction accuracy (as always happens when there are more parameters to fit for). On the other hand, it

seems clear that the effect on $\Delta\mu$ of adding the spin-spin term to the waveform will be far less dramatic than the inclusion of the spin-orbit term β, for two reasons: (i) as shown by Kidder *et al.* [41], for the BH-NS and NS-NS cases, the effect of the spin-spin term on the accumulated phase of the waveform is a factor of at least 20 smaller than the effect of the spin-orbit term, and (ii) the correlation coefficient $|c_{\mu\beta}|$ is so close to 1 because the frequency dependences of the μ and β terms in the waveform phase $\Psi(f)$ are so similar; the μ and spin-spin terms are less similar in their frequency dependence.

Also, by neglecting higher-order multipoles, spin-precession effects, and the details of the final plunge, we have effectively thrown away information that would be contained in the true waveform. In a more complete analysis, this "additional" information could perhaps decrease measurement uncertainties.

4 ACCURACY OF DISTANCE MEASUREMENTS

4.1 Overview

In the previous sections we have investigated how accurately the masses of the inspiraling compact objects can be measured from the phase evolution of the detected gravitational waveforms. The other interesting parameters that are measurable from the outputs of a network of detectors are the distance D to the source, and the angles θ and φ giving its position on the sky. These will be encoded in the amplitudes, phases and arrival times of the signals $h_a(t)$ read out from the detectors. At least three geographically separated detectors will be needed in order to determine the distance [6]. We first describe, in detail, the dependence of the signals $h_a(t)$ on the variables D, θ, and φ.

Let $\mathbf{x}_a$ be the position and $\mathbf{d}_a$ be the polarization tensor of the ath detector in a detector network. By polarization tensor we mean that tensor $\mathbf{d}_a$ for which the detector's output is given in terms of the waves' transverse traceless strain tensor $\mathbf{h}(\mathbf{x}, t)$ by

$$h_a(t) = \mathbf{d}_a : \mathbf{h}(\mathbf{x}_a, t). \tag{5.70}$$

Here the colon denotes a double contraction. If the arms of the detector are in the directions of the unit vectors l and $\mathbf{m}$, then $\mathbf{d}_a = (l \otimes l - \mathbf{m} \otimes \mathbf{m})/2$ [45]. Let $\mathbf{n}$ be a unit vector in the direction given by the angles θ, φ, and let $\mathbf{e}_\mathbf{n}^+$ and $\mathbf{e}_\mathbf{n}^\times$ be a basis for the transverse traceless tensors perpendicular to $\mathbf{n}$. If we demand in the usual way that $\mathbf{e}_\mathbf{n}^A : \mathbf{e}_\mathbf{n}^B = 2\delta^{AB}$, for $A, B = +, \times$, then this basis is unique up to

rotations of the form

$$\mathrm{e}^{+} + i\mathrm{e}^{\times} \to e^{2i\Delta\psi}(\mathrm{e}^{+} + i\mathrm{e}^{\times}). \tag{5.71}$$

The quantities

$$F_a^A(\mathrm{n}) \equiv \mathrm{e}_{\mathrm{n}}^A : \mathrm{d}_a, \tag{5.72}$$

for $A = +, \times$, are the so-called detector beam-pattern functions for the ath detector [12].

A gravitational wave burst coming from the direction n will have the form $\mathrm{h}(t) = h_+(t)\mathrm{e}_{\mathrm{n}}^+ + h_\times(t)\mathrm{e}_{\mathrm{n}}^\times$. By combining the expressions given in Ref. [12] for the waveforms h_+ and $h_\times$ for a coalescing binary source in the quadrupole-moment approximation, together with Eqs. (5.70) and (5.72), we obtain the (Fourier transform of) the signal read out from the ath detector:

$$\tilde{h}_a(f) = R^A{}_B(2\psi)\,\chi_A(v) F_a^B(\mathrm{n})\, e^{2\pi i \tau_a f}\, \tilde{h}_0(f), \tag{5.73}$$

where

$$\tilde{h}_0(f) = \sqrt{\frac{5}{24}}\pi^{-2/3} D^{-1} \mathcal{M}^{5/6} f^{-7/6} \exp\left[i\Psi(f)\right] \tag{5.74}$$

for $f \geq 0$. The phase $\Psi(f)$ is the same as previously given in Eq. (5.65), and depends only on the parameters $\mathcal{M}$, μ, β, t_c, and ϕ_c [46]. In the above equations v denotes $\cos(\iota)$, where ι is the inclination angle between the line of sight and the normal to the plane of the orbit, ψ is a polarization angle, $\tau_a = -\mathrm{n}\cdot\mathrm{x}_a$, $\chi_+(v) = v$, $\chi_\times(v) = i\,(1+v^2)/2$ [47], and $R^A{}_B$ is the rotation matrix

$$R^A{}_B(2\psi) = \begin{pmatrix} \cos(2\psi) & \sin(2\psi) \\ -\sin(2\psi) & \cos(2\psi) \end{pmatrix}. \tag{5.75}$$

The first three factors in Eq. (5.73) taken together are proportional the quantity $Q(\theta, \varphi, \psi, \iota)$ that appears in Eqs. (5.15) and (5.23).

Now the overall amplitude $\mathcal{A}$ of the signal at one detector can be measured to an accuracy (cf. Sec. 2)

$$\frac{\Delta\mathcal{A}}{\mathcal{A}} = \frac{1}{\rho_a}, \tag{5.76}$$

where $\rho_a = (h_a \,|\, h_a)^{1/2}$ is the signal to noise ratio (SNR) measured at that detector. Since

$$\mathcal{A} \propto \frac{Q(\theta, \varphi, \psi, \iota)}{D} \tag{5.77}$$

we expect the accuracy of distance measurements to be very roughly $\Delta D/D \approx 1/\rho$, where $\rho^2 = \sum \rho_a^2$ is the SNR (5.155), giving an accuracy of $\sim$ 10% for typical

detected signals. However from Eq. (5.77) the signal amplitudes are also strongly affected by the angles θ, φ, ψ, and most importantly the inclination angle ι. Hence, there will be correlations between the measured values of D and of these angles, and the accuracy of distance measurement will be reduced relative to the above naive estimate based on Eq. (5.76).

It is straightforward in principle to calculate the effect of all the correlations by calculating the Fisher information matrix (5.10) from the waveform (5.73) for all of the variables D, $\mathbf{n}$, v, and ψ together with the variables $\mathcal{M}$, ϕ_c, t_c, μ and β discussed in Secs. 2 and 3. An analysis of this sort, but without including the post-Newtonian parameters μ and β, has been carried out by Jaranowski and Krolak [15], who numerically calculate the rms error ΔD for various different values of the angular variables. They use the three detector network consisting of the two LIGO detectors and the VIRGO detector in Pisa, Italy, with their planned orientations. Although these authors do not take into account post-Newtonian effects, it seems likely, for reasons which we discuss below in Sec. 4.3 and Appendix C, that their results for ΔD will not be sensitive to this restriction. Similar numerical calculations have been carried out by Marković [9], who assumed the same network of detectors. He identified a useful approximation for calculating $\Delta D/D$, based on identifying those variables with which the distance measurement is most strongly correlated, and neglecting the effect of the much smaller correlations with the other variables.

In this section we present an analytic calculation of $\Delta D/D$ which simplifies the treatments given in Refs. [9, 15]. Our analysis focuses on the information contained in the amplitude and polarization of the detected waves, and thus is largely complementary to the detailed analysis of the phase-evolution information in Sec. 3 above. Because the rms error ΔD depends on several angular variables, it is difficult to explore its behavior over the whole parameter space using numerical calculations of the type in Refs. [9, 15]. Here, by using Marković's approximation, we derive an approximate analytic expression for ΔD, which is valid for any network of detectors.

We also extend the analysis of Refs. [9, 15] in the following two respects. First, we parametrize the dependence of the result on the positions and orientations of all of the detectors in the following useful way. We show that, for a given position θ, φ on the sky, the detector network parameters influence ΔD *only* through (i) the selection of a preferred polarization basis $(\mathbf{e}^+, \mathbf{e}^\times)$ [or equivalently a preferred polarization angle $\psi(\mathbf{n})$, cf. Eq. (5.71) above], and (ii) two quantities $\sigma_D(\mathbf{n})$ and

$\varepsilon_D(\mathbf{n})$, where we call $\sigma_D(\mathbf{n})$ the amplitude sensitivity and $1-\varepsilon_D(\mathbf{n})$ the polarization sensitivity [48]. These quantities are defined in such a way that the total signal-to-noise ratio squared (5.155) of a detected signal coming from the direction n with polarization ψ is of the form [cf. Eq. (5.90) below]

$$\rho^2 \propto \sigma_D(\mathbf{n})\,[1+\varepsilon_D(\mathbf{n})\cos(4\psi+\text{const})\,f(v)\,], \tag{5.78}$$

where the function

$$f(v) \equiv \frac{-(1-v^2)^2}{1+6v^2+v^4} \tag{5.79}$$

is independent of n and ψ. The values of σ_D and ε_D are, as an example, $\sigma_D = 1$ and $\varepsilon_D = 0$ for the case of two detectors at the same location, rotated with respect to each other by 45°, and for vertically incident waves. In Figs. 5.5 and 5.6 below we show plots of these quantities as functions of the angles θ and φ, for the 3-detector, LIGO/VIRGO network.

Second, we extend the analysis beyond the linear, Gaussian approximation outlined in Appendix A, which is normally used to estimate the rms errors. We do this by calculating the exact (within the Marković approximation), non-Gaussian probability distribution for the distance D which incorporates both our *a priori* knowledge and the information obtained from a gravitational wave measurement. This extension becomes important in two different regimes. The first regime is when $v = \cos\iota \to 1$, corresponding to binaries that we perceive to be almost face-on. In the limit $v \to 1$, the value of ΔD predicted by the linear approximation becomes infinite. As shown by Marković [9], this is because two of the signal parameters become degenerate (i.e., the derivatives $\partial\mathbf{h}/\partial\theta^i$ become linearly dependent) as $v \to 1$. Marković gave rough estimates of the effect of this breakdown of the linear formalism on the predicted value of ΔD; the effect is not treated in the exact numeric calculations of Ref. [15]. Here, using the non-Gaussian distribution for D, we obtain an improved approximation to ΔD near the points of degeneracy. The second regime where our non-Gaussian extension of the error-estimation method is important is the limit of low signal-to-noise, and correspondingly of large relative errors in the measured binary parameters. Since the Fisher matrix method of calculating the rms errors in the measured parameters gives essentially the leading order term in an expansion in powers of $(S/N)^{-1}$, this method will be inaccurate at low values of S/N. By using an approximation which takes into account the dominant effects that are non-linear in $(S/N)^{-1}$, we numerically estimate ΔD for a large number of different values of the parameters n, v, and ψ, and statistically determine the distribution of values of $\Delta D/D$ (see Fig. 5.16 below). We show

that the linear estimates for ΔD can be off by factors $\gtrsim 2$, even for signal-to-noise ratios of more than twice the threshold value for detection, due in some cases to large non-Gaussian tails in the PDF for D. Thus, effects that are non-linear in $(S/N)^{-1}$ are often *not* a small correction for typical detected signals.

Our analyses are applicable to binaries at cosmological distances, provided we interpret D as the luminosity distance to the source, and $\mathcal{M}$ as $(1+z)$ times the true chirp mass, where z is the source's redshift [6, 9, 14]. However, a potentially important effect that we neglect is the spin-induced modulation of the signal amplitudes discussed in Sec. 3.2 and Ref. [43]. Hence, our results for ΔD should be regarded as rough estimates (and probably also as lower limits, since it seems most likely that including spin effects in the computation will increase ΔD). However, the tools we develop below will be useful in future, more complete analyses of distance measurement accuracies.

The layout of the rest of this section is as follows. In Sec. 4.2 we calculate the overall SNR squared $\rho^2 = \sum_a \rho_a^2$ for a general detector network, show how the detectors' locations and orientations influence the result only through the functions $\sigma_D(\mathbf{n})$ and $\varepsilon_D(\mathbf{n})$, and derive formulae for these functions in terms of the polarization tensors $\mathbf{d}_a$ of the detectors. In Sec. 4.3, we explain and justify the Marković approximation, and obtain a simple analytic formula for the rms error ΔD. This formula breaks down in the limit when $v \to 1$, and is valid only in the high signal-to-noise ratio limit; in Secs. 4.4 and 4.5 we obtain an improved approximation to ΔD for finite signal-to-noise ratios, which is finite as $v \to 1$, by calculating an accurate, non-Gaussian probability distribution for D. We use throughout the notations of Appendix A.

4.2 The network functions $\sigma_D(\mathbf{n})$ and $\varepsilon_D(\mathbf{n})$

The overall SNR (5.155) and the Fisher information matrix (5.158) are determined by inner products involving the signal $\mathbf{h}(t)$ and its derivatives $\partial\mathbf{h}/\partial\theta^i$ with respect to the signal parameters θ^i. We now show that a large class of these inner products depends on the network properties [i.e., the detector positions $\mathbf{x}_a$ and polarization tensors $\mathbf{d}_a$] only through the two functions of sky location, $\sigma_D(\mathbf{n})$ and $\varepsilon_D(\mathbf{n})$. We start by defining the complex amplitudes

$$\mathcal{A}_B \equiv R^A{}_B(2\psi)\,\chi_A(v)\,e^{-i\phi_c}/D \tag{5.80}$$

which are intrinsic to the incident waves, and the detector amplitudes

$$\mathcal{A}_a = \sum_{B=+,\times} \mathcal{A}_B F_a^B(\mathrm{n}) \tag{5.81}$$

which characterize the signals seen at the various detectors. In terms of these quantities, the signal (5.73) can be written as

$$\tilde{h}_a(f) = \mathcal{A}_a\, e^{2\pi i \tau_a f}\, \tilde{k}(f), \tag{5.82}$$

where $\tilde{k}(f) \equiv D e^{i\phi_c} \tilde{h}_0(f)$ is independent of D and ϕ_c. The inner product of two signals h and h′ written in this way, with amplitude parameters $\mathcal{A}_A$ and $\mathcal{A}'_A$, is given by Eqs. (5.74), (5.82) and (5.134):

$$(\mathrm{h} \,|\, \mathrm{h}') = \Re\left[\mathcal{A}_a^* \mathcal{A}'_b\, \kappa^{ab}\right] (\tilde{k} \,|\, \tilde{k}). \tag{5.83}$$

Here the positive definite Hermitian matrix κ^{ab} is

$$\kappa^{ab} = \frac{\int_0^\infty df\, f^{-7/3}\, [\mathbf{S}_n(f)^{-1}]^{ab}\; e^{2\pi i f(\tau_b - \tau_a)}}{\int_0^\infty df\, f^{-7/3}/S_n(f)}, \tag{5.84}$$

and $S_n(f)$ in the denominator is the average of the spectral noise densities in all the detectors. If the detectors are all identical, and correlated sources of noise [represented by the off-diagonal elements of $\mathbf{S}_n(f)$] are unimportant, then κ^{ab} is just δ^{ab}.

In terms of the wave amplitudes $\mathcal{A}_A$, the inner product (5.83) is, from Eq. (5.81),

$$(\mathrm{h} \,|\, \mathrm{h}') = \Re\left[\mathcal{A}_A^* \mathcal{A}'_B\, \Theta^{AB}\right] (\tilde{k} \,|\, \tilde{k}), \tag{5.85}$$

where the matrix Θ is given by

$$\Theta^{AB}(\mathrm{n}) = \sum_{a,b} F_a^A(\mathrm{n}) F_b^B(\mathrm{n})\, \kappa^{ab}. \tag{5.86}$$

We see that all inner products of the type (5.83) depend on the network parameters only through the 2×2 Hermitian matrix Θ. Two key simplifications now arise. First, correlated sources of noise will presumably be limited to pairs of detectors at the same detector site, so that the detector-network noise matrix (5.130) will have a block-diagonal form with each block corresponding to a detector site. If the detectors at each site are all oriented the same way, as is likely, then the product of beam pattern functions appearing in Eq. (5.86) will be constant over each block in the indices a, b that corresponds to a non-zero subblock of the matrix $\mathbf{S}_n(f)$.

Hence, from Eqs. (5.84) and (5.86), we see that the imaginary part of Θ will vanish. Second, if we change the basis $\mathbf{e}^+$, $\mathbf{e}^\times$ by a transformation of the form (5.71), which amounts to redefining the polarization angle ψ by

$$\psi \to \bar{\psi} = \psi + \Delta\psi, \tag{5.87}$$

then Θ will transform according to $\Theta \to \mathbf{R}(2\Delta\psi) \cdot \Theta \cdot \mathbf{R}(-2\Delta\psi)$. For fixed $\mathbf{n}$, we can, by choosing $\Delta\psi$ suitably, make Θ diagonal, and so be of the form

$$\Theta = \sigma_D \begin{pmatrix} 1+\varepsilon_D & 0 \\ 0 & 1-\varepsilon_D \end{pmatrix}, \tag{5.88}$$

where $0 \le \varepsilon_D \le 1$. This defines the network functions $\sigma_D(\mathbf{n})$ and $\varepsilon_D(\mathbf{n})$. The required value of $\Delta\psi = \Delta\psi(\mathbf{n})$ is given by

$$\tan(4\Delta\psi) = \frac{2\Theta_{+\times}}{\Theta_{++} + \Theta_{\times\times}}. \tag{5.89}$$

The combined SNR (5.155) can be determined in terms of these network functions by combining Eqs. (5.80), (5.85) and (5.88) to give

$$\rho^2 = \rho_0^2\, \sigma_D(\mathbf{n}) \left[c_0(v) + \varepsilon_D(\mathbf{n})\, c_1(v) \cos(4\bar{\psi}) \right], \tag{5.90}$$

where $c_0(v) = v^2 + (1+v^2)^2/4$, $c_1(v) = v^2 - (1+v^2)^2/4 = -(1-v^2)^2/4$, and $\bar{\psi}$ is given by Eqs. (5.87) and (5.89). The quantity

$$\rho_0^2 \equiv D^{-2}(\tilde{k} \,|\, \tilde{k}) \;=\; (\tilde{h}_0 \,|\, \tilde{h}_0) = 4 \int_0^\infty \frac{|\tilde{h}_0(f)|^2}{S_n(f)}\, df \tag{5.91}$$

appearing in Eq. (5.90) is the SNR that would apply to one detector if a face-on ($v = 1$) binary were directly overhead. From Eqs. (5.74) and (5.91), we find $\rho_0 = r_0/D$, where for the noise spectrum (5.4) the distance r_0 is

$$r_0 = 6.5\,\mathrm{Gpc} \left(\frac{\mathcal{M}}{M_\odot} \right)^{5/6} \left(\frac{f_0}{70\,\mathrm{Hz}} \right)^{-2/3} \left(\frac{S_0}{3 \times 10^{-48}\,\mathrm{sec}} \right)^{-1/2}. \tag{5.92}$$

The fidiucal values of the detector parameters S_0 and f_0 used here are those appropriate for the advanced LIGO detectors [3], cf. Sec. 2 above. Note that the dependence of the SNR (5.90) on the polarization angle ψ vanishes when the binary is perceived to be face-on ($v = 1$), as we would expect physically due to rotational invariance about the line of sight. In the opposite limit of edge-on binaries ($v \to 0$), the incident waves are highly linearly polarized, and the SNR

typically depends strongly on ψ, varying by factors of ~ 10 or more as ψ is varied [see Fig. 5.6 below].

We now turn to evaluating the functions σ_D and ε_D. From Eq. (5.88), it is clear that σ_D is just half of the trace of the matrix Θ, which is invariant under rotations. Using Eqs. (5.72) and (5.86) gives

$$2\sigma_D = \left\{ \sum_A (\mathbf{e}^A_{\mathbf{n}})_{ij} \, (\mathbf{e}^A_{\mathbf{n}})_{kl} \right\} \left\{ \sum_{a,b} \kappa^{ab} \, (\mathbf{d}_a)_{ij} \, (\mathbf{d}_a)_{kl} \right\}. \tag{5.93}$$

If we denote the first term in curly brackets by S_{ijkl}, then it is straightforward to show that

$$\begin{aligned} S_{ijkl} \;=\; & -\delta_{ij}\delta_{kl} + (\delta_{ik}\delta_{jl} + \delta_{il}\delta_{jk}) + (\delta_{ij}n_k n_l + \delta_{kl}n_i n_j) \\ & -(\delta_{ik}n_j n_l + \delta_{il}n_j n_k + \delta_{jk}n_i n_l + \delta_{jl}n_i n_k) \\ & +n_i n_j n_k n_l. \end{aligned} \tag{5.94}$$

This yields for the amplitude sensitivity function the formula

$$\begin{aligned} \sigma_D(\mathbf{n}) \;=\; & \frac{1}{2}\kappa^{ab}\,[\,2\,\mathbf{d}_a : \mathbf{d}_b - 4\,\mathbf{n}\cdot(\mathbf{d}_a\cdot\mathbf{d}_b)\cdot\mathbf{n} \\ & + (\mathbf{n}\cdot\mathbf{d}_a\cdot\mathbf{n})(\mathbf{n}\cdot\mathbf{d}_b\cdot\mathbf{n})\,] \end{aligned} \tag{5.95}$$

where we have used the property $\mathrm{Tr}\,\mathbf{d}_a = 0$.

It is similarly straightforward to evaluate the polarization sensitivity $1-\varepsilon_D(\mathbf{n})$. We introduce the notation

$$\langle \mathbf{d}_a \,|\, \mathbf{d}_b \rangle_n \;\equiv\; (\mathbf{d}_a)_{ij}\, S_{ijkl}\, (\mathbf{d}_b)_{kl} \tag{5.96}$$

$$\;=\; 2\,\mathbf{d}_a^{\perp} : \mathbf{d}_b^{\perp} - (\mathrm{Tr}\,\mathbf{d}_a^{\perp})\,(\mathrm{Tr}\,\mathbf{d}_b^{\perp}), \tag{5.97}$$

where $\mathbf{d}_a^{\perp}$ denotes the projection $(\delta_{ik}-n_i n_k)(\delta_{jl}-n_j n_l)\,(\mathbf{d}_a)_{kl}$ of $\mathbf{d}_a$ perpendicular to $\mathbf{n}$. Then, using the relation from Eq. (5.88) that $\mathrm{Tr}\,\Theta^2 = 2\sigma_D^2(1+\varepsilon_D^2)$, and Eqs. (5.72) and (5.86), gives

$$\varepsilon_D(\mathbf{n})^2 = \frac{1}{2\sigma_D(\mathbf{n})^2} \sum_{abcd} \langle \mathbf{d}_a \,|\, \mathbf{d}_b \rangle_n \, \langle \mathbf{d}_c \,|\, \mathbf{d}_d \rangle_n \, \kappa^{ac}\kappa^{bd} \quad - 1. \tag{5.98}$$

To evaluate σ_D and ε_D for the LIGO/VIRGO detector network, we introduce a spherical polar coordinate system (θ,φ) centered at the Earth so that the axis $\theta = 0$ is the Earth's axis of rotation. The angle φ is longitude and $\pi/2-\theta$ is latitude. Let $\mathbf{e}_{\hat{r}} = \mathbf{n}$, $\mathbf{e}_{\hat{\theta}}$ and $\mathbf{e}_{\hat{\phi}}$ be the usual basis of orthonormal vectors. Then for a detector at position θ,φ on the Earth's surface, such that the angle measured

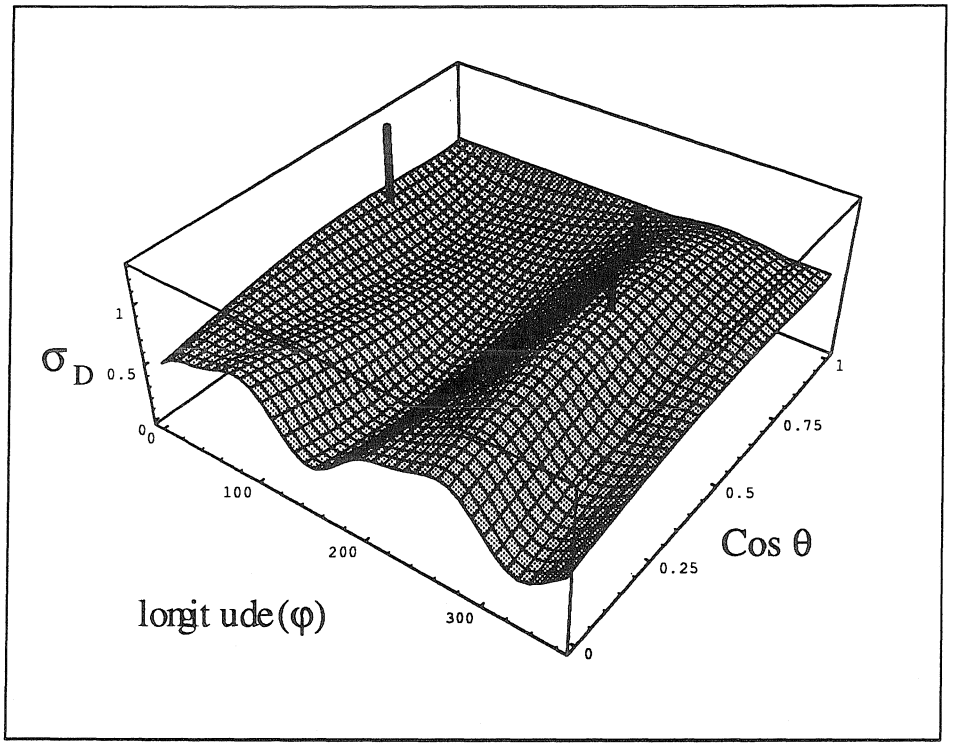

Figure 5.5: The amplitude sensitivity function $\sigma_D(\mathbf{n})$, as a function of position on the sky parametrized by the Earth-fixed coordinates θ and φ, for the detector network consisting of the two LIGO detectors in Hanford, Washington and Livingston, Louisiana, and the VIRGO detector in Pisa, Italy. The axis $\theta = 0$ is the Earth's axis of rotation, and $\varphi = 0$ is 0° longitude. Only sky positions over the northern hemisphere are shown, because σ_D takes the same values at antipodal points. The function $\sigma_D(\mathbf{n})$ has the following meaning: for a source of waves in the direction $\mathbf{n}$, the combined signal-to-noise ratio of the whole network, averaged over all polarization angles ψ of the source (equivalently, averaged over rotations of the source in the plane perpendicular to the line of sight), will be proportional to $\sigma_D(\mathbf{n})$. The thick black lines indicate the positions of the three detectors. This plot can be generated by combining Eqs. (5.95) and (5.99) of the text with the network parameters given after Eq. (5.99).

anticlockwise from the local eastwards directed meridian to the bisector of the detector arms is α, the polarization tensor is

$$\begin{aligned} \mathrm{d} &= -\sin(2\alpha)(\mathrm{e}_{\hat{\theta}} \otimes \mathrm{e}_{\hat{\theta}} - \mathrm{e}_{\hat{\phi}} \otimes \mathrm{e}_{\hat{\phi}})/2 \\ &\quad + \cos(2\alpha)(\mathrm{e}_{\hat{\theta}} \otimes \mathrm{e}_{\hat{\phi}} + \mathrm{e}_{\hat{\phi}} \otimes \mathrm{e}_{\hat{\theta}})/2. \end{aligned} \tag{5.99}$$

The values of $(\theta, \varphi, \alpha)$ for the various detectors are $(59.4°, -90.8°, 243°)$ for the LIGO detector in Hanford, Washington, $(43.5°, -119.4°, 171°)$ for the LIGO detector in Livingston, Louisiana, and $(46.4°, 10.25°, 117°)$ for the VIRGO detector in Pisa, Italy [15]. We assume that the detectors at all three sites are identical and that noise sources are uncorrelated, so that from Eq. (5.84), $\kappa^{ab} = \delta^{ab}$. The resulting plots of σ_D and $1 - \varepsilon_D$ are shown in Figs. 5.5 and 5.6.

4.3 The Marković approximation

We now explain the approximation method used by Marković [9], which we modify slightly below. We start by considering the accuracy $\Delta\mathbf{n}$ with which a given source can be located on the sky. The location $\mathbf{n}$ will be largely determined by "time of flight" measurements between the various detectors, i.e., measurements of the quantities $\tau_a - \tau_b = -\mathbf{n} \cdot (\mathbf{x}_a - \mathbf{x}_b)$ in Eq. (5.73) [6, 15]. Hence, the variables $\mathbf{n}$ and τ_a will be strongly correlated, and $\Delta\mathbf{n}$ will be largely determined by the ratio of the timing accuracies $\Delta(\tau_a - \tau_b)$ to the light travel times between the various detectors. Schutz [6] has estimated the resulting angular resolution to be ~ 1 square degree, which is roughly in agreement with the recent detailed coalescing binary calculations of Jaranowski and Krolak [15]. It is also in rough agreement with numerical simulations of Gürsel and Tinto [7], which were carried out in the context of arbitrary bursts of gravitational waves. Hence, we see from Eq. (5.73) that typical variations in $\mathbf{n}$ will give rise to variations in the measured value of D that are small compared to ΔD. Thus, the correlations between D and $\mathbf{n}$ should be small, and to a good approximation we can treat $\mathbf{n}$ as known when calculating ΔD [9].

In the approximation that $\mathbf{n}$ is constant, we can divide the remaining parameters into two groups. The first consists of the four "amplitude" parameters D, v, ψ, and ϕ_c, which determine the two complex amplitudes $\mathcal{A}_+$ and $\mathcal{A}_\times$ via Eq. (5.80). The second group of parameters consists of $\mathcal{M}$, t_c, μ, together with some spin parameters, which enter only in the phase $\Psi(f)$ of the Fourier transform of the signal, and control the evolution in time of the phase of the waveform [49]. In Appendix

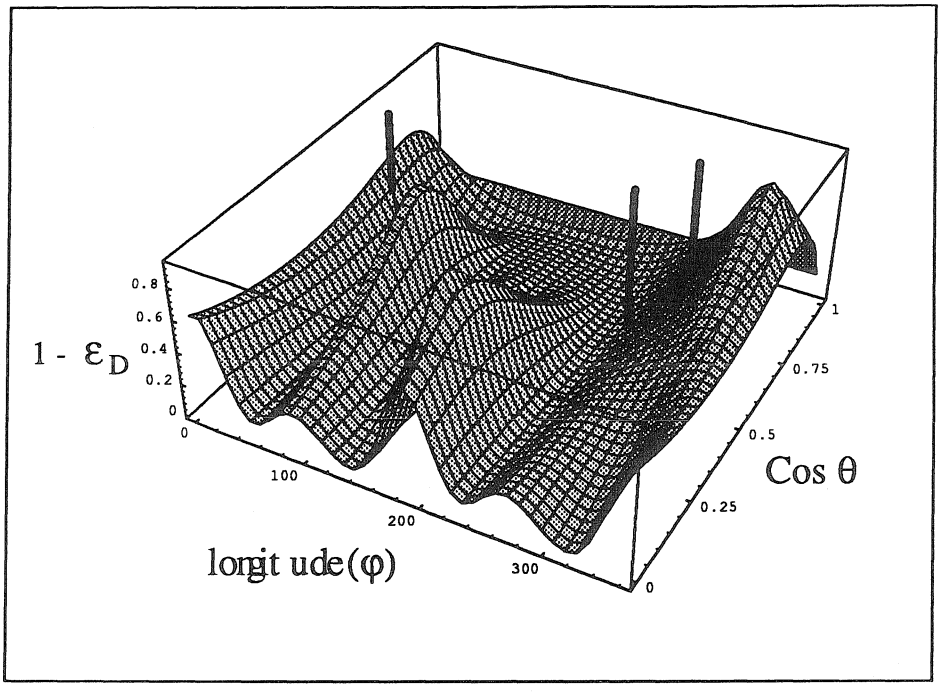

Figure 5.6: The polarization sensitivity function $1 - \varepsilon_D(\mathbf{n})$, for the LIGO/VIRGO detector network; see caption of Fig. 5.5. This plot can be generated by combining Eqs. (5.94), (5.96), (5.98), and (5.99) of the text. The quantity $\varepsilon_D(\mathbf{n})$ essentially measures the "skewness" or asymetry in the sensitivities of the network to the two independent polarization components of waves propagating in the direction $\mathbf{n}$. When $\varepsilon_D \approx 0$, the network has roughly equal sensitivity to both polarization components. When $\varepsilon_D \approx 1$, on the other hand, one polarization component can be measured far more accurately than its orthogonal counterpart. In this case the signal-to-noise ratio for incident, strongly linearly polarized bursts of waves (e.g., those from edge-on coalescing binaries) will depend sensitively on the polarization axis, i.e., it would vary by large factors if the source were rotated in the plane perpendicular to the line of sight. Note that the polarization sensitivity is poor ($\lesssim 0.2$) for directions directly overhead the two LIGO detectors (because the two detectors are nearly parallel), and is typically $\lesssim 0.3$ over most of the sky. Good sensitivity is achieved in isolated regions.

C we show that the second group of parameters decouples from the first to linear order in $1/\rho$, and in the constant $\mathbf{n}$ approximation. More precisely: if one calculates the Fisher matrix (5.158) for all of the variables except $\mathbf{n}$, inverts it to obtain the covariance matrix Σ^{ij}, and takes the 4×4 subblock of Σ^{ij} corresponding to the amplitude group of parameters, then the result is the same as if one computes the Fisher matrix for just the four amplitude parameters alone, and then inverts that. Heuristically what this means is that the effect of the correlations between (D, v, ψ) and all of the parameters $\phi_c, t_c, \mathcal{M}$, etc., can be computed by considering the correlations with just one phase variable, namely ϕ_c, the phase at coalescence [49].

We now calculate the Fisher information matrix (5.158) for the four amplitude parameters D, v, ψ and ϕ_c, and for an arbitrary detector network, as this should yield a good approximation to ΔD. The approximation that was used in Ref. [9] was in fact to consider only D, v, and ψ; below we find [cf. Eqs. (5.101) and (5.103)] that the fractional corrections due to also including ϕ_c are of order $\varepsilon_D(\mathbf{n})\,\sin(4\bar{\psi})$, where $\bar{\psi}$ is given by Eqs. (5.87) and (5.89). Since $0 \leq \varepsilon_D \leq 1$ always, the fractional corrections are always $\lesssim 1$ [50].

From Eq. (5.158), it is clear that the Fisher matrices calculated using two different sets of variables are simply related by transforming with the Jacobian matrix of the variable transformation. Hence, we can use any convenient set of variables to evaluate Γ_{ij} and Σ^{ij}, and afterwards transform to the physical variables of interest. We define the variables α and β by

$$\begin{pmatrix} \alpha \\ \beta \end{pmatrix} = \frac{1}{D} \begin{pmatrix} v \\ (1+v^2)/2 \end{pmatrix}. \tag{5.100}$$

The waveform (5.73) depends linearly on these variables, which simplifies the computation.

Using Eqs. (5.80) – (5.82), (5.85), (5.88), (5.91), (5.158) and the relation $\rho_0 = r_0/D$, we obtain

$$\Gamma_{ij} = r_0^2\, \sigma_D(\mathbf{n})\, [F_{ij} + \varepsilon_D(\mathbf{n})\, G_{ij}]\,, \tag{5.101}$$

where the variables are $\theta^i = (\psi, \alpha, \beta, \phi_c)$. Defining $c_0 = \alpha^2 + \beta^2$, $c_1 = \alpha^2 - \beta^2$, $c_4 = \cos(4\bar{\psi})$, and $s_4 = \sin(4\bar{\psi})$, the matrices $\mathbf{F}$ and $\mathbf{G}$ are given by

$$\mathbf{F} = \begin{bmatrix} 4c_0 & 0 & 0 & 4\alpha\beta \\ 0 & 1 & 0 & 0 \\ 0 & 0 & 1 & 0 \\ 4\alpha\beta & 0 & 0 & c_0 \end{bmatrix} \tag{5.102}$$

and

$$\mathrm{G} = \begin{bmatrix} -4c_1c_4 & -2\alpha s_4 & 2\beta s_4 & 0 \\ -2\alpha s_4 & c_4 & 0 & -\beta s_4 \\ 2\beta s_4 & 0 & -c_4 & \alpha s_4 \\ 0 & -\beta s_4 & \alpha s_4 & c_1c_4 \end{bmatrix}. \tag{5.103}$$

Inverting the matrix (5.101) and taking the 2×2 subblock corresponding to the variables α, β, we find with the help of *Mathematica* that

$$\Sigma^{ij} = \frac{1}{r_0^2\,\sigma_D\,(1-\varepsilon_D^2)} \begin{bmatrix} 1-\varepsilon_D c_4 & 0 \\ 0 & 1+\varepsilon_D c_4 \end{bmatrix}. \tag{5.104}$$

Finally, transforming this with the Jacobian of the transformation (5.100) and taking the (D, D) element of the resulting matrix yields

$$\Delta D^2 = \frac{8D^4}{n_d\, r_0^2}\, \Upsilon(\mathrm{n}, v, \psi)^2, \tag{5.105}$$

where

$$\Upsilon(\mathrm{n}, v, \psi)^2 = \frac{n_d \left[(1+v^2) + \varepsilon_D \cos(4\bar{\psi})\,(1-v^2)\right]}{2\sigma_D\,(1-\varepsilon_D^2)\,(1-v^2)^2}, \tag{5.106}$$

and n_d is the number of detectors. The dimensionless function Υ satisfies

$$\Upsilon(\mathrm{n}, v, \psi) \geq 1, \tag{5.107}$$

since from Eqs. (5.95), (5.97), and (5.88) it follows that $\sigma_D \leq n_d/2$ and $0 \leq \varepsilon_D \leq 1$ always, for any detector network.

Equation (5.105) is the main result of this subsection. We now discuss its properties and range of applicability. First, detailed comparisons show that it reproduces the numerical and graphical results of Jaranowski and Krolak [15] to within a few percent for typical signal-to-noise ratios, which provides justification for the Marković approximation $\Delta \mathrm{n} = 0$ that underlies its derivation. Second, it clearly breaks down and overestimates ΔD when $v \to 1$. As shown by Marković, this is because $\partial \mathrm{h}/\partial D \propto \partial \mathrm{h}/\partial v$ at $v = 1$, so that the linear error-estimation method breaks down. However, it will *underestimate* the true measurement error for sufficiently small values of the SNR ρ, because of the inadequacy of the linear error-estimation formalism in this regime (cf. Appendix A). In Sec. 4.4 below we numerically calculate more accurate values of $\Delta D/D$, and show that even for small values of v, and even for relatively large values of ρ (e.g., $\rho \gtrsim 20$, more than twice the threshold), the results predicted by the formula (5.105) can be off by factors $\gtrsim 2$.

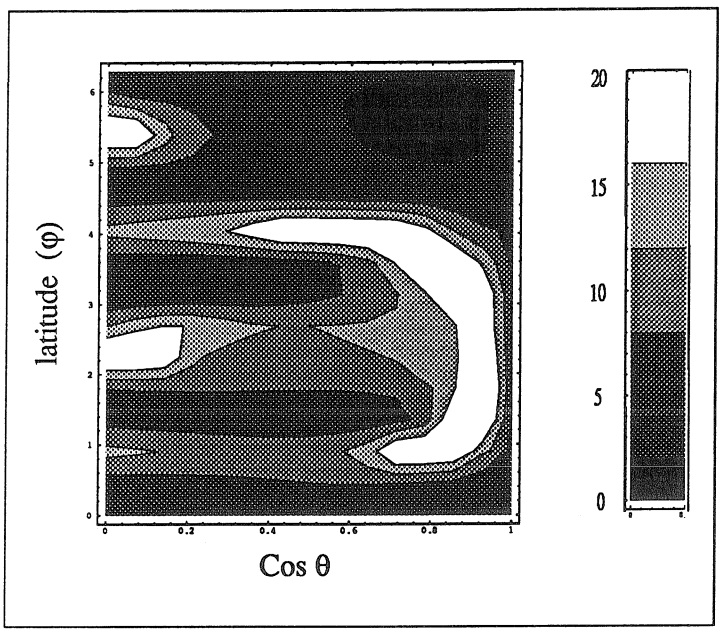

Figure 5.7: The dependence of the distance measurement accuracy $\Delta D/D$ on the sky location $\mathbf{n}$, the polarization angle ψ, and the cosine v of the angle of inclination of the orbit to the line of sight is given by $\Delta D/D \propto \Upsilon(\mathbf{n}, v, \psi)$, where the dimensionless function Υ is defined in Eq. (5.106). Here we plot for the LIGO/VIRGO detector network the quantity $\Upsilon_{\mathbf{max}}$ obtained by maximizing Υ over all polarization angles ψ, at $v^2 = 1/2$, as a function of θ and φ. Higher values of Υ indicated by regions of lighter shading correspond to poorer measurement accuracy.

Hence, the formula (5.105) is of only limited applicablilty. Its main virtue is that it allows one to understand qualitatively how the distance measurement accuracy is influenced by the parameters σ_D, ε_D, ψ, and (to a more limited extent) v; and thereby by using Figs. 5.5 and 5.6 how it varies with sky location $\mathbf{n}$. We now discuss the dependence of $\Delta D/D$ on these parameters.

As the polarization angle ψ is varied, it can be seen that

$$\Upsilon_{\mathbf{min}}(\mathbf{n}, v) \leq \Upsilon(\mathbf{n}, v, \psi) \leq \Upsilon_{\mathbf{max}}(\mathbf{n}, v), \tag{5.108}$$

where $\Upsilon_{\mathbf{min}}$ and $\Upsilon_{\mathbf{max}}$ are given by substituting $\cos(4\bar{\psi}) = \pm 1$ in Eq. (5.106). As an illustration, Figs. 5.7 and 5.8 show $\Upsilon_{\mathbf{min}}$ and $\Upsilon_{\mathbf{max}}$ as functions of $\mathbf{n}$ at $v = 1/\sqrt{2}$. It can be seen that the distance measurement accuracy can vary over the sky by factors of order ~ 20, for binaries at a fixed distance and with fixed

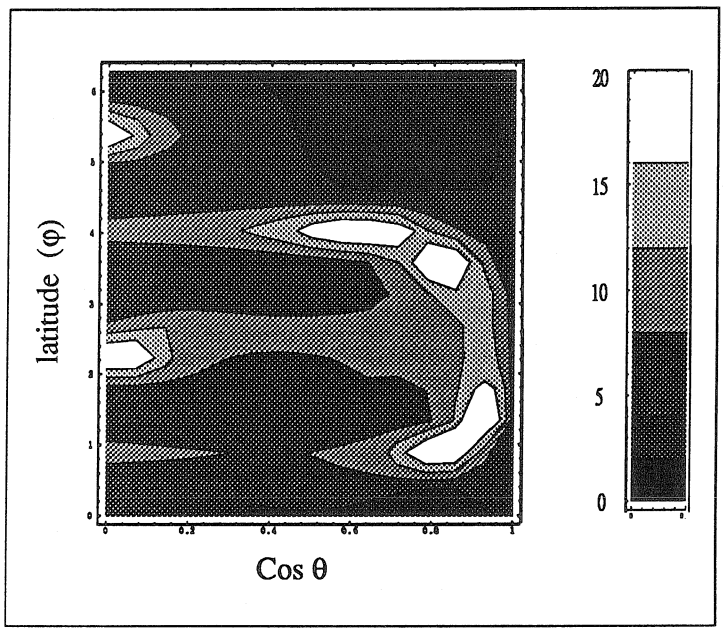

Figure 5.8: The quantity $\Upsilon_{\mathbf{min}}$ which is obtained by minimizing $\Upsilon(\mathbf{n}, v, \psi)$ over ψ, at $v^2 = 1/2$; see caption of Fig. 5.7.

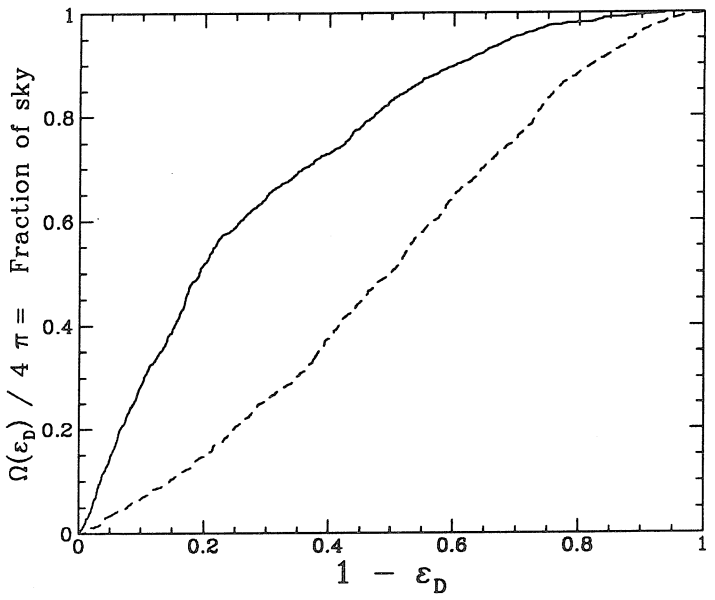

Figure 5.9: The quantity $\Omega(\varepsilon_D)$, which is the solid angle on the sky for which the polarization sensitivity is less than $1 - \varepsilon_D$, for two different detector networks. The solid line indicates the LIGO/VIRGO detector network, and the dashed line a 4-detector network consisting of the LIGO and VIRGO detectors together with a hypothetical detector in Perth, Australia. These plots were generated using 1000 randomly chosen directions n. The great improvement in polarization sensitivity due to the additional detector is apparent: e.g., the polarization sensitivity is ≤ 0.25 over $\sim 60\%$ of the sky for the 3-detector network, but only over $\sim 20\%$ of the sky for the 4-detector network.

inclination angle. The reason for this strong variation of more than an order of magnitude is easy to understand. A key feature of the result (5.106) is the factor of $1/(1 - \varepsilon_D^2)$, which diverges in the limit $\varepsilon_D \to 1$. This divergence is *not* an artifact of our approximate, linear error-estimation method (unlike the divergence in Υ at $v \to 1$). The physical reason for the divergence as $\varepsilon_D \to 1$ is that for directions n such that $1 - \varepsilon_D(\mathbf{n}) \ll 1$, the detector network has very poor ability to disentangle the two polarization components of the incident waves, both of which are needed in order to determine D. As shown in Fig. 5.6, there are large regions on the sky in which the polarization sensitivity $1 - \varepsilon_D$ of the LIGO/VIRGO network is poor, which correspond to the regions of high $\Delta D/D$ in Figs. 5.7 and 5.8 [51].

Part of the reason for the low values of $1 - \varepsilon_D$ for the LIGO/VIRGO network is that the two LIGO detectors are nearly parallel, so that they access essentially

a single polarization component of the gravitational wave field. [They were chosen in this way in order to enhance the reliability of detection of burst sources]. The addition of a fourth detector would greatly improve the polarization sensitivity of the network. In Fig. 5.9 we plot that fraction $\Omega(\varepsilon_D)/4\pi$ of the sky in which the polarization sensitivity is $\leq 1-\varepsilon_D$, for the LIGO/VIRGO network. We also as an illustration plot the same quantity for hypothetical a 4-detector network consisting of the LIGO and VIRGO detectors together with a detector in Perth, Australia, whose parameters [cf. Eq. (5.99) above] are assumed to be $(\theta, \varphi, \alpha) = (121°, 116°, 90°)$.

Lower bounds for $\Delta D/D$ can be obtained by combining Eqs. (5.91), (5.105), and (5.106) and minimizing over $\mathbf{n}$, v, and ψ. If we define

$$\sigma_{\max} = \max_{\mathbf{n}} \sigma_D(\mathbf{n}) \tag{5.109}$$

$$= 1.04 \quad \text{(for LIGO/VIRGO)}, \tag{5.110}$$

we obtain the following lower bounds on $\Delta D/D$:

$$\frac{\Delta D}{D} \geq \frac{2}{\sqrt{\sigma_{\max}}} \frac{D}{r_0}, \tag{5.111}$$

$$\frac{\Delta D}{D} \geq \frac{1}{\rho}, \tag{5.112}$$

together with the upper bound for the overall SNR ρ

$$\rho \leq \sqrt{2\sigma_{\max}}\, \frac{r_0}{D}. \tag{5.113}$$

These bounds remain roughly valid when effects that are nonlinear in r_0/D are approximately taken into account [cf. Figs. 5.13-5.17 below].

4.4 Extension of analysis to beyond the Gaussian approximation

As explained in Appendix A, the Fisher matrix approach to calculating the probability distribution (PDF) for the measured parameters is an approximation whose validity depends in part on the particular set of variables one uses to evaluate the Fisher matrix. In particular, the approximation works best for parameters on which the signal $\mathrm{h}(t)$ depends *linearly*. The key idea for dealing with the degeneracy limit $v \to 1$ is to calculate the Gaussian probability distribution for the amplitudes $\mathcal{A}_A$, which is exact because the signal depends linearly on these amplitudes (see Sec. 5.6 below). Substituting Eq. (5.80) into this PDF then yields

the exact, non-Gaussian distribution for the parameters D, v, ψ and ϕ_c, where we mean "exact" in the context of the Marković approximation $\Delta \mathrm{n} = 0$. From this non-Gaussian distribution, values of ΔD can be determined which are more accurate than those given by Eq. (5.105) in the regime $v \to 1$ and for low signal-to-noise ratios.

In this subsection we calculate so-called Bayesian errors instead of frequentist errors. The distinction is carefully explained in Sec. 5.2 of Appendix A. The distinction is important only beyond leading order in $1/\rho$, and hence unimportant elsewhere in this paper. In practical terms, the use of Bayesian errors means that the rms errors will be expressed as functions of the measured, best-fit values for the source parameters, instead of their true values.

By using Eqs. (5.83) and (5.91) one finds that the exponential factor in Eq. (5.137), given a gravitational wave measurement, is proportional to

$$\exp\left[-\frac{r_0^2}{2}\,(\mathcal{A}_a - \hat{\mathcal{A}}_a)^*(\mathcal{A}_b - \hat{\mathcal{A}}_b)\,\kappa^{ab}\right]. \tag{5.114}$$

Here the quantities $\hat{\mathcal{A}}_a$ are the amplitudes that we measure at each detector (by using matched filtering). The corresponding PDF for the intrinsic amplitudes $\mathcal{A}_A$ is, from Eqs. (5.81) and (5.137),

$$\begin{aligned} p(\mathcal{A}_A) \;&=\; \mathcal{N} p^{(0)}(\mathcal{A}_A) \\ &\quad \times \exp\left[-\frac{r_0^2}{2}\,(\mathcal{A}_A - \hat{\mathcal{A}}_A)^*(\mathcal{A}_B - \hat{\mathcal{A}}_B)\,\Theta^{AB}\right], \end{aligned} \tag{5.115}$$

where

$$\hat{\mathcal{A}}_A \equiv (\Theta^{-1})_{AB} F_a^B \hat{\mathcal{A}}_b\,\kappa^{ab}. \tag{5.116}$$

Here $p^{(0)}(\mathcal{A}_A)$ is our *a priori* PDF for the amplitude parameters, and $\mathcal{N}$ is a normalization constant.

As an aside, Eq. (5.116) provides us with the maximum-likelihood estimator $\hat{D}$ (in the constant n approximation) of the distance to the binary in terms of the measured amplitudes $\hat{\mathcal{A}}_a$. This is because Eq. (5.80), re-expressed in terms of hatted quantities, may be inverted to determine $\hat{D}$ in terms of the $\hat{\mathcal{A}}_A$'s:

$$\hat{D} = \frac{\hat{\beta} - \sqrt{\hat{\beta}^2 - \hat{\alpha}^2}}{\hat{\alpha}^2}, \tag{5.117}$$

where [cf. Eq. (5.100) above]

$$\hat{\alpha}^2 = \frac{1}{2}\left[|\hat{\mathcal{A}}_+|^2 + |\hat{\mathcal{A}}_\times|^2 - |\hat{\mathcal{A}}_+^2 + \hat{\mathcal{A}}_\times^2|\right] \tag{5.118}$$

and

$$\hat{\beta}^2 = \frac{1}{2}\left[|\hat{\mathcal{A}}_+|^2 + |\hat{\mathcal{A}}_\times|^2 + |\hat{\mathcal{A}}_+^2 + \hat{\mathcal{A}}_\times^2|\right]. \tag{5.119}$$

The PDF $p^{(0)}(\mathcal{A}_A)$ in Eq. (5.115) represents our *a priori* information about the distribtion of the parameters $\mathcal{A}_A$ [or eqivalently from Eq. (5.80) of the parameters $(D,\, v,\, \psi,\, \phi_c)$], *given* that a signal has been detected. Since we expect sources to be uniformly distributed in orientation and in space (on the relevant scales of $\gtrsim 100\,\mathrm{Mpc}$), we take

$$\begin{aligned} dp^{(0)} \quad &\propto \quad d\psi\, d\phi_c\, \Theta(1-v^2)\, dv \\ &\qquad \times \Theta(D)\, \Theta(D_{\max} - D)\, D^2 dD. \end{aligned} \tag{5.120}$$

Here Θ is the step function, and the cutoff for distances greater than $D_{\max}$ is a (somewhat crude) representation of our knowledge that very distant sources would not have been detected. A suitable choice for $D_{\max}$ is the distance r_0, cf. Eqs. (5.90) and (5.92) above. Our results below are insensitive to the exact location of this cutoff, but it must be included to make the PDF (5.115) formally normalizable. Now let D_0, v_0, ψ_0 and ϕ_{c0} be the parameters obtained from the amplitudes $\hat{\mathcal{A}}_A$ by inverting Eq. (5.80), so that, in particular, $D_0 = \hat{D}$. Substituting Eqs. (5.80) and (5.120) into (5.115) yields a non-Gaussian PDF for the variables $(D,\, v,\, \psi,\, \phi_c)$ which depends on the parameters $(D_0,\, v_0,\, \psi_0,\, \phi_{c0})$. From this PDF it is straightforward in principle to calculate ΔD, by first integrating over v, ψ, and ϕ_c to determine the reduced PDF $p(D)$ for D alone. If one first expands the argument of the exponential to second order in the quantities $D - D_0$, $v - v_0$, $\psi - \psi_0$, and $\phi_c - \phi_{c0}$, the result obtained is just Eq. (5.105) above, which is accurate to linear order in $1/\rho$.

Thus, in order to go beyond this linear approximation, one has to integrate the PDF (5.115) over v, ψ and ϕ_c. Because this is difficult to do exactly, we now make an approximation which treats the correlations between D and (ψ, ϕ_c) to linear order in $1/\rho$, but treats more precisely the strong correlations bewteen D and v. This approximation should give rough estimates of effects that are nonlinear in $1/\rho$, and moreover removes the singularity in our previous result (5.105) at $v = 1$. The approximation consists of expanding the argument of the exponential in Eq. (5.115) to second order in $\psi - \psi_0$ and $\phi_c - \phi_{c0}$, and integrating over ψ and ϕ_c. One then obtains a function of v, D, v_0, D_0, and ψ_0; the dependence on ϕ_{c0} drops out. This function is of the form (prefactor) $\times$ (exponential factor). The prefactor depends only weakly on D and v in comparison to the exponential factor, so we can approximate it to be constant [52]. We then obtain the following PDF,

which may also be obtained by substituting the transformation (5.100) into the Gaussian PDF for the variables α, β that corresponds to the variance-covariance matrix (5.104).

The result is, in terms of the rescaled distance $\mathcal{D} = D/D_0$,

$$\begin{aligned} dp(v,\mathcal{D}) &= \mathcal{N}\mathcal{D}^2 \exp\Big\{ -\frac{1}{2\Delta_1^2}\left(\frac{v}{\mathcal{D}} - v_0\right)^2 \\ &\quad -\frac{1}{2\Delta_2^2}\left[\frac{1+v^2}{2\mathcal{D}} - \frac{1+v_0^2}{2}\right]^2 \Big\} \\ &\quad \times\Theta(\mathcal{D})\Theta(D_{\max}/D_0 - \mathcal{D})\Theta(1-v^2)dvd\mathcal{D}. \end{aligned} \tag{5.121}$$

Here Θ is the step function, $\mathcal{N}$ is a normalization constant,

$$\Delta_1 = \frac{D_0}{r_0}\sqrt{\frac{1-\varepsilon_D\cos(4\bar{\psi}_0)}{\sigma_D(1-\varepsilon_D^2)}}, \tag{5.122}$$

$$\Delta_2 = \frac{D_0}{r_0}\sqrt{\frac{1+\varepsilon_D\cos(4\bar{\psi}_0)}{\sigma_D(1-\varepsilon_D^2)}}, \tag{5.123}$$

and $\bar{\psi}_0 = \psi_0 + \Delta\psi(\mathrm{n})$ [cf. Eq. (5.89) above]. In terms of these quantities, the previous, approximate result (5.105) is

$$\frac{\Delta D}{D_0} = \frac{2\sqrt{v_0^2\Delta_1^2 + \Delta_2^2}}{1-v_0^2}. \tag{5.124}$$

From the PDF (5.121) one can numerically calculate the reduced pdf for $\mathcal{D}$ alone,

$$p(\mathcal{D}) = \int_{-1}^{1} dv\, p(v,\mathcal{D}), \tag{5.125}$$

and thereby determine ΔD. As an example we show in Fig. 5.10 a plot of $p(D)$ for a particular choice of the parameters D_0, v_0, ψ_0, and for a particular direction on the sky. The non-Gaussian fall off in this figure at large values of D is a general feature, although its magnitude in this example is larger than is typical. It can be seen that the distance measurement accuracy is a factor of ~ 2 worse than that predicted by Eq. (5.105).

Now from Fig. 5.10 it can be seen that the value of D which maximizes $p(D)$ is *not* the same as D_0, i.e., the D-component of the point (v_0, D_0) which maximizes $p(v, D)$. Hence, the "maximum-likelihood" method for estimating signal parameters is ambiguous — the results obtained for one variable depend on whether or

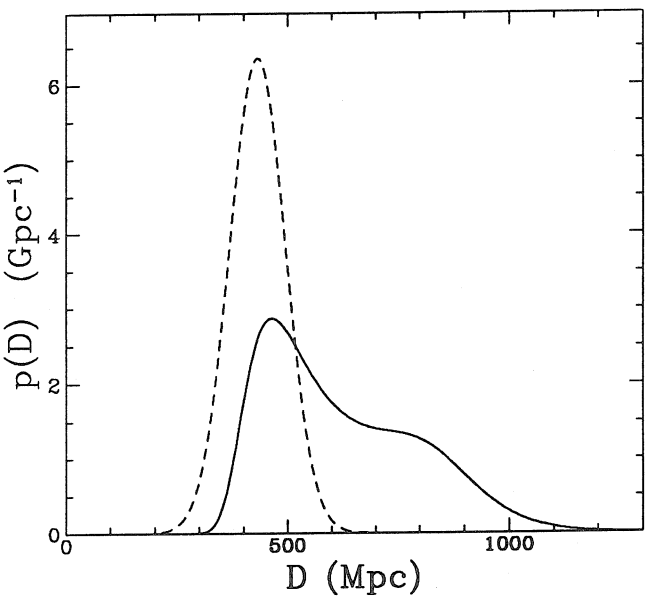

Figure 5.10: An example illustrating the necessity of going beyond the Gaussian approximation. Consider a neutron-star neutron-star binary merger in the direction given by $(\theta, \varphi) = (50°, 276°)$. The LIGO/VIRGO network parameters for this direction are $\sigma_D = 1.03$ and $\varepsilon_D = 0.74$. Suppose that an experimenter determines from the measured signal the following "best-fit" (maximum-likelihood) parameters: distance $D_0 = 432\,\mathrm{Mpc}$ [corresponding to a signal-to-noise ratio of $\rho = 12.8$, assuming the advanced detector sensitivity level (5.4)], masses $M_1 = M_2 = 1.4M_\odot$, cosine of inclination angle $v_0 = 0.31$, and polarization angle $\bar{\psi}_0 = 34°$. Then the distribution that she would infer by a Bayesian analysis for the distance to the source is shown by the solid curve; it is given by Eqs. (5.121), (5.125), and (5.92) of the text. The Gaussian approximation [Eq. (5.105) of the text] to this distribution is shown by the dashed curve. The distance measurement accuracy is atypically poor in this example; see Fig. 5.16 below.

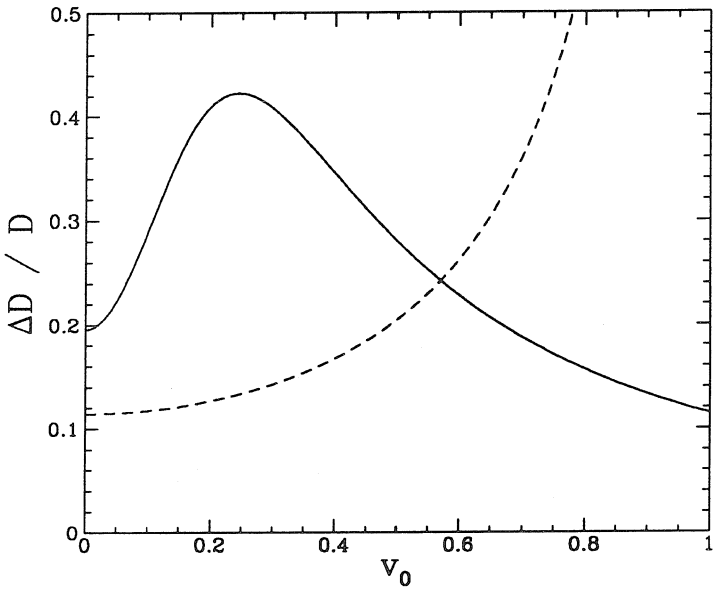

Figure 5.11: The solid line shows the distance measurement accuracy $\Delta D/D$ for the binary merger discussed in the caption of Fig. 5.10 (for which $\Delta_1 = 0.10$, $\Delta_2 = 0.057$), as a function of the cosine of the angle of inclination, v_0. The improvement in accuracy at high values of v_0 is due in part to an increased signal-to-noise ratio there. The dashed curve shows the prediction (5.105) of the linear error-estimation theory, which diverges as $v_0 \to 1$.

not other variables are integrated out before the maximum is taken. As explained in Appendix A, we advocate as the "best-fit" value of D the expected value

$$\langle D\rangle = \int D\, p(D)\, dD = \int D p(v, D) dv dD, \tag{5.126}$$

instead of the maximum-likelihood estimate D_0. [Maximum-likelihood estimation will need to be used, however, to obtain initial estimates of the signal parameters]. Correspondingly, to estimate distance measurement errors we use the quantity

$$\frac{\Delta D}{D} \equiv \frac{\sqrt{\langle \mathcal{D}^2\rangle - \langle \mathcal{D}\rangle^2}}{\langle \mathcal{D}\rangle}. \tag{5.127}$$

This can be calculated numerically from Eqs. (5.121) and (5.125), and in general will depend in a complicated way on the parameters Δ_1, Δ_2, and v_0, and very weakly on the rescaled cutoff $D_{\max}/D_0$. For the binary merger example of Fig. 5.10, we show in Fig. 5.11 how the accuracy (5.127) varies with v_0, and in Fig. 5.12 how it varies (through the parameters Δ_1 and Δ_2) with the distance D_0.

The merger of a BH-NS binary of masses $10M_\odot$ and $1.4M_\odot$ would produce a signal whose amplitude is 2.11 times stronger than the NS-NS merger of Fig. 5.12 [from Eq. (5.92) above]. Hence, taking also into account a cosmological enhancement factor of $(1+z)^{5/6}$ [9], a plot of $\Delta D/D$ versus D_0 for a BH-NS binary otherwise the same as the binary in Fig. 5.10 would look roughly the same as Fig. 5.12, but rescaled to extend to luminosity distances ~ 2 Gpc (the exact value depending on the cosmological model) [9].

4.5 Simulation of what LIGO/VIRGO will measure

In order to explore more completely the distance measurement accuracy (5.127) over the whole parameter space, we carried out the following Monte-Carlo calculation. Random values of D_0, v_0, $\bar{\psi}_0$, θ, and φ were chosen, distributed according to the measure $dD_0^3\, dv_0\, d\bar{\psi}_0\, d\cos\theta\, d\varphi$. Those parameter choices for which the combined SNR (5.91) (for NS-NS binaries) was less than the threshold of 8.5 were discarded, and samples were generated until 1000 NS-NS signals had been "detected." Because of this thresholding procedure (which roughly corresponds to the actual thresolding procedure that will be used), the distribution of values of D_0, v_0 etc. for *detected* events will not be given by $dD_0^3\, dv_0\, d\bar{\psi}_0\, d\cos\theta\, d\varphi$. For example, there is a significant bias in detected events towards high values of v_0, i.e., towards face-on binaries.

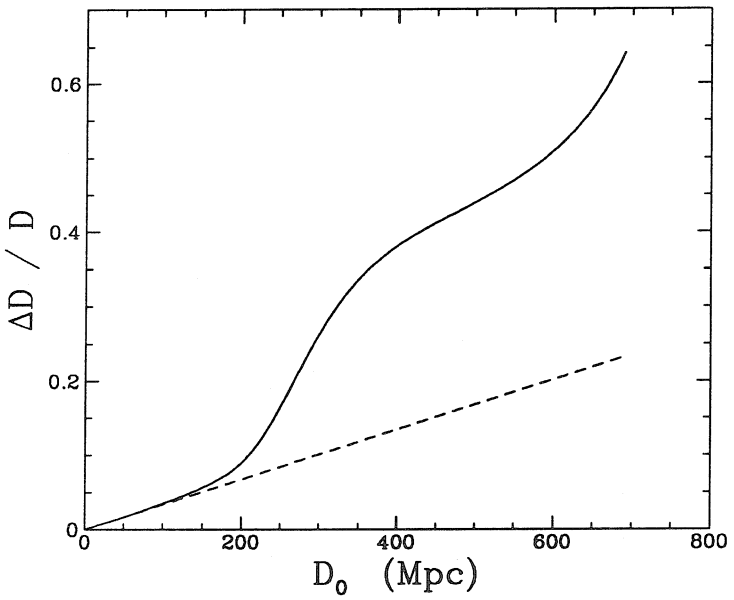

Figure 5.12: The distance measurement accuracies that result from displacing along the line of sight to the Earth, to various distances D_0, the binary merger of Fig. 5.10. As in Fig. 5.11, the dashed curve shows the approximate linear estimate (5.105), and the solid curve shows the more accurate estimate (5.127). The curves terminate at that distance ($\sim$ 700 Mpc) beyond which the merger is no longer visible, assuming the detector sensitivity level (5.4) and a combined signal-to-noise threshold of 8.5.

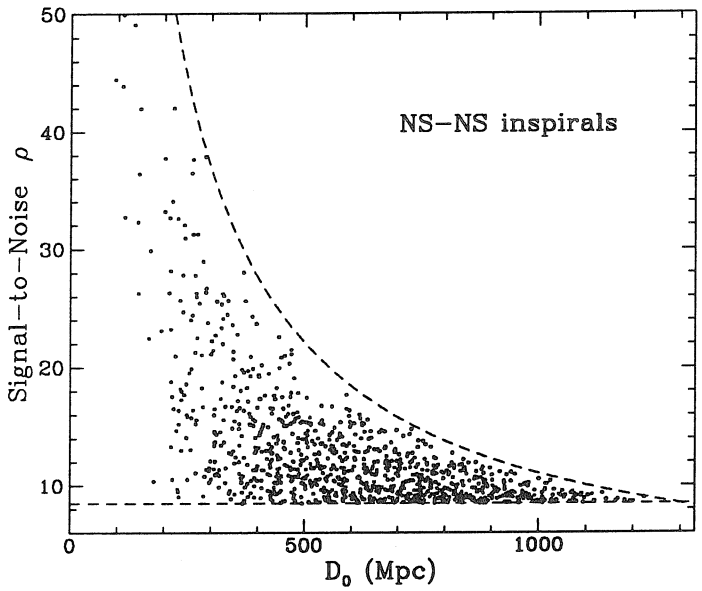

Figure 5.13: The distances D_0 for 1000 NS-NS binaries whose locations and orientations were randomly chosen, and the corresponding predicted signal-to-noise ratios ρ for the LIGO/VIRGO network. The lower dashed line is the signal-to-noise threshold of 8.5, below which sample points were discarded; the upper dashed line shows the maximum possible value (5.113) of ρ at a given distance. Six points with ρ between 50 and 90 are not shown. The number of sources with ρ larger than a given value ρ_* is proportional to ρ_*^{-3}. The detection of this many binary inspirals with the advanced LIGO/VIRGO detectors would take several years, if merger rates are as currently estimated [1,2].

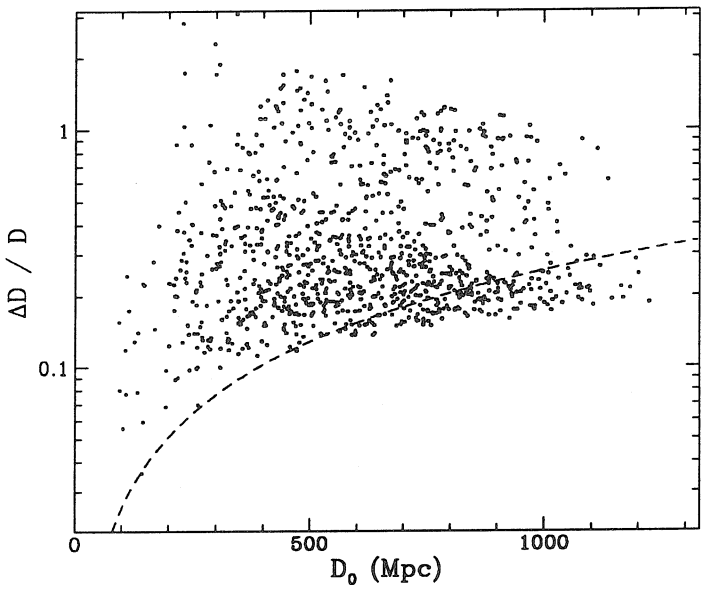

Figure 5.14: The distance measurement accuracy $\Delta D/D$ computed from Eq. (5.127) for the same 1000 NS-NS binaries, versus the distance D_0; see caption of Fig. 5.13. The spread in the values of $\Delta D/D$ is due to different source directions and orientations. Note that the accuracy for sources within 200 Mpc (of which there are estimated to be $\sim$ 3 per year [1,2]) can vary between $\sim$ 2% and $\sim$ 25%. For the most distant detectable sources (at $\sim$ 1200 Mpc), the accuracy can sometimes be as good as $\sim$ 20%. The dashed line shows the theoretical lower bound (5.111) derived using the linear error-estimation formalism; points below this line mostly have values of v_0 close to one for which value the linear error-estimation theory fails.

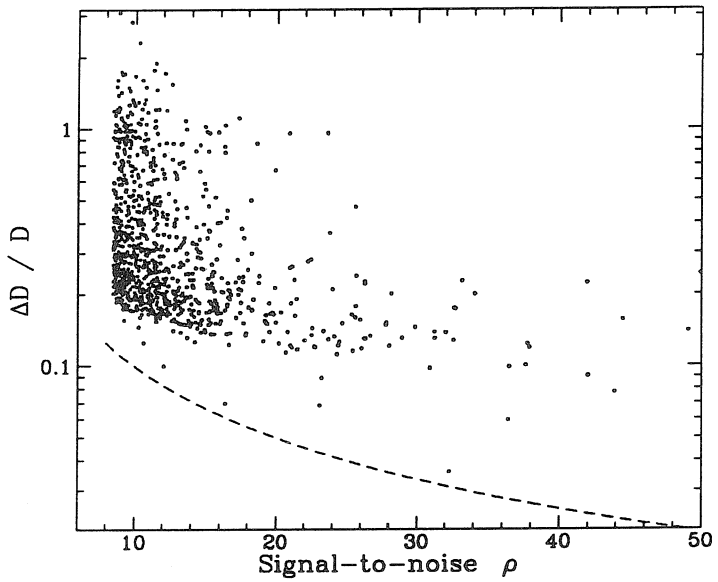

Figure 5.15: Distance measurement accuracy versus signal-to-noise for the same 1000 NS-NS binaries; see caption of Fig. 5.13. The dashed line shows the theoretical lower bound (5.112). As in Fig. 5.13, six points with ρ between 50 and 90 are not shown.

Scatter plots of the distances D_0, signal-to-noise ratios ρ, and distance measurement accuracies (5.127) for these randomly generated data points are shown in Figs. 5.13 – 5.15. We used the LIGO/VIRGO network functions shown in Figs. 5.5 and 5.6. Figures 5.13 – 5.15 give some idea of the potential capability of the LIGO/VIRGO network. The distance scale in these graphs is determined by the detector sensitivity level (5.4) that we have assumed, which is uncertain to within a factor of ~ 2. The distance scale would also be 2 to 3 times larger for NS-BH binaries, as mentioned above. By contrast, the distribution of measurement accuracies, which we show in Fig. 5.16, is independent of the scale of the detector noise. This figure shows that the measurement accuracy will be better than 30% for over half of the detected sources.

A relatively large fraction, about 1/5, of detected events have poor ($\geq 50\%$) measurement accuracies. This is primarily due to the effect discussed in Sec. 4.3: low values of the detector network polarizaion sensitivity $1-\varepsilon_D(\mathbf{n})$ over much of the sky. The effect of the polarization sensitivity can be clearly seen in Fig. 5.17, which is a scatter plot of polarization sensitivity versus distance measurement accuracy.

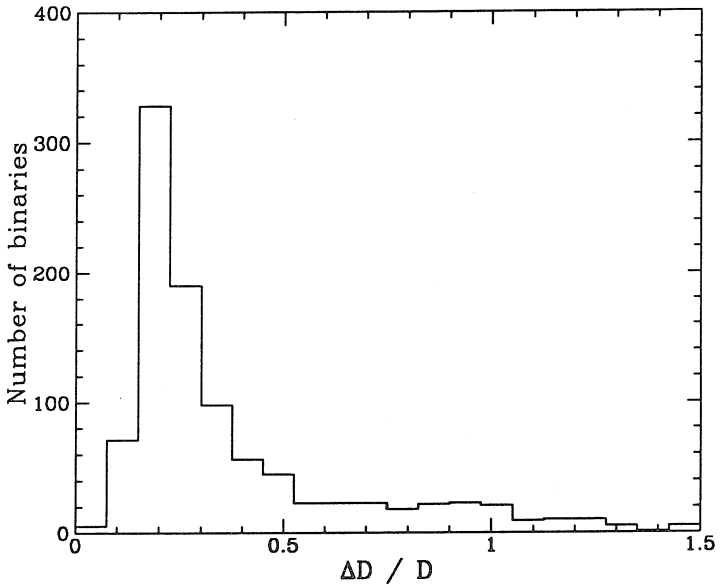

Figure 5.16: The frequency of occurrence of different ranges of $\Delta D/D$, out of a total of 1000 signals, for the LIGO/VIRGO detector network. It can be seen that $\sim$ 8% of detected signals will have distance measurement accuracies of better than 15%, while $\sim$ 60% of them will have accuracies of better than 30%. These conclusions are insensitive to the overall scale of the detectors' intrinsic noise, which essentially sets the event-detection rate. By contrast, they *are* sensitive to the number of detectors in the detector network, and to their orientations; see text and also Fig. 5.9.

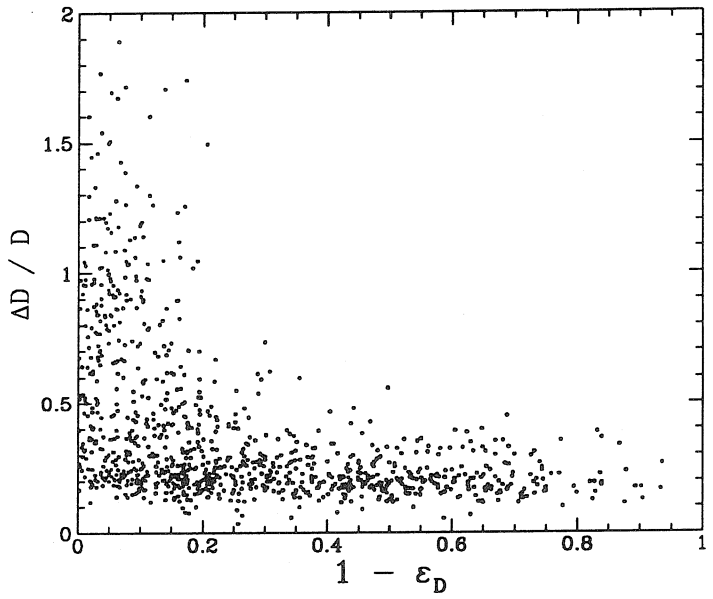

Figure 5.17: Distance measurement accuracy versus the detector network polarization sensitivity $1 - \varepsilon_D(\mathbf{n})$, for 1000 NS-NS binaries; see caption of Fig. 5.13. The strong correlation between very poor distance-measurement accuracy and low polarization sensitivity is evident — essentially all points with $\Delta D/D > 0.5$ have $1 - \varepsilon_D \lesssim 0.2$.

Finally, we emphasise that our results should be regarded as fairly rough estimates, because we have neglected the following effects: (i) The spin-related modulation of the amplitudes $\mathcal{A}_A$ mentioned in in Sec. 4.1 and discussed in Ref. [43]; (ii) The correlations between the variables D, v and ψ, ϕ_c, except to linear order in $1/\rho$; and (iii) the correlations between the parameters D, v, ψ, ϕ_c and the "phase parameters" $\mathcal{M}$, μ, β. As discussed above, we show in Appendix C that these correlations vanish to linear order in $1/\rho$, but there will be some correlation effects at higher order. Despite these neglected effects, we feel that the approximation method that we have used based on Eqs. (5.121) and (5.125) gives results that are more considerably more accurate than previous linear treatments [as summarized by Eq. (5.105)], becuase the dominant correlations at linear order in $1/\rho$ are those between D and v, and we have treated these correlations exactly.

5 CONCLUSIONS

Modulo the caveats in Sec. 3.3, we have confirmed the general conclusion that one can measure the binary's chirp mass $\mathcal{M}$ with rather astonishing accuracy. While our estimates of $\Delta\mathcal{M}/\mathcal{M}$ are a factor of ~ 20 greater than those obtained from the less accurate Newtonian analysis [14, 15], we have found that $\Delta\mathcal{M}/\mathcal{M}$ should still be $0.01\% - 1\%$ for typical measurements.

We have investigated the idea that detailed phase information might also allow accurate determination of the binary's reduced mass μ. A calculation that neglected the effects of the bodies' spins on the waveform suggested that μ might typically be measured to within $\sim 1\%$. However a more complete analysis showed that errors in μ can be substantially masked by compensating errors in the spin parameter β. Including the correlations with β, we estimated that $\Delta\mu/\mu \approx 10\%$ for low-mass (NS-NS) binaries and that $\Delta\mu/\mu \approx 50\%$ for high-mass (BH-BH) binaries. Moreover, $\Delta M_1/M_1$ and $\Delta M_2/M_2$ are generally much greater than $\Delta\mu/\mu$ unless $M_1/M_2 \gg 1$ (BH-NS case).

While these mass-measurement accuracies are somewhat poor, it is useful to keep two points in mind. First, since typical measurements will have $S/N \approx 10$, one should detect events with $S/N \geq 50$ roughly 1% of the time. For the advanced-detector noise curve (5.4), and assuming the coalescence rates estimated in Ref. [2], such strong events should be seen $\sim$ once per year for NS-NS binaries, and several times per year for NS-BH and BH-BH binaries [22]. For these strongest sources, measurement errors will be a factor of ~ 5 lower than their typical values. Second,

the measurement-derived PDF on the parameter space constrains the values of M_1, M_2, and β much more strongly than is indicated by their individual variances, as illustrated in Fig. 5.3 above. The large rms errors are due to correlations between the measured parameters; certain linear combinations of the parameters (eigenvectors of the covariance matrix) are determined with high accuracy [40]. This may be useful when combined with information obtained by other means.

With regard to potential accuracy of distance measurements, our key conclusions are the following:

(i) We have confirmed the general conclusion reached previously [15, 9] that correlations between the distance D and other angular variables (primarily the angle of inclination of the binaries orbit) will reduce ΔD by a factor of typically 2 or 3 from the naive estimate $\Delta D/D = 1/(\text{signal-to-noise})$; see Fig. 5.15 above.

(ii) Distance measurement accuracy will depend strongly on the direction towards the source relative to the detectors, as shown in Figs. 5.7 and 5.8. This is because of the different *polarization sensitivities* of the detector network in different directions, and the fact that the complex amplitudes of both polarization components of the incident waves are needed in order to determine the distance. The polarization sensitivity of the LIGO/VIRGO network is somewhat poor in this regard (because the two LIGO detectors are almost parallel); it would be substantially improved by the addition of a fourth detector. This provides additional motivation for the construction of additional interferometers around the world, which would also improve the angular accuracy of sky-location measurements [7].

(iii) Previous estimates of distance measurement errors have been accurate only to linear order in $1/D$. Our results indicate that this linear approximation will be inadequate for typical detected signals, so that the incorporation of non-linear effects will be necessary in order to accurately ascertain measurement errors [and also to accurately estimate the distances themselves; see Sec. 5.3 of Appendix A].

(iv) We have carried out a Monte-Carlo simulation of distance measurement accuracies for a large number of randomly chosen sources, using a method of calculation which roughly estimates the non-linear effects, and incorporating the amplitude sensitivity and polarization sensitivity of the LIGO/VIRGO detector network. Our results suggest that $\sim 8\%$ of measured distances will be accurate to better than $\sim 15\%$, and that $\sim 60\%$ of them will be accurate to better than 30%.

ACKNOWLEDGMENTS

It is a pleasure to thank the following people for helpful discussions: Theocharis Apostolatos, Lars Bildsten, Sam Finn, Daniel Kennefick, Andrzej Krolak, Dragoljub Marković, Eric Poisson, Bernard Schutz, Cliff Will, Alan Wiseman, and especially Kip Thorne, who provided much of the inspiration for this paper. We are grateful to Finn for sharing with us the results of his research, on which much of our work is based, at a preliminary stage. We thank Thorne and Bildsten for carefully reading the manuscript, and for detailed comments. Our understanding of some subtle issues in parameter estimation owes much to a recent review article by Tom Loredo [53]. This work was supported in part by NSF grant PHY-9213508.

APPENDIX A: ESTIMATION OF SIGNAL PARAMETERS

In this appendix we review some aspects of the statistical theory of estimation of signal parameters as applied to gravitational wave astronomy. This subject has been concisely summarized in Appendix A of Ref. [27], and has recently been treated in detail by Finn [26]. Hence in many places we merely write down the key results, without proof, in order to establish notation and equations for use in the text. However, we also present some extensions to the formalism developed by Finn [26]: We carefully distinguish between Bayesian and frequentist estimates of errors, and discuss the validity of these two methods of error calculation. We show that maximum-likelihood parameter estimation, while useful, is not the optimal data-processing strategy, and, following Davis [54], suggest the use of the so-called Bayes estimator. We derive an expression for the minimum signal-to-noise ratio $(S/N)_{\rm min}$ necessary in order that the usual Gaussian approximation for estimation of measurement accuracy be valid, and explain how to treat degenerate points in parameter space where the Gaussian approximation breaks down. Finally we give a discussion of the effects of including *a priori* information, which corrects the corresponding material in Ref. [26].

5.1 Basic Formulae

The output of a network of detectors can be represented as a vector $\mathrm{s}(t) = (s_1(t), \ldots, s_{n_d}(t))$, where n_d is the number of detectors, and $s_a(t)$ is the strain

amplitude read out from the ath detector. There will be two contributions to the detector output $\mathbf{s}(t)$ — the intrinsic detector noise $\mathbf{n}(t)$ (a vector random process), and the true gravitational wave signal $\mathbf{h}(t)$ (if present):

$$\mathbf{s}(t) = \mathbf{h}(t) + \mathbf{n}(t). \tag{5.128}$$

We assume that the signal is a burst of known form, but depending on several unknown parameters $\theta = (\theta^1, \ldots, \theta^k)$, so that $\mathbf{h}(t) = \mathbf{h}(t;\theta)$. Thus, we do not consider the cases of periodic or stochastic waves [12]. We also assume for simplicity that the detector noise is stationary and Gaussian. For the LIGO and VIRGO detectors, the stationarity assumption is justified for the analysis of short, burst waves [27]. However, the actual noise may have important non-Gaussian components, the implications of which for the purposes of signal detection thresholds and data analysis are not yet fully understood. We do not deal with this issue here.

With these assumptions, the statistical properties of the detector noises can be described by the auto-correlation matrix

$$\begin{aligned} C_n(\tau)_{ab} &= \langle s_a(t+\tau) s_b(t)\rangle - \langle s_a(t+\tau)\rangle \langle s_b(t)\rangle \\ &= \langle n_a(t+\tau) n_b(t)\rangle - \langle n_a(t+\tau)\rangle \langle n_b(t)\rangle, \end{aligned} \tag{5.129}$$

where the angular brackets mean an ensemble average or a time average. The Fourier transform of the correlation matrix, multiplied by two, is the power spectral density matrix:

$$S_n(f)_{ab} = 2\int_{-\infty}^{\infty} d\tau\, e^{2\pi i f\tau} C_n(\tau)_{ab}. \tag{5.130}$$

This satisfies the formal equation

$$\langle \tilde{n}_a(f)\, \tilde{n}_b(f')^*\rangle = \frac{1}{2}\delta(f-f') S_n(f)_{ab}, \tag{5.131}$$

together with

$$\left\langle \exp\left\{ i\int dt\, \mathbf{w}(t)\cdot\mathbf{n}(t)\right\}\right\rangle = \exp\left\{-\frac{1}{2}\int_0^{\infty} df\, \tilde{\mathbf{w}}^\dagger\cdot\mathbf{S}_n\cdot\tilde{\mathbf{w}}\right\}, \tag{5.132}$$

for any sufficiently well-behaved test functions $w_a(t)$. Here tildes denote Fourier transforms, according to the convention that

$$\tilde{h}(f) = \int_{-\infty}^{\infty} e^{2\pi i f t} h(t) dt.$$

We note that there are two different commonly used definitions of power spectral density in the literature. The above convention is used in Refs. [3, 12, 26, 35, 44].

The alternative convention is to use a spectral noise density defined by $S_n^{(2)}(f) \equiv S_n(f)/2$, as used in Refs. [21, 27, 55, 56, 57].

The Gaussian random process $\mathrm{n}(t)$ determines a natural inner product $(\ldots|\ldots)$ and associated distance or norm on the space of functions $\mathrm{h}(t)$. As discussed in Sec. 2.2, this is defined so that the probability that the noise takes a specific value $\mathrm{n}_0(t)$ is

$$p[\mathrm{n} = \mathrm{n}_0] \propto e^{-(\mathrm{n}_0|\mathrm{n}_0)/2}, \tag{5.133}$$

and it is given by [28]

$$(\mathrm{g}\,|\,\mathrm{h}) \equiv 4\,\Re \int_0^\infty df\; \tilde{g}_a(f)^* \left[\mathrm{S}_n(f)^{-1}\right]^{ab} \tilde{h}_b(f), \tag{5.134}$$

where $\Re$ means "the real part of". It also satisfies the equation [26]

$$\langle\, (\mathrm{n}|\mathrm{g})\; (\mathrm{n}|\mathrm{h})\,\rangle \;=\; (\mathrm{g}|\mathrm{h})\,, \tag{5.135}$$

for any functions g and h.

In this paper we are interested only in the estimation of signal parameters once a gravitational wave burst has been detected. Thus, we suppose that we have measured some detector output $\mathrm{s}(t)$, and that it satisfies the appropriate criterion for us to conclude that it contains a signal of the form $\mathrm{h}(t;\tilde{\theta})$ for some unknown set of parameters $\tilde{\theta}$:

$$\mathrm{s}(t) = \mathrm{h}(t;\tilde{\theta}) + \mathrm{n}(t). \tag{5.136}$$

The central quantity of interest is then the probability distribution function (PDF) for $\tilde{\theta}$ given the output $\mathrm{s}(t)$. As Finn has shown [26], this is given by

$$p[\tilde{\theta}\,|\,\mathrm{s},\,\mathrm{detection}] = \mathcal{N}\, p^{(0)}(\tilde{\theta})\; e^{-\frac{1}{2}\left(\mathrm{h}(\tilde{\theta})-\mathrm{s}\,\middle|\,\mathrm{h}(\tilde{\theta})-\mathrm{s}\right)}. \tag{5.137}$$

Here $\mathcal{N} = \mathcal{N}(\mathrm{s})$ is a normalization constant, and $p^{(0)}(\tilde{\theta})$ is the PDF that represents our *a priori* knowledge.

5.2 Two types of measurement accuracy

We now discuss how to characterize the accuracy of measurement of the parameters θ. Normally statistical "one sigma" experimental errors are defined operationally in terms of the average of the actual errors over an ensemble of repeated identical measurements (which corresponds mathematically to the width of an appropriate PDF). Now in practice one cannot repeat or duplicate a given gravitational wave measurement, but in principle one can do so by waiting a sufficiently long time

and throwing away all detected signals that do not match the original one. In this manner one can operationally define an ensemble of "identical" measurements. The notion of error which results then depends in a crucial way on what is meant by "identical." One can either demand that the signals $\mathbf{h}(t)$ incident on the detectors be identical and consider the resulting spread in the values of the detector outputs $\mathbf{s}(t)$ given by Eq. (5.136), or demand that the detector outputs $\mathbf{s}(t)$ be identical and consider the resulting spread in the values of the incident signals $\mathbf{h}(t)$. The two notions of error which result can be called Bayesian errors and frequentist errors, adopting the terminology from common usage in a more general context [53]. We now discuss in more detail the definition and meaning of these two types of error, in order to clarify the relationship between our method of calculating measurement error and previous work in this area [26, 27, 15, 62]. The following discussion is based on that of Loredo [53].

In the frequentist approach, one first specifies the algorithm the experimenters should use to determine the "best-fit" values $\hat{\theta}$ of the parameters θ from the gravitational wave measurement $\mathbf{s}$:

$$\hat{\theta} = \hat{\theta}(\mathbf{s}). \tag{5.138}$$

This is also called a statistic or estimator. Next, one assumes that Eq. (5.136) holds for some value of $\tilde{\theta}$, and by substituting this equation into Eq. (5.138), and using Eq. (5.133), one derives the PDF $p(\hat{\theta}\,|\tilde{\theta})$ for $\hat{\theta}$ given $\tilde{\theta}$. Then the expected value with respect to this PDF of $\hat{\theta}^i - \tilde{\theta}^i$,

$$\begin{aligned} b^i &= \langle \hat{\theta}^i \rangle - \tilde{\theta}^i, \\ &= \int \hat{\theta}^i p(\hat{\theta}|\tilde{\theta})\, d\hat{\theta} \; - \tilde{\theta}^i, \end{aligned} \tag{5.139}$$

gives the "bias" b^i of the estimator $\hat{\theta}(\mathbf{s})$. The diagonal elements of the expected value of $(\hat{\theta}^i - \tilde{\theta}^i)\,(\hat{\theta}^j - \tilde{\theta}^j)$ characterize the measurement error. More specifically, we define

$$\begin{aligned} \Sigma^{ij}_{\mathrm{FREQ}} &= \Sigma^{ij}_{\mathrm{FREQ}}[\tilde{\theta}; \hat{\theta}(\cdot)] \\ &= \left\langle \left\{ \hat{\theta}^i[\mathbf{h}(\tilde{\theta}) + \mathbf{n}] - \tilde{\theta}^i \right\} \left\{ \hat{\theta}^j[\mathbf{h}(\tilde{\theta}) + \mathbf{n}] - \tilde{\theta}^j \right\} \right\rangle_{\mathbf{n}}. \end{aligned} \tag{5.140}$$

Here the notation on the first line indicates that Σ_{FREQ} depends on the functional form of the estimator $\hat{\theta}$ as well as the assumed signal parameters $\tilde{\theta}$, and the angular brackets on the second line denote expectation value with respect to the noise $\mathbf{n}$. The matrix (5.140) is a measure of parameter-extraction accuracy that includes

the effect of the bias, since

$$\Sigma^{ij}_{\rm FREQ} = \langle \delta\hat{\theta}^i \, \delta\hat{\theta}^j \rangle + b^i b^j, \tag{5.141}$$

where $\delta\hat{\theta}^i \equiv \hat{\theta}^i - \langle \hat{\theta}^i \rangle$.

The physical meaning of the quantity (5.140) is the following. Suppose that a large number of identical gravitational wave trains, described by the parameter values $\tilde{\theta}$, impinge on the detector network. For each measured signal, the experimenters calculate using the algorithm $\hat{\theta}$ the best-fit values of the source parameters. Then the rms average deviation of these best-fit values from the true value $\tilde{\theta}$ is given by Eq. (5.140). Moreover, the usual method of implementing a Monte-Carlo simulation of the measurement process would also predict errors given by (5.140) [62].

In the frequentist method, one focuses attention on a particular incident signal $\mathrm{h}(t;\tilde{\theta})$, and considers different possible measured detector outputs $\mathrm{s}(t)$. By contrast, in the Bayesian approach, one focuses attention on a particular measured detector output s. The error in measurement is simply taken to be the width (variance-covariance matrix) of the PDF (5.137) for the true value $\tilde{\theta}$ of θ given the measurement s. Thus,

$$\begin{aligned} \Sigma^{ij}_{\rm BAYES} &= \Sigma^{ij}_{\rm BAYES}[\mathrm{s}; p^{(0)}(\cdot)] \\ &= \int (\tilde{\theta}^i - \langle \tilde{\theta}^i \rangle)\,(\tilde{\theta}^j - \langle \tilde{\theta}^j \rangle)\, p(\tilde{\theta} \,|\, \mathrm{s})\, d\tilde{\theta}, \end{aligned} \tag{5.142}$$

where $\langle \tilde{\theta}^i \rangle = \int \tilde{\theta}^i \, p(\tilde{\theta} \,|\, \mathrm{s}) d\tilde{\theta}$. Note that this measure of error depends on different quantities than its frequentist counterpart (5.140) — the measured signal s, and the *a priori* PDF $p^{(0)}$.

The physical meaning of the quantity (5.142) is the following. Suppose that a large number of different gravitational wave trains are incident upon the detector network, where the distribution of the wave parameters $\tilde{\theta}$ is given by the PDF $p^{(0)}$. Only a small fraction of these will produce, at the output of the detectors, the signal $\mathrm{s}(t)$. In this small fraction, however, there will be some spread of values of the parameters $\tilde{\theta}$, because of different realizations of the detector noise $\mathrm{n}(t)$ that combine with the incident waves to produce the measured signal according to Eq. (5.136). This spread is characterized by the matrix (5.142).

The measure of error (5.142) characterizes the total amount of information that is contained in the measured signal s, which is independent of how the experimenters choose to process this signal. In practical situations, however, one typically would like to know what accuracy can be achieved by a given, imperfect,

data-processing algorithm (e.g., one which takes a manageable amount of computer time). It is possible to define a more general Bayesian error that is appropriate for the situation where a particular algorithm or statistic $\hat{\theta}(\cdot)$ is chosen to estimate the signal parameters θ from the measured signal s. This measure of error is

$$\begin{aligned} \Sigma^{ij}_{\rm BAYES} &= \Sigma^{ij}_{\rm BAYES}[{\rm s}, \hat{\theta}({\rm s}); p^{(0)}(\cdot)] \\ &= \int (\tilde{\theta}^i - \hat{\theta}({\rm s}))\,(\tilde{\theta}^j - \hat{\theta}({\rm s}))\,p(\tilde{\theta} \mid {\rm s}) d\tilde{\theta}. \end{aligned} \tag{5.143}$$

Physically this quantity is just the (square of the) rms average, over the small fraction of incident waves discussed above, of the difference between the true value $\tilde{\theta}$ of the parameters and the "measured value" $\hat{\theta}({\rm s})$. It is clear that the rms errors $\Sigma^{ii}_{\rm BAYES}[{\rm s}, \hat{\theta}({\rm s}); p^{(0)}(\cdot)]$ will be minimized and take on their minimum values $\Sigma^{ii}_{\rm BAYES}[{\rm s}; p^{(0)}(\cdot)]$ when one choses for $\hat{\theta}$ the so-called Bayes estimator [54]

$$\hat{\theta}^i_{\rm BE}({\rm s}) \equiv \int \tilde{\theta}^i\, p(\tilde{\theta} \mid {\rm s}) d\tilde{\theta}. \tag{5.144}$$

One final point about Bayesian errors is the following. Suppose that the experimenters calculate from the measured signal s the best-fit value $\hat{\theta} = \hat{\theta}({\rm s})$, and then discard all the remaining information contained in the signal s. Then there are very many signals s′ that could have been measured and that are compatible with the experimenters' measurements, in the sense that $\hat{\theta}({\rm s}') = \hat{\theta}$ [26]. Correspondingly, there is a larger spread of possible values of $\tilde{\theta}$, and hence the predicted rms measurement errors based on the measurement $\hat{\theta}$ alone are given by the following modification of Eq. (5.143):

$$\begin{aligned} \Sigma^{ij}_{\rm BAYES} &= \Sigma^{ij}_{\rm BAYES}[\hat{\theta}; p^{(0)}(\cdot)] \\ &= \int (\tilde{\theta}^i - \hat{\theta})\,(\tilde{\theta}^j - \hat{\theta})\,p(\tilde{\theta} \mid \hat{\theta}) d\tilde{\theta}. \end{aligned} \tag{5.145}$$

Here $p(\tilde{\theta} \mid \hat{\theta})$ is the probability distribution introduced by Finn [26] for the true parameter values $\tilde{\theta}$ given the estimated values $\hat{\theta}$. It is given by the standard Bayesian formula

$$p(\tilde{\theta} \mid \hat{\theta}) = \bar{\mathcal{N}}\, p^{(0)}(\tilde{\theta})\, p(\hat{\theta} \mid \tilde{\theta}), \tag{5.146}$$

where $\bar{\mathcal{N}} = \bar{\mathcal{N}}(\hat{\theta})$ is a normalization constant that depends on $\hat{\theta}$. Note that the matrix (5.145) depends only on the measured value $\hat{\theta}$ of the estimator and not on its functional form $\hat{\theta}(\cdot)$.

The predicted measurement error (5.145) differs from the previously defined measurement error (5.143) because the measured signal s contains information

about the likely size of the error, so that it matters if s is discarded. For example, suppose that a detector-output data train contains a signal from a coalescing binary, and that by some standard algorithm the experimenters determine best-fit values of the binaries parameters. Then given these best-fit values, one can estimate the likely size of the measurement error — this is given by Eq. (5.145). However, if they also determined that the data train contains an uncommonly large non-Gaussian burst of noise that accounts for 20% of the estimated signal amplitude, the estimates of the likely parameter-extraction errors would clearly have to be modified.

Which of the above-defined measurement errors is appropriate to assess the capability of the LIGO/VIRGO detector network? It is generally accepted that, if one has a given measurement s, the Bayesian approach is the fundamental and correct one, and that the frequentist approach is justified only to the extent that it reproduces the results of Bayesian analyses. This is essentially because, given a particular measurement s, it is irrelevant to consider an ensemble of other, different measurements s′ [53]. However, for our purpose of trying to *anticipate* the capability of gravitational wave detectors before any measurements are available, it seems that this message looses its bite. It certainly seems reasonable to imagine a fixed gravitational wave-train incident upon the detector network, and to inquire about the spread (5.140) in measured values of the source parameters due to differing realizations of the detector noise.

In fact, there is a certain sense in which frequentist errors and Bayesian errors are equivalent, which is well known: the average of the predicted frequentist error over the whole parameter space is the same as a suitable average of the predicted Bayesian error. Thus, in a sense the same errors are being calculated in each case; it is just their dependence on parameters that is being changed. In particular, if the predicted errors do not vary strongly with the parameters $\tilde{\theta}$, then the two types of error will be approximately equal. A precise statement of this "equality of averages" which is straightforward to derive is

$$\begin{aligned} \int d\tilde{\theta}\ \ & p^{(0)}(\tilde{\theta})\,\Sigma^{ij}_{\mathrm{FREQ}}[\tilde{\theta};\hat{\theta}(\cdot)] \\ &= \int \frac{\mathcal{D}\mathbf{s}}{\mathcal{N}(\mathbf{s})}\,\Sigma^{ij}_{\mathrm{BAYES}}[\mathbf{s},\hat{\theta}(\mathbf{s});p^{(0)}(\cdot)] \qquad (5.147) \\ &= \int \frac{d\hat{\theta}}{\bar{\mathcal{N}}(\hat{\theta})}\,\Sigma^{ij}_{\mathrm{BAYES}}[\hat{\theta};p^{(0)}(\cdot)]. \qquad (5.148) \end{aligned}$$

Here the various matrices Σ^{ij} are defined in Eqs. (5.140), (5.143), and (5.145),

respectively, and the factors $\mathcal{N}(\mathrm{s})$ and $\bar{\mathcal{N}}(\hat{\theta})$ are the normalization constants appearing in Eqs. (5.137) and (5.146), respectively. The (formal) measure $\mathcal{D}\mathrm{s}$ is defined such that

$$\langle F[\mathrm{n}]\rangle = \int \mathcal{D}\mathrm{n}\, F[\mathrm{n}]\, e^{-(\mathrm{n}|\mathrm{n})/2}, \tag{5.149}$$

for any functional $F[\mathrm{n}]$ of the noise n.

Because of this equality of averages, we conclude that either Bayesian or frequentist errors can be used to anticipate the capabilities of LIGO/VIRGO, essentially because one is only interested in the range of possible errors and not their value at a fixed point in parameter space. Similarly, if one is using Bayesian errors, it is appropriate to use the matrix (5.145) instead of (5.143) to anticipate measurement accuracies, since from Eqs. (5.147) and (5.148) the measure of error (5.145) is simply an average of (5.143) over values of s for which $\hat{\theta}(\mathrm{s}) = \hat{\theta}$. This conclusion has already been reached in a recent paper of Finn's [26] in which he advocates the use of what in our notation is essentially $\Sigma^{ij}_{\mathrm{BAYES}}[\hat{\theta}_{\mathrm{ML}}; p^{(0)}(\cdot)]$, where $\hat{\theta}_{\mathrm{ML}}$ is the so-called maximum-likelihood estimator (see below). [However, his calculation of this quantity does not incorporate the *a priori* PDF quite correctly, as we show below.] Previous analyses of parameter-extraction accuracy for gravitational wave detectors by Echeverria [58] and by Krolak and collaborators [15, 27, 35, 62] have used the frequentist error $\Sigma^{ij}_{\mathrm{FREQ}}[\tilde{\theta}; \hat{\theta}_{\mathrm{ML}}(\cdot)]$. By contrast, in Sec. 4 of this paper we have calculated the Bayesian error

$$\Sigma^{ij}_{\mathrm{BAYES}}[\mathrm{s}; p^{(0)}(\cdot)] = \Sigma^{ij}_{\mathrm{BAYES}}[\mathrm{s}, \hat{\theta}_{\mathrm{BE}}(\mathrm{s}); p^{(0)}(\cdot)], \tag{5.150}$$

because, as we argue below, it is more accurate to use $\hat{\theta}_{\mathrm{BE}}$ rather that $\hat{\theta}_{\mathrm{ML}}$.

One final important point about the two types of error is the following well-known fact: to leading order in $1/\rho$, where ρ is the signal-to-noise ratio [Eq. (5.155) below], the two approaches yield identical results. More specifically, assuming the Gaussian noise statistics (5.133), we have

$$\Sigma^{ij}_{\mathrm{FREQ}}[\tilde{\theta}; \hat{\theta}_{\mathrm{ML}}(\cdot)] = \Sigma^{ij}_{\mathrm{BAYES}}[\hat{\theta}_{\mathrm{ML}}; p^{(0)}(\cdot)] \;\times \left[1 + O(\rho^{-1})\right] \tag{5.151}$$

when $\hat{\theta}_{\mathrm{ML}} = \tilde{\theta}$. Moreover the same quantity [given by Eq. (5.162) below] is also obtained to leading order using the Bayes estimator (5.144), and also from the estimator-independent measure of error (5.142). This is essentially because to this order, all the PDFs are Gaussian. These assertions are straightforward to prove using the tools developed by Finn [26], and moreover are well-known in more general statistical contexts. Hence the distinctions that we have been drawing

only matter when effects that are non-linear in $1/\rho$ contribute significantly to the predicted accuracies (as for example when measuring distances to coalescing binaries), or when ρ is sufficiently small that the *a priori* information represented by $p^{(0)}$ becomes significant. [However, this may be the rule rather than the exception for typical detected gravitational wave bursts; see Sec. 4.4 above.]

5.3 Choice of data-processing algorithm $\hat{\theta}(\cdot)$

Given a particular measurement $\mathbf{s}$, the PDF (5.137) in principle contains all the information contained in the measurement about the source parameters $\tilde{\theta}$. However in practice one often wants to focus on a small portion of this information, by calculating a "best estimate" value $\hat{\theta}(\mathbf{s})$ together with estimates of the statistical errors. The choice of estimator $\hat{\theta}(\cdot)$ is determined both by practical considerations, and by whatever criteria are adopted to judge "good" estimators; there is no unique choice.

One obvious criterion is to choose that estimator which minimizes the expected error in parameter extraction. However, one could choose to minimize either Bayesian or frequentist errors, and also the errors depend on the parameter values ($\tilde{\theta}$ or $\hat{\theta}$). If one minimizes the average over parameter space of the measurement error [as given by the common value of Eqs. (5.2)], then the resulting best estimator is just the Bayes estimator (5.144), which we have used in Sec. 4.4. Its use for gravitational wave data analysis has been suggested by Davis [54]. Unfortunately, as Davis indicates, calculation of the Bayes estimator is very computationally intensive, as it involves a multidimensional integral of a function whose evaluation at each point requires the calculation of an inner product of the type (5.134). Our application of the Bayes estimator in Sec. 4.4 was an exception in this regard, because all the inner products could be evaluated analytically. In more general situations the inner products would have to be calculated numerically. Hence, it seems likely that the Bayes estimator will be used only after preliminary estimates of the signal parameters have been made using Wiener optimal filtering. The use of the Bayes estimator also goes by the name of "non-linear filtering" [54].

A simpler estimator that has been proposed by Finn [26, 14], Krolak [62] and others in the gravitational wave data analysis context is the so-called maximum-likelihood estimator $\hat{\theta}_{\rm ML}(\mathbf{s})$. This defined to be the value of $\tilde{\theta}$ which maximizes the PDF (5.137). It is convenient because it is closely related to the Wiener optimal filtering method [12] that will be used to detect the signals — the detection

procedure outlined in Sec. 1 will essentially return the maximum-likelihood estimates of the source parameters (see below). However, once the signals have been detected, it will not be necessary to use only maximum-likelihood estimation — other estimation methods can be used to give better results. Hence, the quantities $\Sigma^{ij}_{\rm BAYES}[\hat{\theta}_{\rm ML}; p^{(0)}(\cdot)]$ or $\Sigma^{ij}_{\rm FREQ}[\tilde{\theta}; \hat{\theta}_{\rm ML}(\cdot)]$ represent the *potential* accuracy of measurements only to leading order in $1/\rho$. (They would represent the actual accuracy if maximum-likelihood estimation were to be the only estimation method used). We note that the quantities $\hat{\theta}_{\rm ML}(\mathbf{s})$ and $\hat{\theta}_{BE}(\mathbf{s})$ can differ by as much as $\gtrsim 30\%$ for detected gravitational wave signals, as for example in Fig. 5.10 above where $\langle D \rangle = 1.44 D_0$.

Maximum-likelihood estimation also has the following disadvantages. First, as discussed in Sec. 4.4, the maximum-likelihood estimator for a particular variable does not necessarily maximize the reduced PDF for that variable obtained by integrating over the other variables. By contrast, the value of the Bayes estimator (5.144) for a given variable does not depend on whether or not other variables have been integrated out. Second, the best-fit point obtained by the maximum-likelihood method depends on the choice of variables used to parametrize the waveform $\mathbf{h}(t; \tilde{\theta})$. For example, in Sec. 3 of this paper we could have used as variables either the individual masses M_1 and M_2 of the binaries components, or the chirp and reduced masses $\mathcal{M}$ and μ. Since probability distributions for (M_1, M_2) and $(\mathcal{M}, \mu)$ are related by a non-trivial Jacobian factor, a local maximum of one of them will not correspond to a local maximum of the other. A slightly different kind of maximum-likelihood estimator, which maximizes the likelihood ratio $\Lambda(\tilde{\theta}) \propto \exp[-(\mathbf{h}(\tilde{\theta}) - \mathbf{s} \,|\, \mathbf{h}(\tilde{\theta}) - \mathbf{s})/2]$ instead of the PDF (5.137), does not suffer from this problem. This is the maximum-likelihood estimator that is usually discussed in the statistics literature. However, it does not take into account in any way our *a priori* knowledge.

We conclude that calculations of measurement accuracy using $\hat{\theta}_{\rm ML}$ represent the true potential measurement accuracy only to leading order in $1/\rho$. If this leading order approximation becomes invalid (as occurs for sufficiently small SNR's), then one should use instead either the Bayesian error (5.150) or $\Sigma^{ij}_{\rm BAYES}[\hat{\theta}_{\rm BE}; p^{(0)}(\cdot)]$. One could also use $\Sigma^{ij}_{\rm FREQ}[\tilde{\theta}; \hat{\theta}_{\rm BE}(\cdot)]$, but this is much more difficult to calculate than (5.150) when the large ρ limit does not apply.

5.4 Relation between maximum-likelihood estimation and Wiener optimal filtering

In Sec. 2, we discussed a method for finding best-fit parameters $\hat{\theta}$ which was based on maximizing the overlap of the measured signal with theoretical templates [cf. Eq. (5.2) above]. We now briefly indicate the relationship of this method to the maximum-likelihood procedure. That the two methods are equivalent in general has been shown by Echeverria [59].

Given the measured signal $\mathrm{s}(t)$, define for any θ the quantity

$$\rho[\theta] = \frac{(\mathrm{h}(\theta) \,|\, \mathrm{s})}{\sqrt{(\mathrm{h}(\theta) \,|\, \mathrm{h}(\theta))}}. \tag{5.152}$$

This is the signal-to-noise ratio (SNR) defined in Eq. (5.2), and is calculated by integrating the signal $\mathrm{s}(t)$ against a Wiener optimal filter whose Fourier transform is proportional to $\mathrm{S}_n(f)^{-1} \cdot \tilde{\mathrm{h}}(f;\theta)$. The quantity $\rho[\theta]$ is a random variable with Gaussian PDF of unit variance. Its expected value is zero if no signal is present, when $\mathrm{s}(t) = \mathrm{n}(t)$. If a signal is present, so that Eq. (5.136) holds for some $\tilde{\theta}$, then the expected value of $\rho[\theta]$ is

$$\langle\, \rho[\theta] \,\rangle = \frac{(\mathrm{h}(\theta) \,|\, \mathrm{h}(\tilde{\theta}))}{\sqrt{(\mathrm{h}(\theta) \,|\, \mathrm{h}(\theta))}}. \tag{5.153}$$

Now if the *a priori* probability $p^{(0)}(\tilde{\theta})$ can be approximated to be constant, then the value $\hat{\theta}_{\mathrm{ML}}$ of $\tilde{\theta}$ which maximizes the PDF (5.137) for a given signal s also maximizes $\rho[\theta]$ [59]. Hence we can find $\hat{\theta}_{\mathrm{ML}}$ (up to the overall amplitude of the signal [60]) by computing the overlap (5.152) of the signal with various templates, and by choosing the template which gives the maximum overlap.

When a signal is present and the signal-to-noise ratio is large, the maximum value $\rho[\hat{\theta}_{\mathrm{ML}}]$ of $\rho[\theta]$ will approximately given by

$$\rho[\hat{\theta}_{\mathrm{ML}}]^2 \approx (\mathrm{h}(\tilde{\theta}) \,|\, \mathrm{h}(\tilde{\theta})) \;\approx (\mathrm{h}(\hat{\theta}_{\mathrm{ML}}) \,|\, \mathrm{h}(\hat{\theta}_{\mathrm{ML}})). \tag{5.154}$$

The quantity

$$\rho^2 = (\mathrm{h}(\tilde{\theta}) \,|\, \mathrm{h}(\tilde{\theta})) \tag{5.155}$$

is what is usually referred to as the (square of) the SNR of the signal $\mathrm{h}(t;\tilde{\theta})$. When correlated sources of noise are unimportant so that the matrix (5.130) is diagonal, this overall SNR will be given by combining in quadrature the SNR's for each individual detector, cf. Eq. (5.3) above.

5.5 The Gaussian approximation and conditions for its validity

We now consider the high signal-to-noise limit in which many of the subtleties that we have been discussing become unimportant. In particular, in this limit the Bayes and maximum-likelihood estimators become identical. From Eq. (5.137), the maximum-likelihood estimator $\hat{\theta}_{\rm ML}$ satisfies

$$(\mathbf{h}_{,i}(\hat{\theta}_{\rm ML}) \,|\, \mathbf{h}(\hat{\theta}_{\rm ML}) - \mathbf{s}) - [\ln p^{(0)}]_{,i}(\hat{\theta}_{\rm ML}) = 0, \tag{5.156}$$

where the subscript $,i$ means derivative with respect to θ^i for $1 \le i \le k$, and k is the number of parameters. If the *a priori* information is unimportant so that the last term in Eq. (5.156) is negligible, then as outlined in Sec. 3 the following simple geometric interpretation applies: Let $\mathcal{S}$ be the finite dimensional surface formed by the set of all signals $\mathbf{h}(t;\theta)$ in the space of all possible signals $\mathbf{h}(t)$. Then the measured signal $\mathbf{s}(t)$ will generally not lie on the surface $\mathcal{S}$, and the best-fit point $\mathbf{h}(t;\hat{\theta}_{\rm ML})$ is just that point on $\mathcal{S}$ that is closest to $\mathbf{s}(t)$, where distance is measured with the Euclidean "probability distance" derived from the inner product (5.134). Correspondingly, $\mathbf{h}(\hat{\theta}_{\rm ML})$ can be obtained by just dropping a perpendicular from $\mathbf{s}(t)$ onto the surface $\mathcal{S}$, which is the content of Eq. (5.156) and is illustrated in Fig. 5.1.

When the SNR ρ is sufficiently large, one can find approximate expressions for $\Sigma_{\rm FREQ}[\tilde{\theta}; \hat{\theta}_{\rm ML}(\cdot)]$ and $\Sigma_{\rm BAYES}[\hat{\theta}_{\rm ML}; p^{(0)}(\cdot)]$. Such a calculation has been carried out by Finn [26]. We now briefly outline the calculation, and also extend it to calculate the next to leading order terms in an expansion in $1/\rho$, in order to determine how large ρ needs to be for the leading order term to be a good approximation. Throughout this subsection we assume that the *a priori* PDF $p^{(0)}$ is approximately constant; in subsection 5.6 below we consider the effects of *a priori* knowledge.

First we find an approximate solution to Eq. (5.156). Abbreviating $\hat{\theta}_{\rm ML}$ as $\hat{\theta}$, inserting Eq. (5.136) into Eq. (5.156) and expanding in the difference $\delta\theta = \hat{\theta} - \tilde{\theta}$, we obtain

$$\hat{\theta}^i = \tilde{\theta}^i + \left(\Gamma(\tilde{\theta})^{-1}\right)^{ij} (\mathbf{n} \,|\, \mathbf{h}_{,j}) + \delta^{(2)}\theta^i + O(\mathbf{n}^3). \tag{5.157}$$

Here

$$\Gamma(\tilde{\theta})_{ij} \equiv (\mathbf{h}_{,i}(\tilde{\theta}) \,|\, \mathbf{h}_{,j}(\tilde{\theta})) \tag{5.158}$$

is the so-called Fisher information matrix [cf. Eq. (5.10) above]. The second-order term $\delta^{(2)}\theta$ is

$$\delta^{(2)}\theta^i \;=\; \left(\mathbf{n} \,|\, \mathbf{h}^i{}_j\right) \left(\mathbf{n} \,|\, \mathbf{h}^j\right) \tag{5.159}$$

$$- \quad \left[\left(\mathrm{h}^i{}_j \,|\, \mathrm{h}_k\right) + \frac{1}{2}\left(\mathrm{h}^i \,|\, \mathrm{h}_{jk}\right)\right]\left(\mathrm{n}\,|\,\mathrm{h}^j\right)\left(\mathrm{n}\,|\,\mathrm{h}^k\right).$$

In this expression and below we have for brevity omitted the commas denoting derivatives, and all quantities are evaluated at $\tilde{\theta}$. We lower and raise indices with the tensor (5.158) and its inverse, so that, for example,

$$\mathrm{h}^i_j \equiv \left(\Gamma^{-1}\right)^{ik} \mathrm{h}_{,kj}. \tag{5.160}$$

Equations (5.157) and (5.133) now determine the PDF $p(\hat{\theta}|\tilde{\theta})$. Using Eq. (5.135) and its extension to fourth order moments, and Eqs. (5.157) and (5.140), we obtain

$$\Sigma^{ij}_{\mathrm{FREQ}}[\tilde{\theta}; \hat{\theta}_{\mathrm{ML}}(\cdot)] = (\Gamma^{-1})^{ij} + {}^{(2)}\Sigma^{ij}. \tag{5.161}$$

At leading order, $p(\hat{\theta}|\tilde{\theta})$ is a multivariate Gaussian with mean $\tilde{\theta}$ and variance-covariance matrix given by the first term in Eq. (5.161):

$$\Sigma = \Gamma^{-1}, \tag{5.162}$$

cf. Eq. (5.9) above. The correction term in Eq. (5.161) is

$$\begin{aligned} {}^{(2)}\Sigma^{ij} &= \left(\mathrm{h}^i{}_k \,|\, \mathrm{h}^{jk}\right) - \left(\mathrm{h}^i{}_k \,|\, \mathrm{h}_l\right)\left(\mathrm{h}^{jk} \,|\, \mathrm{h}^l\right) \\ &+ \frac{1}{4}\left(\mathrm{h}^i \,|\, \mathrm{h}^k{}_k\right)\left(\mathrm{h}^j \,|\, \mathrm{h}^l{}_l\right) + \frac{1}{2}\left(\mathrm{h}^i \,|\, \mathrm{h}_{kl}\right)\left(\mathrm{h}^j \,|\, \mathrm{h}^{kl}\right). \end{aligned} \tag{5.163}$$

In the case where there is only one variable so that $\theta = (\theta^1, \ldots, \theta^k) = (\theta^1)$, it follows from Eqs. (5.161) and (5.163) that

$$\Sigma^{11}_{\mathrm{FREQ}} = \frac{1}{(\mathrm{h}' \,|\, \mathrm{h}')}\left[1 + \frac{(\mathrm{h}'' \,|\, \mathrm{h}'')}{(\mathrm{h}' \,|\, \mathrm{h}')^2} - \frac{1}{4}\frac{(\mathrm{h}'' \,|\, \mathrm{h}')^2}{(\mathrm{h}' \,|\, \mathrm{h}')^3}\right], \tag{5.164}$$

where primes denote derivatives with respect to θ^1. The correction terms in the square brackets in this expression will be small whenever

$$||\mathrm{h}''|| \ll ||\mathrm{h}'||^2. \tag{5.165}$$

Using Eqs. (5.134), (5.167), the equation $\rho^2 = (\mathrm{h} \,|\, \mathrm{h})$, and assuming for simplicity that $\mathbf{S}_n(f) = S_n(f)\mathbf{1}$, this reduces to the condition

$$\rho^2 \gg \frac{\langle\langle (\tilde{\mathrm{h}}''^{\dagger} \cdot \tilde{\mathrm{h}}'')/(\tilde{\mathrm{h}}^{\dagger} \cdot \tilde{\mathrm{h}}) \rangle\rangle}{\langle\langle (\tilde{\mathrm{h}}'^{\dagger} \cdot \tilde{\mathrm{h}}')/(\tilde{\mathrm{h}}^{\dagger} \cdot \tilde{\mathrm{h}}) \rangle\rangle^2}, \tag{5.166}$$

where for any function of frequency $F(f)$, we define the weighted average $\langle\langle F(f) \rangle\rangle$ to be $(F\mathrm{h} \,|\, \mathrm{h}) \,/\, (\mathrm{h} \,|\, \mathrm{h})$, i.e.,

$$\langle\langle\, F(f) \,\rangle\rangle \equiv \frac{\int_0^\infty df\, F(f)\, \tilde{\mathrm{h}}^{\dagger} \cdot \mathbf{S}_n^{-1} \cdot \tilde{\mathrm{h}}}{\int_0^\infty df\, \tilde{\mathrm{h}}^{\dagger} \cdot \mathbf{S}_n^{-1} \cdot \tilde{\mathrm{h}}}. \tag{5.167}$$

Equations (5.165) or (5.166) give sufficient conditions for the Gaussian approximation to be valid, when there is only one unknown parameter θ^1. When there are several unknown parameters, a generalization of Eq. (5.165) is obtained by interpreting the prime to mean the operator $v^i\partial/\partial\theta^i$ that differentiates in some direction v^i in the space of parameters θ, and requiring the condition to hold for all directions v^i. This yields the condition

$$||\mathbf{h}_{,ij}\, v^i\, v^j|| \ll ||\mathbf{h}_{,i}\, v^i||^2 = \Gamma_{ij}\, v^i\, v^j, \tag{5.168}$$

which is required to hold for all v^i. We note that, although Eq. (5.161) does correctly indicate the regime (5.166) where the Gaussian approximation is valid, the correction term ${}^{(2)}\Sigma^{ij}$ is *not* an accurate expression for the leading order correction to the measurement accuracy, because as we have argued above the true potential measurement accuracy is given by using the estimator $\hat{\theta}_{\rm BE}(\cdot)$ and not $\hat{\theta}_{\rm ML}(\cdot)$.

One frequent source of confusion about the leading order expression (5.162) for the measurement error is the following. A general theorem in statistics called the Cramer-Rao inequality [27, 56] states that for *any* unbiased estimator $\hat{\theta}$ [61],

$$\Sigma_{\rm FREQ}[\tilde{\theta};\hat{\theta}(\cdot)] \;\geq\; \Gamma(\tilde{\theta})^{-1}. \tag{5.169}$$

Hence, one might imagine that the quantity (5.162) is a lower bound for the accuracy obtainable by most reasonable estimators, and also for low signal-to-noise ratios. That this is not the case can be seen from the following consideration, which we discuss in the body of the paper: at degenerate points $\tilde{\theta}_0$ for which the signal derivatives $\partial\mathbf{h}/\partial\theta^i$ become linearly dependent, the matrix (5.158) becomes degenerate, and the predicted rms errors given by the matrix (5.162) become infinite. More careful calculations of, for example, $\Sigma_{\rm FREQ}[\tilde{\theta};\hat{\theta}_{\rm ML}(\cdot)]$ at such degenerate points, going beyond linear order, give finite results. Hence the inverse of the Fisher matrix is *not* a generic, useful lower bound. The reason that the Cramer-Rao inequality does not apply is that most estimators are not unbiased and cannot easily be made so. When one generalizes the inequality (5.169) to incorporate the effects of bias [56], an extra factor appears on the right-hand side multiplying the Fisher matrix, which can be small. This can allow $\Sigma_{\rm FREQ}[\tilde{\theta};\hat{\theta}(\cdot)]$ to be much smaller than the inverse of the Fisher matrix, for some statistics $\hat{\theta}$.

5.6 Incorporation of *a priori* probabilities

We now turn to the effects of *a priori* information. First, we remark that it is not necessary for *a priori* information to be very detailed or restrictive in order that

it have a significant effect on parameter-extraction accuracy. All that is necessary is that it be more restrictive than the information contained in the waveform, for some of the parameters θ^i. In other words it will be important whenever the statistical error $\langle(\Delta\theta^i)^2\rangle$ which we obtain from Eq. (5.162) for some parameter θ^i is much larger than our *a priori* constraints on θ^i. For example, this would be the case if we obtained rms errors for measurements of the dimensionless spin parameter a of a black hole to be larger than one, since we expect $|a| \leq 1$ always. If we include such poorly determined variables in a calculation of the variance-covariance matrix Σ and neglect the *a priori* restrictions, then the results obtained for the rms error in θ^i may be severely overestimated. This is not unexpected; what is more surprising is that due to the effects of correlations, the rms errors obtained for the other parameters may also be overestimated by large factors (see, e.g., Sec. 3.2 above). We now extend the approximate calculations of the previous subsection to incorporate *a priori* information, and also now calculate Bayesian as well as frequentist errors. Our results in this subsection correct Eq. (3.19) of Ref. [26].

Roughly speaking, *a priori* information will be unimportant when the PDF $p^{(0)}$ does not vary substantially within one or two sigma of the best-fit point $\hat{\theta}$. This condition is logically independent of the condition (5.166), although both will be satisfied in the high ρ limit. Hence, we can treat separately deviations from the leading order measurement accuracy (5.162) that are due to second-order derivatives $\mathbf{h}_{,ij}$ of the signal [cf. Eq. 5.163 above], and that are due to *a priori* information. In the remainder of this subsection we therefore assume the condition (5.166) and consistently neglect all second-order derivatives $\mathbf{h}_{,ij}$. In particular we treat the Fisher matrix (5.158) as a constant in this approximation. [Note that our results will be exact in the case where the dependence of $\mathbf{h}(\tilde{\theta})$ on the parameters $\tilde{\theta}$ is exactly linear, as in Sec. 4.4 above.]

We start by considering the Bayes error (5.142). When we neglect second-order derivatives of $\mathbf{h}$ we find that the PDF (5.137) takes the form

$$p[\tilde{\theta}\,|\,\mathrm{s},\,\mathrm{detection}] = \mathcal{N}'\,p^{(0)}(\tilde{\theta})\,\exp\left[-\frac{1}{2}\Gamma_{ij}(\tilde{\theta}^i - s^i)\,(\tilde{\theta}^j - s^j)\right]. \tag{5.170}$$

Here we have decomposed the measured signal according to

$$\mathbf{s} = s^j\mathbf{h}_{,j} + \mathbf{s}^\perp, \tag{5.171}$$

where $\left(\mathbf{h}_{,i}\,|\,\mathbf{s}^\perp\right) = 0$ for $1 \leq i \leq k$, and have absorbed a factor of $\exp\left[-||\mathbf{s}^\perp||^2/2\right]$ into the normalization constant $\mathcal{N}'$. If the PDF $p^{(0)}$ simply restricts the allowed

ranges of the parameters, then the PDF (5.170) is a truncated Gaussian distribution whose variance-covariance matrix $\Sigma_{\rm BAYES}[\mathbf{s}; p^{(0)}(\cdot)]$ will normally be within a factor of ~ 2 or so of Γ^{-1}. If $p^{(0)}$ is approximately Gaussian with variance-covariance matrix Σ_0, then we see from Eqs. (5.142) and (5.170) that

$$\Sigma_{\rm BAYES}[\mathbf{s}; p^{(0)}(\cdot)] = \left\{\Gamma + \Sigma_0^{-1}\right\}^{-1}. \tag{5.172}$$

This is the formula which we use in Sec. 3.2 above to incorporate our *a priori* knowledge about the spin parameter β.

Next we calculate an approximate expression for the second type of Bayesian error given by Eq. (5.145), which is appropriate for the situation where we discard all information about the measured signal $\mathbf{s}$ except the best estimate values $\hat{\theta}(\mathbf{s})$ of the parameters. For simplicity, we assume that $p^{(0)}(\tilde{\theta})$ is a Gaussian with mean θ_0 and width Σ_0. We also use the maximum-likelihood estimator $\hat{\theta}_{\rm ML}$; however, the same results are obtained for the Bayes estimator $\hat{\theta}_{\rm BE}$. From Eqs. (5.156) and (5.136) and neglecting second-order derivatives of $\mathbf{h}$, we find

$$\left(\Sigma_1^{-1}\right)_{ij} (\hat{\theta}^j_{\rm ML} - \tilde{\theta}^j) = (\mathbf{h}_{,i} \,|\, \mathbf{n}) + \left(\Sigma_0^{-1}\right)_{ij} (\theta_0^j - \tilde{\theta}^j), \tag{5.173}$$

where $\Sigma_1^{-1} \equiv \Gamma + \Sigma_0^{-1}$. Together with Eq. (5.135) this implies that

$$p(\hat{\theta}_{\rm ML}|\tilde{\theta}) \propto \exp\left[-\frac{1}{2}\mathbf{v}^{\rm T} \cdot \Gamma \cdot \mathbf{v}\right], \tag{5.174}$$

where

$$\mathbf{v} = \hat{\theta} - \Sigma_1 \cdot \Gamma \cdot \tilde{\theta} - \Sigma_1 \cdot \Sigma_0^{-1} \cdot \theta_0 \tag{5.175}$$

$$= \Sigma_1 \cdot \Gamma \cdot \left(\tilde{\theta} - \text{ const}\right). \tag{5.176}$$

Using Eqs. (5.140), (5.174), and (5.175) we see that the result (5.161) becomes modified to read

$$\Sigma_{\rm FREQ}[\tilde{\theta}; \hat{\theta}_{\rm ML}(\cdot)] = \Gamma^{-1} + \mathbf{b} \otimes \mathbf{b}, \tag{5.177}$$

where the bias $\mathbf{b} = \Sigma_1 \cdot \Sigma_0^{-1} \cdot (\theta_0 - \tilde{\theta})$. A more interesting quantity is the Bayesian error (5.145), which from Eqs. (5.146) and (5.176) is given by

$$\Sigma_{\rm BAYES}[\hat{\theta}_{\rm ML}; p^{(0)}(\cdot)]^{-1} = \Sigma_{\rm BAYES}[\hat{\theta}_{\rm BE}; p^{(0)}(\cdot)]^{-1} \tag{5.178}$$

$$= \Sigma_0^{-1} + \Gamma \cdot \Sigma_1 \cdot \Gamma \cdot \Sigma_1 \cdot \Gamma.$$

This expression gives approximately the same results as Eq. (5.172), the differences never being more than $\sim 25\%$. The variances Σ^{ii} given by Eq. (5.178) are always

larger than those given by Eq. (5.172), as a result of our having thrown away all the information in s apart from $\hat{\theta}(\mathbf{s})$.

The result (5.178) disagrees with a corresponding analysis of Finn [Eq. (3.19) of Ref. [26]]. The reason for the disagreement is that Finn solves Eq. (5.156) to obtain $\tilde{\theta}$ as a function of $\hat{\theta}_{\rm ML}$ and n, and then invokes the PDF (5.133) of the noise to find $p(\tilde{\theta}|\hat{\theta}_{\rm ML})$. This method of calculation [analogous to the method used for calculating $p(\hat{\theta}_{\rm ML}|\tilde{\theta})$] is invalid because it implicitly assumes that

$$p[\mathbf{n} = \mathbf{n}_0 \,|\, \hat{\theta}_{\rm ML}] \;=\; p[\mathbf{n} = \mathbf{n}_0], \tag{5.179}$$

which is not the case. The fact that Eq. (5.179) does not hold can be seen from the joint PDF for $\tilde{\theta}$, $\hat{\theta}_{\rm ML}$ and n, which is

$$\begin{aligned} p[\hat{\theta}_{\rm ML}, \tilde{\theta}, \mathbf{n}] \;\;\propto\;\; & p^{(0)}(\tilde{\theta})\, e^{-(\mathbf{n}\,|\,\mathbf{n})/2} \\ & \times \delta(\hat{\theta}_{\rm ML} - \hat{\theta}_{\rm ML}[\mathbf{h}(\tilde{\theta}) + \mathbf{n}]). \end{aligned} \tag{5.180}$$

5.7 Treatment of degenerate variables

As we have noted in Sec. 4.4, the accuracy of the linear approximation (5.168) which yields the simple PDF (5.170), depends in part on what set of variables θ^i are used in the calculation. A different PDF will be obtained from this approximation if one first makes a non-linear change of co-ordinates $\theta^i \rightarrow \bar{\theta}^i(\theta^j)$. Hence, the PDF (5.170) will approximate most closely the true PDF when it is computed using variables for which $\mathbf{h}_{,ij}$ is as small as possible.

Consequently, there are two qualitatively different ways in which the linear approximation may break down. First, for sufficiently low signal-to-noise ratios, the extrinsic curvature of the surface $\mathcal{S}$ formed by the set of waveforms $\mathbf{h}(t;\theta)$ may be sufficiently large that Eq. (5.168) is not a good approximation for *any* set of coordinates θ^i. In this case the "Gaussian" method breaks down completely. Second, the approximation may break down simply because of a bad choice of coordinates. This is usually the case at points of degeneracy where the vectors $\mathbf{h}_{,i}$ become linearly dependent, which we discuss in Secs. 3 and 4 and at the end of Sec. 5.5 above. At such points the linear approximation method breaks down, but can usually be remedied by making such a nonlinear change of variables. One then obtains a PDF in terms of the original variables which is non-Gaussian, as in Sec. 4.4 above, from which measurement errors can be calculated. As has been pointed out by Marković [9], measurement errors at such points typically scale like $1/\sqrt{\rho}$ instead of like $1/\rho$.

APPENDIX B: APPROXIMATE CONSTANCY OF THE SPIN PARAMETER β THAT INFLUENCES THE WAVEFORM'S PHASE

The leading order contribution of the bodies' spins to the secular growth of the gravitational-wave phase has been derived by Kidder, Will and Wiseman [41], and is given by the term proportional to $4\pi - \beta$ in Eq. (5.59). The quantity β is defined by Eq. (5.60) and depends on the masses of the two bodies M_1 and M_2, their spins $\vec{S}_1$ and $\vec{S}_2$, and the unit vector in the direction of the orbital angular momentum $\hat{L}$. Over the course of the inspiral β will evolve, because the directions of the vectors $\hat{L}$, $\vec{S}_1$, $\vec{S}_2$ will be changing due to spin-orbit and spin-spin interactions.

Nevertheless, in our analysis in the body of the paper, we have assumed that the factor $\chi = 4\pi - \beta$ which appears in Eq. (5.59) can be treated as constant. This assumption is necessary to make the analysis tractable. In this appendix, we present evidence which strongly suggests that χ is always constant apart from some small amplitude oscillations, showing that our assumption of constant χ is a reasonable one for all coalescing binaries. We calculate the evolution of χ by integrating the orbit-averaged equations (3.2) governing the evolution of the spins, using both analytic and numerical methods. A more complete discussion of the evolution of the spins and orbital angular momentum, and of their influence on the emitted gravitational waves, can be found in Ref. [43].

We start by introducing some dimensionless variables. Let $\hat{S}_j$ be the unit vector in the direction of $\vec{S}_j$ for $j = 1, 2$, and define

$$\alpha_1 = \hat{S}_1 \cdot \hat{L}, \tag{5.181}$$

$$\alpha_2 = \hat{S}_2 \cdot \hat{L}, \tag{5.182}$$

$$\alpha_3 = \hat{S}_1 \times \hat{S}_2 \cdot \hat{L}, \tag{5.183}$$

and

$$\alpha_4 = \hat{S}_1 \cdot \hat{S}_2. \tag{5.184}$$

The α_j's are not all independent variables as they satisfy the constraint

$$\alpha_1^2 + \alpha_2^2 + \alpha_3^2 + \alpha_4^2 = 1 + 2\,\alpha_1\alpha_2\alpha_4. \tag{5.185}$$

The reason that it is convenient to use these variables is the following. The spin-evolution equations (3.2) comprise nine equations in nine unknowns, with

three conserved quantities (the magnitudes of the three vectors). Thus, there are effectively six degrees of freedom. If we specify the three independent values of the variables $\alpha_1, \ldots, \alpha_4$, then the remaining three degrees of freedom can be parametrized by an overall rotation matrix. More precisely, given the vectors $\hat{S}_1$, $\hat{S}_2$ and $\hat{L}$, there will be a unique rotation matrix $\mathbf{R}$ which takes $\hat{L}$ into $\hat{L}' = \hat{e}_z$ (the unit vector along the z axis), $\hat{S}_1$ into a vector $\hat{S}_1'$ in the x-z plane, and $\hat{S}_2$ into some $\hat{S}_2'$. The vectors $\hat{S}_1$, $\hat{S}_2$ and $\hat{L}$ are determined by $\mathbf{R}$ and by the variables $\alpha_1, \ldots, \alpha_4$. Hence, the variables $\alpha_j(t)$ for $1 \leq j \leq 4$ and $\mathbf{R}(t)$ can be used instead of the vectors themselves to parameterize a solution to the spin-evolution equations. Now it turns out that the evolution of the α_j's *decouples* from the evolution of $\mathbf{R}$, in the sense that each $d\alpha_j/dt$ depends only on $\alpha_1, \ldots, \alpha_4$ and is independent of $\mathbf{R}$. This greatly simplifies our analysis.

If we use units in which $M = 1$ and define $s_j = |\vec{S}_j|$ for $j = 1, 2$, then we obtain from Eqs. (3.2), (5.181) and (5.13) the following coupled system of equations for $\alpha_1, \ldots, \alpha_4$:

$$\frac{d\alpha_1}{dr} = \frac{-15}{128\mu}\left[\frac{1}{M_2} - \frac{s_1\alpha_1}{L}\right] s_2\alpha_3 \tag{5.186}$$

$$\frac{d\alpha_2}{dr} = \frac{15}{128\mu}\left[\frac{1}{M_1} - \frac{s_2\alpha_2}{L}\right] s_1\alpha_3 \tag{5.187}$$

$$\frac{d\alpha_4}{dr} = \frac{-15\alpha_3}{128\mu}\left[\left(\frac{M_2}{M_1} - \frac{M_1}{M_2}\right) L + s_1\alpha_1 - s_2\alpha_2\right]. \tag{5.188}$$

Here $L \equiv \mu\sqrt{r}$ denotes the magnitude of the orbital angular momentum, and we have changed the dependent variable from time t to orbital separation r. The omitted equation for $d\alpha_3/dr$ can be obtained by combining Eqs. (5.185) – (5.188). From Eq. (5.60), the spin parameter β is given in terms of these variables by

$$\begin{aligned}\beta &= \frac{113}{12}(s_1\alpha_1 + s_2\alpha_2) \\ &\quad + \frac{25}{4M_1M_2}\left(M_2^2 s_1\alpha_1 + M_1^2 s_2\alpha_2\right).\end{aligned} \tag{5.189}$$

We have numerically integrated the equations (5.186) – (5.188) for various initial spin and angular momentum directions, for the cases of NS-NS, NS-BH and BH-BH binaries. We assumed all neutron stars have masses of $1.4\,M_\odot$, and black holes have masses $10\,M_\odot$. We integrated inwards, starting at that value of r at which the emitted waves enter the LIGO/VIRGO waveband at 10 Hz, and ending at $r = 6M$ near the last stable circular orbit [30]. In the special case that one of the spins vanishes, it can be seen from Eqs. (3.2) and (5.60) that β will be conserved

[43]. Hence we took both spins to be non-vanishing. We also assumed that their magnitudes are maximal, so that $s_j = M_j^2$ for $j = 1, 2$ [cf. Sec. 3.2], as these are the values which can be expected to give the largest changes in β.

Typical results are shown in Figs. 5.18 - 5.19. The factor $\chi = 4\pi - \beta$ undergoes small oscillations with an amplitude of order 0.1 which is small compared to the mean value of χ. This mean value depends on the mass ratio and on the initial spin directions, but always lies between $4\pi - \beta_{\max} \approx 3$ and $4\pi + \beta_{\max} \approx 22$, where $\beta_{\max}$ is as given in Sec. 3.2. The angles between the vectors given by $\alpha_1, \ldots, \alpha_4$ also oscillate, all with the same frequency. [This frequency is *not* the frequency with which the total spin $\vec{S} = \vec{S}_1 + \vec{S}_2$ precesses around $\vec{L}$ [43], as that precession does not change the angles between the vectors, and thus is not described by Eqs. (5.186) – (5.188)].

Some insight into the behavior of the general solutions to Eqs. (5.186) – (5.188) can be gained by considering the special case when the magnitude of one of the spins (say $\vec{S}_1$) is small, so that $s_1 \equiv |\vec{S}_1|/M^2 \ll 1$. This condition will sometimes be satisfied by NS-NS and BH-BH binaries, but will always be satisfied by NS-BH binaries since all compact bodies satisfy $|\vec{S}_j| \lesssim M_j^2$. Now it is possible to perturbatively analyse the equations and find approximate analytic solutions, to first order in s_1; these will be close to the true solutions when $s_1 \ll 1$. As we now describe, in this approximation the amplitude of the oscillations of β (and hence also of χ) is always smaller than $\sim 1/4$, for all initial spin directions and for all mass-ratios. Although rapidly spinning NS-NS and BH-BH binaries will not satisfy $s_1 \ll 1$, nevertheless we find that amplitudes of the oscillations of β in the numerical solutions agree roughly with those predicted by the small spin approximation. [For some special initial spin directions, such as $\alpha_1 = \alpha_3 = 0$, the analytic solutions are poor approximations to the numerical solutions, but in all such cases that we have checked, the amplitudes of the β oscillations are still $\lesssim 0.2$]

The solutions to first order in s_1 can be written as

$$\alpha_j(r) = \alpha_j^{(0)}(r) + \alpha_j^{(1)}(r)\, s_1 + \mathcal{O}(s_1^2), \tag{5.190}$$

for $1 \leq j \leq 4$. Now as we have already mentioned, it can be seen from Eqs. (3.2) and (5.60) that when $s_1 = 0$, the angle between $\vec{S}_2$ and $\vec{L}$ is conserved, so that β is constant. However, in this case the angles between the small spin $\vec{S}_1$ and the other two vectors will not be conserved. Thus, the zeroth order solutions $\alpha_j^{(0)}$ will be non-constant. We start by deriving these solutions.

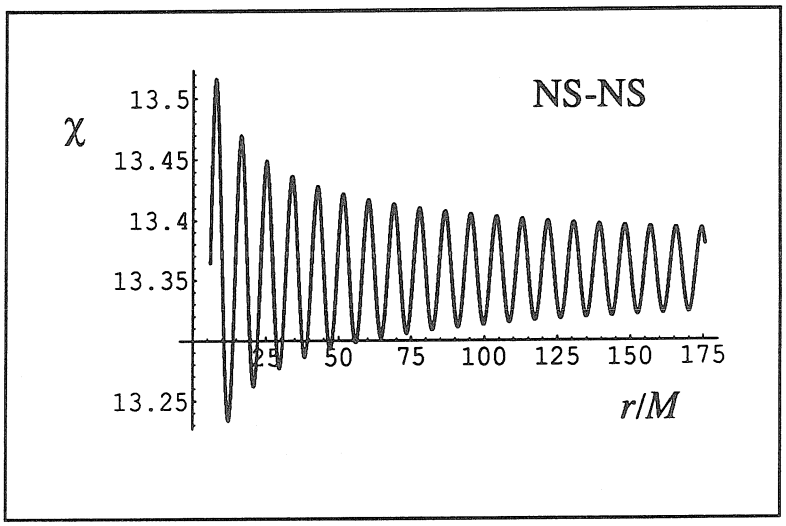

Figure 5.18: During the last few minutes of inspiral, the angles between the bodies' spins $\vec{S}_1$, $\vec{S}_2$ and the orbital angular momentum $\vec{L}$ all oscillate, in addition to and separately from the precession of the total spin $\vec{S} = \vec{S}_1 + \vec{S}_2$ around $\vec{L}$. This oscillation gives rise to an oscillation of the parameter $\chi = 4\pi - \beta$ which governs the contribution of the spins to the accumulated phase of the emitted gravitational waves [cf. Eq. (5.59)]. Here we show a typical plot of χ as a function of the orbital separation r, for a NS-NS binary. The spin and orbital angular momentum directions were taken to be $\vec{S}_1 \propto \vec{i} + \vec{k}$, $\vec{S}_2 \propto -\vec{j}$ and $\vec{L} \propto \vec{i} + \vec{j}$ at the initial gravitational wave frequency of 10 Hz. The spin of each neutron star was assumed to have the maximal magnitude of $(1.4M_\odot)^2$, corresponding to a rotation period of a few miliseconds. It can be seen that in each case the amplitude of oscillation of χ is very small compared to its mean value, so that to a good approximation we can take $\chi =$ constant.

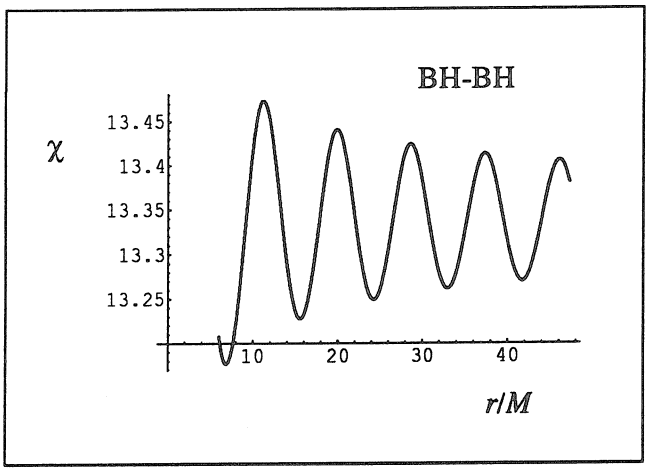

Figure 5.19: The evolution of χ for a BH-BH binary; see caption of Fig. 5.18. Both black holes were assumed to be maximally rotating.

Substituting $s_1 = 0$ into Eqs. (5.186) - (5.188) we find that $\alpha_2^{(0)}$ is constant, i.e., $\alpha_2^{(0)} = \alpha_{2,i} \equiv \alpha_2(r_i)$, where r_i is the initial orbital separation, and that

$$\frac{d\alpha_1^{(0)}}{dr} = -h_1 \alpha_3^{(0)} \tag{5.191}$$

$$\frac{d\alpha_4^{(0)}}{dr} = -h_4 \alpha_3^{(0)}. \tag{5.192}$$

Here

$$h_1 = -\frac{15 s_2}{128 \mu M_2}, \tag{5.193}$$

$$h_4 = \frac{15}{128 \mu} \left(s_2 \alpha_{2,i} + L\, \delta \right), \tag{5.194}$$

and $\delta \equiv (M_1^2 - M_2^2)/(M_1 M_2)$. The coefficient h_4 is non-constant as $L = \mu\sqrt{r}$ depends on r. However, since it will typically vary slowly compared to the oscillations in the angles, we can approximate it to be constant. [The evolution of h_4 gives rise to a slow evolution in the amplitude and frequency of the oscillations of the $\alpha_j^{(0)}$'s]. Defining

$$\alpha_\pm \equiv h_4 \alpha_1^{(0)} \pm h_1 \alpha_4^{(0)} \tag{5.195}$$

we find that $\alpha_-(r)$ is constant, $\alpha_-(r) = \alpha_{-,i} \equiv \alpha_-(r_i)$, and

$$\frac{d\alpha_+}{dr} = -2h_1 h_4 \alpha_3^{(0)}. \tag{5.196}$$

This equation can be solved by combining it with the constraint (5.185). To zeroth order in s_1, the constraint can be expressed using Eq. (5.195) in the form

$$\alpha_3^{(0)}(r)^2 + \nu^2 \left[\alpha_+(r) - \hat{\alpha}_+\right]^2 = \kappa^2, \tag{5.197}$$

where

$$\nu = \frac{\nu_0}{2h_1 h_4}, \tag{5.198}$$

$$\nu_0^2 = h_1^2 + h_4^2 - 2h_1 h_4 \alpha_{2,i}, \tag{5.199}$$

$$\kappa^2 = 1 - \alpha_{2,i}^2 - (1 + \alpha_{2,i}^2)\frac{\alpha_{-,i}^2}{\nu_0^2}, \tag{5.200}$$

$$\hat{\alpha}_+ = -(h_1^2 - h_4^2)\frac{\alpha_{-,i}}{\nu_0^2}. \tag{5.201}$$

Combining Eqs. (5.196) and (5.197) yields the solutions

$$\alpha_3^{(0)}(r) = \alpha_{3,i}\cos\Phi + \nu(\alpha_{+,i} - \hat{\alpha}_+)\sin\Phi \tag{5.202}$$

$$\alpha_+(r) = \hat{\alpha}_+ - \frac{\alpha_{3,i}}{\nu}\sin\Phi + (\alpha_{+,i} - \hat{\alpha}_+)\cos\Phi, \tag{5.203}$$

where $\alpha_{+,i} = \alpha_+(r_i)$, $\alpha_{3,i} = \alpha_3(r_i)$, and

$$\Phi = \nu_0(r - r_i). \tag{5.204}$$

Note that ν_0 is the frequency of oscillation of the $\alpha_j^{(0)}$'s — frequency with respect to changing orbital radius r, not changing time t.

Analytic expressions for the functions $\alpha_1^{(0)}, \ldots, \alpha_4^{(0)}$ can now be obtained by combining Eqs. (5.193) - (5.195) and (5.198) - (5.203). These expressions depend in a complex way on all of the initial spin direction parameters $\alpha_{1,i}$, $\alpha_{2,i}$ and $\alpha_{4,i}$, and also on s_2, on the mass ratio M_1/M_2, and on the initial orbital separation r_i/M. For the equal mass case $M_1 = M_2$, the "frequency" ν_0 is given by

$$\nu_0^2 = \frac{s_2^2}{M_2^2}\left[\frac{255}{4096} + \frac{1125}{16384}\alpha_{2,i}^2\right]. \tag{5.205}$$

Values of ν_o for $M_1 \neq M_2$ are typically much larger than this.

The first-order corrections $\alpha_j^{(1)}(r)$ can be obtained using the zeroth order solutions and Eqs. (5.186) - (5.188). However, we are only interested in determining

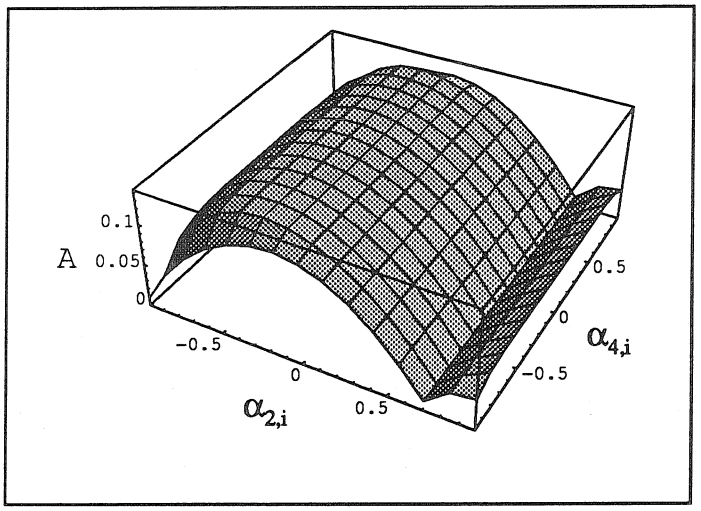

Figure 5.20: When one of the spins is small, the evolution of the parameter $\chi = 4\pi - \beta$ is approximately given by $\chi = \chi_0 + \mathcal{A}\cos[\nu_0 r + \text{const}]$, where the "frequency" ν_0 and amplitude $\mathcal{A}$ are slowly varying functions of r. Here we show the amplitude $\mathcal{A}$ for an equal-mass binary, at an orbital separation of $r = 6M$, as a function of $\alpha_{2,i} = \hat{S}_2 \cdot \hat{L}$ and $\alpha_{4,i} = \hat{S}_1 \cdot \hat{S}_2$, where the maximum is taken over the remaining angles.

the leading order behavior of β, and for this purpose we need only evaluate $\alpha_2^{(1)}$. From Eqs. (5.187) and (5.202), this is given by

$$\begin{aligned}\alpha_2^{(1)}(r) &= \frac{15}{128\mu\nu_0}\left[\frac{1}{M_1}-\frac{s_2\alpha_{2,i}}{L}\right] \\ &\quad\times\left[\alpha_{3,i}\sin\Phi-\nu\left(\alpha_{+,i}-\hat{\alpha}_+\right)(\cos\Phi-1)\right].\end{aligned} \tag{5.206}$$

Substituting Eqs. (5.206) and (5.198) – (5.203) into (5.189) gives a result of the form

$$\beta(r)=A+B\cos\Phi+C\sin\Phi, \tag{5.207}$$

where the constants B and C are first order in s_1. The resulting expression for the total amplitude of oscillation $\mathcal{A}=\sqrt{B^2+C^2}$ in terms of the variables $\alpha_{1,i},\ldots,\alpha_{4,i}$, M_1/M_2 and r is complicated and not very illuminating, so we do not reproduce it here. Instead we show in Figs. 5.20 and 5.21 the quantity $\mathcal{A}_{\max}=\mathcal{A}_{\max}[\alpha_{2,i},\alpha_{4,i}]$ obtained in the following way: (i) Use Eq. (5.185) to eliminate $\alpha_{3,i}$ in terms of $\alpha_{1,i}$, $\alpha_{2,i}$ and $\alpha_{4,i}$. (ii) Numerically maximize over values of $\alpha_{1,i}$ that lie in the range between the values $\alpha_{2,i}\,\alpha_{4,i}\pm\sqrt{(1-\alpha_{2,i}^2)(1-\alpha_{4,i}^2)}$ allowed by Eq. (5.185). (iii) Choose the maximal spin magnitudes $s_1=M_1^2$, $s_2=M_2^2$. (iv) Choose the final orbital separation $r=6M$, the value for which the amplitude $\mathcal{A}$ will most likely be largest. It can be seen from these plots that for all choices of initial conditions, $\mathcal{A}\leq 0.25$.

In the special case that $M_1=M_2$, the formulae simplify and we find that $\mathcal{A}\propto 1/\sqrt{r}$ (this is not true in general). Specifically we find in this case that

$$\begin{aligned}B &= \frac{376}{384\sqrt{r}}\Big[\alpha_{1,i}\,\alpha_{2,i}-2\alpha_{4,i} \\ &\quad+\frac{15}{128}\left(4-\alpha_{2,i}^2\right)\left(\alpha_{1,i}\,\alpha_{2,i}+2\alpha_{4,i}\right)\nu_0^{-2}\Big],\end{aligned} \tag{5.208}$$

and

$$C=-\frac{235}{512}\,\frac{\alpha_{2,i}\,\alpha_{3,i}}{\sqrt{r}\nu_0}, \tag{5.209}$$

where ν_0 is given by Eq. (5.205).

To summarize, we have determined the evolution of the quantity $\chi=4\pi-\beta$ both numerically, for a wide range of initial conditions, and analytically, in the regime where $|\vec{S}_1|\ll M^2$. In all cases we find that the amplitude of the oscillations of χ is ≤ 0.25.

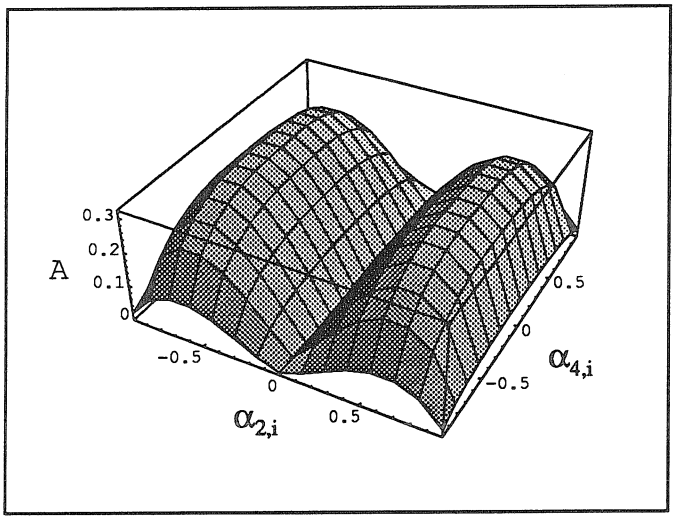

Figure 5.21: As in Fig. 5.20, but for a NS-BH binary with $M_1/M_2 = 1.4/10$.

APPENDIX C: THE DECOUPLING OF PHASE AND AMPLITUDE PARAMETERS IN THE FISHER INFORMATION MATRIX

The phase $\Psi(f)$ of the Fourier transform of the waveform can be written in the form

$$\Psi(f) = \sum_{n=1,2,\cdots} c_n (f/f_0)^{\alpha_n}, \tag{5.210}$$

where $(\alpha_1, \alpha_2, \alpha_3, \ldots) = (0, 1, -5/3, -1, -2/3, \ldots)$, and the parameters c_1, c_2, c_3, c_4 etc. are simply related to the parameters ϕ_c, t_c, $\mathcal{M}$, μ, β etc., via Eq. (5.65). The number of variables c_n will depend on the post-Newtonian order to which $\Psi(f)$ is calculated; the following analysis holds for any number of these variables. We can make a linear transformation to new variables

$$d_m = U_m^{\ n} c_n \tag{5.211}$$

in such a way that

$$\frac{\partial \mathbf{h}}{\partial d_1} = \frac{\partial \mathbf{h}}{\partial c_1} = i\mathbf{h}, \tag{5.212}$$

and that for $m \geq 2$ [49],

$$\left(i\mathrm{h}\left|\frac{\partial \mathrm{h}}{\partial d_m}\right.\right) \propto \sum_n (\mathbb{U}^{-1})^n{}_m \int_0^\infty df\, \frac{|\tilde{h}_0|^2}{S_n(f)}(f/f_0)^{\alpha_n} = 0. \tag{5.213}$$

The key point now is that the inner product

$$\Gamma_{am} = \left(\frac{\partial \mathrm{h}}{\partial \mu^a}\left|\frac{\partial \mathrm{h}}{\partial d_m}\right.\right),$$

where μ^a is any of the "amplitude" parameters D, ψ, v and d_1, will also be proportional to the right-hand side of Eq. (5.213) for $m \geq 2$, and so will vanish. This can be seen from the structure of Eq. (5.73). Consequently, in the new variables D, v, ψ, and d_m, $m = 1, 2, \ldots$, the Fisher matrix (5.158) will be block diagonal, which establishes the result stated in Sec. 4.3.

Bibliography

[1] R. Narayan, T. Piran, and A. Shemi, Astrophys. J. **379**, L17 (1991).

[2] E. S. Phinney, Astrophys. J. **380**, L17 (1991).

[3] A. Abrmovici, W. E. Althouse, R. W. P. Drever, Y. Gürsel, S. Kawamura, F.J. Raab, D. Shoemaker, L. Sievers, R. E. Spero, K. S. Thorne, R. E. Vogt, R. Weiss, S. E. Whitcomb, and M. E. Zucker, *LIGO: The Laser Interferometer Gravitational-wave Observatory*, Science **256**, 325 (1992).

[4] C. Bradaschia *et al.*, Nucl. Instrum. & Methods **A289**, 518 (1990); also in *Gravitation: a Banff Summer Institute*, ed. R. Mann and P. Wesson (World Scientific, Singapore, 1991).

[5] A. V. Tutukov and L. R. Yungelson, Mon. Not. R. Astron. Soc. **260**, 675 (1993).

[6] B.F. Schutz, Nature **323**, 310 (1986); B.F. Schutz, Class. Quantum Gravity **6**, 1761 (1989).

[7] Y. Gursel and M. Tinto, Phys. Rev. D **40**, 3884 (1990).

[8] C. Cutler, T. A. Apostolatos, L. Bildsten, L. S. Finn, É. E. Flanagan, D. Kennefick, D. M. Marković, A. Ori, E. Poisson, G. J. Sussman, and K. S. Thorne, Phys. Rev. Lett. **70**, 2984 (1993).

[9] D. Marković, Phys. Rev. D., in press.

[10] B. F. Schutz, *Hubble Constant from Gravitational Wave Observations*, in H. Sato and T. Nakamura, Eds., *Gravitational Collapse and Relativity*, (World Scientific, Singapore), pp. 350-368.

[11] D.F. Chernoff and L.S. Finn, Astrophys. J. **411**, 5 (1993).

[12] K.S. Thorne, in *300 Years of Gravitation*, ed. S.W. Hawking and W. Israel (Cambridge University Press, Cambridge, 1987), pp. 330-458.

[13] C. Cutler, L. S. Finn, E. Poisson and G. J. Sussman, Phys. Rev. D **47**, 1151 (1993).

[14] L. S. Finn and D. F. Chernoff, Phys. Rev. D **47**, 2198 (1993).

[15] P. Jaranowski and Andrzej Krolak, *Optimal Solution to the Inverse Problem for the Gravitational Wave Signal of a Coalescing Compact Binary*, in preparation.

[16] P. C. Peters, Phys. Rev. **136**, B1224 (1964).

[17] However eccentricities may not be negligible for binaries formed in dense star-clusters in galactic nuclei; see G. D.Quinlan and S.L. Shapiro, Astrophys. J **321**, 199 (1987).

[18] L. Bildsten and C. Cutler, Astrophys. J. **400**, 175 (1992).

[19] C. Kochanek, Astrophys. J., **398**, 234 (1992).

[20] A rapidly rotating neutron star will be somewhat oblate, and therefore, compared to a point-mass, its potential energy will be modified by a term proportional to its quadrupole moment times the second derivative of the gravitational potential at its center-of-mass [18]. However this correction to the orbital energy is of second post-Newtonian order, and thus is of higher order than the other post-Newtonian effects considered in this paper.

[21] L. A. Wainstein and V. D. Zubakov,*Extraction of Signals from Noise* (Dover Publications, Inc., New York, 1962).

[22] E. Flanagan and K. S. Thorne, in preparation.

[23] K.S. Thorne, private communication.

[24] The noise spectrum to which Eq. (5.5) is an approximate analytic fit is given by the sum of the following terms from Ref. [14]: Eq. (4.1), with parameters $\eta I_0 = 60\,\mathrm{W}$, $L = 4\,\mathrm{km}$, $f_c = 130\,\mathrm{Hz}$, $\lambda = 5.1 \times 10^{-7}\,\mathrm{m}$, and $A^2 = 5 \times 10^{-5}$; Eq. (4.3) with the modifications to Eq. (4.2) of $f_0 \to f^2/f_0$ in the numerator and $f f_0/Q_0 \to f_0^2/Q_0$ in the denominator, and with parameters $Q_0 = 10^9$, $T = 300\,^\circ\mathrm{K}$, $f_0 = 1\,\mathrm{Hz}$; and Eq. (4.4), similarly modified, with parameters

$f_{\rm int} = 14\,{\rm kHz}$ and $Q_{\rm int} = 10^6$. Eqs. (4.2) and (4.4) are modified in order to describe structural damping [25] which is now thought to be the likely dominant damping mechanism in the thermal modes [23].

[25] P.R. Saulson, Phys. Rev. D **42**, 2437 (1990).

[26] L. S. Finn, Phys. Rev. D **46**, 5236 (1992).

[27] S.V. Dhurandhar, A. Krolak, B.F. Schutz and W.J. Watkins, *Gravitational Wave Astronomy with Broadband Detectors. I. Extraction of Coalescing Binary Signals*, in preparation.

[28] Note that this definition differs by a factor of two from that found in Ref. [26]. Our definition is chosen to correspond to the quadratic form "$x_i(\Sigma^{-1})_{ij}x_j$" which appears in finite-dimensional Gaussian PDFs, cf. Eq. (5.133) above.

[29] L.S. Finn, A. Ori, and K.S. Thorne, unpublished.

[30] The last stable circular orbit is not exactly at $r = 6M$ because of the fact that r is the orbital separation in de Donder gauge and not the Schwarschild radius, and also because of the finite mass-ratio. However, this orbit will be close to $r = 6M$; see L. E. Kidder, C. M. Will and A. G. Wiseman, Class. Quant. Grav. **9**, L125 (1992).

[31] The calculation is simplified if one first defines the moments

$$\overline{f^k} \equiv \frac{\left(f^k h \,|\, h\right)}{(h\,|\,h)},$$

where the inner product (|) is given by Eq. (5.6). As pointed out by Finn and Chernoff [14], all the elements of Γ_{ij} can expressed in terms of the orbital parameters and a few of the moments $\overline{f^k}$. This continues to hold true when post-Newtonian corrections are added to the signal. A useful identity is $\left(f^j h \,|\, i f^k h\right) = 0$ for all real j and k, by Eq. (5.6).

[32] R. V. Wagoner and C. M. Will, Astrophys. J **210**, 764 (1976); **215**, 984 (1977).

[33] A. G. Wiseman, Phys. Rev. D **46**, 1517 (1992).

[34] E. Poisson, Phys. Rev. D **47**, 1497 (1993).

[35] A. Krolak in *Gravitational Wave Data Analysis*, ed. B. F. Schutz (Reidel 1989), p. 59.

[36] R. Epstein and R. V. Wagoner, Astrophys. J **197**, 717 (1975), and **215**, 984 (1977).

[37] In fact, due to the spin-induced precession of the orbital plane described in Sec. 3.2, in general k will be a slowly varying function of time instead of a constant. We neglect this small effect.

[38] L. Blanchet and T. Damour, Phys. Rev. D **46**, 4304 (1992).

[39] Somewhat inconsistently, we neglect the delta-function contribution to the derivatives $\partial\tilde{h}(f)/\partial\mathcal{M}$ and $\partial\tilde{h}(f)/\partial\mu$ that comes from varying the cut-off frequency. While a sharp cut-off gives a acceptable approximation to $h(f)$ (and is easy to work with analytically), it gives a terrible approximation for the derivatives of $h(f)$. Our somewhat careless attitude towards the high-frequency end of the waveform is justified by the fact that the detector noise $S_n(f)$ rises steeply at high frequency, so very little signal-to-noise is accumulated there.

[40] The pattern of how the predicted rms errors change, when one includes extra variables in the calculation of the Fisher matrix (5.10) which are strongly correlated with the original variables, can be simply understood by considering the approximation in which all but two of the variables are fixed. The predicted measurement accuracy for a variable x, when its correlations with other variables are neglected, is $\delta x = (h_{,x}|h_{,x})^{-1/2}$. When we include the effects of correlations with another variable y, described by the correlation coefficient

$$c_{xy} = \frac{\Sigma^{xy}}{\sqrt{\Sigma^{xx}\Sigma^{yy}}} = -\frac{(h_{,x}|h_{,y})}{\sqrt{(h_{,x}|h_{,x})\,(h_{,y}|h_{,y})}},$$

then from Eqs. (5.10) and (5.11) we find that: (i) The rms error in x is now $\Delta x = \delta x/\sqrt{1-c_{xy}^2}$, and thus is increased by a large factor if $|c_{xy}|$ is close to one; and (ii) if $1 - c_{xy}^2 \ll 1$, the eigenvalues of the variance-covariance matrix (5.162) are approximately $(\delta x^{-2} + \delta y^{-2})^{-1}$ and $(\delta x^2 + \delta y^2)/(1 - c_{xy}^2)$, where $\delta y = (h_{,y}|h_{,y})^{-1/2}$. Thus, if δx and δy are comparable, one linear combination of x and y will be measurable with an accuracy comparable to δx, i.e., that accuracy predicted when correlations are neglected; and the orthogonal linear combination will have an rms error that is larger than this by a factor $\sim 1/\sqrt{1-c_{xy}^2}$.

[41] L. E. Kidder, C. M. Will and A. G. Wiseman, Phys. Rev. D **47**, R4183 (1993).

[42] B. M. Barker and R. F. O'Connell, Gen. Rel. and Grav. **11**, 149 (1979).

[43] T. A. Apostolatos, C. Cutler, G. J. Sussman, and K. S. Thorne, in preparation.

[44] A. Krolak, J. A. Lobo, B. J. Meers, Phys. Rev. D **43**, 2470 (1991).

[45] R. L. Forward, Phys. Rev. D **17**, 379 (1978).

[46] In this section we interpret the parameter t_c to be the time at which the coalescence would be observed by a hypothetical detector at the origin of spatial coordinates $\mathbf{x}$.

[47] We use a definition of the polarization angle ψ which differs from that in Ref. [12] by 90°, which accounts for the fact that our χ_+ and $\chi_\times$ are given by the expressions in Ref. [12] interchanged with one sign flipped.

[48] Other detector network parameters, such as the distances between the detectors, affect strongly the angular resolution $\Delta\mathbf{n}$ of measurements of sky location, but affect only weakly the distance measurement accuracies. This is due to the decoupling discussed in Sec. 4.3 and Appendix C.

[49] We have here ignored the fact that a factor of $\mathcal{M}^{5/6}$ appears in the signal amplitudes; this is unimportant because $\mathcal{M}$ will be measured to much higher relative accuracy ($\sim 10^{-3}$) than the amplitudes ($\sim 10^{-1}$). In other words we in fact calculate $\Delta D_1/D_1$, where $D_1 \equiv D\mathcal{M}^{-5/6}$; for all practical purposes this is the same as $\Delta D/D$.

[50] In fact we have compared the values of ΔD given by the approximation used in Ref. [9] to those given by Eq. (5.105), and found that they never differ by more than 10% for any values of σ_D, ε_D, v, and ψ.

[51] Another way to think about this is to associate a signal-to-noise ratio with each polarization component (with respect to fiducial axes determined by the detector network, cf. Eq. (5.89) above) of the incident waves; the distance measurement accuracy will essentially be determined by the smaller of the two signal-to-noise ratios.

[52] It is simplest to calculate this prefactor using the variables α and β defined by Eq. (5.100) instead of D and v. In fact it diverges at $v = 1$, because of the fact that $\partial\mathbf{h}/\partial\psi \propto \partial\mathbf{h}/\partial\phi_c$ in this limit. This divergence would seem to contradict our claim that the prefactor does not depend strongly on v and D.

In the special case where $\varepsilon_D = 0$, a more careful calculation of the integral over ψ and ϕ_c (without first expanding to quadratic order in $\psi - \psi_0$ and $\phi_c - \phi_{c0}$) shows that the effective prefactor remains finite at $v = 1$; we expect similar behavior for $\varepsilon_D \neq 0$. In the case $\varepsilon_D = 0$ we obtain

$$p(v, D) \propto p^{(0)}(v, D) F(\omega\hat{\omega})\, F(\zeta\hat{\zeta})\, e^{-(\Delta\omega^2 + \Delta\zeta^2)/2},$$

where $\omega = (\alpha + \beta)/\sqrt{2\sigma_D} r_0$, $\zeta = -(\alpha - \beta)/\sqrt{2\sigma_D} r_0$, and $\hat{\omega}$, $\Delta\omega$ etc. are similarly defined in terms of $\hat{\alpha}, \hat{\beta}$ [cf. Eqs. (5.118) and (5.119) above] and $\Delta\alpha \equiv \alpha - \hat{\alpha}$, $\Delta\beta \equiv \beta - \hat{\beta}$. The prefactor function F is

$$\begin{aligned} F(x) &\equiv \frac{1}{2\pi} \int_0^{2\pi} e^{-x(1-\cos\theta)} d\theta \\ &\approx \begin{cases} \frac{1}{\sqrt{2\pi x}} & x \gg 1 \\ 1 - x & x \ll 1. \end{cases} \end{aligned}$$

Thus the prefactor is regular and slowly varying despite the apparent divergence $\propto 1/\sqrt{\zeta} \propto 1/(1 - v)$ that would be obtained by doing a Gaussian integral over the angles ψ and ϕ_c.

[53] T. Loredo, in *Statistical Challenges in Modern Astronomy*, Eds. E.D. Feigelson and G.J. Babu, Springer-Verlag, New York (1992).

[54] M. H. A. Davis, in *Gravitational Wave Data Analysis*, Ed. B.F. Schutz, Kluwer Acad. Pub. (1989).

[55] B. S. Sathyaprakash and S. V. Dhurandhar, Phys. Rev. D 44, 3819 (1991).

[56] C. W. Helstrom, *Statistical Theory of Signal Detection* (Pergamon Press, 2nd ed., 1968).

[57] B. F. Schutz, in *The Detection of Gravitational Radiation* (Cambridge University Press, Cambridge, England, 1989).

[58] F. Echeverria, Phys. Rev. D **40**, 3914 (1989).

[59] F. Echeverria, unpublished Ph.D. thesis, California Institute of Technology, addendum to Ch. 2 (1993).

[60] In fact this method can determine all the parameters $\theta = (\theta^1, \ldots, \theta^k)$, *except* for the overall amplitude of the signal which drops out of Eq. (5.152). To obtain the overall amplitude one must use Eq. (5.156); see Ref. [59] for more details.

[61] Throughout this paper we use the term *Fisher matrix* to refer to the matrix (5.158); strictly speaking, this term as defined in, e.g., Ref. [56] refers to a quantity which coincides with the matrix (5.158) only when the noise is Gaussian. The Cramer-Rao inequality is usually stated in terms of this more general Fisher matrix.

[62] For an example of such a Monte-Carlo simulation, see K. Kokkotas, A. Krolak, and G. Tsegas, in preparation.

Table 1: The rms errors for signal parameters and the correlation coefficient $c_{\mathcal{M}\mu}$, calculated assuming spins are negligible. The results are for a single "advanced" detector, the shape of whose noise curve is given by Eq. (5.4). M_1 and M_2 are in units of solar masses, while Δt_c is in units of msec. The rms errors are normalized to a signal-to-noise ratio of $S/N = 10$; the errors scale as $(S/N)^{-1}$, while $c_{\mathcal{M}\mu}$ is independent of S/N.

M_1	M_2	$\Delta\phi_c$	Δt_c	$\Delta\mathcal{M}/\mathcal{M}$	$\Delta\mu/\mu$	$c_{\mathcal{M}\mu}$
2.0	1.0	1.31	0.721	0.0038 %	0.39 %	0.899
1.4	1.4	1.28	0.713	0.0040 %	0.41 %	0.906
10	1.4	1.63	1.01	0.020 %	0.54 %	0.927
15	5.0	2.02	1.44	0.113 %	1.5 %	0.954
10	10	1.98	1.43	0.16 %	1.9 %	0.958

Table 2: The rms errors for signal parameters and the correlation coefficients $c_{\mathcal{M}\mu}$, $c_{\mathcal{M}\beta}$, and $c_{\mu\beta}$, calculated using spin-dependent waveforms. The results are for a single "advanced" detector, the shape of whose noise curve is given by Eq. (5.4). For the rows marked with a † (and *only* for those rows), the variance-covariance matrix has been "corrected" to approximately account for the fact that the spin parameter β must satisfy $|\beta| < \beta_{max} \approx 8.5$. The rms errors are normalized to a signal-to-soise ratio of $S/N = 10$. Except for rows marked with a †, errors scale as $(S/N)^{-1}$, while the correlation coefficients are independent of S/N. Except for rows marked with a †, if β had been chosen non-zero with M_1 and M_2 unchanged, then $\Delta\mathcal{M}/\mathcal{M}$, $\Delta\mu/\mathcal{M}$, and $c_{\mathcal{M}\mu}$ would have been unchanged (but $\Delta\beta$, $c_{\mathcal{M}\beta}$, and $c_{\mu\beta}$ would have been altered). As in Table I, M_1 and M_2 are in units of $M_\odot$, while Δt_c is in msec. The results for the LIGO/VIRGO network of detectors, for a signal with combined signal-to-noise ratio from all the detectors of 10, will be approximately the same as those shown here; see text.

M_1	M_2	β	$\Delta\phi_c$	Δt_c	$\Delta\mathcal{M}/\mathcal{M}$	$\Delta\mu/\mu$	$\Delta\beta$	$c_{\mathcal{M}\mu}$	$c_{\mathcal{M}\beta}$	$c_{\mu\beta}$
2.0	1.0	0	4.13	1.14	0.034 %	8.44 %	1.04	-0.988	0.993	-0.9989
1.4	1.4	0	4.09	1.13	0.034 %	9.65 %	1.24	-0.988	0.993	-0.9991
10	1.4	0	6.24	2.03	0.19 %	15.2 %	1.99	-0.990	0.994	-0.9994
5	1.4	0	4.89	1.44	0.10 %	13.4 %	1.73	-0.989	0.994	-0.9992
15	5	0	9.26	3.53	1.06 %	76.4 %	11.4	-0.992	0.994	-0.99980
15	5	0 †	5.77	2.40	0.64 %	45.8 %	6.81	-0.978	0.984	-0.9995
10	10	0	9.26	3.53	1.42 %	125 %	19.5	-0.992	0.994	-0.99988
10	10	0 †	4.13	1.92	0.59 %	49.9 %	7.79	-0.953	0.964	-0.9992

Table 3: Measurement accuracies, including spins, as in Table II except that we the take shape of the noise curve to be given by Eq. (5.5).

M_1	M_2	β	$\Delta\phi_c$	Δt_c	$\Delta\mathcal{M}/\mathcal{M}$	$\Delta\mu/\mu$	$\Delta\beta$	$c_{\mathcal{M}\mu}$	$c_{\mathcal{M}\beta}$	$c_{\mu\beta}$
2.0	1.0	0	2.21	0.47	0.021 %	5.12 %	0.641	-0.986	0.992	-0.9988
1.4	1.4	0	2.19	0.46	0.021 %	5.84 %	0.757	-0.986	0.992	-0.9990
10	1.4	0	3.90	1.06	0.13 %	10.1 %	1.33	-0.990	0.994	-0.9993
5	1.4	0	2.81	0.66	0.065 %	8.47 %	1.11	-0.988	0.993	-0.9992
15	5	0	6.72	2.40	0.75 %	55.1 %	8.18	-0.992	0.994	-0.99980
15	5	0 †	4.95	1.85	0.55 %	39.7 %	5.90	-0.985	0.989	-0.9996
10	10	0	6.72	2.40	1.00 %	90.0 %	14.0	-0.992	0.994	-0.99988
10	10	0 †	3.71	1.49	0.53 %	46.7 %	7.27	-0.972	0.978	-0.9995